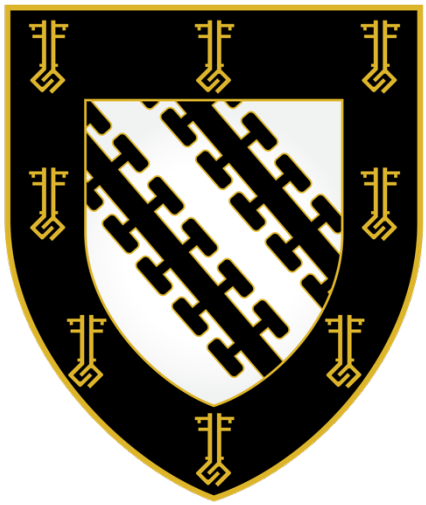
Investigation of autoantibodies to soluble, onconeural or transmembrane autoantigens in patients with autoimmune-mediated neurological diseases

Pao-Sheng Chang





Exeter College, University of Oxford

Oxford Autoimmune Neurology Group

Nuffield Department of Clinical Neurosciences





Trinity 2022

Dedication

To my wife Jiahui (Shirley) Huang, my parents and wider family, my supervisors and colleagues in lab

I am very grateful for your physical and emotional supports all the way through my DPhil journey especially during the unexpected Covid-19 strike

Many thanks, I love you all!

Abstract

Antibodies in patients with PNS or antibody mediated autoimmune disease are polyclonal and bind different protein epitopes. Some are linear and flexible while others are rigid or made up of loops that only come together in three-dimensional space in the native protein structure. Methods where the antigen is denatured, such as western blot, where detergent is used to extract the target from cells, or reagents, such as formaldehyde, are used to preserve test substrates are inferior to live cell-based assays (CBA). Regardless of whether the epitope is linear and flexible, or rigid, or conformational, the native protein provides targets for both antibody types. Modifying the target structure in any way reduces the test accuracy, hence live CBAs are the gold-standard for antibody detection in patients with autoimmune antibody associated diseases. These tests can also be applied to soluble molecules such as leucine-rich, glioma inactivated 1 (LGI1) by linking it to the cell membrane. In this thesis, live assays for the detection of autoantibodies to soluble cytokines, integral membrane proteins and onconeural antigens were developed. The association of cytokine antibodies and thymoma is concluded, the ability to express cytosolic and nuclear proteins on the surface of a cell for antibody detection is demonstrated for the first time for onconeural antibodies and a multiplex flow assay for the detection of antibodies to aquaporin-4 (AQP4) or myelin oligodendrocyte glycoprotein (MOG) in the same sample has been developed.

The cytokine assay includes an extracellular myc-tag to evaluate surface expression of each cytokine. Assays for autoantibodies to IL-6, IL-12, IL-17A, IL-17F, IL-22, IL-23, IFNα2, IFNα8 and IFNω1 were developed and autoantibodies to IFNα2 and IL-12 were found most frequently in patients with a thymoma. In a cohort of 126 autoimmune

myasthenia gravis (aMG) patients, the assay sensitivities were 80% and 64% respectively. In the same cohort, 93.3% of aMG patients with both autoantibodies had been diagnosed with thymoma. It was hoped that these cytokine antibodies could predict a relapse in patients after thymectomy, but the endpoint titres of autoantibodies to IFNα2 and IL-12 from most TAMG patients were above the cut-offs years after patients' thymectomy. Regarding the detection of cytokine autoantibodies, there was excellent correlation between the newly developed live CBAs and luciferase immunoprecipitation system (LIPS), with the benefit that the multi-subunit cytokines, e.g., IL-12 and IL-23, could be assayed by our live CBAs as IL-12B homodimer, or IL-12 and IL-23 heterodimers.

Multiple live CBAs for onconeural antibodies were developed including HuD, NOVA1, CRMP5, CDR2L, Amphiphysin and ZIC4, all of which were expressed above the surface of HEK293T cells. They were incorporated into a vector that included a CASPR2 signal sequence for surface expression and a CASPR2 transmembrane and cytosolic domain to retain the proteins on near the cell surface and an eGFP tag to locate transfected cells in this transient transfection system. The same strategy did not work for Ma1, Ma2, CDR2, SOX1 and KLHL11 but they did over-express as cytosolic antigens. The main reason for surface expression of these targets is to eliminate the background of cytosol and nuclear staining seen in fixed CBAs and immunohistochemistry (IHC).

Our live CBAs identified all antibody positive samples sent from two centres of excellence in Spain and USA (cohorts with 69 serum and 21 CSF samples in total). In addition, our live CBAs didn't pick up 8/12 samples, which had been identified seropositive by line blots only (HuD Ab+, n=1, NOVA1 Ab+, n=1; CDR2 Ab+, n=5;

Amphiphysin Ab+, n=1), from patients without high-risk PNS and tumour. Therefore, our eGFP-tagged live CBAs are diagnostically more specific than line blots for the prediction of tumours and are multiplexable compared to tissue-based fixed IHC.

In order to quantitate and multiplex these assays a quadruplex CBA and flow cytometry assay were developed. The quadruplex CBA depended on specific localisation of transfection reagent while the flow cytometry system required addition of colour to distinguish cells transfected with different antibody targets. CellTrace Violet dye proved useful for color-coding cell populations. The quadruplex assay (HuD, NOVA1, Amphiphysin and CDRL2) by either CBA or flow cytometry were able to reproduce data from individual assays.

Lastly, we applied DsRed2 reporter to live flow cytometry CBA (F-CBA) for detecting autoantibodies to AQP4 M23 and MOG α1 isoforms. Our live AQP4 F-CBA was very sensitive with high signal-to-noise ratio, but our live MOG F-CBA had a higher background, as expected from the literature. This duplex test requires further optimisation before being implemented in a routine diagnostic laboratory. To summarize, this thesis narrates the developments and screening results of our live and permeabilized CBAs for detecting autoantibodies to soluble cytokines, onconeural antigens and transmembrane proteins. The CBAs we developed could also benefit clinicians to predict the corresponding tumours for early and better managements.

Declaration

I declare that this thesis submitted for Doctoral of Philosophy (DPhil) degree in Clinical Neurosciences at the University of Oxford is the results of my own original works unless otherwise stated. Figures and tables that have been adapted from studies previously published by others have been acknowledged and appropriately referenced. As a member of Oxford Autoimmune Neurology Group (OANG), my experiments were performed at Nuffield Department of Clinical Neurosciences (NDCN), under the supervision of Dr. Patrick Joseph Waters and Professor Maria Isabel Leite. The funding was generously provided by Nuffield Department of Clinical Neurosciences, University of Oxford and Ministry of Education in Taiwan. At the time of writing up this thesis, none of the results have been published elsewhere. Also, I hereby state that no part of this thesis has been submitted for any other degree at this or any other university. This thesis has approximately 46500 words (excluding references).

Covid-19 Impact Statements

The Covid-19 pandemic began when I was at the 2nd year of my DPhil research journey. Firstly, my DPhil project was an entirely lab-based project that required continuous access to laboratory facilities. This was, however, not possible from early March 2020 to end August 2020 when the labs were shut down completely due to the pandemic. This resulted in the loss of 6 months of time to run experiments. In my case, I didn't pass my first transfer in January 2020 due to the high risk of my proposed study and the immaturity of my preliminary data. Hence during lockdown period, I worked consistently to rearrange my old data, and propose a new project about Good's syndrome. However, around August 2020, my supervisor Dr. Patrick Waters considered the limited amount of remaining time, I then began to work with Dr. Hannah Fox - a post-doctoral researcher in our group, on a paraneoplastic project, and we completed the molecular cloning works together after the labs re-opened in end August 2020.

Although I passed my second transfer in October 2020 with presenting a new proposal, the drastic change of my research trajectory made me really panic, worrying that I wouldn't be able to compensate the time I loss during the lockdown. Besides, although the labs re-opened in September 2020, they were running below full capacity, in accordance with recommended safety guideline, especially as our labs based in a hospital facility, which required more stringent safety measures. However, I have kept moving forward conscientiously to produce sufficient data for my thesis writing. In fact, the data in chapter IV and V had been generated from September 2020 to early April 2022 (around one and a half years in total). I understand that more research questions can be investigated, and more works can be done in my research field (for instance,

surface express the onconeural antigens, which weren't successfully expressed with using the original method), but I have put in everything to produce 3 result chapters (story lines) for my DPhil thesis despite having the limited amount of time.

To me, the pandemic and its protracted lockdown have affected my productivity, both in the lab and in writing up this thesis, and to some extent on the state of my mental health. However, it is beyond my expectation that I have been able to complete my DPhil research and writing up so far, and I am so grateful for the physical and mental supports from my supervisors - Dr. Patrick Waters and Prof. Maria Isabel Leite, my partner, family and close friends.

Acknowledgements

I would like to take this opportunity to express my appreciation to my wife Jiahui (Shirley) Huang, my parents and wider family, who have given me lots of confidence and reassurance for me to achieve the highest academic degree in Oxford. They always tell me to trust in myself and never give up becoming the person I would like to be. Here, I want to thank my wife Shirley, who has accompanied me during the tough times of my DPhil study. Thank you for your unconditional and self-sacrificial love for us to mutually grow and edify one another. I am so glad to have you as a part of my life for going through the ups and downs together in the following decades. Also, the emotionally supports from my parents in Taiwan have contributed lots to my daily momentum and perseverance. Although I haven't seen them for a long time due to the pandemic, they encouraged me frequently during our video chats and helped me with my finance after the end of my funding period. I can't wait to meet them in Taiwan during this Christmas to share all the exciting things Shirley and I have experienced in Oxford.

Moreover, my supervisors have also played an important role for me finish my study in Oxford. I still remember in November 2017 Professor Maria Isabel Leite responded to my email with a warm greeting and encouragement for me to pursue a DPhil degree in Oxford. Also, I am grateful to my primary supervisor Dr. Patrick Waters (Paddy), who has patiently guided me step by step to think and communicate as a scientist. When I failed my first transfer, Paddy encouraged me a lot saying he would support my works and intensify our regular meetings. Every time we discussed my works, he always challenged my scientific thinking and reminded me to stick on the topic when answering questions. The habit of critical thinking has not only improved my academic

works but also transformed me as a problem-solver in my daily life. Without the supervision from my supervisors, I would never imagine completing my DPhil study in Oxford.

Furthermore, I would like to thank my colleagues and friends in NDCN. Each of them has inspired me a lot during their academic talks and our conversations. All of them are opened to questions and happy to help each other out. Here, I specially thank Dr. Hannah Fox, who guided and worked with me for a period of time to develop a paraneoplastic CBA panel. In addition, I would like to thank my funding bodies in UK and Taiwan to sponsor my living expenses for 3 years and 6 months. Last but not least, I would like to give thanks to my St. Andrew's church family, bible study home group and pastor Dan Heyward for consistently praying for my study, relationship and personal wellbeing in the recent years. In the end, I want to thank my Lord Jesus Christ, providing me with all the wisdoms and wonderful people in my life. Thank you for leading me to a tough but achievable journey for molding me to become a better person and scientist.

Table of Contents

Dedication……2

Abstract……3

Declaration……6

Covid-19 Impact Statements……7

Acknowledgements……9

Table of Contents……11

List of Abbreviations……17

List of Figures……20

List of Tables……25

1. Chapter I: General Introduction……27

1.1. Autoimmune-mediated neurological diseases ……28

1.2. Paraneoplastic neurological syndromes ……31

1.2.1. The evolution of PNS diagnostic criteria……32

1.2.2. Immunology of PNS……40

1.2.3. Pathology of autoimmune myasthenia gravis - a lower-risk PNS ……42

1.2.4. Autoimmune-mediated demyelinating diseases with lower-risk autoantibodies……45

1.2.4.1. NMOSD……45

1.2.4.2. MOGAD……47

1.2.5. Therapeutic strategies……48

1.3. Methods for detecting autoantibodies……49

1.3.1. Methods for detecting autoantibodies to soluble cytokines……49

1.3.2. Methods for detecting autoantibodies to onconeural antigens……51

1.3.3. Methods for detecting autoantibodies to transmembrane proteins……52

1.3.4. Multiplex technologies for detecting autoantibodies……....53
1.4. DPhil Research Rationales……..…54
1.5. Principle Aims…….……..54
2. Chapter II: Materials and Methods…….…55
2.1. Clinical Materials ……..……....56
2.2. In-house Methods and Materials…….……..56
2.2.1. Molecular cloning……56
2.2.1.1. Restriction enzyme based cloning…….……56
2.2.1.1.1. Polymerase chain reaction (PCR).…….……..56
2.2.1.1.2. Gel electrophoresis……57
2.2.1.1.3. Gel extraction……...58
2.2.1.1.4. Restriction enzyme digestion……59
2.2.1.1.5. Ligation……59
2.2.1.2. Site-directed mutagenesis (SDM)……..60
2.2.1.2.1. SDM-PCR……60
2.2.1.2.2. Kinase, ligase & DpnI (KLD) treatment……60
2.2.1.3. Transformation and plating……61
2.2.1.4. Colony PCR……..61
2.2.1.5. Plasmid amplification……..62
2.2.1.5.1. Miniprep……62
2.2.1.5.2. Maxiprep..……63
2.2.1.6. Sanger sequencing……..64
2.2.2. Cell-based assay (CBA) ……64
2.2.2.1. Culture of HEK293T cells……64
2.2.2.2. Poly-L-lysin coating……..65

2.2.2.3. Transient transfection……..66
2.2.2.4. Methods for detecting antibody binding by CBA……67
2.2.2.4.1. Live CBA……...67
2.2.2.4.2. Permeabilized CBA……..70
2.2.2.5. Imaging, scoring and data analysis……73
2.2.3. Flow cytometry CBA (F-CBA)……...75
2.2.3.1. Cell culture, transfection and harvest……75
2.2.3.2. Methodologies of F-CBA……..75
2.2.3.2.1. Methods for labelling dead cells……75
2.2.3.2.2. Methods for detecting antibody binding……77
2.2.3.2.2.1. Live F-CBA……..77
2.2.3.2.2.2. Permeabilized F-CBA…….....78
2.2.3.2.3. Strategies of gating and analysis……..80
3. Chapter III: Detection of autoantibodies to soluble cytokines associated with thymoma in patients with autoimmune myasthenia gravis……83
3.1. Introduction……...84
3.1.1. Autoimmune myasthenia gravis……..84
3.1.2. Autoantibodies to soluble cytokines associated with thymoma…….85
3.2. Research Rationales……..86
3.3. Study Aims……...87
3.4. Methods. ……..87
3.4.1. Samples……..87
3.4.2. Construct design……88
3.4.2.1. The DsRed2-reporting cytokine surface expression platform…...88
3.4.2.2. Flexible amino acid extension……88

3.4.2.3. The myc-tagged cytokine surface expression platform……89
3.4.3. The myc-tagged live CBA to detect autoantibodies to soluble cytokines……91
3.4.4. Luciferase immunoprecipitation system (LIPS) assay……93
3.5. Results……95
3.5.1. Development of live cell-based assays for detecting autoantibodies to soluble cytokines……95
3.5.2. Attempt to improve CBA sensitivity by extending the flexible amino acid linker……97
3.5.3. Introduction of a myc tag to quantify cytokine surface expression…….99
3.5.4. Quantification of cytokine surface expression by endpoint titrating DyLight 550 anti-myc tag antibody……...104
3.5.5. Autoantibodies to soluble cytokines among healthy individuals were not discriminated by age……106
3.5.6. Autoantibodies to IFNαs and IL-12 were better diagnostic biomarkers to predict the presence of thymoma……..110
3.5.7. Live CBA and LIPS assays showed good correlations……..116
3.6. Discussion……..120
4. Chapter IV: Detection of onconeural autoantibodies in patients with paraneoplastic neurological syndromes……124
4.1. Introduction……..……125
4.1.1. Paraneoplastic neurological syndromes……..…...125
4.1.2. The available methods to detect onconeural autoantibodies……127
4.2. Research Rationales……128
4.3. Study Aims……..129

4.4. Methods……..129
4.4.1. Samples……129
4.4.2. Construct design……..131
4.4.3. Cell-based Assay (CBA) ……132
4.4.3.1. eGFP-tagged simplex live CBAs……..133
4.4.3.2. eGFP-tagged live quadruplex CBAs……134
4.5. Results……136
4.5.1. The eGFP-tagged live and permeabilized cell-based assays to detect onconeural autoantibodies……136
4.5.2. Live CBA results: Barcelona cohort……..145
4.5.3. Live CBA results: Mayo Clinic cohort……155
4.5.4. The eGFP-tagged quadruplex live CBA for detecting autoantibodies to HuD NOVA1, CDR2L and CRMP5 simultaneously……162
4.6. Discussion……..167
5. Chapter V: Flow cytometry cell-based assays to detect autoantibodies……..170
5.1. Introduction……171
5.2. Research Rationales……172
5.3. Study Aims……..173
5.4. Methods……..173
5.4.1. Samples……173
5.4.2. Construct design……..175
5.4.3. Flow cytometry CBA (F-CBA) ……176
5.4.3.1. Methods for color-coding cells……..176
5.4.3.2. Methods for detecting multiple autoantibodies via F-CBA……177
5.4.3.3. Strategies of gating and analysis…… 181

5.5. Results……...186
5.5.1. The simplex eGFP-tagged live F-CBA to detect HuD autoantibodies..186
5.5.2. Optimization of live CRMP5 F-CBA……..190
5.5.3. Development of live cell-labelling protocol for multiplex purposes…..197
5.5.4. The eGFP-tagged quadruplex live F-CBA for simultaneously detecting autoantibodies to HuD, Amphiphysin, NOVA1 and CDR2L…….202
5.5.5. The quadruplex permeabilized F-CBA for simultaneously detecting autoantibodies to CRMP5, SOX1, Ma1 and Ma2…….210
5.5.6. The DsRed2-reporiting simplex live F-CBAs for detecting autoantibodies to AQP4 M23 and MOG α1 isoforms…….216
5.6. Discussion……..227
6. General Discussion…….231
6.1. Summary and discussion of key findings……232
6.1.1. Myc-tagged, surface expressed cytokines in live CBAs detect autoantibodies and predict the presence of thymoma 232
6.1.2. Live eGFP-tagged CBAs were superior to line blots for antibody detection in PNS patients ……235
6.1.3. The F-CBAs were developed to quantify autoantibodies binding under simplex and multiplex settings…….236
6.2. Research Limitations…….239
6.3. Future Avenues……..240
7. Appendix…….242
8. References……,,,….261

List of Abbreviations

AA	Antibiotic-antimycotic
Ab	Antibodies
AChR	Acetylcholine receptor
ADEM	Acute disseminated encephalomyelitis
AIRE	Autoimmune regulator
aMG	Autoimmune myasthenia gravis
ANA	Anti-nuclear antibodies
AQP4	Aquaporin-4
AutoAb	Autoantibodies
BSA	Bovine serum albumin
CASPR2	Contactin-associated protein-like 2
Cas9	CRISPR-associated protein 9
CBA	Cell-based assay
CDR2	Cerebellar degeneration related protein 2
CDR2L	Cerebellar degeneration related protein 2 like
CRISPR	Clustered regularly interspaced short palindromic repeats
CRMP5	Collapsin response mediator protein 5
DAPI	4′,6-diamidino-2-phenylindole
DC	Dendritic cells
DMEM	Dulbecco's Modified Eagle Medium
ELISA	Enzyme-linked immunosorbent assay
FBS	Fetal bovine serum
F-CBA	Flow cytometry CBA
GBS-BE	Guillain-Barré syndrome spectrum disorder with brainstem encephalitis

HGG	Hypogammaglobulinemia
IHC	Immunohistochemistry
IIF	Indirect immunofluorescence
KLHL11	Kelch like family member 11
LB	Line blots
LETM	Longitudinally extensive transverse myelitis
LGI1	Leucine rich glioma inactivated 1
LIPS	Luciferase immunoprecipitation system
LRP5	Low-density lipoprotein receptor-related protein 4
MG	Myasthenia gravis
MOG	Myelin oligodendrocyte glycoprotein
MOGAD	MOG antibody-associated disease
mTEC	Medullary thymic epithermal cells
MuSK	Muscle-specific tyrosine kinase
NIR	Near infrared
NMDAR	N-methyl-D-aspartate receptors
NMOSD	Neuromyelitis optica spectrum disorder
NOVA1	NOVA alternative splicing regulator 1
NPV	Negative predictive values
PCD	Paraneoplastic cerebellar degeneration
PNS	Paraneoplastic neurological syndromes
PPV	Positive predictive values
RIA	Radioimmunoassay
RyR	Ryanodine receptor
SCLC	Small-cell lung cancer

SFEMG Single-fiber electromyography

SOX1 SRY-related HMG-box 1

WB Western blots

7-AAD 7-amino-actinomycin D

List of Figures

Figure 1.1: The overview of my DPhil research……31

Figure 1.2: The flow chart of classifying the suspected PNS patients into definite or possible PNS group……37

Figure 2.1: The DsRed2-reporting live CBA to detect IL-22 IgG autoantibodies……69

Figure 2.2: The eGFP-tagged permeabilized CBA for detecting IgG autoantibodies to intracellular antigen……..71

Figure 2.3: Example of CBA scoring……..74

Figure 2.4: The step-by-step gating strategies of F-CBA……81

Figure 3.1: The cDNA sequence synthesized by IDT gBlocks technology……..89

Figure 3.2: The steps to remove the cDNA of DsRed2……...90

Figure 3.3: The myc-tagged live CBA to detect cytokine autoantibodies……..……..92

Figure 3.4: The luciferase immunoprecipitation system (LIPS) assay to detect cytokine autoantibodies……...94

Figure 3.5: The live cell-based assays for detecting autoantibodies to IFNα2 and IL-12……..……..96

Figure 3.6: Live CBAs versus LIPS assays for detecting autoantibodies to IFNα2, IL-12 and IL-22……...96

Figure 3.7: Improving IL-12 autoantibodies detection through linker extension……..98

Figure 3.8: Introducing a myc tag into live IL-22 CBA……...100

Figure 3.9: Optimizing the staining protocol to resolve non-specific binding…….103

Figure 3.10: Quantifying cytokine surface expressions by endpoint titrating DyLight 550 anti-myc tag antibody……...105

Figure 3.11: The mutated myc tag hindered the access of DyLight 550 anti-myc tag antibody……..106

Figure 3.12: The results of our myc-tagged live CBAs to detect cytokine autoantibodies when screening healthy sera……..……109
Figure 3.13: The correlations between the endpoint titres of autoantibodies to IFNα2, IFNα8, IFNω1 and IL-12……..112
Figure 3:14: The sensitivity and specificity of our myc-tagged live CBAs for detecting autoantibodies to IFNα2 and IL-12……113
Figure 3.15: The endpoint titre distributions of autoantibodies to IFNα2 and IL-12..114
Figure 3.16: The endpoint titres of autoantibodies to IFNα2 and IL-12 remained high years after thymectomy……...115
Figure 3.17: The percentage of samples picked up by live CBAs and LIPS assays……116
Figure 3.18: The correlations between live CBAs and LIPS assays for detecting autoantibodies to IFNα2 and IL-12……117
Figure 3.19: Our live IL-12 CBA recognized autoantibodies to either IL-12 heterodimer or IL-12B homodimer……..118
Figure 4.1: The design of HuD surface expression construct……..132
Figure 4.2: The eGFP-tagged simplex live CBA to detect onconeural autoantibodies……134
Figure 4.3: The eGFP-tagged quadruplex live CBA to detect onconeural autoantibodies……136
Figure 4.4: The eGFP-tagged live CBAs could detect the commercial antibodies to surface-expressing HuD, NOVA1, CRMP5, CDR2L, ZIC4 and Amphiphysin……137
Figure 4.5: The eGFP-tagged live CBAs couldn't detect the commercial antibodies to intracellular Ma1, Ma2, CDR2, SOX1 and KLHL11……..138

Figure 4.6: The eGFP-tagged permeabilized CBAs could detect the commercial antibodies to intracellular Ma1, Ma2, CDR2, SOX1 and KLHL11……..139
Figure 4.7: DyLight 594 anti-human IgG Fc antibody produced lower CBA cut-offs than AF568 anti-human IgG (H+L) antibody……..140
Figure 4.8: The high background noise in permeabilized Ma1 CBA was evident compared to live NOVA1 CBA despite applying DyLight 594 anti-human IgG Fc antibody……...141
Figure 4.9: The permeabilized CBAs identified samples from patients with both PNS and tumours…..……...143
Figure 4.10: The results of eGFP-tagged live CBAs to detect onconeural autoantibodies in Barcelona samples……148
Figure 4.11: The correlations between the results from live CBAs and line blots….154
Figure 4.12: The results of live CBAs to detect onconeural autoantibodies in Mayo Clinic samples……...157
Figure 4.13: The correlations between the endpoint titres of live CBAs and IIFs from Mayo Clinic samples……161
Figure 4.14: The eGFP-tagged quadruplex live CBA for detecting autoantibodies to HuD, NOVA1, CDR2L and CRMP5 simultaneously……...163
Figure 4.15: The quadruplex live CBA generated comparable endpoint titres compared to individual simplex live CBAs……165
Figure 5.1: Methods of multiplex live and permeabilized F-CBAs……...180
Figure 5.2: The step-by-step gating strategies of eGFP-tagged quadruplex live F-CBA……...183
Figure 5.3: The step-by-step gating strategies of quadruplex permeabilized F-CBA……...184

Figure 5.4: The simplex live F-CBA to detect HuD autoantibodies……186
Figure 5.5: The titration results between using DyLight 594 or PE anti-human IgG Fc as secondary antibody……..……188
Figure 5.6: A pilot live HuD F-CBA screen to detect HuD autoantibodies……189
Figure 5.7: The strategy to expose the C-terminal epitopes of CRMP5……192
Figure 5.8: The new eGFP-tagged live CRMP5 F-CBA improved the binding of CRMP5 autoantibodies……..193
Figure 5.9: The permeabilized CRMP5 F-CBA further improved the access of CRMP5 autoantibodies to CRMP5……..195
Figure 5.10: The permeabilized CRMP5 F-CBA was the optimal assay to detect CRMP5 autoantibodies……196
Figure 5.11: CellTrace Violet was the optimal live cell-labelling dye for multiplex purposes……198
Figure 5.12: The octaplex live cell-labelling method was developed……..201
Figure 5.13: The results of quadruplex live F-CBA for detecting autoantibodies to HuD, Amphiphysin, NOVA1 and CDR2L……..204
Figure 5.14: The ΔMFI_x from quadruplex live F-CBA correlated well with the 1:20 CBA visual scores from live CBAs for detecting autoantibodies to HuD, Amphiphysin, NOVA1 and CDR2L……208
Figure 5.15: The results of quadruplex permeabilized F-CBA for detecting autoantibodies to CRMP5, SOX1, Ma1 and Ma2……213
Figure 5.16: The DsRed2-reporting simplex live F-CBAs for detecting autoantibodies to AQP4 M23 and MOG α1 isoforms……217
Figure 5.17: Live AQP4 M23 F-CBA was robust and correlated well with live AQP4 M23 CBA……219

Figure 5.18: Live MOG α1 F-CBA couldn't' distinguish the samples between MOG α1 Ab CBA+ and double negative cohorts with the cut-off……..221
Figure 5.19: The Duplex live F-CBA for simultaneously detecting autoantibodies to AQP4 M23 and MOG α1 isoforms……..……...223
Figure 5.20: Our duplex live F-CBA presented similar results with using 1:100 diluted AF488 anti-human IgG1 antibody……..226

List of Tables

Table 1.1: Summary of common classical and non-classical PNS……32

Table 1.2: Summary of onconeural autoantibodies and their associated tumour..…33

Table 1.3: PNS Care scoring system…….39

Table 1.4: 2015 revised criteria for diagnosing NMOSD……...46

Table 2.1: PCR program……..57

Table 2.2: Summary of the restriction enzymes used in my research……..59

Table 2.3: SDM-PCR program……60

Table 2.4: Methods of transient transfection in 6- and 96-well plate…….67

Table 2.5: Methods of live CBA. Applied to 24- and 96-well plate…….69

Table 2.6: Methods of permeabilized CBA applied to 24- and 96-well plate……...71

Table 2.7: Summary of the commercial antibodies used in CBAs…….72

Table 2.8: Summary of the viability dyes used in F-CBAs……..76

Table 2.9: Summary of the commercial antibodies used in F-CBAs…….78

Table 3.1: Classification of autoimmune myasthenia gravis……..85

Table 3.2: Demographics of the participants at the time of sampling……...88

Table 3.3: Methods of myc-tagged live CBA applied to 24- and 96-well plate……92

Table 3.4: The number and percentages of CBA positive aMG samples in each cohort…….111

Table 3.5: Summary of autoantibodies to IFNα2 and/or IL-12 in each cohort……...114

Table 4.1: Summary of onconeural autoantibodies investigated in our study……...126

Table 4.2: Summary of the samples from Barcelona and Mayo Clinic……...130

Table 4.3: Methods of transient transfection in 6- and 96-well plate……..132

Table 4.4: Methods of live CBA applied to 24- and 96-well plate……134

Table 4.5: Summary of the Barcelona samples picked up by eGFP-tagged live HuD NOVA1, CDR2L, Amphiphysin and CRMP5 CBAs……151
Table 4.6: The diagnostic accuracy of our live CBAs for detecting onconeural autoantibodies in Barcelona samples……...152
Table 4.7: Summary of the Mayo Clinic samples picked up by eGFP-tagged live HuD, NOVA1, CDR2L, CRMP5 and ZIC CBAs……160
Table 5.1: Summary of the remaining samples from Barcelona and Mayo Clinic…174
Table 5.2: The diagnostic methods for detecting autoantibodies to AQP4 M23 and MOG α1 isoforms……175
Table 5.3: Summary of tested live cell-labelling dyes……177
Table 5.4: Summary of the samples picked up by quadruplex live F-CBA for detecting autoantibodies to HuD, Amphiphysin, NOVA1 and CDR2L……..209
Table 5.5: Summary of the samples picked up by quadruplex permeabilized F-CBA for detecting autoantibodies to CRMP5, SOX1, Ma1 and Ma2……215
Table 7.1: The primer pairs for restriction enzyme-based cloning……..257
Table 7.2: The primer pairs for site-directed mutagenesis (SDM)……..258
Table 7.3: The primer pairs for Sanger sequencing……..260

Chapter I

General Introduction

1.1. Autoimmune-mediated neurological diseases

This thesis focuses on investigating autoimmune-mediated neurological diseases by developing live cell-based assays (CBAs) to detect autoantibodies to the corresponding antigens. Under the umbrella of autoimmune-mediated neurological diseases, the pathology could be either antibody-mediated or antibody associated. The domains of my DPhil research is summarized as Figure 1.1.

Pathogenic autoantibodies are usually against surface accessible proteins where they can bind in vivo and modify the target protein function, or the cell that expresses the protein, e.g., myasthenia gravis (MG), autoimmune encephalitis or neuromyelitis optica spectrum disorders (NMOSD) (Tozzoli, 2020). When autoantibodies bind to the surface antigens, the antigen-receptor signaling or cell effector functions can be disturbed by the antibody-induced internalization or the activation of complement (Elkon and Casali, 2008).

In 1957, Dr. Ernst Witebsky proposed “Witebsky’s postulates” to support scientists evaluating if a disease had autoimmune origins (Witebsky et al., 1957). The postulates included four criteria: (1) the direct demonstration of free circulating antibodies active at body temperature, (2) the recognition of the specific antigen targeted by autoantibodies, (3) the production of autoantibodies to the same antigen in experimental animals after immunization and (4) the pathological changes in the tissues of immunized experimental animals similar to those found in patients. Later in 1993, the criteria of Witebsky’s postulates were revisited and further validated by (1) passively transferring human pathogenic autoantibodies to the experimental animals, (2) inducing human autoimmune phenotypes in animals via transferring pathogenic

autoantigens or $CD4^+$ T cells, (3) identifying excessive amount of antibody or immune cell deposits within lesions and (4) isolating autoantibodies or autoreactive T cells from the organs attacked by the autoimmune responses (Rose and Bona, 1993). Experimentally, the direct proofs of autoantibody pathogenicity were normally assessed by the passive transfer studies. For instance, passively transferred of the CSF from encephalitis patients with NMDA receptor antibodies. The rodents presented the memory deficits and the reduction of NMDA receptor density at hippocampal neurons (Planaguma et al., 2015, Hughes et al., 2010). In addition, the experimental NMOSD-like pathology, including aquaporin-4 (AQP4) loss, granulocyte infiltration, perivascular complement deposition and acute axonal injury, could be produced by intracerebrally injecting the AQP4-IgG seropositive sera and human complement into murine models (Lucchinetti et al., 2014). In general, the antibody-mediated neurological diseases response well to immunotherapy, another indication that autoantibodies play a significant role in the etiology of these diseases (Dalmau and Rosenfeld, 2020).

On the other hand, the autoantibodies in antibody-associated neurological diseases, e.g., paraneoplastic neurological syndromes (PNS), do not appear to be involved in the disease pathogenesis but are a surrogate (Graus et al., 2021). In this disease group, the autoantibodies target the nuclear or cytoplasmic antigens expressed in the human neuro-glial system, which may be ectopically expressed in the associated tumours, so these antigens were termed as onconeural antigens (Hoftberger et al., 2015). The pathogenic mechanism is considered to be mainly through T cell mediated cellular destruction. This may suppress tumour growth early in the disease course, but ultimately the neuro-glial cellular damage is irrecoverable (Roberts et al., 2009, Zhang

et al., 2014, Pignolet et al., 2013). Unlike, antibody-mediated neurological diseases, the antibody-associated paraneoplastic syndromes response poorly to immunotherapy, but stabilization or even improvement of neurological syndromes can happen after the removal of tumours, if they are diagnosed early enough (Dalmau and Rosenfeld, 2020). Also, the appearance of onconeural autoantibodies is highly associated with the existence of specific tumour types, e.g., Hu antibodies and small-cell lung cancer. The neurological syndromes in the majority of patients preceded their tumour diagnoses, so the detection of onconeural autoantibodies is important for clinicians to find and remove the tumours as early as possible, and to keep searching for tumours if none are found (Gozzard and Maddison, 2010).

In addition to antibodies to membrane proteins, some tumours such as thymomas, are associated with autoantibodies to type I interferons, IL-12 and Th17 cytokines (Meager et al., 1997, Meager et al., 2003). Although these cytokine autoantibodies may not directly contribute to the syndromes of myasthenia gravis, they can lead to opportunistic infections among the patients with thymic malignancy by neutralizing the functions of type I interferons and Th1/17 cytokines (Burbelo et al., 2010). In patients with AChR antibody positive autoimmune myasthenia gravis (aMG), the detection of cytokine autoantibodies can be helpful in suggesting the presence of thymoma.

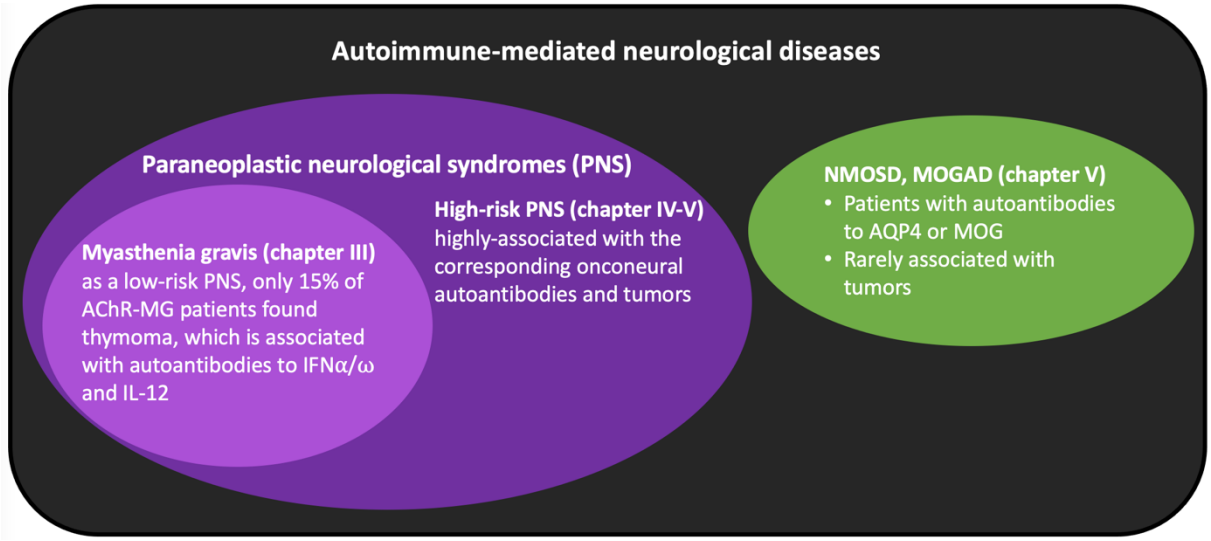


Figure 1.1: The overview of my DPhil research. Under the umbrella of autoimmune-mediated neurological diseases, my DPhil research focuses on developing live cell-based assays to detect autoantibodies among patients with paraneoplastic neurological syndrome, myasthenia gravis, NMOSD and MOGAD. In each study, the autoantibody targets were underlined, and the chapters for each were mentioned within the brackets.

1.2. Paraneoplastic neurological syndromes

Remotely triggered by particular tumours with an autoimmune-mediated etiology, paraneoplastic neurological syndromes (PNS) are a group of rare neurological conditions that affect patients' central and peripheral nervous systems, and neuromuscular junctions (Darnell and Posner, 2003, Honnorat and Antoine, 2007, Dalmau and Rosenfeld, 2020). PNS developed in 1/334 patients with cancers, and the prevalence of PNS is 4.37 per 100,000 (Vogrig et al., 2020). In this section, PNS diagnostic criteria, pathology, and therapeutic approaches are reviewed.

1.2.1. The evolution of PNS diagnostic criteria

In 1995, PNS were firstly classified as classical and non-classical PNS (Posner, 1995). Classical PNS are a group of syndromes where a specific tumour is found associated with a specific antibody in more than 70% of individuals. The targets are most often located in the cytosol or nucleus and are expressed by both the tumours and the nervous system, hence onconeural autoantibodies. Non-classical PNS are a relatively newer group of patients who have antibodies to either integral membrane or membrane associated proteins. All have an associated neurologic disease but the frequency of individuals with the syndrome who have an associated cancer is lower (between 40-70%). Table 1.1 summarizes the common classical and non-classical PNS interrupting different nervous systems, and Table 1.2 summarizes the well-defined and partially categorized onconeural autoantibodies and their associated tumours.

Table 1.1: Summary of common classical and non-classical PNS (Leypoldt and Wandinger, 2014, Graus et al., 2004)

Classical PNS	Non-classical PNS
Affecting central nervous system	
Encephalomyelitis	Optic neuritis
Limbic encephalitis	Myelitis/necrotizing myelopathy
Subacute cerebellar degeneration	Brainstem encephalitis
Opsoclonus-myoclonus	Stiff-person syndrome
Affecting peripheral nervous system	
Subacute sensory neuronopathy	Multiplex mononeuropathy
Chronic intestinal pseudo-obstruction	Pure autonomic neuropathies
	Polyradiculoneuropathy
Affecting neuromuscular junction and muscle	
Lambert-Eaton myasthenic syndrome	Myasthenia gravis
Dermatomyositis	Neuromyotonia

Table 1.2: Summary of onconeural autoantibodies and their associated tumours (Leypoldt and Wandinger, 2014, Graus et al., 2004)

Antibody Target	PNS	Associated tumour	PPV for predicting tumour	Frequency in cancer patient without PNS
Well characterized				
Hu: HuD	Encephalomyelitis; sensory neuronopathy; chronic gastrointestinal pseudo-obstruction; paraneoplastic cerebellar degeneration (PCD); limbic encephalitis	Small cell lung cancer (SCLC)	98%	16%
Yo: CDR2, CDR2L	PCD	Breast and ovarian cancers	98%	1%
CRMP5	Encephalomyelitis; chorea; sensory neuronopathy; sensorimotor neuropathy; chronic gastrointestinal pseudo-obstruction; PCD; limbic encephalitis	SCLC, thymoma	96%	9%

Antibody Target	PNS	Associated tumour	PPV for predicting tumour	Frequency in cancer patient without PNS
Well characterized				
Ri: NOVA1	Opsoclonus–myoclonus syndrome, rhombencephalitis, cerebellar degeneration, myelitis, jaw dystonia, laryngospasm	Breast and ovarian cancers, SCLC	97%	4%
Ma2, “Ma1 + Ma2”*	Limbic encephalitis, rhombencephalitis, PCD*	Testicular cancer, SCLC*	96%	0%
Amphiphysin	Stiff-person syndrome, limbic encephalitis, rhombencephalitis, cerebellar degeneration, polyneuropathy	Breast cancer, SCLC	95%	1%
SOX1	Lambert-Eaton myasthenic syndrome (LEMS)	SCLC	93%	N/A
Partially characterized				
Tr/DNER	PCD	Lymphoma	89%	0%

Antibody Target	PNS	Associated tumour	PPV for predicting tumour	Frequency in cancer patient without PNS
Partially characterized				
ANNA3	Neuropathy, cerebellar degeneration, limbic encephalitis	SCLC	91%	0%
PCA2	Encephalitis, Lambert–Eaton myasthenic syndrome, polyneuropathy	SCLC	100%	2%
ZIC4	PCD	SCLC	88%	16%
mGluR1	PCD	Lymphoma	50%	N/A

In 2004, Graus et al. provided a more rigorous PNS diagnostic criteria to classify the suspected PNS patients into definite or possible PNS group (Graus et al., 2004). Even if the panel acknowledged that “possible” PNS group may include both the true PNS patients and patients with unrelated neurological deficits and tumours, the possible PNS criteria could still be useful to identify the patients whose syndromes may deteriorate in the future and upgrade to definite PNS. Below summarizes the official guidelines allowing clinicians to classify the suspected PNS patients into the correct group. Figure 1.2 provide a workflow of how the criteria work to define a suspected PNS patient.

Definite PNS (fulfil any)

1. A classical syndrome and cancer that develops within five years of the diagnosis of the neurological disorder.
2. A non-classical syndrome that resolves or significantly improves after cancer treatment without concomitant immunotherapy, provided that the syndrome is not susceptible to spontaneous remission.
3. A non-classical syndrome with onconeural antibodies (well characterized or not) and cancer that develops within five years of the diagnosis of the neurological disorder.
4. A neurological syndrome (classical or not) with well characterized onconeural antibodies (anti-Hu, Yo, CRMP5, Ri, Ma2, or amphiphysin), and no cancer.

Possible PNS (fulfil any)

1. A classical syndrome, no onconeural antibodies, no cancer but at high risk to have an underlying tumour.

2. A neurological syndrome (classical or not) with partially characterized onconeural antibodies and no cancer.
3. A non-classical syndrome, no onconeural antibodies, and cancer present within two years of diagnosis.

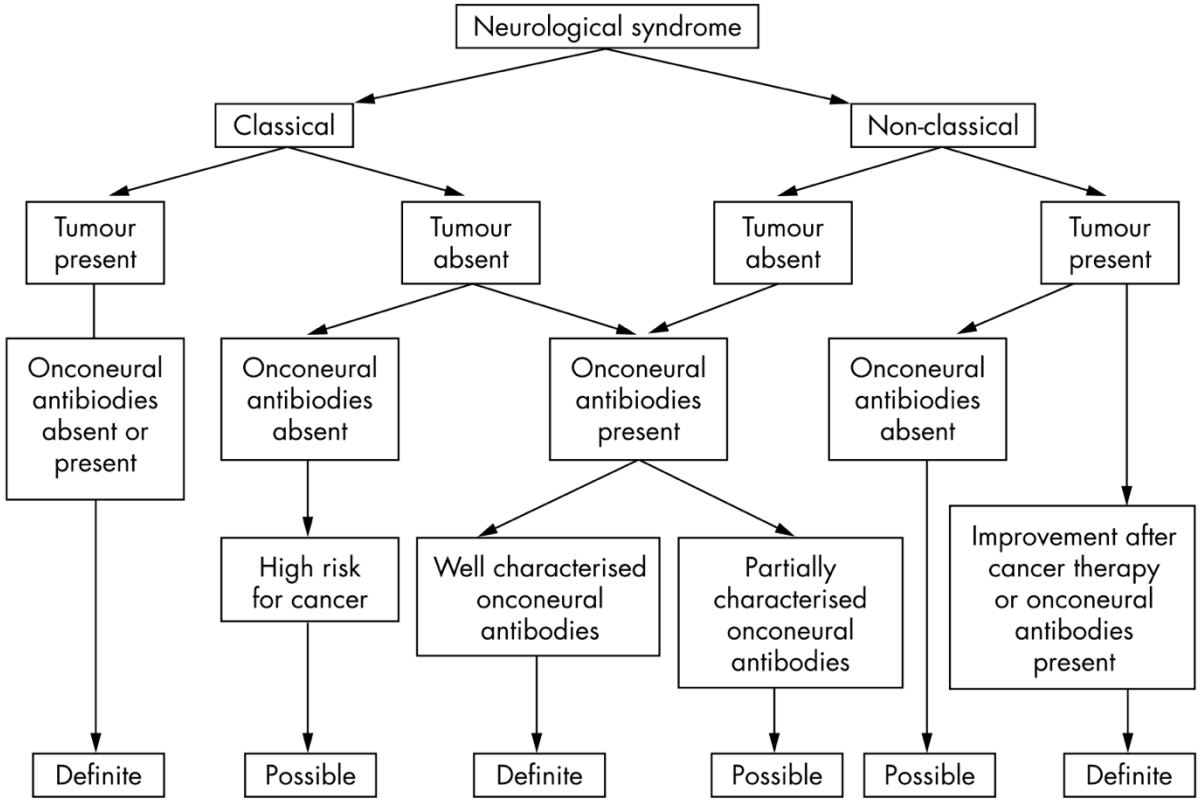


Figure 1.2: The flow chart of classifying the suspected PNS patients into definite or possible PNS group. The chart was adapted from (Graus et al., 2004).

Even with the 2004 international criteria in place, the varying PNS incidences, ranging from 1.6 to 8.9 per million-person-year in population-based epidemiologic studies imply that underdiagnosis or misdiagnosis of PNS remains an issue due to a wide range of differential diagnosis (Vogrig et al., 2020, Hebert et al., 2020, Shah et al., 2022). For instance, paraneoplastic Lambert-Eaton myasthenic syndrome (LEMS) is often misdiagnosed as non-paraneoplastic aMG by sharing similar symptoms, and the complication also exists between the diagnosis of paraneoplastic cerebellar degeneration and non-paraneoplastic Miller-Fisher syndrome (Leypoldt and Wandinger, 2014).

In addition, the relationship between onconeural autoantibodies, neurological deficits and the underlying tumours has been found complicated. Up to 50% of PNS patients with tumours may not be diagnosed with the particular onconeural autoantibodies, which however could be detected in up to 16% of neurologically asymptomatic patients with tumours (Karim and Jacob, 2012, Monstad et al., 2009). Besides, the underlying tumours in up to 11% of patients diagnosed as definite PNS may not be found for up to 20 months (Karim and Jacob, 2012). In addition, laboratories have moved from tissue-based immunohistochemistry or immunofluorescence and cell-based assays to line blots because of their convenience. However, recent publications suggest that the line blots lack both specificity and sensitivity, they have a poor positive predictive value and line blots for many targets have little or no clinical value (Ruiz-Garcia et al., 2020, Dechelotte et al., 2020, Budhram et al., 2018).

To achieve better classification of PNS, in 2021, Graus et al. updated the PNS diagnostic criteria (Graus et al., 2021). The updated criteria incorporated newly

discovered onconeural antigens, like KLHL-11, and new pathogenic autoantibodies to neuronal surface antigens, such as NMDAR and CASPR2 in neurological syndromes and they are associated with particular cancers. The terms classical and non-classical PNS have been replaced with: high-risk, intermediate-risk and low-risk, to demonstrate the degree of tumour association with PNS phenotype and autoantibodies to neuro-glial targets. Finally, a PNS-Care scoring system, as Table1.3, was established to classify the suspected PNS patients into definite, probably, possible or non-PNS group.

Table 1.3: PNS Care scoring system (Graus et al., 2021)

	Score
Clinical diagnosis	
High-risk PNS phenotypes, including encephalomyelitis, limbic encephalitis (LE), rapidly progressive cerebellar syndrome, opsoclonus-myoclonus, sensory neuronopathy, gastrointestinal pseudo-obstruction (enteric neuropathy), Lambert-Eaton myasthenic syndrome	3
Intermediate-risk PNS phenotype, including encephalitis other than well-defined LE, Morvan's syndrome, isolated myelopathy, stiff-person syndrome, paraneoplastic polyradiculoneuropathies	2
Defined phenotype epidemiologically not associate with cancer	0
In-lab diagnostic results	
High-risk autoantibodies (> 70% cancer association) Autoantibodies to HuD, CRMP5, SOX1, PCA2, Amphiphysin, NOVA1, CDR2, CDR2L, Ma1, Ma2, Tr/DNER and KLHL-11	3
Intermediate-risk autoantibodies (30-70% cancer association) Autoantibodies to AMPAR, $GABA_BR$, mGluR5, P/Q VGCC, NMDAR, CASPR2 (if with Morvan's syndrome)	2

Lower-risk autoantibodies (< 30% cancer association) Autoantibodies to mGluR1, $GABA_AR$, CASPR2, GFAP, GAD65, LGI1, DPPX, GlyR, AQP4, MOG	0
Seronegative	0
Presence of tumour	
Found; consistent with PNS phenotype and (if present) onconeural autoantibodies, or not consistent but found onconeural antigen ectopically expressed in tumour tissue	4
Not found or not consistent with PNS phenotype and (if present) onconeural autoantibodies, but follow-up < 2 years	1
Not found and follow-up ≥ 2 years	0
PNS Classification (add on the scores)	
Definite PNS	≥ 8
Probable PNS	6-7
Possible PNS	4-5
Non-PNS	≤ 3

The additional neuro-glial targets and the holistic stratification of PNS phenotype and onconeural autoantibodies clarify the PNS diagnostic criteria. Below, the pathological features and therapeutic strategies of classical PNS, myasthenia gravis (MG, a non-classical PNS) and two autoimmune-mediated demyelinating diseases (NMOSD and MOGAD) with low-risk autoantibodies are introduced.

1.2.2. Immunology of PNS

PNS patients develop autoantibodies to neuro-glial targets expressed either on the cell surface or within the cytosol. Both scenarios are thought to share the same causation: tumour-triggered autoimmunity, which is attributed to the ectopic expression of neuro-glial antigens within the particular tumours (Pignolet et al., 2013). There is limited

histological evidence demonstrating the ectopic expression of HuD in patients' SCLC, and the ectopic expression of CDR2L and NMDAR in patients' ovarian tumours and teratomas respectively (Small et al., 2018, Szabo et al., 1991, Day et al., 2014). Dalmau et al. found 17/20 SCLC from the patients with anti-HuD autoantibodies ectopically expressed HuD, but only 4/30 SCLC from the seronegative patients ectopically expressed HuD (Dalmau et al., 1995). As a latest update, Al-Diwani et al. recently discovered the disease specific germinal centres in ovarian teratoma collect from patients with NMDAR-encephalitis (Al-Diwani et al., 2022). This may have limited advantage as some patients with tumours and specific antibodies survive longer than those with the same tumour without antibodies (Lipka et al., 2020).

When onconeural autoantibodies target cell surface antigens, they can internalise NMDARs, block the $GABA_BR$ binding site or interfere with synaptic protein-protein interactions between LGI1 and ADAM22/23 (Dalmau et al., 2017). However, onconeural autoantibodies to intracellular neuro-glial antigens, such as HuD an RNA-binding protein, are not thought to play a direct pathogenic role in PNS. Although one *in vitro* study suggested direct anti-neuronal effects of human anti-HuD autoantibodies on rat myenteric plexus cultures (Schafer et al., 2000), another active immunization study, despite including high titre anti-HuD autoantibodies, showed no neurological deficit in mice (Smitt et al., 1995). Likewise, Tanaka et al. found neither passive transfer of anti-CDR2 antibodies into mice brain nor active immunisation of mice with human CDR2 led to Purkinje cell loss or any PNS-like phenotype (Tanaka et al., 1994). On the other hand, the higher CD8/CD3 T cell ratio and more frequent apposition of CD8 cytotoxic T cells to neurons accompanying neuronal loss were reported in the patients with anti-HuD or anti-Ma2 autoantibodies rather than the patients with autoantibodies

to NMDAR (Bien et al., 2012). Therefore, CD8 T cells or autoantibodies to cell surface antigens but not intracellular antigens are believed to associate with the immunopathology of PNS. Besides, genetics may also play a role. Small et al. demonstrated overexpression of CDR2L in in PCD-associated ovarian tumours in patients with Yo antibodies, but also discovered two-thirds of the tumours showed somatic mutations in the homologous proteins CDR1 and CDR2 (Small et al., 2018). This study suggests the genetic alternations in antigens (or close homologues) ectopically expressed in particular tumours may break immune tolerance.

1.2.3. Pathology of autoimmune myasthenia gravis - a lower-risk PNS

As one of the lower-risk PNS, only 10-15% of myasthenia gravis (MG) patients have an associated thymoma, which suggests the generation of AChR antibodies is infrequently due to over-expression in a thymoma (Engels, 2010). Serologically, MG patients have diverse autoantibodies associated with overlapping clinical syndromes: 80% have autoantibodies against the acetylcholine receptor (AChR), 4% against the muscle-specific tyrosine kinase (MuSK), 2% against the low-density lipoprotein receptor-related protein 4 (LRP4), and some are seronegative (5%) (Gilhus and Verschuuren, 2015). However, thymoma is only found among MG patients with AChR autoantibodies, frequently concomitant with autoantibodies to titin and ryanodine receptor (RyR) (Gilhus et al., 2019, Skeie et al., 2006). Additionally, 12% of patients with thymoma-associated MG (TAMG) have autoantibodies to CV2/CRMP5, even though the target has not been identified yet in thymoma (Totland et al., 2021). Below, I introduce the function of the thymus and the autoimmune basis of AChR antibody generation due to thymic lymphoid hyperplasia or thymoma.

The thymus is a primary lymphoid organ critical for T cell maturation and central tolerance (Marx et al., 2021). It is large at birth, gradually involuting and replaced by adipose tissues during normal aging. The production of functional, mature T cells declines as we become older (Haynes et al., 2000). After developing in the bone marrow, immature CD4/CD8 double negative T cells enter the thymus through the corticomedullary junction. Within the thymic cortex, immature T cells undergo VDJ recombination to form functional T cell receptor (TCR) before developing into CD4/CD8 double positive T cells near the thymic capsule (Marx et al., 2021). Here, central tolerance, i.e., positive and negative selection, occurs (Klein et al., 2014). Inside the thymic cortex, positive selection selects the functional T cells, which can recognize the self-antigens presented by cortical epithelial cells (cTEC) via MHC molecules. The selected T cells then develops into either CD4 or CD8 single positive T cells. Subsequently, inside the thymic medulla, negative selection deletes the autoreactive T cells, which strongly bind to the tissue-restricted antigens (TRA) presented by medullary epithelial cells (mTEC). The expression of TRA is also known as promiscuous gene expression (PGE) and is partially regulated by a transcriptional factor encoded by autoimmune regulator (AIRE) gene (Perniola, 2018). A portion of these TRA is transferred to thymic conventional dendritic cells to support the deletion of autoreactive T cells and to facilitate the development of natural regulatory T cells (nTreg) inside the thymic medulla (Kroger et al., 2017). In summary, the thymus is a critical immune checkpoint to delete the nonfunctional/autoreactive T cells and generate Treg that combines to prevent the development of autoimmune T cells.

Clinically, our thymus may become autoimmunogenic under two pathological circumstances - thymic lymphoid hyperplasia and thymoma where the tolerogenic

environment becomes disorganized. Firstly, thymic lymphoid hyperplasia is characterized by the presence of lymphoid germinal centers in thymic medulla, which are observed in around 70% of patients with early-onset myasthenia gravis (EOMG) and associated with AChR autoantibodies (Berrih-Aknin and Le Panse, 2014). The inflammatory nature of hyperplastic thymus can also attract peripheral B cells, activated T cells and dendritic cells by overexpressing CXCL13, CCL21 and CXCL12 (Berrih-Aknin, 2016). Within the autoimmunogenic environment, individual subunits of AChR expressed by thymic myoid cells can trigger the production of AChR autoantibodies (Berrih-Aknin, 2016).

Secondly, thymoma, characterized as thymic epithelia neoplasm, is rare with an incidence of 1.5 cases per million person-years in the US but without gender or age discrimination (Engels, 2010). Owing to the absence of AIRE-expressing mTEC and thymic myoid cells in 95% of patients with thymoma, the autoreactive T cells recognizing muscular antigens, e.g., AChR, escape leading to the production of autoantibodies to AChR (Marx et al., 2010a). Despite around 40% of patients with thymoma developing autoimmune myasthenia gravis, thymoma is also associated with other autoantibodies and autoimmune diseases, such as Morvan's syndrome happening in 2% of thymoma patients with autoantibodies to contactin-associated protein-like 2 (Caspr2), systemic lupus erythematosus happening in 2% of thymoma patients with autoantibodies to dsDNA and Grave's disease happening in 1-4% of thymoma patients with autoantibodies to thyroid peroxidase (Marx et al., 2010b, Bernard et al., 2016).

To conclude, thymoma can trigger anti-AChR autoimmunity and drive clinical MG. However, the low frequency of thymoma in patients with AChR antibody associated aMG makes it a lower-risk clinical presentation when considering cancer screens.

1.2.4. Autoimmune-mediated demyelinating diseases with lower-risk autoantibodies

In the 2021 PNS diagnostic criteria, autoantibodies to aquaporin-4 (AQP4) and myelin oligodendrocyte glycoprotein (MOG) were characterized as low-risk autoantibodies because patients with their respectively associated diseases - neuromyelitis optica spectrum disorder (NMOSD) and MOG-antibody associated disease (MOGAD), rarely have an associated cancer.

1.2.4.1. NMOSD

NMOSD is an aquaporin-4 antibody mediated, complement-dependent astrocytopathy with secondary demyelination. Patients can present with visual loss, mobility issues, bowel and bladder dysfunction as well as persistent nausea or vomiting. The visual loss can be unilateral or bilateral, and the spinal cord lesions are often longitudinal (at least involve 3 spinal cord segments) and the lesions are characteristically transverse with a swollen appearance. These features can occur in isolation or together. Children present more often with optic neuritis and develop spinal cord features over time while adults more often present with transverse myelitis but frequently do not develop visual issues (Iorio et al., 2013, Liu et al., 2021). Optic neuritis attacks are normally more severe than those seen in patients with multiple sclerosis, with more frequent permanent visual loss. Longitudinal extensive transverse myelitis (LETM) is characteristic of NMOSD, but not pathognomonic. In 2015, the international consensus

diagnostic criteria for NMOSD expanded the original diagnostic criteria from 2006 where the antibody status took a more central role. These criteria also included people without the AQP4-IgG to support clinical care, hence ignoring biology. These seronegative patients likely have a heterogeneous mix of other disorders (Wingerchuk et al., 2015). Table 1.4 summarizes the updated NMOSD diagnostic criteria published in 2015.

Table 1.4: 2015 revised criteria for diagnosing NMOSD (Wingerchuk et al., 2015)

Diagnostic criteria for NMOSD with AQP4-IgG (fulfil all)

1. At least 1 core clinical characteristic*
2. Positive test for AQP4-IgG using best available detection method (cell-based assay strongly recommended)
3. Exclusion of alternative diagnosis, such as MS or others identified as red flags (Wingerchuk et al., 2015)

Diagnostic criteria for NMOSD without AQP4-IgG or NMOSD with unknown AQP4-IgG status (fulfil all)

1. At least 2 core clinical characteristics* occurring as a result of one or more clinical attacks and meeting all of the following requirements:
   a. At least 1 core clinical characteristic* must be optic neuritis, acute myelitis with LETM, or area postrema syndrome
   b. Dissemination in space (2 or more different core clinical characteristics)
   c. Fulfilment of additional MRI requirements (Wingerchuk et al., 2015)
2. Negative tests for AQP4-IgG using best available detection method, or testing unavailable
3. Exclusion of alternative diagnosis, such as MS or others identified as red flags (Wingerchuk et al., 2015)

Core clinical characteristics*

1. Optic neuritis
2. Acute myelitis

3. Area postrema syndrome: episode of otherwise unexplained hiccups or nausea and vomiting
4. Acute brainstem syndrome
5. Symptomatic narcolepsy or acute diencephalic clinical syndrome with NMOSD-typical diencephalic MRI lesions
6. Symptomatic cerebral syndrome with NMOSD-typical brain lesions

---

1.2.4.2. MOGAD

MOGAD includes many clinical features found in patients with NMOSD including associated with optic neuritis, myelitis. But the associated clinical features are broader and also include brainstem encephalitis and acute disseminated encephalomyelitis (ADEM) (Reindl and Waters, 2019, Jarius et al., 2018). Although there are overlaps with AQP4 antibody positive NMOSD, MOGAD is considered a distinct disease entity (Dos Passos et al., 2018). Compared to patients with AQP4-Ab positive NMOSD, monophasic rather than relapsing disease course is more frequent in MOGAD patients, which can lead to more favorable prognosis (Borisow et al., 2018). In addition, while the spinal cord lesions tend to affect cervicothoracic segments in NMOSD patients, MOGAD patients are often found spinal cord lesions in their thoracolumbar segments, but overlap is frequent (Sato et al., 2014, Kitley et al., 2014). Unlike the very clear animal models and excellent clinical response either Rituximab (which targets B cells), or the complement C5 monoclonal antibody inhibitor eculizumab in AQP4-antibody positive NMOSD, there is no clear data on the pathogenic nature of MOG-antibody and the response to Rituximab is mixed. *In vivo* and *ex vivo* demyelination studies were partially successful (Reindl and Waters, 2019, Peschl et al., 2017). Part of this issue may be due to the underappreciated lack of reactivity of MOG-IgG to rat or mouse tissue in early animal models. Others demonstrated intrathecally injected human cross-

reactive MOG-Abs could enhance T cell infiltration and trigger complement-mediated demyelination in rats (Spadaro et al., 2018). To summarize, MOGAD is a distinct disease entity to NMOSD. The presence of antibodies define a non-MS demyelinating disease entity, but the role of antibodies in the disease course is not clear hence, MOG-antibody is “associated with” rather than “mediating” the disease course of MOGAD.

1.2.5. Therapeutic strategies

The treatment decisions for PNS patients are recommended before understanding the role of the autoantibodies (Blaes, 2021). In general, the patients with pathogenic autoantibodies binding to surface-expressed antigens are more responsive to immunosuppressive treatments than the patients with onconeural autoantibodies to intracellular antigens. The first-line treatments include corticosteroids, steroid sparing agents such as azathioprine or mycophenolate mofetil, intravenous immunoglobulins (IVIg), plasma exchange, or a combination of these treatments (Dalmau and Graus, 2018). If the first-line treatments are not effective, rituximab or cyclophosphamide are considered as the second-line treatment (Graus et al., 2016). More recent treatments undergoing clinical trials include Tocilizumab, an anti-interleukin-6 receptor antibody, which has been used off-label in rituximab refractory patients (Lee et al., 2016a).

On the other hand, most classical PNS patients with autoantibodies to intracellular onconeural antigens don’t experience improvements after immunosuppressive treatments (Blaes, 2021). Previous controlled immunosuppressive studies on PNS patients with onconeural autoantibodies suggested the treatments including immunosuppressants, IVIg, plasma exchange or cyclophosphamide showed ineffective therapeutic outcomes: 30-50% of patients remained severely disabled (de

Jongste et al., 2015, Berzero et al., 2018). Only anti-tumour therapies demonstrated stabilization, or improvement though rare, of patients' neurological syndromes (Graus et al., 1997). Otherwise, patients' immunosuppressive treatments are required to be initiated shortly after the onset of PNS in order to see better therapeutic outcomes (Blaes et al., 1999). Therefore, it is critical for clinicians to early diagnose and manage the particular tumours from patients diagnosed with classical PNS.

1.3. Methods for detecting autoantibodies

In this section, the available methods for detecting autoantibodies to soluble cytokines, onconeural antigens and transmembrane proteins, also some multiplex strategies are reviewed.

1.3.1. Methods for detecting autoantibodies to soluble cytokines

Current methods to detect polyclonal IgG antibodies to human cytokines can be classified as solid- or fluid-phase assays (Meager and Wadhwa, 2014). In all methods, the source and characteristics of cytokine targets are critical for assay performance. Assays based on E. coli produced recombinant cytokines may differ in post-translational modifications and overall structure from mammalian cell produced cytokines (Wadhwa and Thorpe, 2010).

ELISA is a conventional solid-phase methods to quantify cytokine autoantibodies, and it can be performed under direct, indirect, sandwich/bridging manner (Meager, 2000, Wadhwa et al., 2003, Mire-Sluis et al., 2004). However, because the 'capture' cytokines are immobilized on ELISA plate before performing direct or indirect ELISA, their conformational epitopes may be changed, thus leading to false negative results

(Meager and Wadhwa, 2014). Depending on the size of the antigen, there may also be an issue with competition for epitopes with the capture antibody. In order to improve the issue of epitope masking, Gross et al developed a streptavidin/biotin-coated bridging ELISA, where they elevate the 'capture' cytokine above the ELISA plate surface. They improved the test metrics for anti-EPO antibody detection compared to traditional ELISA (Gross et al., 2006). Additionally, electrochemiluminescence (ECL)-based detection systems can be substituted for the conventional enzymes such as streptavidin–alkaline phosphatase to achieve a higher sensitivity and a greater dynamic range (Cludts et al., 2010, Swanson et al., 1999).

Fluid-phase methods include radioimmunoassay (RIA) and luciferase immunoprecipitation system (LIPS), which suspend the labelled cytokine targets in solution, perhaps allowing better access to the epitopes before immunoprecipitating the cytokine-antibody complex for quantification, depending on the size and location of tags (Meager and Wadhwa, 2014, Meager, 2000). For RIA, the cytokine can be directly labelled with radio-iodine isotopes, such as ^{35}S-methionine (Oftedal et al., 2008). In others, the cytokine targets were fused with *Renilla* or *Gaussia* luciferase in LIPS assay, after immunoprecipitation, coelenterazine - the substrate of luciferase, were added before quantification of emitted light at 550-570 nm (Burbelo et al., 2010, Karner et al., 2016). Despite making cytokines more accessible to autoantibodies, LIPS assays have high background and it is hard to predict if there are any unintended interactions between the fused cytokine and luciferase (Meager and Wadhwa, 2014).

1.3.2. Methods for detecting autoantibodies to onconeural antigens

To detect onconeural autoantibodies, commercial line blots (PNS+2 blot, Ravo Diagnostika; EUROLINE PNS 12 Ag, Euroimmun) or western blots have been used to detect multiple onconeural autoantibodies at once (Dechelotte et al., 2020). This is by immobilizing recombinant, denatured antigens of interest on a nitrocellulose strip before incubating with patient's serum or CSF. If the sample has antibodies to denatured antigen, a band appears at the corresponding location on the strip. However, the diagnostic utility of line blots is limited because only 0-80% of line blot positive samples were agreed by secondary methods: immunohistochemistry (IHC) or permeabilized cell-based assay (CBA). These numbers are antigen specific with nearly all targets showing less than 50% of positive results agreed by a second test and a large minority with less than 10% with clinically useful positive results (Ruiz-Garcia et al., 2020, Dechelotte et al., 2020). In another study, the positive predicative value of using line blots alone was 39% (Budhram et al., 2018). So, line blots lack specificity, but they also lack sensitivity. A recent study reported that commercial line blots didn't pick up 8% of patients' sera that tested seropositive for CRMP5 autoantibodies via indirect immunofluorescence (IIF) or permeabilized CBA (Sabater et al., 2016). Therefore, international experts recommend confirmation of commercial line blots results by a second method (fixed IHC, IIF or CBA), and only the double positive or IHC/CBA negative results are interpreted in the content of patients' clinical presentations (Binks et al., 2022). Further, screening patients' sera and CSF improves the diagnostic accuracy (Graus et al., 2016).

1.3.3. Methods for detecting autoantibodies to transmembrane proteins

Given the fact that some autoantibody targets are integral membrane proteins expressed in the cell membrane, live CBA or live flow cytometry CBA (live F-CBA) are superior to ELISA or FIPA to quantify the autoantibodies to extracellular epitopes of transmembrane proteins such as AQP4, MOG, CASPR2 and AChR (Irani et al., 2010, Chan et al., 2010, Prasad and Chen, 2019, Leite et al., 2008). In 2008, Leite et al. found an increase in the cell based AChR antibody test sensitivity when they co-expressed the AChR clustering protein rapsyn. They identified 28/38 (66%) sera from patients with clinically diagnosed MG who were seronegative AChR-RIA were picked up by live CBA (Leite et al., 2008). In 2012, a multicenter AQP4-Ab study also suggested live CBA (73.3%) and live flow cytometry CBA (76.7%) were more sensitive than ELISA (60%) and tissue-based IIF (48.3%) for detecting AQP4-Ab from NMOSD patients, with all methods equally specific (100%) in a relatively small control cohort of 86 individual samples (Waters et al., 2012). Similarly for MOG-Ab detection, both live CBA and live F-CBA were more sensitive and specific than ELISA and RIA for MOG-IgG1 antibodies to the MOG α1 isoform and more specific than ELISA to exclude the false positive sera from patients with MS and AQP4-Ab^{+} NMOSD. (Reindl and Waters, 2019, Reindl et al., 2020). There is an issue with MOG-IgG antibody assays. When CBAs are run at a serum dilution of 1:20 we find healthy individuals, MS patients, epilepsy patients with MOG antibodies. We can increase the cut-off to make the tests more specific, but we will miss some cases. This issue is highlighted in a very recent paper by Sechi et al. who found a PPV for a non-MS demyelinating disease of 72% when the cut-off was set at 1:20 (Sechi et al., 2021). If we include only samples with an endpoint titre of 1:100 or above, the PPV is 82%, but it reaches 100% when we use a 1:1000 cut-off. Unfortunately, only 17/91 true positive cases, defined by treating

clinicians, had a titre of greater than 1:1000. This remains an issue. All in all, contemporary studies suggest live CBA and live F-CBA are superior to other traditional solid- or fluid-phase assays for detecting autoantibodies native cell surface antigens.

1.3.4. Multiplex technologies for detecting autoantibodies

There are commercially available Luminex® technologies to detect onconeural autoantibodies in the sera from PNS patients with 6 onconeural antigens on individual color-coded polystyrene beads (Maat et al., 2013). In addition, FirePlex® high-throughput immunoassay enables multiplex quantification of up to 10 protein analytes in 384-well plate format (Atabakhsh, 2019). However, Luminex® and FirePlex® technologies require using specific microplate readers, and the commercial products are costly. To simply barcode individual cell populations for multiplex purposes, the concept of fluorescent cell barcoding (FCB) is more flexible and applicable to live F-CBA (Krutzik et al., 2011). FCB is achieved by labelling individual cell populations with the cell labelling dyes at different concentrations before combining them in a multiplex master-mix. Alternatively, FCB can also be achieved by establishing individual stable cell lines expressing each antigenic target of interest and different combinations of fluorescent proteins (like GFP, YFP and mKO2) before combining them in a multiplex master-mix (Maetzig et al., 2018). By doing so, autoantibodies binding to individual cell populations can be easily identified in flow cytometry.

1.4. DPhil Research Rationales

The methods currently available for detecting autoantibodies to soluble cytokines, intracellular onconeural antigens and transmembrane proteins have been described in this chapter. As for my first DPhil research rationale, past studies have demonstrated live CBAs are more sensitive and specific for detecting AQP4-, MOG- and AChR-specific autoantibodies compared to other antibody detection methods. Line blots and ELISA are not sensitive or specific, hence we identified the needs for accurate assays to detect antibodies associated with cancers, the targets of which are frequently intracellular. Flow-cytometry is a quantitative method for antibody detection and removes the objective issues of visual scoring. Hence, development of a multiplexable F-CBA platform to detect and quantify autoantibodies to well-known targets are hypothesized to improve autoimmune diagnostics and set the platform for future assay implementations. In summary, there exists a need for rapid, accurate antibody diagnostics that are quantitative and multiplexable while maintaining native epitopes for patients' autoantibodies to recognize.

1.5. Principle Aims

1. Established live CBA platforms to detect autoantibodies to soluble thymoma-associated cytokine, onconeural antigens, and transmembrane proteins
2. Compared our newly developed CBA platform with LIPS, fixed IHC, IIF and commercial line blots
3. Developed live F-CBA platform to improve objective quantitation for autoantibodies to native proteins
4. Multiplexed the assays to improve assay efficiency while maintaining test accuracy

Chapter II

Materials and Methods

2.1. Clinical Materials

The clinical materials we used were plasma, sera and CSF samples from our sample stock or our collaborators. The samples were stored in -20°C freezer. Ethical approval (REC16/YH/0013) was obtained from the Central University Research Ethics Committee. The origin, patient demographics and clinical details of sample donors are summarized in each result chapter.

2.2. In-house Methods and Materials

In Chapter II, the generic in-house methods and materials applied in my research are described with study-specific details mentioned in each result chapter, respectively.

2.2.1. Molecular cloning

2.2.1.1. Restriction enzyme based cloning

2.2.1.1.1. Polymerase chain reaction (PCR)

PCR was used to amplify the cDNAs of targeted antigens. Primers were designed 5' and 3' of the targeted cDNAs with the appropriate restriction sites incorporated for digestion purposes. In a 0.2 ml eppendorf (60-0082, Biologix), 10 µl of 2X GoTaq® Master Mix (M7122, Promega; containing Taq DNA polymerase, dNTPs, MgCl2 and reaction buffers at optimal concentrations), 1 µl of forward primer (5 µM), 1 µl of reverse primer (5 µM), 1 µl of DNA template (200 ng/µl) and 7 µl of nuclease-free water (NFH_2O, BP2484-100, Fisher Bioreagents) were combined. PCR reactions were performed in a T100™ Thermal Cycler (1861096, BIO-RAD). Table 2.1 summarizes the PCR cycling conditions followed to amplify the targeted cDNAs, with the annealing temperature calculated using NEB Tm Calculator (https://tmcalculator.neb.com/#!/main). The

sequences of cDNA clones and primer pairs used in my research are summarized in the Appendix.

Table 2.1: PCR program

Step	Temperature	Time	Cycle
1. Denaturation	95°C	3 minutes	1 cycle
2. Denaturation	95°C	30 seconds	35 cycles
3. Annealing	55-68°C*	30 seconds	
4. Elongation	72°C	1 minute	
5. Elongation	72°C	10 minutes	1 cycle
6. Stand-by	4°C	for short-term storage	N/A

* The annealing temperature could vary between primer pairs

2.2.1.1.2. Gel electrophoresis

One percent agarose gels were made by adding 0.5 g of UltraPure™ agarose (16500, Thermo Fisher Scientific) to 50 ml of 1X Tris-acetate-EDTA (TAE) buffer (B49, Thermo Fisher Scientific) in a conical flask. The mixture was heated up in the microwave for approximately 1 minute, or until the agarose had completely dissolved in the TAE buffer. Once completely dissolved, the gel was allowed to cool down at room temperature (RT) for 5 minutes. Then, 5 µl of SYBR Safe (S33102, Thermo Fisher Scientific) was added and mixed thoroughly before decanting the mixture into a mold with tooth combs attached. The gel was cooled down at RT for 15 minutes, or until the agarose gel had solidified, avoiding exposure to light. Before being loaded into each well, the 20 µl of PCR product was mixed with 4 µl of 6X purple gel loading dye (B7024S, NEB). In addition, 10 µl of BenchTop 1kb DNA ladder (G754A, Promega) and 100bp DNA ladder (G8291, Promega) were loaded into separated wells. The samples were run in runVIEW electrophoresis tanks (CSL-RVMSMIDI-S, Cleaver

Scientific), which were powered by PowerPac™ basic power supply (1645050, BIO-RAD), at 100V for 30 minutes to separate the PCR-amplified cDNA fragments according to sizes.

2.2.1.1.3. Gel extraction

The areas of gel with targeted bands, including the amplified cDNA fragments, were removed from the agarose gels by scalpel blade (0101, SWANN-MORTON) and collected in individual 1.5 ml eppendorfs (KC131, Appleton). The Monarch® DNA gel extraction kit (T1020L, New England Biolabs) was used to extract the DNA of interest from agarose gel. In details, 400 µl of dissolving buffer was added to dissolve 100 mg of agarose gel by placing in 50°C water bath for 15 minutes. Then, the DNA within the dissolved gel was captured by the filter of collection column via centrifugation and washed with 200 µl of wash buffer. Lastly, the DNA was eluted in 15 µl of NFH_2O, and its concentration measured by NanoDrop™ One UV-Vis spectrophotometer (ND-ONE-W, Thermo Fisher Scientific). The machine was washed with 10 µl of NFH_2O, blanked with 1.2 µl of NFH_2O before loading 1.2 µl of DNA solution for measurement. Apart to measuring the concentration of DNA, the ratio of absorbance at 260 nm and 280 nm is used to assess the purity of DNA, and ratio of around 1.8 is acceptable. If the 260/280 ratio is lower than 1.8, it may indicate the presence of protein, phenol or other contaminants that absorb strongly at or near 280 nm. On the other hand, the ratio of absorbance at 260 nm and 230 nm is used as a secondary measure of DNA purity, and the expected ratio shall sit between 2 to 2.2. If the 260/230 ratio is lower than 2, it may indicate the presence of contaminants, like EDTA and Guanidine HCL, which absorb at 230 nm.

2.2.1.1.4. Restriction enzyme digestion

In a 0.2 ml eppendorf, 2 µg of DNA (PCR-amplified cDNA fragment or vector), 2 µl of each appropriate restriction enzyme, 1 µl of CutSmart buffer (B7204, New England Biolabs) and NFH_2O were added to a final digestion master mix volume of 10 µl. The master mix was then placed in a 37°C incubator overnight. After overnight digestion, the digested cDNA fragment and vector were separated and extracted from 1% agarose gel via gel electrophoresis and extraction methods described in 2.2.1.1.2 and 2.2.1.1.3. Table 2.2 summarizes the restriction enzymes used in my research.

Table 2.2: Summary of the restriction enzymes used in my research

Product Name	Company	Catalogue Number
NheI-HF	New England Biolabs	R3131
SalI-HF	New England Biolabs	R3138
HindIII	New England Biolabs	R0104
XhoI	New England Biolabs	R0146
XbaI	New England Biolabs	R0145
XmaI	New England Biolabs	R0180

2.2.1.1.5. Ligation

In a 0.2 ml eppendorf, 50 ng of digested cDNA fragment, 50 ng of digested vector, 1 µl of T4 DNA ligase reaction buffer (B0202S, New England Biolabs), 1 µl of T4 DNA ligase (M0202S, New England Biolabs) and NFH_2O to a final ligation master mix volume of 10 µl, were added. The mixture was incubated at RT for 1 hour before heat-inactivating the T4 ligase at 65°C for 30 minutes. Finally, the ligation product was placed on ice for transformation steps.

2.2.1.2. Site-directed mutagenesis (SDM)

2.2.1.2.1. SDM-PCR

The Q5® site-directed mutagenesis kit (E0554S, New England Biolabs) was used to facilitate DNA insertions, substitutions and deletions. In a 0.2 ml eppendorf, 10 µl of Q5 Hot Start high-fidelity 2X master mix, 2 µl of forward primer (5 µM), 2 µl of reverse primer (5 µM), 1 µl of DNA template (25 ng/µl) and 5 µl of NFH_2O were added to a final volume of 20 µl reaction master mix. SDM primer pairs were designed using NEBaseChanger® (https://nebasechanger.neb.com/), and their sequences summarized in Appendix. Table 2.3 summarizes the SDM-PCR cycling conditions used to perform site-directed mutagenesis.

Table 2.3: SDM-PCR program

Step	Temperature	Time	Cycle
1. Denaturation	95°C	30 seconds	1 cycle
2. Denaturation	95°C	10 seconds	25 cycles
3. Annealing	55-69°C*	30 seconds	
4. Elongation	72°C	2 minutes	
5. Elongation	72°C	2 ½ minutes	1 cycle
6. Stand-by	4°C	for short-term storage	N/A

* The annealing temperature could vary between primer pairs.

2.2.1.2.2. Kinase, ligase & DpnI (KLD) treatment

Following SDM-PCR, KLD treatment was applied to digest the old plasmids, which contained methylated sites for DpnI to recognize and digest. In a 0.2 ml eppendorf, 1 µl of PCR product, 5 µl of 2X KLD reaction buffer, 1 µl of 10X KLD enzyme mix and 3 µl of NFH_2O were mixed to a final volume of 10 µl, and the master mix incubated at RT for 10 minutes.

2.2.1.3. Transformation and plating

Following PCR and KLD treatment, 5 µl of the PCR product was mixed with 25 µl of 5-α competent *E. coli* (C2987, New England Biolabs) and placed on ice for 30 minutes before heat-shocked in 42°C water bath for 45 seconds. The transformation product was then recovered on ice for 5 minutes before adding 470 µl of pre-warmed SOC outgrowth media (B9020S, New England Biolabs). The mixture was shaken in a 37°C incubator for an hour, and then the *E. coli* was centrifuged at 3000 *xg* for 5 minutes. The supernatant was aspirated, and the pellet resuspended in 200 µl of fresh SOC outgrowth media. 110 µl of resuspended *E. coli* were plated onto LB agar plates (L2897, Sigma-Aldrich) containing 0.1 mg/ml ampicillin (A1001-25, Cambridge Bioscience) or 0.05 mg/ml kanamycin (MN800A-1, Cambridge Bioscience) as appropriate, and the plate was incubated in a 37°C incubator overnight. A ligation control was included in all experiments, consisting of the double-digested vectors without the inserts, so the E. coli colonies wouldn't grow due to the lack of circular vector containing the antibiotic resistant gene. Besides, a negative control was included as well by transformed the E. coli with 5 µl of NFH_2O.

2.2.1.4. Colony PCR

The next day, 10 colonies were picked by p200 pipette tips from each plate, and colony PCR performed to screen for successful constructs after molecular cloning. In each 0.2 ml eppendorf, 10 µl of 2X GoTaq® Master Mix, 1 µl of forward primer (5 µM), 1 µl of reverse primer (5 µM) and 8 µl of NFH_2O were added to a final colony PCR master mix volume of 20 µl, with the addition of one colony. To amply the targeted cDNAs, the same PCR cycling conditions were used as Table 2.1. Successful cloning was

indicated by a band of the correct fragment size following gel electrophoresis of the colony PCR products.

2.2.1.5. Plasmid amplification

The QIAGEN Plasmid Miniprep and Maxiprep kits (12123/12162, QIAGEN) were used to amplify the successfully cloned plasmid DNA. The protocols of each are described below.

2.2.1.5.1. Miniprep

Whilst selecting colonies for colony PCR, the corresponding pipet tips were ejected into individual 15 ml falcon tubes (62.554.502, Sarstedt) containing 5 ml of LB media (L3022, Sigma-Aldrich) containing 0.1 mg/ml ampicillin or 0.05 mg/ml kanamycin as appropriate. *E. coli* cultures were shaken in a 37°C incubator overnight. The next day, 0.5 ml of individual *E. coli* cultures were thoroughly mixed with 0.5 ml of glycerol (G5516, Sigma-Aldrich) in a 2 ml microtube with screwed cap (72.694.004, Sarstedt), Glycerol stocks were stored in a -80°C freezer. A further 3 ml of *E coli* cultures was transferred to 1.5 ml Eppendorf tubes and the cultures centrifuged at 10,000 *xg* for 5 minutes to pellet the *E. coli*. The pellets were resuspended in 250 µl of resuspension buffer (P1), lysed with 250 µl of lysis buffer (P2) and the cell lysates then neutralized with 350 µl of neutralizing buffer (N3). The neutralized lysates were centrifuged at 17,900 *xg* for 10 minutes, and the supernatants transferred to QIAprep 2.0 spin columns. The columns were centrifuged at 17,900 *xg* for 1 minute, and the flow-through discarded. Then, the plasmid DNA was washed with 0.75 ml of wash buffer (PE) containing 80% of pure ethanol, and the columns were centrifuged at 10,000 *xg* for 3 minutes to remove the remaining ethanol. Lastly, the plasmid DNA was eluted

into new 1.5 ml Eppendorf tubes with 55 µl of pre-warmed NFH_2O, and the concentration of plasmid DNA measured by NanoDrop.

2.2.1.5.2. Maxiprep

To amplify the plasmid DNA to a larger scale, around 200 µl of the glycerol stocks were looped into a 50 ml falcon tube (62.547.254, Sarstedt) containing 10 ml of LB media containing 0.1 mg/ml ampicillin or 0.05 mg/ml kanamycin as appropriate. The pre-cultured *E. coli* was shaken in a 37°C incubator for 8 hours before transferring to a 3 L conical flask with 500 ml of LB media containing 0.1 mg/ml ampicillin or 0.05 mg/ml kanamycin as appropriate. The flask was shaken overnight in a 37°C incubator. The next day, the LB media with confluent E. coli was transferred to a 500 ml centrifuge bottle, and the bottle centrifuged at 5000 *xg* for 30 minutes to pellet the *E. coli.* The pellet was resuspended in 8 ml of resuspension buffer (P1), then lysed with 8 ml of lysis buffer (P2), and the cell lysate neutralized with 8 ml of neutralizing buffer (S3). The neutralized lysate was transferred to a QIAfilter cartridge and incubated at RT for 10 minutes. A plunger was gently inserted into the QIAfilter cartridge to filter the cell lysate into a new 50 ml falcon tube. Then, 5 ml of binding buffer (BB) was added to the clear lysate and mixed thoroughly before transferred the lysate to a QIAGEN Plasmid *Plus* spin column with a tube extender attached. Using a vacuum pump (2522C-02, Welch) set to 300 mbar, the lysate was drawn through the column to Vac-Man ® manifold (A7231, Promega), and the plasmid DNA was washed with 0.7 ml of wash buffer (PE) containing 80% of pure ethanol. The column was then placed into a 2 ml collection tube and centrifuged at 10,000 *xg* for 3 minutes to remove the remaining ethanol. Lastly, the plasmid DNA was eluted into a new 1.5 ml Eppendorf tube with

400 µl of pre-warmed NFH_2O, and the concentration of plasmid DNA measured by NanoDrop.

2.2.1.6. Sanger sequencing

Plasmid DNA and sequencing primers were diluted to 100 ng/µl and 3.2 pmol/µl, respectively. Sanger sequencing was performed by Source Bioscience Ltd., with all orders submitting online (https://www.sourcebioscience.com/genomics/sanger-sequencing/). Sequencing results were aligned using the online Clustal Omega multiple sequence alignment platform (https://www.ebi.ac.uk/Tools/msa/clustalo/), with alignments inspected by eye to select successfully cloned plasmids. The sequencing primers used in my research are summarized in Appendix.

2.2.2. Cell-based assay (CBA)

2.2.2.1. Culture of HEK293T cells

A frozen aliquot of human embryonic kidney cells containing the SV40 T-antigen (HEK293T cells) was carefully removed from the liquid nitrogen, and the aliquot thawed in a warm water bath before transferring to a 15 ml falcon tube. Supplemented culture media was prepared by mixing 445 ml of Dulbecco's Modified Eagle's Medium high glucose (DMEM, D6429, Sigma-Aldrich) with 50 ml of fetal bovine serum (FBS, F7524, Thermo Fisher Scientific) and 5 ml of Antibiotic-Antimycotic (AA, 15240-062, Thermo Fisher Scientific). 10 ml of supplemented DMEM culture media was added into the 15 ml falcon tube, and the tube centrifuged at 800 *xg* for 5 minutes to pellet the cells. The supernatant was aspirated, and the pellet resuspended in 10 ml of fresh DMEM culture media before transferring to a T25 culture flask (430639, Corning). The cells were then

cultured for 3 days in a 37°C incubator with 5% CO_2 until confluent (>95%) and then routinely spilt twice a week into new T175 culture flasks (83.3912.002, Sarstedt) to maintain a healthy cell line.

To harvest HEK293T cells, the culture media was aspirated, and the cells incubated with 5 ml of 0.5% trypsin-EDTA in PBS (15400-054, Thermo Fisher Scientific) at RT for 3 minutes. Then, 25 ml of DMEM supplemented culture media was added, and the mixture transferred to a 50 ml falcon tube before centrifuging at 800 *xg* for 5 minutes to pellet the cells. The pellet was resuspended in 10 ml of supplemented DMEM culture media, from which 20 µl was taken to mix with 20 µl of 0.04% trypan blue in PBS (93595, Sigma-Aldrich). 20 µl of the mixture was loaded into each side of Countess™ cell counting chamber slide (C10228, Thermo Fisher Scientific), and the number of cells was quantified using a Countess™ 3 FL automated cell counter (AMQAF2000, Thermo Fisher Scientific). The remaining cells were then diluted to the desired concentration using supplemented DMEM culture media before seeding into PLL pre-treated culture plates.

2.2.2.2. Poly-L-lysine coating

Poly-L-lysine hydrobromide (PLL, P1399, Sigma-Aldrich) was used to coat 96-well culture plates (655090, Sigma-Aldrich) and coverslips (diameter = 13 mm, 631-0149, VWR) in 6-well culture plates (83.3920.300, Sarstedt). 0.01% PLL working solution was prepared by mixing 5 ml of 1% PLL with 495 ml of phosphate buffer saline (PBS) then filtering through the 0.22 µm filter (FPE204500, Guangzhou JET Bio-Filtration). 1 L of PBS was prepared by adding 10 PBS tablets (BR0014G, OXOID) into 1L of distilled water before autoclaving at 115°C for 30 minutes. In 96-well plate, 150 µl of

0.01% PLL solution was added in each well and incubated at RT overnight. In 6-well plates, 4 coverslips were placed into each well before adding 3 ml of 0.01% PLL working solution per well and incubating at RT for overnight. The PLL solution was then aspirated from 96-well and 6-well plates, and the plates dried in a laminar flow hood before storing at RT prior to use.

2.2.2.3. Transient transfection

Our transient transfection protocol was reviewed by the Genetic Modification Safety Committee (Reference code - NDCN_GM011). On day 1, the HEK293T cells were seeded onto the PLL-coated coverslips or plates. On day 2, the plasmid DNA was transiently transfected into the cells using polyethylenimine (PEI) at a PEI to DNA weight ratio of 2.8:1. To prepare a PEI working solution (5.626 µg/µl), 45 mg of solid PEI (408727, Sigma-Aldrich) was diluted in 8 ml of distilled water, and the pH was adjusted to 7.2 using hydrochloric acid solution (HCl, H9892, Sigma-Aldrich). For transfection, the plasmid DNA and PEI working solution were separately mixed with unsupplemented DMEM before combining and incubating at RT for 10 minutes. The transfection mix was then evenly allocated to each well and the plates incubated for 6 hours in a 37°C incubator with 5% CO_2. Following transfection, the culture media was changed to fresh supplemented DMEM culture media to allow cell recovery overnight in a 37°C incubator with 5% CO_2. Table 2.4 summarizes the transient transfection methods applied to 6- and 96-well plates, respectively.

Table 2.4: Methods of transient transfection in 6- and 96-well plate

Materials	6-well plate	96-well plate
Seeding amount on day 1	860,000 cells per well	30,000 cells per well
Seeding volume on day 1	3 ml per well	150 µl per well
Plasmid DNA	3 µg per well	12.6 µg per plate
PEI	1.5 µl per well	6.3 µl per plate
Unsupplemented DMEM (mixed with DNA or PEI separately)	Per well: Filled up to 25 µl along with DNA or PEI before combining together	Per plate: Filled up to 500 µl along with DNA or PEI before combining together
Volume of allocated transfection mix	50 µl per well without aspirating the original media	Per plate: 14 ml of DMEM (with FBS and AA) was added to 1ml of transfection mix. After aspirating the original media, 150 µl of master mix was allocated to each well
Volume of supplemented DMEM culture media	3 ml per well	150 µl per well

2.2.2.4. Methods for detecting antibody binding by CBA

2.2.2.4.1. Live CBA

On day 3, the plasma/sera/CSF samples were allocated into 24- or 96-well plates and diluted in the sample buffer, which consisted of 20 mM HEPES (H3375, Sigma-Aldrich) and 1% bovine serum albumin (BSA, A9647, Sigma-Aldrich) in DMEM. 4% formaldehyde in PBS (F003, TAAB) and the wash buffer, consisting of 20 mM HEPES in DMEM, were prepared, alongside Dako mounting media (S3023, Agilent) supplemented with 15 µl of DAPI solution (564907, BD Biosciences).

For 24-well plate CBAs, individual coverslips were carefully transferred cell-side up from 6-well plates to each well of pre-prepared 24-well plates containing diluted

plasma/sera/CSF samples (83.3922, Sarstedt) using forceps. The staining was done in 2-layer manner with diluted blood samples, 4% formaldehyde in PBS and diluted secondary antibodies applied sequentially. There were two washes after each incubation step. The coverslips were lastly mounted on superfrost microscope slides (631-0909, VWR) with one drop of DAPI-supplemented mounting media. For 96-well plate CBA, the cells were directly stained in 96-well plates, and the cells in each well mounted by adding one drop of DAPI-supplemented mounting media. Mounted coverslips/96-well plates were stored at 4°C.

Taking DsRed2 co-expressing live CBA for example, the antigen, here interleukin-22 (IL-22), was anchored to a C-terminal domain of Caspr2 protein and expressed 17 amino acid height above the surface of live HEK293T cells. Co-expressed but not attached to IL-22, DsRed2 was encoded after an internal ribosome entry site (IRES). The cells were fixed by 4% formaldehyde after primary but before secondary incubation, and the nuclei were labelled by DAPI in blue. Figure 2.1 provides a schematic of using live CBA to detect IL-22 autoantibodies, with Table 2.5 summarizing the live CBA methodology applied to 24- and 96-well plate. The commercial antibodies used in live CBAs were summarized in Table 2.7.

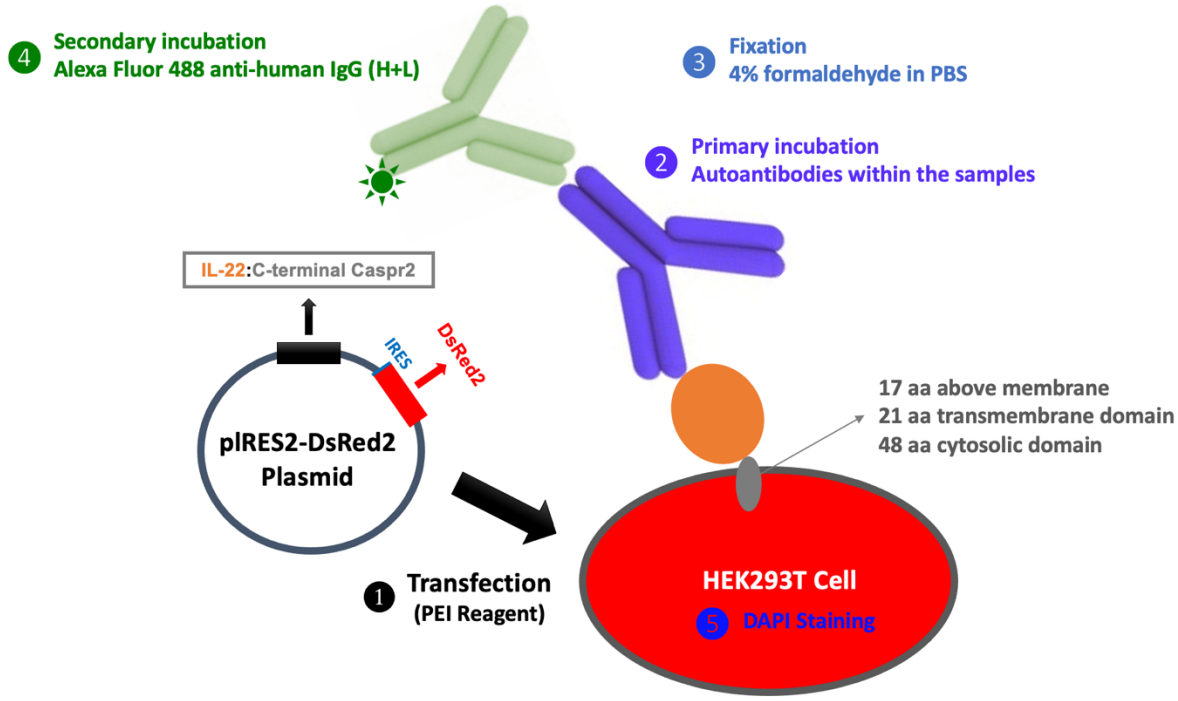


Figure 2.1: The DsRed2-reporting live CBA to detect IL-22 IgG autoantibodies. On day 2, the HEK293T cells were transfected with pIRES2-DsRed2 plasmid, which contained the cDNA of IL-22 and C-terminal Caspr2 domain, to surface-express IL-22 above the plasma membrane of HEK cells. On day 3 at RT, the transfected HEK cells were incubated with diluted blood samples, washed, fixed with 4% formaldehyde, washed, then incubated with 1:750 diluted AF488 anti-human IgG (H+L) antibody. Lastly, the cells were mounted by DAPI added mounting media.

Table 2.5: Methods of live CBA applied to 24- and 96-well plate

Experimental steps	24-well plate	96-well plate
1. CSF, plasma or serum sample (desired dilution)	250 µl, at RT for an hour	60 µl, at RT for an hour
2. Washed twice with DMEM/20 mM HEPES	250 µl each	180 µl each
3. Fixation	250 µl, at RT for 10 minutes	150 µl, at RT for 10 minutes
4. Washed twice with DMEM/20 mM HEPES	250 µl each	180 µl each
5. Secondary antibodies (1:750 dilution)	250 µl, at RT for 45 minutes	100 µl, at RT for 45 minutes

6. Washed twice with DMEM/20 mM HEPES	250 µl each	180 µl each
7. Mounting	One drop of mounting media (supplemented 1:1000 diluted DAPI)	
8. Storage	Stored at 4°C	

2.2.2.4.2. Permeabilized CBA

To access the intracellular targets, the cells were fixed with 4% formaldehyde in PBS, washed twice with PBS, permeabilized in 0.3% Triton X-100 in PBS (X100, Sigma-Aldrich) and then blocked at 4°C overnight with 10% normal serum from the host of secondary antibody, e.g., normal goat serum (NGS, ab7481, Abcam) and normal rat serum (NRS, ab7488, Abcam), and 0.1% Triton X-100 in PBS. Subsequently, the sample incubation, washes and secondary incubation were the same as live CBA, except samples and secondary antibodies were diluted in the sample buffer, consisting of 1% normal serum and 0.1% Triton X-100 in PBS, and the cells were washed twice by PBS. Figure 2.2 provides a schematic of permeabilize CBA to detect IgG autoantibodies to intracellular antigen. Table 2.6 summarizes the permeabilized CBA methodology of permeabilized CBA applied to 24- and 96-well plate. The commercial antibodies used in permeabilized CBAs were summarized in Table 2.7.

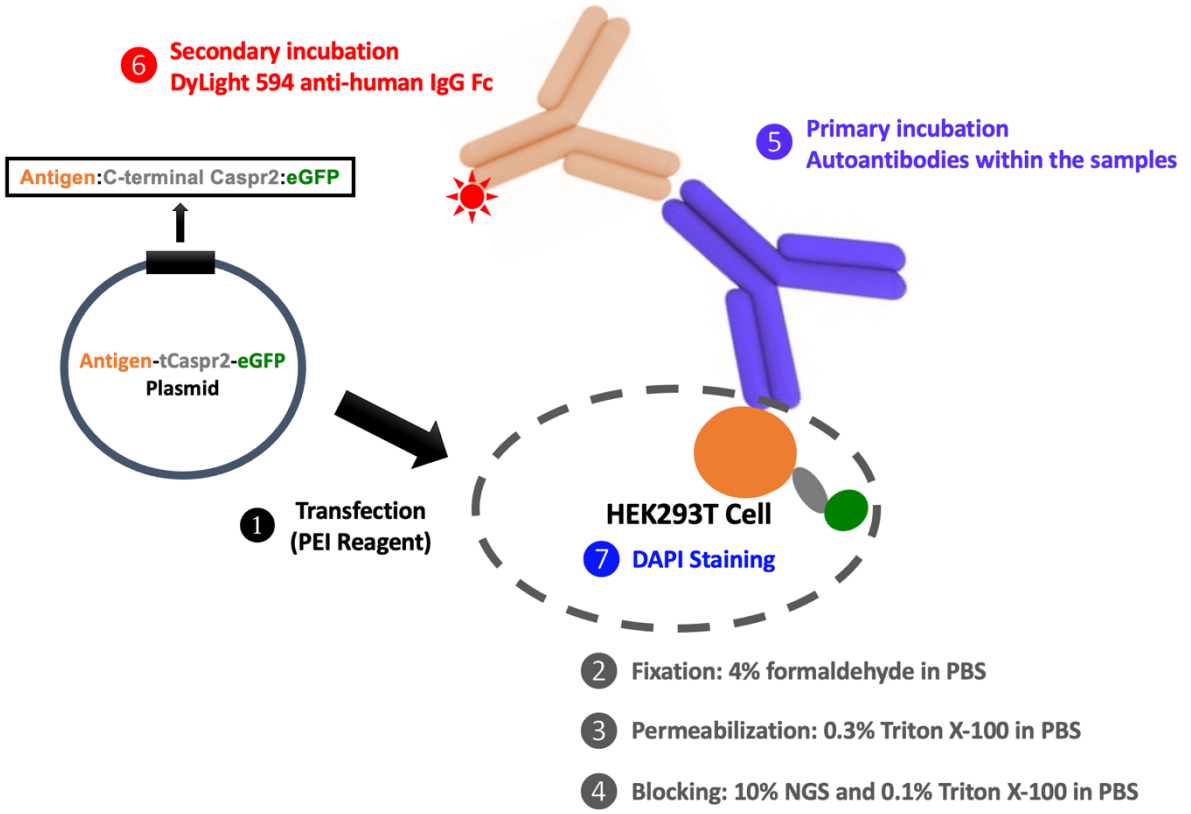


Figure 2.2: The eGFP-tagged permeabilized CBA for detecting IgG autoantibodies to intracellular antigen. On day 2, the HEK293T cells were transfected with the plasmid to intracellularly express the targeted antigen. The antigen was C-terminally tethered to a truncated Caspr2 C-terminal domain and an eGFP. On day 3, the cells were fixed with 4% formaldehyde at RT, washed, permeabilized with 0.3% Triton X-100 at RT, then blocked with 10% normal goat serum (NGS) in 0.1% Triton X-100 solution overnight at 4°C. On day 4, the permeabilized cells were incubated with diluted blood samples, washed, then incubated with 1:750 diluted DyLight 594 anti-human IgG Fc antibody. Lastly, the cells were mounted by DAPI-added mounting media.

Table 2.6: Methods of permeabilized CBA applied to 24- and 96-well plate

Experimental steps	24-well plate	96-well plate
1. Fixation	250 µl, at RT for 10 minutes	150 µl, at RT for 10 minutes
2. Washed twice with PBS	250 µl each	180 µl each
3. Permeabilization	250 µl, at RT for 10 minutes	150 µl, at RT for 10 minutes

4. Blocking	250 µl, at 4°C overnight	150 µl, at 4°C overnight
5. Washed twice with PBS	250 µl each	180 µl each
6. CSF, plasma or serum sample (desired dilution)	250 µl, at RT for an hour	60 µl, at RT for an hour
7. Washed twice with PBS	250 µl each	180 µl each
8. Secondary antibodies (1:750 dilution)	250 µl, at RT for 45 minutes	100 µl, at RT for 45 minutes
9. Washed twice with PBS	250 µl each	180 µl each
10. Mounting	One drop of mounting media (supplemented 1:1000 diluted DAPI)	
11. Storage	Stored in 4°C	

Table 2.7: Summary of the commercial antibodies used in CBAs

Product name	**Company**	**Catalog #**
Goat anti-human IgG (H+L), Alexa Fluor 488	Thermo Fisher	A-11013
Goat anti-human IgG (H+L), Alexa Fluor 568	Thermo Fisher	A-21090
Goat anti-human IgG Fc, DyLight 488	Thermo Fisher	SA5-10134
Goat anti-human IgG Fc, DyLight 594	Abcam	ab97005
Goat anti-rabbit IgG Fc, Alexa Fluor 488	Abcam	ab150089
Goat anti-rabbit IgG (H+L), Alexa Fluor 568	Thermo Fisher	A-11011
Goat anti-rabbit IgG (H+L), Alexa Fluor 594	Thermo Fisher	A-11012
Rabbit anti-human IL23A antibody	Abcam	ab45420
Rabbit anti-human HuD polyclonal antibody	Thermo Fisher	PA5-97703
Rabbit anti-human ZIC4 polyclonal antibody	Thermo Fisher	PA5-56392
Rabbit anti-human CDR2L polyclonal antibody	Thermo Fisher	PA5-54552
Rabbit anti-human NOVA1 polyclonal antibody	Thermo Fisher	PA5-52063
Rabbit anti-human NOVA2 polyclonal antibody	Thermo Fisher	PA5-83784
Rabbit anti-human Amphiphysin polyclonal antibody	Thermo Fisher	PA5-82701

Rabbit anti-human CRMP5 polyclonal antibody	Thermo Fisher	PA5-84896
Rabbit anti-human SOX1 polyclonal antibody	Sigma-Aldrich	SAB1300687
Rabbit anti-human Ma2 polyclonal antibody	Thermo Fisher	PA5-30982
Rabbit anti-human CDR2 polyclonal antibody	Thermo Fisher	PA5-54903
Rabbit anti-human KLHL11 polyclonal antibody	Sigma-Aldrich	HPA054269
Rabbit anti-mouse IgG (H+L), Alexa Fluor 568	Thermo Fisher	A-11061
Mouse anti-myc tag antibody, DyLight 550	Abcam	ab117511
Mouse anti-human Ma1 polyclonal antibody	Sigma-Aldrich	SAB1406802

2.2.2.5. Imaging, scoring and data analysis

For imaging and scoring purposes, a compact cell culture inverted microscope (CKX53, OLYMPUS) and an upright fluorescent microscope (DM2500, Leica) were used to capture the fluorescent signal, which was representative of the amount of secondary antibody binding. The fluorescent signal was visually scored from 0 (no binding) to 4 (very strong labelling of virtually all transfected cells), and the endpoint titre was defined as the reciprocal value of highest dilution to give a CBA score of 1. Taking IL-22 live CBA as example, Figure 2.3 demonstrates how each CBA score appeared under the microscope, and the endpoint titre of IL-22 autoantibodies in that TAMG plasma was 3200. In general, the cut-off of each CBA was set above the highest endpoint titre of targeted autoantibody from healthy sera, and any sample with endpoint titre higher than the cut-off was reported seropositive for the targeted autoantibody. Then, the sensitivity, specificity, positive and negative predictive values of each CBA were calculated. The definitions of each diagnostic term are as below.

Sensitivity

The proportion of people with the disease diagnosed seropositive by our CBA

Specificity

The proportion of people without the disease diagnosed seronegative by our CBA

Positive predictive value (PPV)

The proportion of people with a positive CBA result who actually have the disease

Negative predictive value (NPV)

The proportion of people with a negative CBA result who don't have the disease

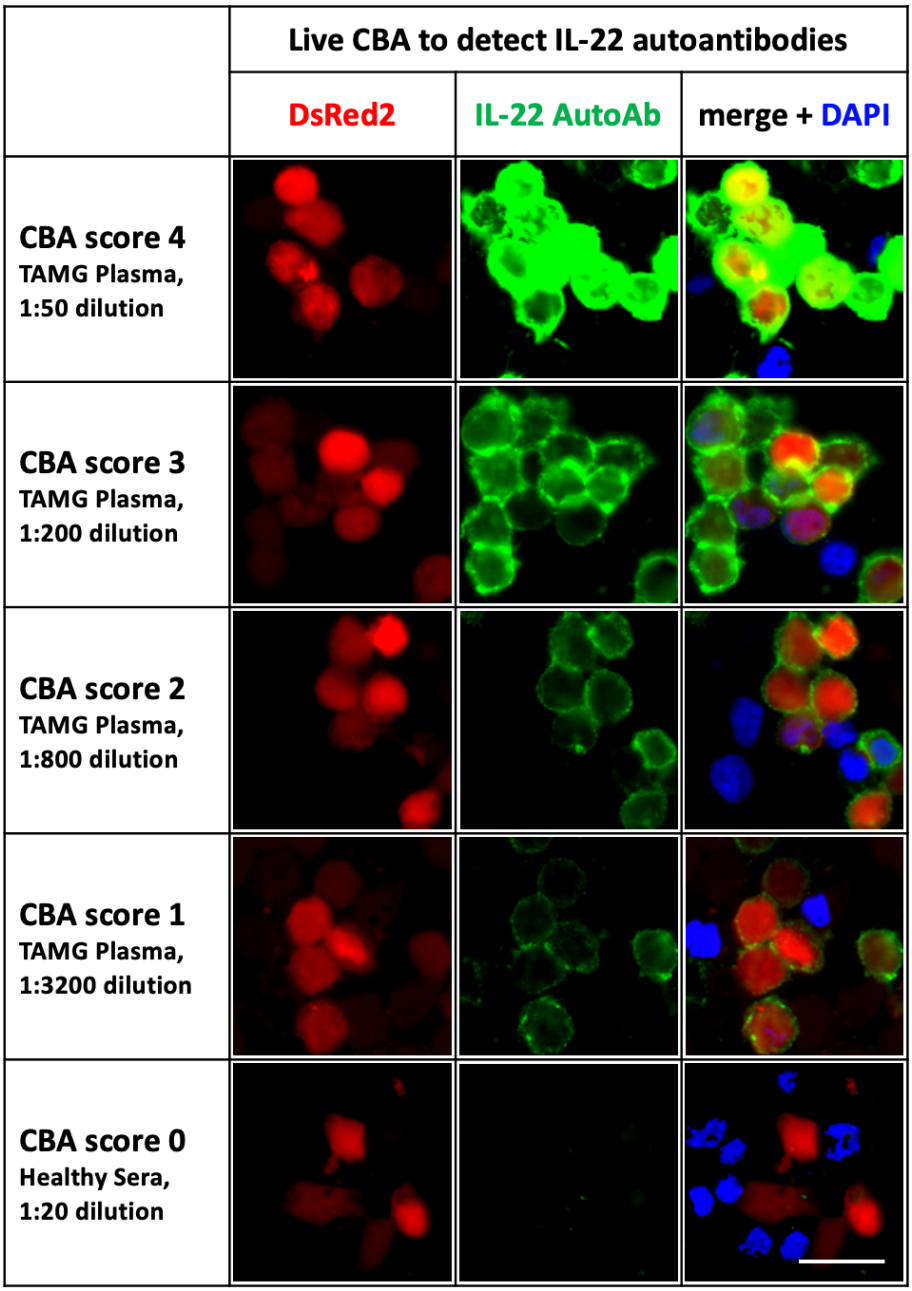


Figure 2.3: Example of CBA scoring. Under IL-22 live CBA platform, a TAMG plasma with IL-22 autoantibodies (endpoint titre = 3200) was diluted from 1:50 to 1:3200, and the images representing each CBA score were cropped. The more intense the antibody binding the higher the score with the brightest green fluorescence shown above scoring a 4 and the dimmest scoring a 1. We have used a strong positive sample and diluted it to show how we score the assay, but routinely samples are tested at a serum dilution of 1:50 before titrating down. Then, the endpoint titre is determined, which was 3200, as can be seen in the sample scoring a 1. A healthy serum screened at a dilution of 1:20 dilution was scored 0. DsRed2 was a red transfection marker regulated by internal ribosome entry site (IRES) on the same expression plasmid. The signals of secondary antibody binding were in green as Alexa Fluro 488 was conjugated to anti-human IgG H+L secondary antibody. The cell nuclei were labelled by DAPI in blue. Magnification x 400. Scale bar = 25 μm.

2.2.3. Flow cytometry CBA (F-CBA)

2.2.3.1. Cell culture, transfection and harvest

On day 1, 860,000 HEK293T cells were seeded per well in 6-well plate (without coated with PLL) and cultured in supplemented DMEM in a 37°C incubator with 5% CO_2. On day 2, the cells in each well were transiently transfected with 3 μg of plasmid DNA as previously described (see Table 2.4). On day 3, after the removal of original culture media, the transiently transfected HEK293T cells were harvested by FACS buffer, consisting of 3% FBS and 2 mM EDTA (15575-038, Thermo Fisher Scientific) in PBS. The cells were then quantified and kept on ice in FACS buffer.

2.2.3.2. Methodologies of F-CBA

2.2.3.2.1. Methods for labelling dead cells

To fluorescently label dead cells, LIVE/DEADTM fixable near-IR amine-reactive dead cell stain kit (L10119, Thermo Fisher Scientific) and 7-AAD viability staining solution (420404, BioLegend) were used as dead cell labelling dyes. Due to its reversible nuclei-labelling property, 7-AAD was applied before acquisition in our live but not

permeabilized F-CBA to label the nuclei of dead cells because the nuclei of live cells would be labelled with 7-AAD after permeabilization (Schmid et al., 2007). Alternatively, LIVE/DEADTM fixable near-IR amine-reactive dye, which irreversibly reacted with free amines in the cytosol and on the surface of dead cells (Perfetto et al., 2006), was applied before the fixation step in our permeabilized F-CBA. The dye can only react with free amines on the surface of live cells, which resulted in > 50-fold dimer staining compared to dead cells. Table 2.8 summarizes the properties, timing and methods of using both viability dyes.

Table 2.8: Summary of the viability dyes used in F-CBAs

	Fixable amine-reactive dye	**7-AAD viability dye**
Properties	• Irreversibly reacting with free amines in the cytosol and on the surface of dead cells • Applicable to our permeabilized F-CBA	• Reversibly labelling the nuclei of dead cells • Applicable to our live F-CBA
Timing of usage	Before the fixation step in our permeabilized F-CBA	Before acquisition in our live F-CBA
Method of usage	A new vial of fixable viability dye was reconstituted by 50 µl of DMSO provided in the kit. In a 15 ml falcon tube, 10 million cells were resuspended in 10 ml of FACS buffer, containing 1:1000 diluted fixable viability dye, and incubated in dark at RT for 20 minutes before washing once with 10 ml of FACS buffer.	In 96-well plate, the cells were resuspended in 80 µl of FACS buffer, containing 1:100 diluted 7-AAD viability dye. Before acquisition, the cells were incubated in dark at RT for at least 10 minutes.

2.2.3.2.2. Methods for detecting antibody binding

2.2.3.2.2.1. Live F-CBA

To detect antibody binding on the surface of transiently transfected and suspended HEK cells, live F-CBA was performed in 96-well conical bottom plates (277143, Thermo Fisher Scientific) with staining 100,000 cells per well. The sera and CSF samples were screened in 1:20 and 1:4 dilution, respectively. Our F-CBAs followed a 2-layer staining protocol similar to our CBAs, with diluted blood samples and secondary antibodies applied sequentially. The samples and secondary antibodies were diluted in FACS buffer, and the cells were washed twice with FACS buffer after each antibody staining step. Lastly, at least 10,000 cells in each well were acquired by BD LSRII cytometer at medium flow rate (60 µl per minute) or through high throughput screening mode (HTS, 3 µl per second). The commercial antibodies used in live F-CBAs were summarized in Table 2.9. Below displays the step-by-step live F-CBA staining protocol.

Live F-CBA staining protocol

1. 100,000 transfected HEK cells per well were allocated into a 96-well conical buttom plate
2. The plate was centrifuged at 800 *xg* for 2 minutes to pellet the cells, and then the supernatant was flicked off
3. The cells were resuspended by 100 µl of blood sample (1:20 diluted sera or 1:4 diluted CSF), and incubated on ice for 40 minutes
4. Repeat step 2
5. The cells were washed twice with 180 µl of FACS buffer (repeat step 2 between each wash)
6. Repeat step 2
7. The cells were resuspended by 100 µl of 1:200 diluted secondary antibody, and incubated on ice in dark for 30 minutes
8. Repeat step 2

9. The cells were washed twice with 180 µl of FACS buffer (repeat step 2 between each wash)
10. Repeat step 2
11. The cells were resuspended by 80 µl of FACS buffer, containing 1:100 diluted 7-AAD viability dye
12. The cells were incubated at RT in dark for at least 10 minutes before acquired by BD LSRII

Table 2.9: Summary of the commercial antibodies used in F-CBAs

Product name	**Company**	**Catalog #**
Goat anti-human IgG Fc, DyLight 488	Thermo Fisher	SA5-10134
Goat anti-human IgG Fc, Alexa Fluor 488	BioLegend	410705
Goat anti-human IgG Fc, DyLight 594	Abcam	ab97005
Rat anti-human IgG Fc, PE	BioLegend	410708
Rat IgG2a, κ Isotype Ctrl antibody, PE	BioLegend	400508
Mouse anti-human IgG1, Alexa Fluor 488	Thermo Fisher	A-10631

2.2.3.2.2.2. Permeabilized F-CBA

The saponin-based permeabilization kit (Cyto-Fast™ Fix/Perm Buffer Set, 426803, BioLegend) was used to gently permeabilize cell membrane. In a 15 ml falcon tube, 10 million cells were incubated with 1.5 ml of Cyto-Fast™ Fix/Perm buffer at RT for 20 minutes. The cells were then centrifuged at 500 *xg* for 5 minutes, aspirating the supernatant and washed once with 10 ml of 1X Cyto-Fast™ Perm/Wash buffer. Following the same centrifugation and aspiration steps, the cells were blocked with 10 ml of 10% normal serum in 1X Cyto-Fast™ Perm/Wash buffer at RT for 30 minutes. There was one wash after blocking step, and then the cells were allocated to 96-well conical bottom plates (100,000 cells/well). Followingly, the 2-layer staining protocol was identical to live F-CBA, and at least 10,000 cells in each well were acquired by BD

LSRII cytometer. The commercial antibodies used in permeabilized F-CBAs were summarized in Table 2.9. Below displays the step-by-step permeabilized F-CBA staining protocol.

Permeabilized F-CBA staining protocol

1. 10,000,000 transfected HEK cells were allocated into a 15 ml Falcon tube
2. The tube was centrifuged at 800 *xg* for 2 minutes to pellet the cells, and then the supernatant was aspirated
3. The cells were resuspended by 10 ml of FACS buffer, containing 1:1000 diluted amine-reactive dye, and incubated in dark at RT for 20 minutes
4. Repeat step 2
5. The cells were washed once with 10 ml of FACS buffer
6. Repeat step 2
7. The cells were resuspended by 1.5 ml of Cyto-Fast™ Fix/Perm buffer at RT for 20 minutes
8. The tube was centrifuged at 500 *xg* for 5 minutes to pellet the cells, and then the supernatant was aspirated
9. The cells were washed once with 10 ml of 1X Cyto-Fast™ Perm/Wash buffer
10. Repeat step 8
11. The cells were incubated with 10 ml of 10% normal serum in 1X Cyto-Fast™ Perm/Wash buffer at RT for 30 minutes
12. Repeat step 8
13. The cells were washed once with 10 ml of FACS buffer
14. Repeat step 8
15. The cells were resuspended by 10 ml of FACS buffer
16. 100,000 processed cells were allocated into a 96-well conical bottom plate
17. The plate was centrifuged at 800 *xg* for 2 minutes to pellet the cells, and then the supernatant was flicked off
18. The cells were resuspended by 100 µl of blood sample (1:20 diluted sera or 1:4 diluted CSF), and incubated on ice in dark for 40 minutes
19. Repeat step 17

20. The cells were washed twice with 180 µl of FACS buffer (repeat step 15 between each wash)
21. Repeat step 17
22. The cells were resuspended by 100 µl of 1:200 diluted secondary antibody, and incubated on ice in dark for 30 minutes
23. Repeat step 17
24. The cells were washed twice with 180 µl of FACS buffer (repeat step 15 between each wash)
25. Repeat step 17
26. The cells were resuspended by 80 µl of FACS buffer before acquiring by BD LSRII

2.2.3.2.3. Strategies of gating and analysis

Following acquisition, the data files were exported into and analyzed using FlowJo software (version 10.8.1). Figure 2.4a-c show the gating strategy employed to gate on live and singlet HEK cells. Subsequently, the signal of DsRed2, intracellularly expressed as a reporter, was plotted on the y-axis, and the signal of DyLight 488, conjugated to anti-human IgG Fc secondary antibody, was plotted on the x-axis. The threshold to distinguish $DsRed2^{neg}$ and $DsRed2^{+}$ populations was defined by using untransfected HEK293T cells, 99.4% of which were below the threshold of y=40 (Figure 2.4b). Next, using 2^{nd} Ab only control as reference, the high $DsRed2^{+}$ threshold was set above the "median + 10 x median absolute deviation percentile (MADP)" of fluorescence intensities on the y-axis in $DsRed2^{+}$ population (Figure 2.4c). Then, the same gates were applied to every sample to quantify the median fluorescence intensities on the x-axis (MFI_x) of $DsRed2^{neg}$ and high $DsRed2^{+}$ populations, and then ΔMFI_x was calculated as "MFI_x (high $DsRed2^{+}$) - MFI_x ($DsRed2^{neg}$)" (Figure 2.4d). The cut-off was set above "mean + 6 x standard deviation" of the ΔMFI_x from healthy sera.

The signal-to-noise ratio was calculated as "average ΔMFI_x of the samples in targeted group ÷ (mean + 3 x standard deviation) of the ΔMFI_x from healthy sera".

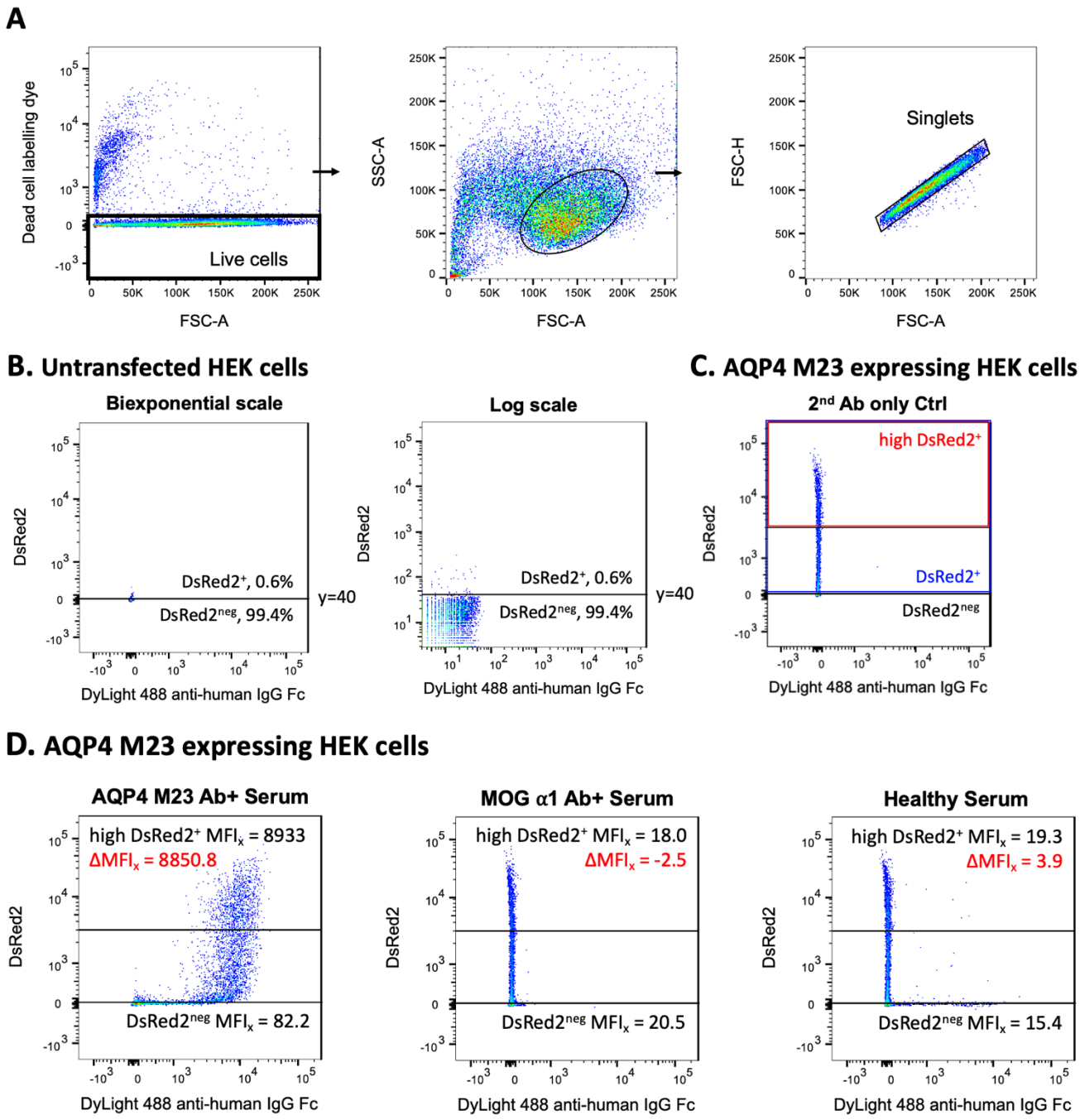


Figure 2.4: The step-by-step gating strategies of F-CBA. (a) Taking AQP4 M23 live F-CBA as example, the live cells population was gated on before plotting its side scatter area (SSC-A) on the y-axis and its forward scatter area (FSC-A) on the x-axis. Next, the core of live HEK cell cloud was gated on before plotting its forward scatter height (FSC-H) on the y-axis and its FSC-A on the x-axis. Then, the singlets were gated on. (b) The singlets of the untransfected HEK293T cells were plotted as DsRed2

signal on the y-axis and secondary antibody signal on the x-axis. The same sample was plotted in biexponential and log scales. The threshold was y=40, and the percentages of events in DsRed2^{neg} and DsRed2^{+} gates were quoted. (c) As a gating reference, the live singlets of secondary antibody only control was gated to define the high DsRed2^{+} population. Each population in the plot was colored-coded with their legends. (d) Here, the live substrate was AQP4 M23, and the sera with autoantibodies to AQP4 M23 and MOG α1 isoforms, respectively, and a healthy serum were screened. The MFI_x of DsRed2^{neg} and high DsRed2^{+} populations were mentioned at the top right corner of each population, and the ΔMFI_x of each sample were quoted in red.

Chapter III

Detection of autoantibodies to soluble cytokines associated with thymoma in patients with autoimmune myasthenia gravis

3.1. Introduction

3.1.1. Autoimmune myasthenia gravis

Autoimmune myasthenia gravis (aMG) is an antibody-medicated disorder. Patients present with fatigable muscle weaknesses due to antibody-mediated disruption of signal transduction at the neuromuscular junction (Gilhus et al., 2019). The aMG patients are classified by their antibody profiles, ages of MG onset and thymic abnormalities as summarized in Table 3.1 (Marx et al., 2010b, Gilhus and Verschuuren, 2015, Gilhus et al., 2019). Most aMG patients have autoantibodies to nAChR, and they can be separated by the age of 50 into two subgroups, i.e., early-onset myasthenia gravis (EOMG) and late-onset myasthenia gravis (LOMG), both without radiologically evident thymoma. As for the patients with thymoma-associated myasthenia gravis (TAMG), all have polyclonal autoantibodies to nAChR, 95% to titin and 75% the ryanodine receptor (RyR) (Skeie et al., 2006). Up to 10% of aMG patients don't have autoantibodies to nAChR but have IgG4 autoantibodies to muscle-specific kinase (MuSK). Besides, a few clinically defined MG patients who are seronegative for autoantibodies to nAChR and MuSK may have autoantibodies to low-density lipoprotein receptor-related protein 4 (LRP4) and agrin, although further investigations of these antibodies and their antigenic targets are required (Gilhus et al., 2019, Gilhus and Verschuuren, 2015).

Table 3.1: Classification of autoimmune myasthenia gravis

aMG Subgroup	Antibody Target	Percentage of MG patients	Age of MG Onset	Thymic Abnormality
EOMG	nAChR	20-25%	< 50 yrs old	LFH
LOMG	nAChR	40-50%	> 50 yrs old	Thymic involution
TAMG	nAChR	10-15%	Vary	Thymoma
MuSK MG	MuSK	5-10%	Vary	Normal
Seronegative MG	LRP4, agrin	5-10%	Vary	Normal

3.1.2. Thymoma-associated cytokine autoantibodies

As we have seen, patients with TAMG can have autoantibodies to multiple proteins including the nAChR, titin and the ryanodine receptor. In addition, some TAMG patients have autoantibodies to cytokines such as interferon alpha (IFN-α; 70%), interferon omega (IFN-ω, 60%) and interleukin-12 (IL-12; 50%), and fewer having autoantibodies to IL-6, IFN-β and Th17/22 cytokines (Kisand et al., 2011, Meager et al., 2003, Marx et al., 2010a, Karner et al., 2016). Some of these autoantibodies to IFN-α (30.8%), IFN-ω (30.8%) and IL-12 (14.3%) have also been found in LOMG patients, although to a lesser extent (Meager et al., 2003). It was previously shown that some of these autoantibodies may be more frequently found in MG patients with thymoma and particularly in those with recurrent thymoma after thymectomy (Meager et al., 2003). For instance, Buckley et al. observed the high prevalence of autoantibodies to IFN-α and IL-12 in TAMG cohort, and their titres increased significantly at the recurrence of patients' thymoma (Buckley et al., 2001).

3.2. Research Rationales

Solid-phase enzyme-linked immunosorbent assay (ELISA) and fluid-phase detection assays, e.g., radioimmunoassay (RIA) and luciferase immunoprecipitation system (LIPS) have been used to quantify the autoantibodies to soluble cytokines (Meager, 2000, Bendtzen and Svenson, 2011). Previous works demonstrated issues with some of these techniques, such as the changes in cytokine conformation to create unspecific epitopes or to hinder essential epitopes (Meager and Wadhwa, 2014, Wadhwa and Thorpe, 2010). Our group has promoted the use of live cell-based assays (CBA) in autoimmune neurology to keep the antigen structure as native as possible while hiding membrane or submembrane aspects of each target which are not accessible to circulating antibodies. Leite et al. improved the detection of autoantibodies to acetylcholine receptors (AChR) via live CBA with co-expressing AChR with the cytosolic clustering molecule - rapsyn. They detected autoantibodies to rapsyn-clustered AChR in 66% (25/38) of the sera previously tested negative by RIA (Leite et al., 2008). Also, Waters et al. have found live CBAs having greater sensitivity (73%) to detect autoantibodies to aquaporin-4 (AQP4) in a neuromyelitis optica spectrum disorder (NMOSD) cohort compared to commercial ELISA (60%), indirect immunofluorescence (48.3%) and fluorescence immunoprecipitation (53.3%) (Waters et al., 2012). To date, the accuracy of other tests for new antigens identified in the field of autoimmune neurology have been improved by the use of live CBAs, e.g., AQP, MOG, NMDAR, LGI1 and CASPR2. The use of this technology for soluble molecules was firstly demonstrated in 2010 where autoantibodies to soluble LGI1 were detected when LGI1 was expressed extracellularly with linked to a transmembrane domain (Irani et al., 2010). In this chapter, I described our attempts to expand on this initial work for developing a live cell-based system to detect autoantibodies to soluble cytokines,

following this to look at the frequency of autoantibodies to cytokines in the plasma and serum samples from aMG patients with or without thymoma.

3.3. Study Aims

I. Develop a live CBAs to detect autoantibodies to soluble cytokines
II. Increase assay sensitivity by extending the extracellular amino acid linker
III. Introduce myc tag as a reporter to quantify cytokine surface expression
IV. Measure the frequency of autoantibodies to different cytokines in aMG patients with or without the presence of thymoma
V. Compare the results generated by our live CBAs and the published luciferase immunoprecipitation system (LIPS) assays

3.4. Methods

3.4.1. Samples

A total of 217 plasma and sera samples from a historical collection of frozen samples stored in -20 °C freezer. All blood donors have been consented. With study group demographics summarized in Table 3.2, the aMG samples were derived from Prof. Maria Isabel Leite, Prof. Nick Willcox and Dr. Philip Ambrose's clinic, and the healthy sera were taken from OANG sample stocks. An age of 50 was selected to distinguish between early (< 50 years of age) and late-onset MG (≥ 50 years of age); both groups were without radiologically evident thymoma. All aMG patients were reported seropositive for AChR autoantibody and diagnosed with muscle jitter via single-fiber electromyography (SFEMG). The aMG patients from Dr Ambrose's clinic were all bled before thymectomy and the initiation of immunosuppressant therapy. All other aMG patients were mostly bled at their earliest available clinic visits following diagnosis to

avoid treatment effects. Besides, there were 2 additional plasma samples from the thymoma patients with systemic sclerosis and neuromyotonia, respectively, given by Prof. Nick Willcox's.

Table 3.2: Demographics of the participants at the time of sampling

	TAMG	LOMG	EOMG	HC
N	46	60	41	68
M:F Ratio	0.31	2.16	0.41	0.70
Median Age	52.0	71.0	37.0	40.5
Age Range	(24. 80)	(51, 90)	(18, 67)	(20, 87)

3.4.2. Construct design

3.4.2.1. The DsRed2-reporting cytokine surface expression platform

We decided to use an pIRES2-DsRed2 vector initially so that the fluorescence was not directly linked to the antigen for transmembrane proteins. This vector was then used to test the idea that we could detect antibodies to soluble cytokines such as IL-22, C-terminally linked to the transmembrane and cytosolic domains of Caspr2 to tag the soluble molecule to the membrane but keep the cytokine conformational. The cDNA of IL-6, IL-12A, IL-12B, IL-17A, IL-17F, IL-23A, IFNα2, IFNα8 and IFNω1 were subcloned to replace the cDNA of IL-22 via NheI and SalI restriction sites, as described in Chapter II.

3.4.2.2. Flexible amino acid extension

According to conformational flexibility scale, Glycine (G), Serine (S), Alanine (A), Aspartic acid (D) and Asparagine (N) are the top-5 most flexible β-turn forming amino acids compared to Valine (V) and Isoleucine (I), which are the rigid β-sheet forming

amino acids (Huang and Nau, 2003). Two flexible amino acid extensions were created, which was (Glycine-Glycine-Serine)$_4$ and 36 flexible amino acid extensions (composed of G, S, A, D and N). The GGS$_4$ extension was introduced between the cDNA of IL-22 and C-terminal Caspr2 domain via site-directed mutagenesis. On the other hand, the 939bp cDNA sequence, containing the 36 flexible amino acid extension, was synthesized by IDT gBlocks technology, and cloned into pIRES2-DsRed2 vector through NheI (GCTAGC) and XmaI (CCCGGG) restriction sites (Figure 3.1).

GATCACAGATCTTCAGGCTAGCCCACCATGGCCGCCCTGCAGAAATCTGTGAGCTCTTTCCT
TATGGGGACCCTGGCCACCAGCTGCCTCCTTCTCTTGGCCCTCTTGGTACAGGGAGGAGCAG
CTGCGCCCATCAGCTCCCACTGCAGGCTTGACAAGTCCAACTTCCAGCAGCCCTATATCACC
AACCGCACCTTCATGCTGGCTAAGGAGGCTAGCTTGGCTGATAACAACACAGACGTTCGTCT
CATTGGGGAGAAACTGTTCCACGGAGTCAGTATGAGTGAGCGCTGCTATCTGATGAAGCAGG
TGCTGAACTTCACCCTTGAAGAAGTGCTGTTCCCTCAATCTGATAGGTTCCAGCCTTATATG
CAGGAGGTGGTGCCCTTCCTGGCCAGGCTCAGCAACAGGCTAAGCACATGTCATATTGAAGG
TGATGACCTGCATATCCAGAGGAATGTGCAAAAGCTGAAGGACACAGTGAAAAAGCTTGGAG
AGAGTGGAGAGATCAAAGCAATTGGAGAACTGGATTTGCTGTTTATGTCTCTGAGAAATGCC
TGCATTGTCGACGGTGGCAGTGCTGATAATGCAGGTGGCAGTGATAATGCTGACAATGGTGG
CAGTGGAGGGAGCGCCGACAACGCGGGAGGGAGCGACAACGCCGACAACGGAGGGAGCGGAC
AAGGCCAAGCTATAAGAAATGGAGTCAACAGAAACTCGGCTATCATTGGAGGCGTCATTGCT
GTGGTGATTTTCACCATCCTGTGCACCCTGGTCTTCCTGATCCGGTACATGTTCCGCCACAA
GGGCACCTACCATACCAACGAAGCAAAGGGGGCGGAGTCGGCAGAGAGCGCGGACGCCGCCA
TCATGAACAACGACCCCAACTTCACAGAGACCATTGATGAAAGCAAAAAGGAATGGCTCATT
TGACCCGGG

Figure 3.1: The cDNA sequence synthesized by IDT gBlocks technology. The cDNA of IL-22 is in blue, the 36 flexible amino acid extension is in pink, the cDNA of C-terminal Caspr2 domain is in green, the Kozak sequence is underlined and the restriction sites (NheI: GCTAGC; SalI: GTCGAC; XmaI: CCCGGG) are in yellow.

3.4.2.3. The myc-tagged cytokine surface expression platform

Because DsRed2 is regulated by IRES, its intracellular expression couldn't represent the amount of cytokine expressed on the surface of HEK cells. Therefore, the myc tag was introduced within the 36 flexible amino acid extension, allowing fluorophore-

conjugated anti-myc tag antibody to recognize then to quantify the surface expression levels of targeted cytokines.

Before introducing myc tag, a XbaI restriction site was introduced before the cDNA of DsRed2, which was removed through XbaI digestion and self-ligation (Figure 3.2). Then, the myc tag (EQKLISEEDL) was introduced before, in the middle of and after the 36 flexible amino acid extension in IL-22 surface-expressing construct before subcloning other targeted cytokines to replace IL-22.

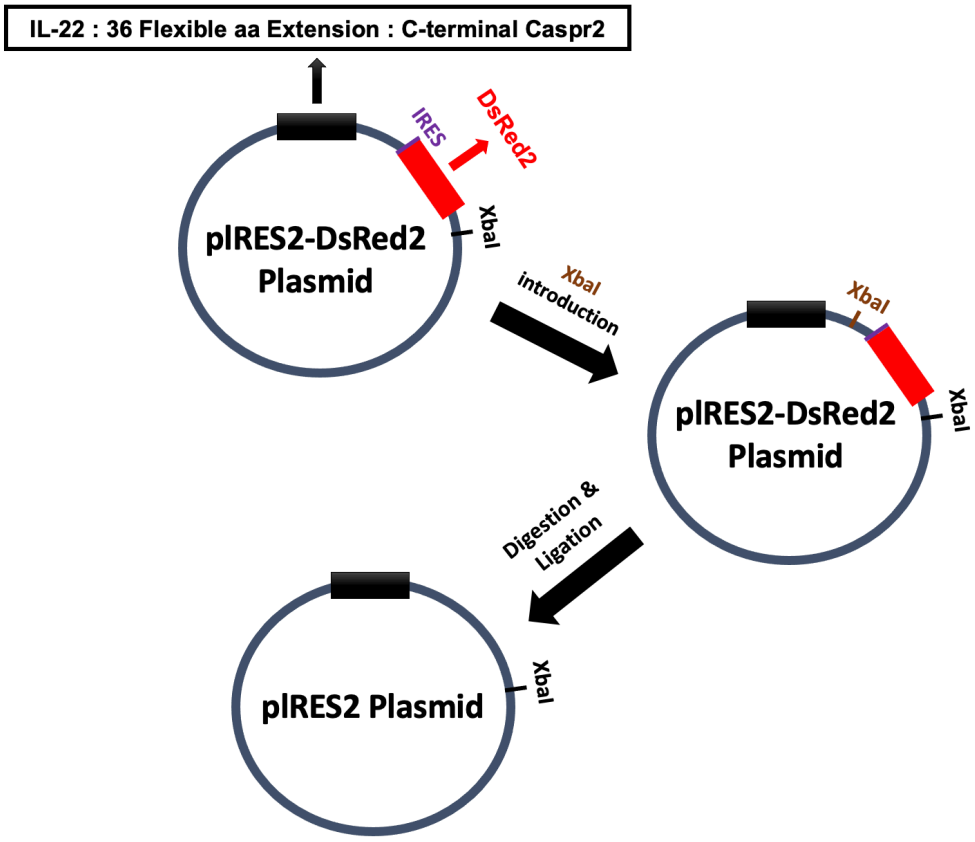


Figure 3.2: The steps to remove the cDNA of DsRed2. The cDNA of DsRed2 was removed by introducing a XbaI restriction site at its upstream before performing XbaI digestion and self-ligation.

3.4.3. The myc-tagged live CBA for detecting autoantibodies to soluble cytokines

In Chapter II, the details of cell seeding, transfection and DsRed2-reporting live CBA have been described (Figure 2.1). To note, the expression of IL-12 and IL-23 heterodimer was achieved by co-transfecting the same amount of their subunits, for instance IL-12A + IL-12B or IL-12B + IL-23A, in each well, so the total amount of transfected DNA and PEI was doubled compared to the single transfection method.

As we introduced the myc tag into the 36 flexible amino acids extension, below describes the method of myc-tagged live CBA. Figure 3.3 provides a schematic of using myc-tagged live CBA to detect cytokine autoantibodies. On day 3, the transfected HEK cells were incubated with plasma or serum samples diluted in DMEM/20 mM HEPES/1% BSA at RT for one hour. Cells were then washed twice with 20 mM HEPES in DMEM before being incubated with anti-human IgG Fc DyLight 488 secondary antibody (1:750 diluted in 20 mM HEPES and 1% BSA in DMEM) and anti-myc tag DyLight 550 monoclonal antibody (1:1000 diluted in 20 mM HEPES and 1%BSA in DMEM) at RT for 45 minutes. Cells were then washed twice with 20 mM HEPES in DMEM and then fixed with PBS/4% formaldehyde at RT for 10 minutes. Lastly, the cells were washed twice with PBS then mounted with DAPI-supplemented mounting media. Table 3.3 summarizes the myc-tagged live CBA methods applied to 24- and 96-well plate. The endpoint titre was defined as the reciprocal value of sample dilution given a CBA score of 1. In this chapter, the cut-offs were set above the highest endpoint titres of individual cytokine autoantibodies from 68 healthy sera after

excluding the outliers, whose endpoint titers was higher than “median + 6 x standard deviation” of the endpoint titres from the 68 healthy sera.

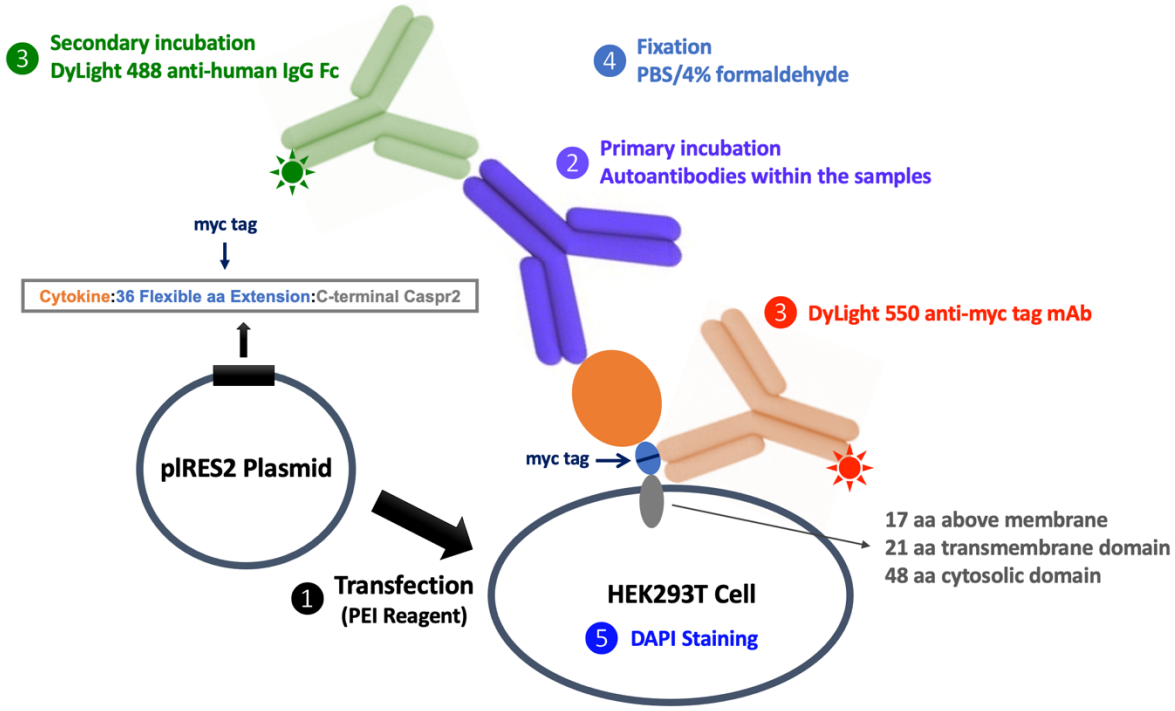


Figure 3.3: The myc-tagged live CBA to detect cytokine autoantibodies. On day 2, the HEK293T cells were transfected with myc-tagged cytokine surface-expressing plasmid to express our targeted cytokines above the membrane of HEK cells. On day 3, the cells were incubated with diluted bloods samples, washed, then incubated with 1:1000 diluted DyLight 550 anti-myc-tag monoclonal antibody and 1:750 diluted DyLight 488 anti-human IgG Fc antibody. Next, the cells were fixed by 4% formaldehyde. Lastly, the cells were mounted by DAPI-added mounting media.

Table 3.3: Methods of myc-tagged live CBA applied to 24- and 96-well plate

Experimental steps	24-well plate	96-well plate
1. Plasma or serum sample (desired dilution)	250 µl, at RT for an hour	60 µl, at RT for an hour
2. Washed twice with DMEM/20 mM HEPES	250 µl each	180 µl each
3. Secondary antibodies (1:750 dilution), anti-myc tag antibodies (1:1000 dilution)	250 µl, at RT for an hour	100 µl, at RT for an hour

4. Washed twice with DMEM/20 mM HEPES	250 µl each	180 µl each
5. Fixation	250 µl, at RT for 10 minutes	150 µl, at RT for 10 minutes
6. Washed twice with PBS	250 µl each	180 µl each
7. Mounting	One drop of mounting media (supplemented 1:1000 diluted DAPI)	
8. Storage	Stored at 4°C	

3.4.4. Luciferase immunoprecipitation system (LIPS) assay

The luciferase immunoprecipitation system is a published fluid-phase antibody detection method, and the works were done by Dr. Karner (Karner et al., 2016). IL-6, IL-12, IL-17A, IL-17F, IL-22, IL-23 and IFNα2 were cloned into modified pPK-CMV-F4 fusion vector (PK-MB-P013500, PromoCell). Through single or co-transfection manner, each targeted cytokine (subunit), N-terminally linked to a *Gaussia* luciferase (GLuc), was expressed by HEK cells. After 48 hours, the fusion proteins were obtained by collecting the DMEM culture media. The sera samples were incubated with fusion protein solution (2 x 10^6 luminescence units) overnight at 4°C. The next day, the samples were incubated with Protein G beads at room temperature for 1 hour in 96-well microfilter plates (MSRPN0410, Merck Millipore) to pull down the antibody-GLuc:cytokine complex. After washing out the unbound fusion proteins, coelenterazine (the substrate of Luciferase, GAR-2B, Targeting Systems) was added, and luminescence intensity (LU) of 480 nm emission signal was measured by VICTOR X Multilabel Plate Readers (PerkinElmer Life Sciences). Figure 3.4 provides a schematic of using LIPS assay to detect cytokine autoantibodies. The results are presented as relative LU, which was the sample LU divided by the average LU of healthy control samples (N=56). The cut-offs of each cytokine autoantibody were set to the mean plus

3 standard deviations of the relative LUs of healthy samples. In this chapter, we compared 25 plasma samples pre-screened by LIPS assay with antigen specific CBAs for IL-6, IL-12, IL-17A, IL-17F, IL-22, IL-23 and IFNα2.

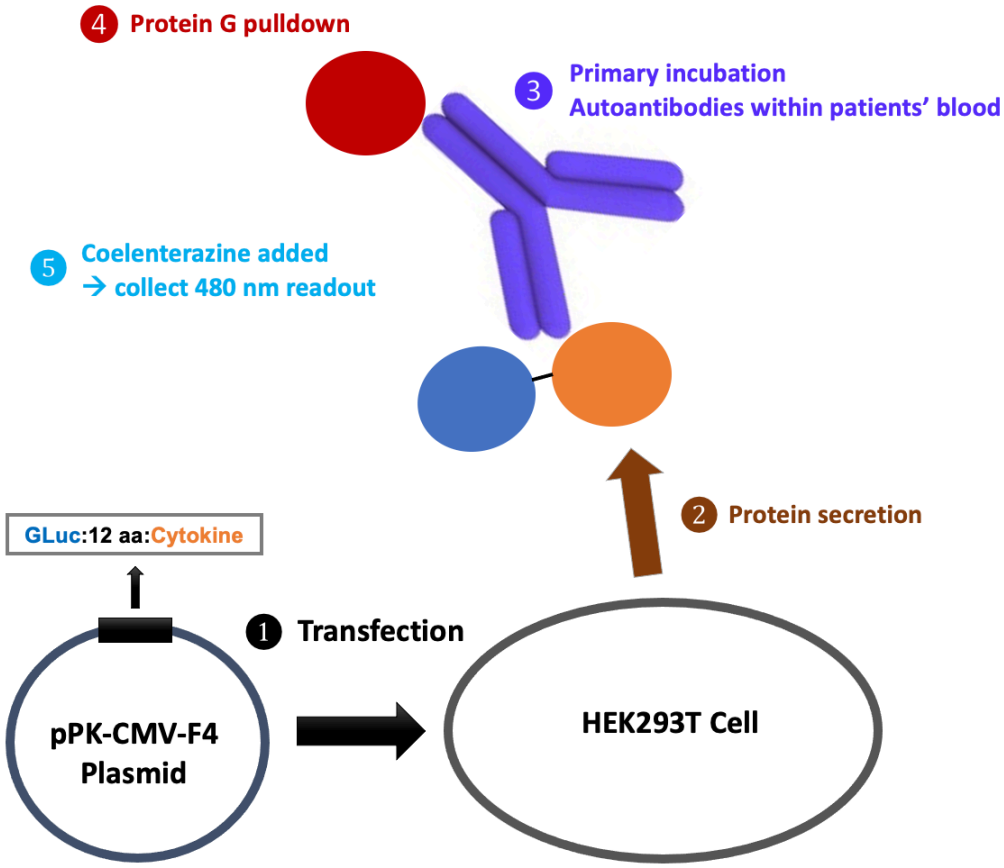


Figure 3.4: The luciferase immunoprecipitation system (LIPS) assay to detect cytokine autoantibodies. The HEK293T cells were transfected with pPK-CMV-F4 plasmid, which contained the cDNA of targeted cytokine N-terminally linked with Gaussia luciferase (GLuc). After 48 hours, the culture media with fusion proteins was collected. Then, the sera samples were incubated with the collected media overnight at 4°C. The next day, the samples were incubated with Protein G beads to pull down the antibody-GLuc:cytokine complex. Lastly, coelenterazine was added, and 480 nm emission wavelength was measured by plate reader.

3.5. Results

3.5.1. Development of live cell-based assays for detecting autoantibodies to soluble cytokines

In 2010, Irani et al. developed a live cell-based surface expression platform to detect autoantibodies to leucine-rich glioma inactivated 1 protein (LGI1), which is a soluble molecule associating specifically with Kv1.1 subunits in the CNS presynaptic terminals (Irani et al., 2010). The assay was successful by fusing LGI1 to the transmembrane domain of CASPR2, LGI1 autoantibodies were able to bind to targeted antigen expressed on the surface of HEK 293T cells.

Inspired by the method, we established a live cell-based assay (CBA) to detect autoantibodies to soluble cytokines. Initially, IL-22 had been anchored by the C-terminus of CASPR2 domain that included 17 extracellular amino acids, the transmembrane and the cytosolic domains (as described in Chapter II). On the same construct, the cDNA of DsRed2, regulated by IRES and situated downstream of the cDNA of IL-22, was used as an intracellular transfection reporter. The cDNAs of other cytokines including IL-12A, IL-12B and IFNα2 replaced IL-22 in individual vectors.

To demonstrate our platform, firstly we screened two plasma samples with autoantibodies to IFNα2 and IL-12, respectively, pre-validated by LIPS assays. Our IFNα2 and IL-12 CBAs specifically identified the corresponding autoantibodies in patients' samples and showed no antibody binding signal on the irrelevant targets (Figure 3.5). Next, we screened 7 plasma samples from TAMG patients that

demonstrated positivity by the LIPS assays. We found excellent concordance between our live CBAs and the LIPS assays (Figure 3.6).

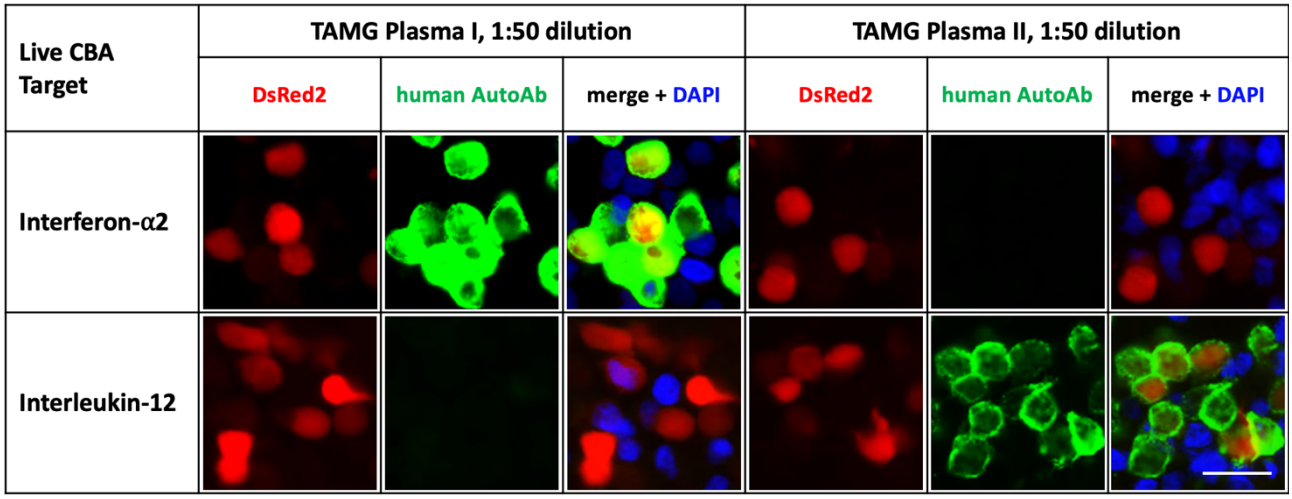


Figure 3.5: The live cell-based assays for detecting autoantibodies to IFNα2 or IL-12. TAMG Plasma I and Plasma II were reported having autoantibodies to IFNα2 and IL-12, respectively, via LIPS assays. The DsRed2 was in red, the secondary antibody bindings to IFNα2/IL-12 autoantibodies were in green, and the nuclei labelled by DAPI were in blue. Magnification x 400. Scale bar = 25 μm.

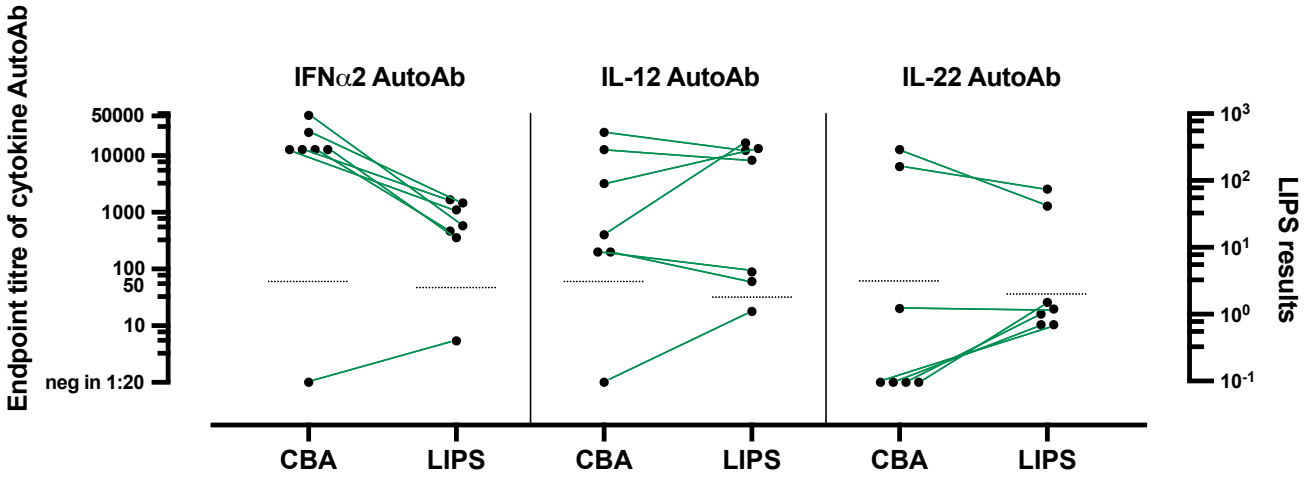
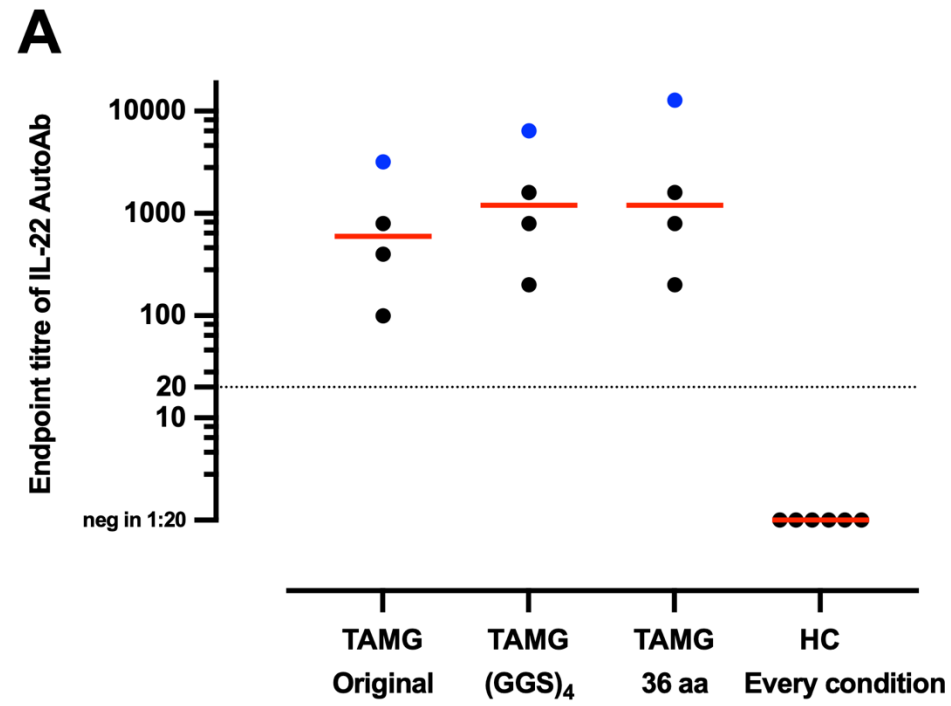


Figure 3.6: Live CBAs versus LIPS assays for detecting autoantibodies to IFNα2, IL-12 and IL-22. The CBA endpoint titres of individual cytokine autoantibodies are captured on the left y-axis, and the LIPS data are associated with the right y-axis. The green lines paired up the same samples screened by both assays. The cut-offs of each live CBA and LIPS assay were as dotted black lines.

Although our DsRed2-reporting live CBAs showed good fidelity with the published LIPS assays, we wondered if the assay sensitivity could be further improved by extending the amino acid linker between targeted antigens and the C-terminus of CASPR2 domain.

3.5.2. Attempt to improve CBA sensitivity by extending the flexible amino acid linker

We thought that the limited linker length (18 aa) of our original construct between the HEK cell membrane and the cytokine may limit antibody binding to the membrane proximal aspect of the target cytokines. To develop a more sensitive assay, we compared two flexible linker extensions, i.e., GGS_4 and 36 flexible amino acid extension, between IL-22 and C-terminal Caspr2. Four TAMG plasma pre-validated with IL-22 autoantibodies by LIPS assay and 6 healthy sera were screened on each modified CBA. There was a maximum of 4-time signal enhancement when the linker between IL-22 and truncated C-terminal CASPR2 domain was extended (36 amino acids longer), and all 6 negative healthy sera were tested negative at 1:20 dilution (1:20 CBA visual scores = 0; Figure 3.7a). As the TAMG plasma sample with the highest endpoint titre of IL-22 autoantibodies (the blue dots in Figure 3.7a) was screened at 1:3200 dilution, the improvement of antibody access was significant cross 3 live CBA platforms with different lengths of linker (Figure 3.7b). Hence, we selected the 36 flexible amino acids extended IL-22 surface expression construct for subsequent CBA developments.



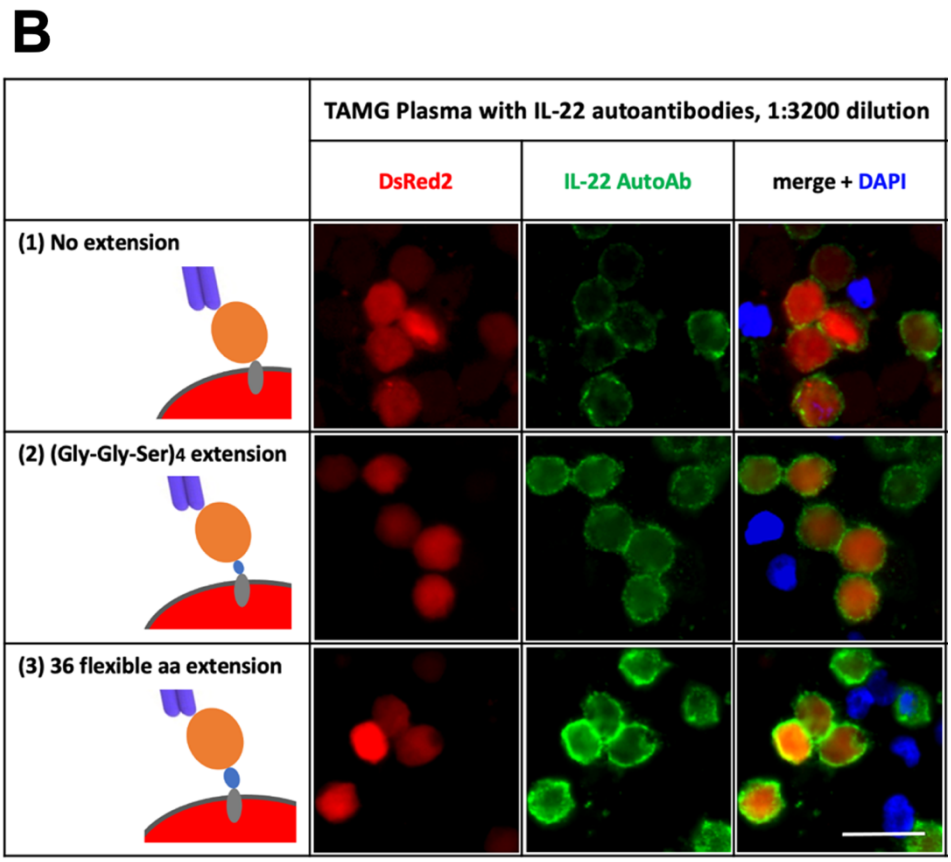


Figure 3.7: Improving IL-22 autoantibodies detection through linker extension. (a) The endpoint titres of IL-22 autoantibodies were plotted on the y-axis, and the types of samples and linker extensions were mentioned below the x-axis. The medians were as red lines, and the cut-off was as the dotted black line. (b) The images displayed the

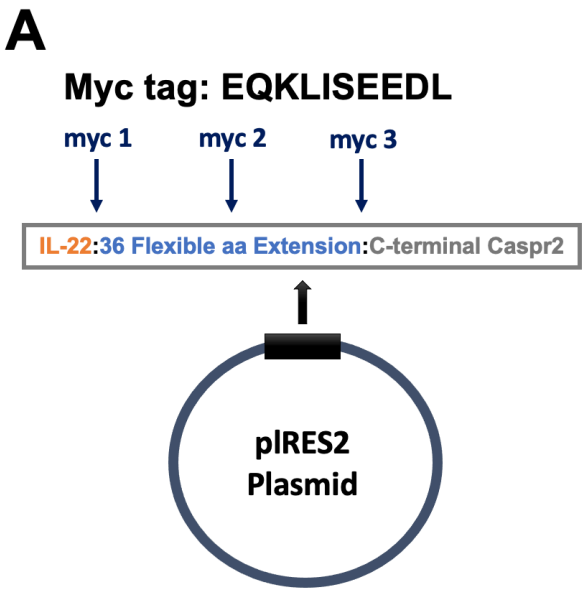
binding of IL-22 autoantibodies to IL-22 when using the (1) original, (2) $(Gly\text{-}Gly\text{-}Ser)_4$ extended or (3) 36 flexible amino acids extended IL-22 surface expression construct. The same sample, from a patient with TAMG, at 1:3200 dilution was used in all cases. The DsRed2 was in red, the secondary antibody binding was in green, and the nuclei labelled by DAPI were in blue. Magnification x 400. Scale bar = 25 μm.

As DsRed2 is expressed in the cytosol, it could not be used as a measure of cytokine surface expression. In addition, Mizuguchi et al. found the gene regulated by IRES only manifested 20-50% of the expression level compared to the same gene regulated by the 5' cap-dependent CMV promotor (Mizuguchi et al., 2000). Therefore, we decided to remove DsRed2 and introduce another reporter, which shared the same expression level with our targeted cytokines.

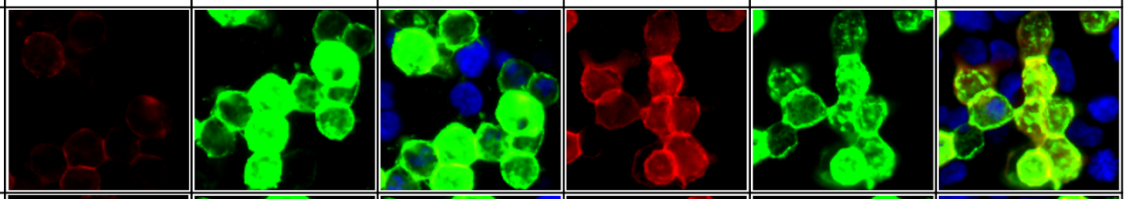
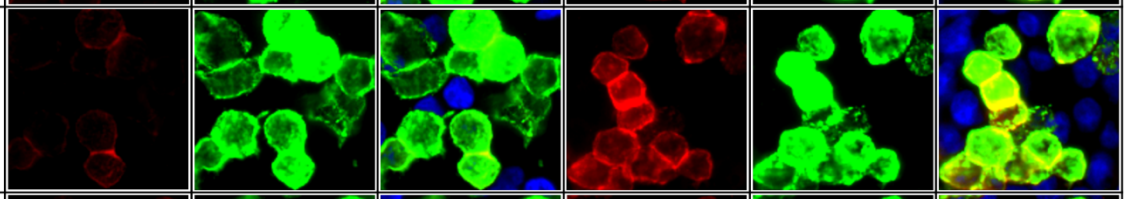
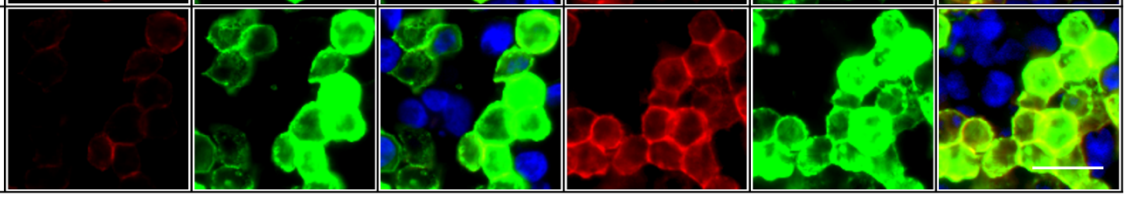
3.5.3. Introduction of a myc tag to quantify cytokine surface expression

Alternatively, a myc tag, which is a 10 amino acids long peptide (EQKLISEEDL), has many commercially available antibodies that bind it, often with a mature conjugated fluorophore. Hence, the cDNA encoding the DsRed2 was removed, and the cDNA of the myc tag was introduced individual at three distinct positions: just before the 36 flexible amino acid linker extension (myc 1 position), in the middle of the extension (myc 2 position) or after the extension (myc 3 position) on our IL-22 surface expression construct (Figure 3.8a). Then, we used DyLight 550 anti-myc tag monoclonal antibody to quantify the surface expression of IL-22. However, during assay optimization, we found that 4% formaldehyde fixation prevents the binding of anti-myc tag antibody to its epitope in all constructs (Figure 3.8b). This was possibly due to the presence of a lysine residue within the myc tag, where a side-chain amino group could be converted into imine by formaldehyde, before cross-linked with a second amino group, thereby compromising the native myc tag epitope (Tayri-Wilk et al., 2020). Therefore, we

decided to fix the cells in the end thus after the application of anti-myc tag antibody. Next, the DyLight 550 anti-myc tag antibody was titrated. The myc 1, myc 2 and myc 3 constructs, with the myc tag introduced at different locations in the 36 flexible amino acids extension, had the same endpoint titre of 8000 (Figure 3.8c). Besides, Figure 3.12 demonstrated the specificity of our DyLight 550 anti-myc tag antibody. As there were no difference in the endpoint titres of DyLight 550 anti-myc tag antibody no matter where the myc tag was introduced, the myc 2 introduced IL-22 surface expression construct was selected for subsequent CBA developments.



B

	4% formaldehyde fixation before anti-myc tag mAb			4% formaldehyde fixation after secondary antibody		
	IL-22:myc tag	IL-22 AutoAb	merge + DAPI	IL-22:myc tag	IL-22 AutoAb	merge + DAPI
IL-22:myc1						
IL-22:myc2						
IL-22:myc3						

Fix before anti-myc tag monoclonal antibody

Primary incubation → Fixation → Mouse DyLight 550 anti-myc tag mAb → Goat AF488 anti-human IgG (H+L) 2nd Ab → DAPI mounting

Fix after secondary antibody

Primary incubation → Mouse DyLight 550 anti-myc tag mAb → Goat AF488 anti-human IgG (H+L) 2nd Ab → Fixation → DAPI mounting

C

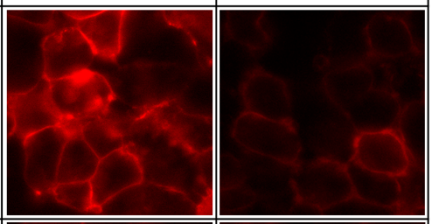
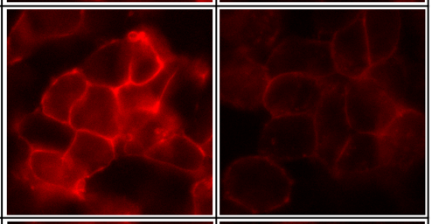
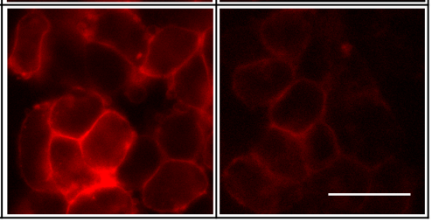
	1:1000 dilution	1:8000 dilution
IL-22:myc 1		
IL-22:myc 2		
IL-22:myc 3		

Figure 3.8: Introducing a myc tag into live IL-22 CBA. (a) The image demonstrates the introduction of myc tag just before, in the middle or after the 36 flexible amino acids linker extension. (b) The images demonstrated the effect of 4% formaldehyde fixation applied before staining the cells with 1:1000 diluted DyLight 550 anti-myc tag monoclonal antibody or applied after staining the cells with secondary antibody. The binding of anti-myc tag antibody was in red, the secondary antibody binding to IL-22 autoantibodies was in green, and the nuclei labelled by DAPI were in blue. The staining steps of each method were mentioned below. (c) The DyLight 550 anti-myc tag antibody was titrated, and the images displayed the access of 1:1000 and 1:8000 diluted anti-myc tag antibodies to myc tag at three distinct positions in our myc-tagged live IL-22 CBAs. The binding of anti-myc tag antibody was in red. Magnification x 400. Scale bar = 25 μm.

In addition to the fixation issue, we discovered that goat AF488 anti-human IgG (H+L) antibody bound to mouse DyLight 550 anti-myc tag monoclonal antibody when screen a healthy serum without IL-22 autoantibodies (Protocol I in Figure 3.9). Although the binding wasn't significant, it may generate issues when screen low positive samples. Therefore, we tried 4 staining protocols with different staining orders and anti-human IgG antibody (Figure 3.9). Finally, we chose Protocol IV as it was the most efficient and demonstrated no detectable cross reactivity.

Protocol I
Primary incubation → Mouse DL 550 anti-myc tag mAb → Goat AF488 anti-human IgG (H+L) 2nd Ab → Fixation → DAPI

Protocol II
Primary incubation → Goat AF488 anti-human IgG (H+L) 2nd Ab → Mouse DL 550 anti-myc tag mAb → Fixation → DAPI

Protocol III
Primary incubation → Mouse DL 550 anti-myc tag mAb → Goat DL 488 anti-human IgG Fc 2nd Ab → Fixation → DAPI

Protocol IV
Primary incubation → Mouse DL 550 anti-myc tag mAb + Goat DL 488 anti-human IgG Fc 2nd Ab → Fixation → DAPI

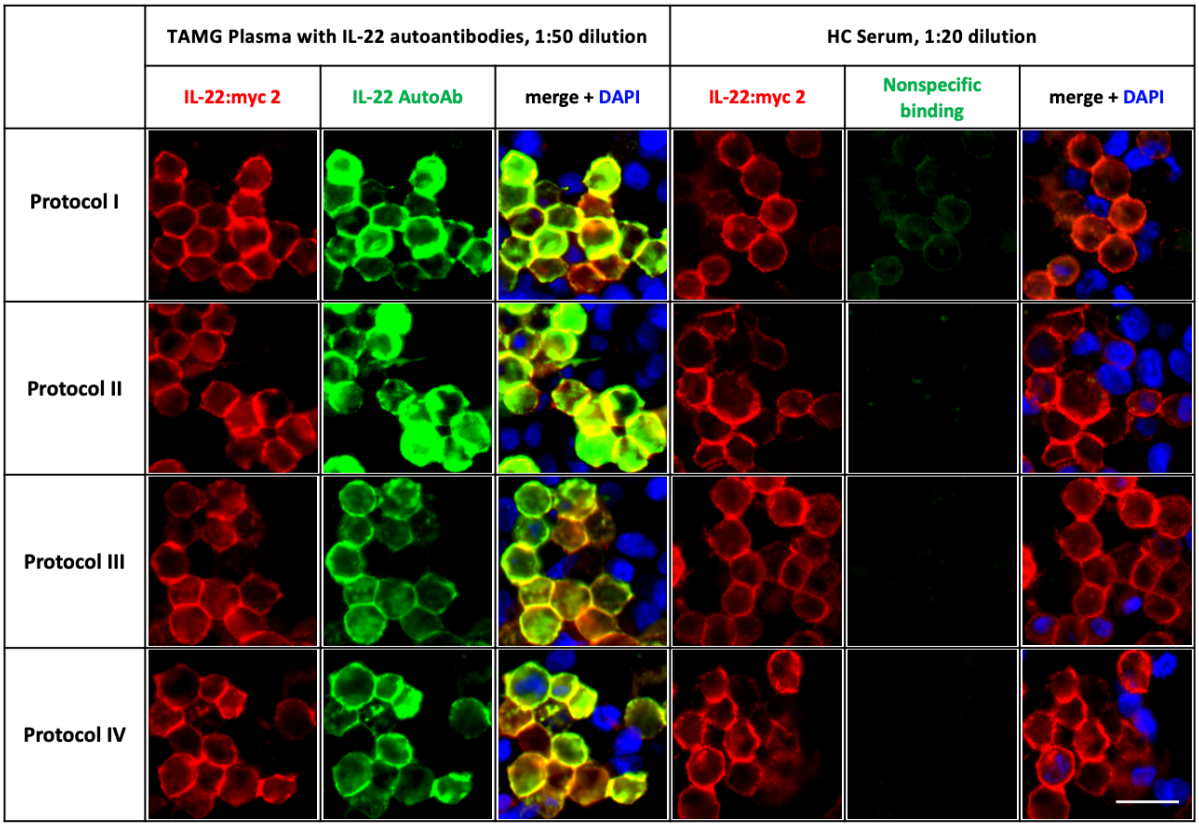


Figure 3.9: Optimizing the staining protocol to resolve non-specific binding. The details of each staining protocol are listed and color-coded above. IL-22 surface expression is shown in red, IL-22 autoantibodies in plasma from a patient with TAMG are shown in green, and DAPI is shown in bleu in the first three columns. Healthy control sera with apparent low-level IL-22 autoantibodies is shown in green in column 5 labelled 'nonspecific binding'. When the type or order of secondary antibodies is modified this binding disappears while the IL-22 specific autoantibodies remain. Off target binding is displayed in the column labelled 'nonspecific binding'. The Magnification x 400. Scale bar = 25 µm.

3.5.4. Quantification of cytokine surface expression by endpoint titrating DyLight 550 anti-myc tag antibody

After generating a staining protocol, we then subcloned IL-6, IL-12A, IL-12B, IL-17A, IL-17F, IL-23A, IFNα2, IFNα8 and IFNω1 to replace the cDNA of IL-22 in our myc tag live CBA construct. To quantify the relative expression levels of each targeted cytokine, we titrated the DyLight 550 anti-myc tag monoclonal antibody on individual cytokine 96-well plate live CBAs from 1:500 to 1:48000 and recorded their endpoint titres. The experiment was done thrice to confirm the endpoint titres. Because the myc tag is part of the construct, this is our readout of antigen surface expression. Of the single-transfected cytokine targets, IL-17F had the highest surface expression level, with IFNα2 and IFNα8 demonstrating the lowest surface expression levels (Figure 3.10a). The different signal sequences of each cytokine may lead to the variation of cytokine surface expression levels.

On the other hand, because in nature IL-12A and IL-23A express in a heterodimer fashion after respectively dimerizing with IL-12B, we co-transfected the cells with the cDNA containing IL-12 or IL-23 subunits to surface-express IL-12 or IL-23 heterodimers (Figure 3.10b). To investigate the expression levels of IL-12A and IL-23A without the interference of the myc tag in IL-12B construct, we mutated the myc tag in Il-12B construct from EQKLISEEDL to EGGGGGEEDL to avoid it being recognized by anti-myc tag DyLight 550 antibody (Figure 3.11). The endpoint titres suggested the surface expressions of IL-12A and IL-23A were doubled when co-transfecting the cells with IL-12B construct (first 4 columns in Figure 3.10b). To echo this, R. Jalah et al. found IL-12B could stabilize and increase the secretion of IL-12A in the form of IL-12 heterodimer (Jalah et al., 2013).

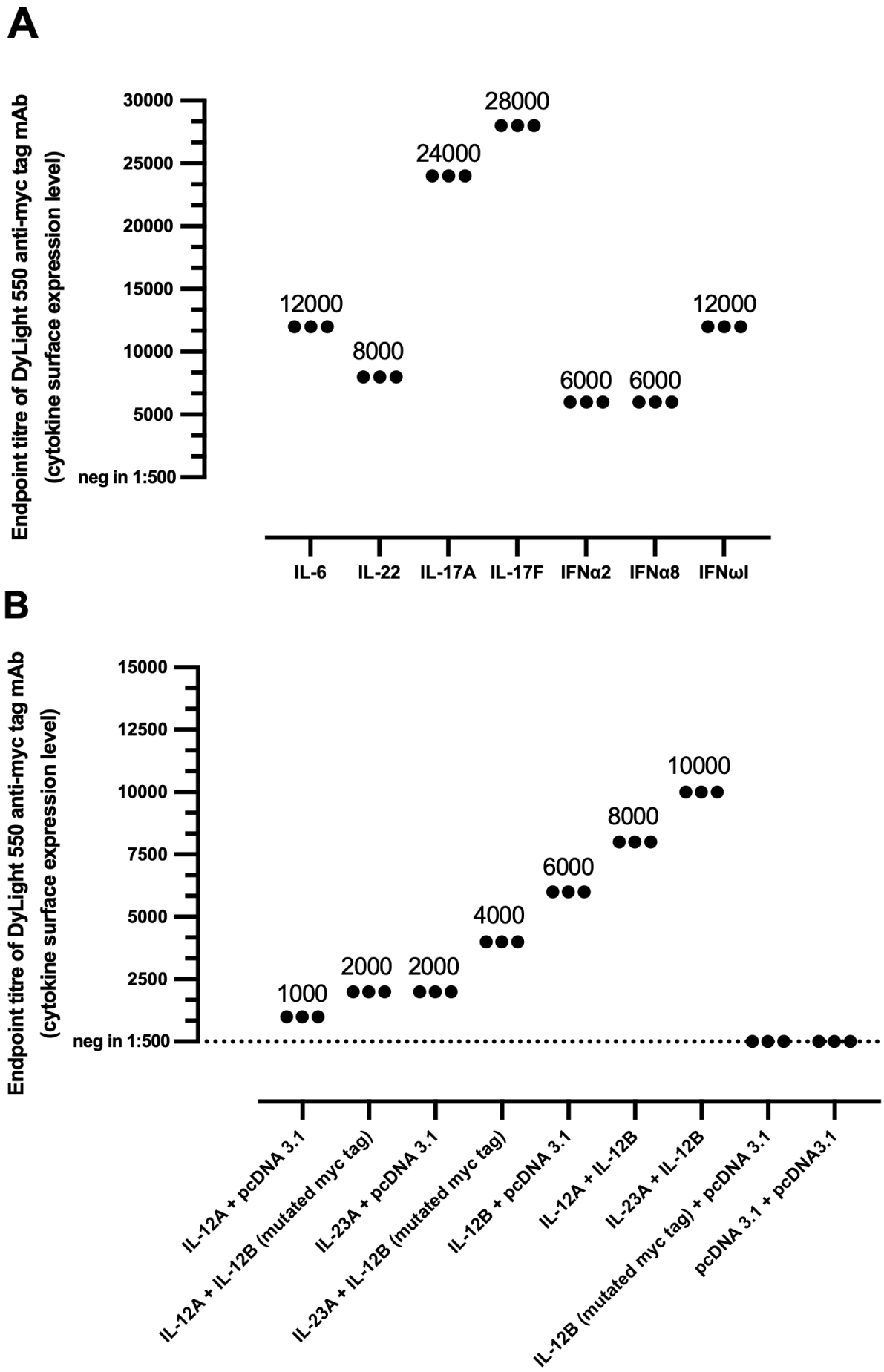

A
Endpoint titre of DyLight 550 anti-myc tag mAb
(cytokine surface expression level)
30000
25000
20000
15000
10000
5000
neg in 1:500
12000
8000
24000
28000
6000
6000
12000
IL-6
IL-22
IL-17A
IL-17F
IFNα2
IFNα8
IFNωI
B
Endpoint titre of DyLight 550 anti-myc tag mAb
(cytokine surface expression level)
15000
12500
10000
7500
5000
2500
neg in 1:500
1000
2000
2000
4000
6000
8000
10000
IL-12A + pcDNA 3.1
IL-12A + IL-12B (mutated myc tag)
IL-23A + pcDNA 3.1
IL-23A + IL-12B (mutated myc tag)
IL-12B + pcDNA 3.1
IL-12A + IL-12B
IL-23A + IL-12B
IL-12B (mutated myc tag) + pcDNA 3.1
pcDNA 3.1 + pcDNA3.1

Figure 3.10: Quantifying cytokine surface expressions by endpoint titrating DyLight 550 anti-myc tag antibody. (a-b) Under (a) single transfection and (b) co-transfection manners, the y-axis displayed the endpoint titers of anti-myc tag DyLight 550 antibody, and the transfected cDNAs were mentioned below the x-axis. The pcDNA3.1 was a blank plasmid used to equalize the amount of transfected DNA in each assay.

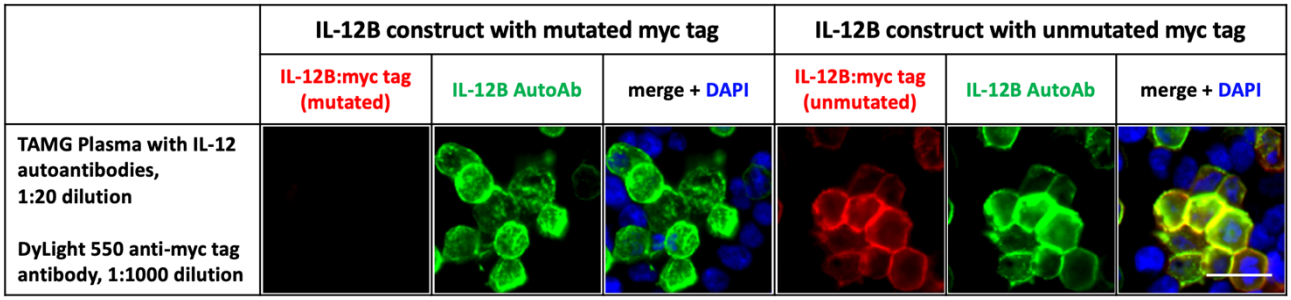


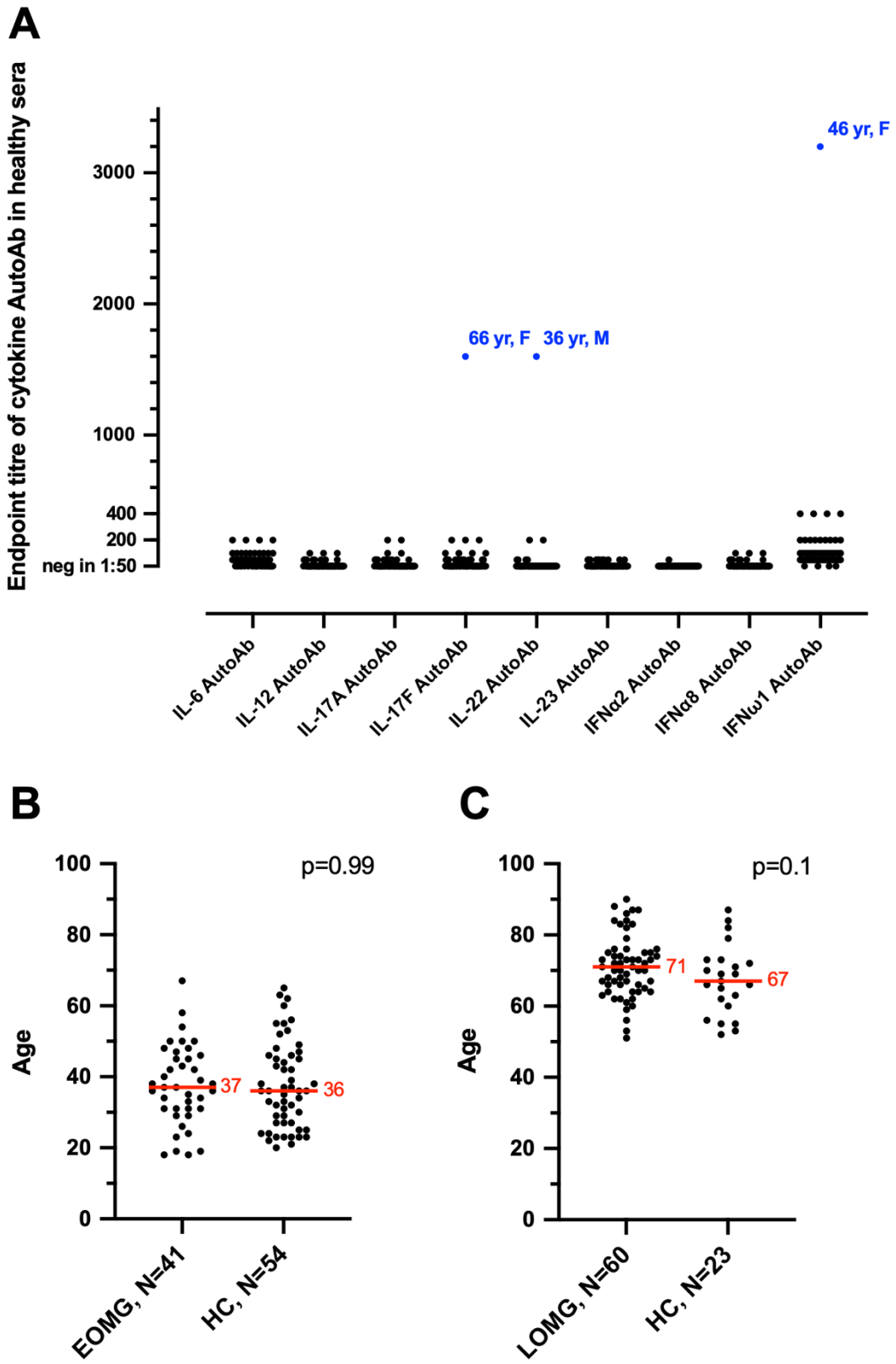
Figure 3.11: The mutated myc tag hindered the access of DyLight 550 anti-myc tag antibody. A TAMG plasma with IL-12B autoantibodies were screened in 1:20 dilution by live IL-12B CBAs with (left) or without (right) the mutated myc tag. The anti-myc tag antibody binding was in red, the secondary antibody binding to IL-12B autoantibodies was in green, and the nuclei labelled by DAPI were in blue. Magnification x 400. Scale bar = 25 μm.

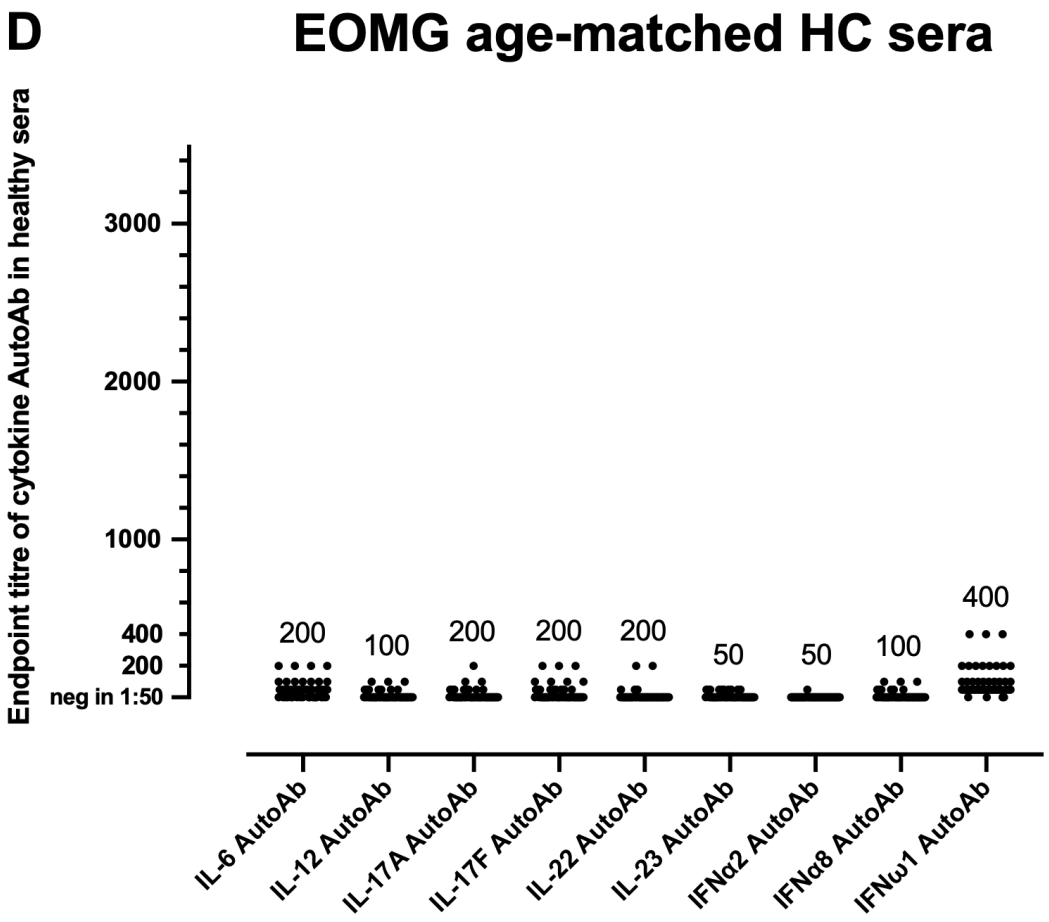
Summarizing in brief, we had established a myc-tag cytokine surface expression platform allowing us to detect autoantibodies to soluble cytokines. Followingly, we applied this technology to screen the plasma and sera samples taken from aMG patients and healthy volunteers for predicting the presence of thymoma.

3.5.5. Autoantibodies to soluble cytokines among healthy individuals were not discriminated by age

We screened plasma or serum samples from 46 TAMG patients, 60 LOMG patients, 41 EOMG patients and 68 healthy individuals by live CBAs to detect autoantibodies to IL-6, IL-12, IL-17A, IL-17F, IL-22, IL-23, IFNα2, IFNα8 and IFNω. Assay cut-offs were supposed to set above the highest endpoint titres of each cytokine autoantibodies

among 68 healthy individuals. However, we found 3 healthy sera with relatively high endpoint titres (between 1600 to 3200) of autoantibodies to IL-17F, IL-22 or IFNω1 respectively (Figure 3.12a). Their endpoint titres were higher than the median plus 6 standard deviations of the endpoint titres when detecting the autoantibodies to IL-17F, IL-22 or IFNω1 among 68 healthy sera, indicating those healthy sera had specific autoantibodies to these cytokines. Our data suggested cytokine autoantibodies exist in healthy individuals less frequently than in patients with autoimmune diseases. Furthermore, the healthy controls were age-matched with the EOMG and LOMG patients to understand if age could impact on the levels of cytokine autoantibodies in healthy sera (Figure 3.12b-c). Our results suggested there was no difference in the highest endpoint titres when measuring individual cytokine autoantibodies between the age-matched healthy cohorts after the removal of outliers (Figure 3.12d-e). Hence, we decided to use all the healthy control samples as a single cohort for setting cut-offs of detecting individual cytokine autoantibodies.


A
Endpoint titre of cytokine AutoAb in healthy sera
3000
2000
1000
400
200
neg in 1:50
46 yr, F
66 yr, F
36 yr, M
IL-6 AutoAb
IL-12 AutoAb
IL-17A AutoAb
IL-17F AutoAb
IL-22 AutoAb
IL-23 AutoAb
IFNα2 AutoAb
IFNα8 AutoAb
IFNω1 AutoAb
B
p=0.99
Age
100
80
60
40
20
0
37
36
EOMG, N=41
HC, N=54
C
p=0.1
Age
100
80
60
40
20
0
71
67
LOMG, N=60
HC, N=23


D
EOMG age-matched HC sera
Endpoint titre of cytokine AutoAb in healthy sera
3000
2000
1000
400
200
neg in 1:50
200
100
200
200
200
50
50
100
400
IL-6 AutoAb
IL-12 AutoAb
IL-17A AutoAb
IL-17F AutoAb
IL-22 AutoAb
IL-23 AutoAb
IFNα2 AutoAb
IFNα8 AutoAb
IFNω1 AutoAb

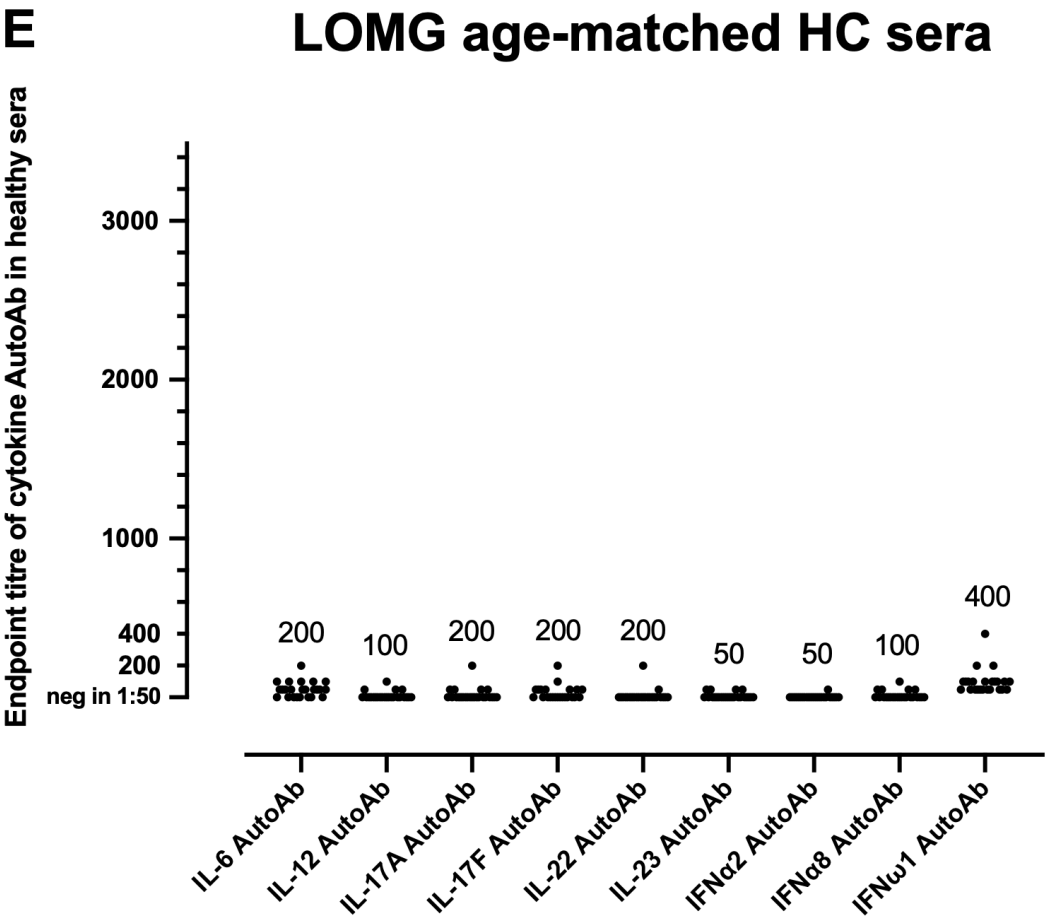

E
LOMG age-matched HC sera
Endpoint titre of cytokine AutoAb in healthy sera
3000
2000
1000
400
200
neg in 1:50
200
100
200
200
200
50
50
100
400
IL-6 AutoAb
IL-12 AutoAb
IL-17A AutoAb
IL-17F AutoAb
IL-22 AutoAb
IL-23 AutoAb
IFNα2 AutoAb
IFNα8 AutoAb
IFNω1 AutoAb

Figure 3.12: The results of our myc-tagged live CBAs to detect cytokine autoantibodies when screening healthy sera. (a) The y-axis displayed the endpoint titres of individual cytokine autoantibodies when screening the 68 healthy sera by myc-tagged live CBAs, and the detected cytokine autoantibodies were mentioned below the x-axis. The ages and sexes of the 3 healthy sera with high endpoint titres of autoantibodies to IL-17F, IL-22 and IFNω1, respectively, were highlighted in blue. (b-c) The healthy individuals were age-matched to (b) EOMG and (c) LOMG cohorts. The p-values were calculated by student T-test, and the medians were as red lines. (d-e) After excluding the outliers, the y-axis displayed the endpoint titres of individual cytokine autoantibodies when screening the (d) EOMG and (e) LOMG age-matched healthy sera by myc-tagged live CBAs, and the detected cytokine autoantibodies were mentioned below the x-axis. The highest endpoint titres of each assay were mentioned above each column.

3.5.6. Autoantibodies to IFNαs and IL-12 were better diagnostic biomarkers to predict the presence of thymoma

After the cut-offs were set, we applied them to determine the positivity of individual cytokine autoantibodies in the patients with AChR autoantibody associated MG. Among all 46 TAMG samples, 25 out of 46 samples were taken prior to thymectomy (pre-Tx), and 21 out of 46 samples were taken after thymectomy (post-Tx). Table 3.4 summarizes the number and percentages of aMG samples diagnosed with the corresponding cytokine autoantibodies in each cohort. From our results, we found our live CBAs for detecting autoantibodies to IFNα2, IFNα8, IFNω1 and IL-12 were more sensitive than others at determining the presence of thymoma. Due to structural similarity, the endpoint titres of autoantibodies to IFNα2, IFNα8 were highly matched correlated when screening TAMG cohort (Figure 3.13a). However, 5/46 TAMG samples seropositive for IFNα2 autoantibodies couldn't be picked up by our live IFNω1 CBA because of the relatively high cut-off (Figure 3.13b). Besides, when screening the same TAMG samples, the endpoint titres of autoantibodies to IFNα2 and IL-12 showed weaker correlation and concordance, suggesting their epitopes were distinct (Figure

3.13c). Here, we decided to apply our live IFNα2 and IL-12 CBAs for our future screens because autoantibodies to IFNα2 and IL-12 were better diagnostic marker to predict the presence of thymoma compared to the other cytokine autoantibodies.

Table 3.4: The number and percentages of CBA positive aMG samples in each cohort

	Autoantibodies to				
Sample cohort	**IL-6**	**IL-12**	**IL-17A**	**IL-17F**	**IL-22**
All TAMG, N=46	3 (6.5%)	27 (58.7%)	3 (6.5%)	1 (2.2%)	5 (10.9%)
Pre-Tx TAMG, N=25	3 (12.0%)	16 (64.0%)	3 (12.0%)	1 (4.0%)	5 (20.0%)
Post-Tx TAMG, N=21	0 (0%)	11 (52.4%)	0 (0%)	0 (0%)	0 (0%)
LOMG, N=60	3 (5.0%)	1 (1.7%)	0 (0%)	1 (1.7%)	1 (1.7%)
EOMG, N=41	3 (7.3%)	3 (7.3%)	0 (0%)	0 (0%)	0 (0%)
HC, N=68	0 (0%)	0 (0%)	0 (0%)	1 (1.47%)	1 (1.47%)

Table 3.4 (cont'd)

	Autoantibodies to			
Sample cohort	**IL-23**	**IFNα2**	**IFNα8**	**IFNω1**
All TAMG, N=46	14 (30.4%)	32 (69.6%)	32 (69.6%)	26 (56.5%)
Pre-Tx TAMG, N=25	9 (36.0%)	20 (80.0%)	20 (80.0%)	18 (72.0%)
Post-Tx TAMG, N=21	5 (23.8%)	12 (57.1%)	12 (57.1%)	8 (38.1%)
LOMG, N=60	1 (1.7%)	9 (15.0%)	10 (16.7%)	8 (13.3%)
EOMG, N=41	3 (7.3%)	1 (2.4%)	0 (0%)	1 (2.4%)
HC, N=68	0 (0%)	0 (0%)	0 (0%)	0 (0%)

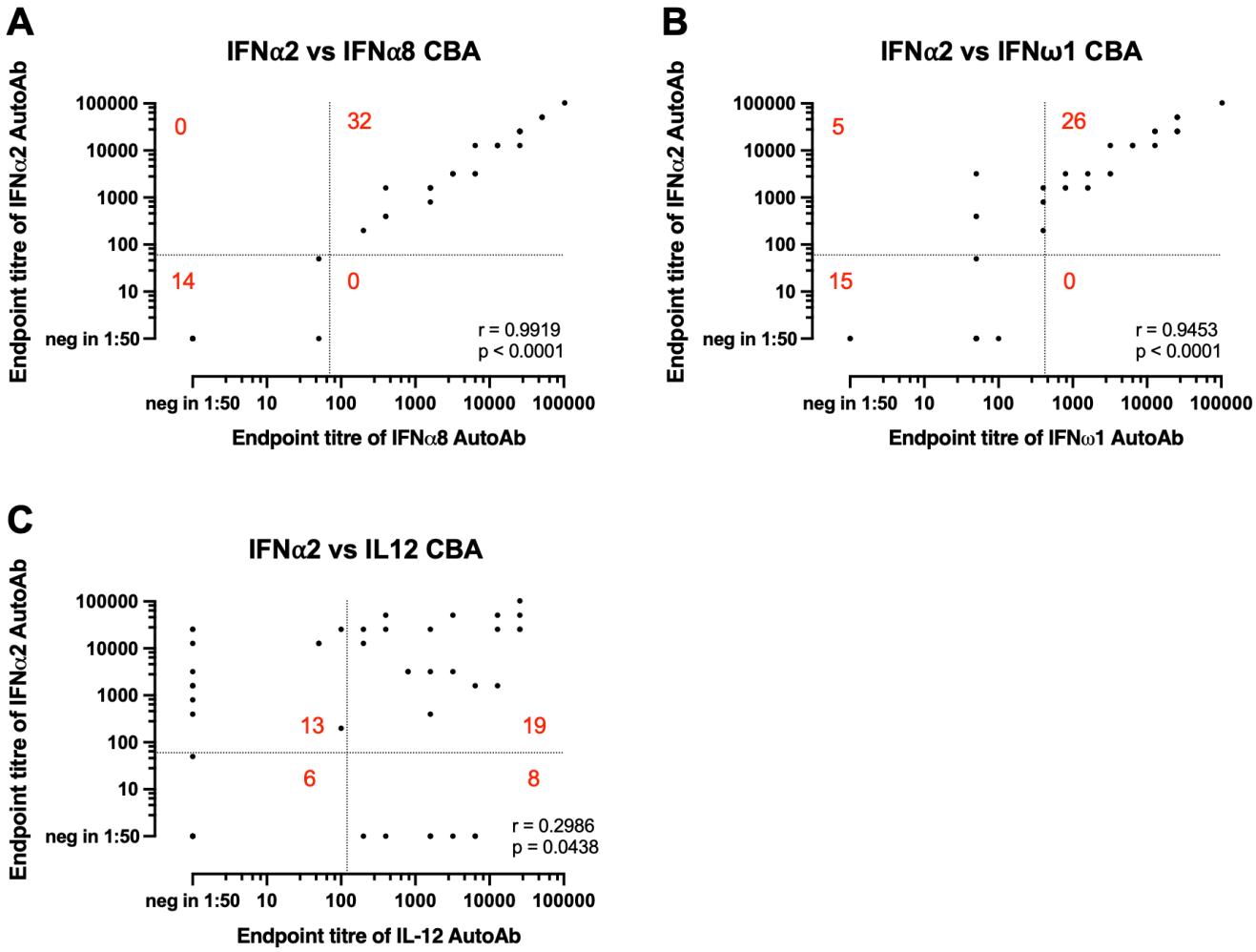


Figure 3.13: The correlations between the endpoint titres of autoantibodies to IFNα2, IFNα8, IFNω1 and IL-12. (a-c) The y-axis displayed the endpoint titres of IFNα2 autoantibodies from the 46 TAMG samples, and the x-axis displayed the endpoint titres of autoantibodies to (a) IFNα8, (b) IFNω1 and (c) IL-12 from the same samples. The number of samples in each quadrant were mentioned in red. The r and p-values were calculated via Spearman nonparametric correlation test. The cut-offs of each assay were as dotted black lines.

In addition, we found our live IFNα2 and IL-12 CBAs were more sensitive to predict the presence of thymoma from patients in the pre-Tx TAMG cohort rather than the whole TAMG cohort (Figure 3.14). Because when including the post-Tx patients in the TAMG cohort we screened, the sensitivities of both assays were underestimated, the pre-Tx TAMG cohort shall be the most representative TAMG cohort to demonstrate the utility of our live CBAs.

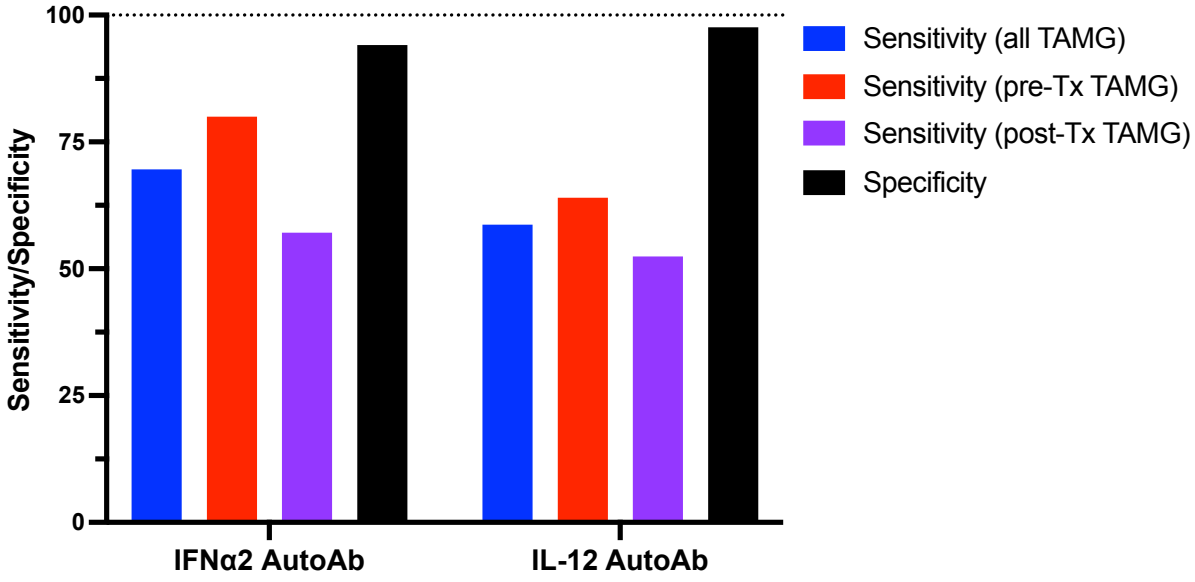


Figure 3.14: The sensitivity and specificity of our myc-tagged live CBAs for detecting autoantibodies to IFNα2 and IL-12. The chart displays the sensitivities and specificities of individual live CBAs to predict the presence of thymoma. The sensitivities of whole TAMG cohort were plotted as blue columns, the sensitivities of pre-Tx TAMG cohort were plotted as red columns, the sensitivity of post Tx TAMG cohort were plotted as purple columns. The specificities were plotted as black columns.

When plotting out the endpoint titres from live IFNα2 and IL-12 CBAs, the distribution of endpoint titres suggested pre-Tx TAMG cohort was optimal still to predict the presence of thymoma among all the aMG patients and healthy individuals (Figure 3.15). However, our live IFNα2 CBA was relatively lack of specificity compared to our live IL-12 CBA because there were 9/60 (15%) LOMG samples from patients without radiologically evident thymomas found seropositive for IFNα2 autoantibodies via our live CBA (Figure 3.15a). To resolve this issue, we analyzed the samples with autoantibodies to both IFNα2 and IL-12 (Table 3.5). Although the new analysis decreased the sensitivity to 56%, but it demonstrated higher positive predictive value (PPV) to predict the presence of thymoma, which was 93.3%.

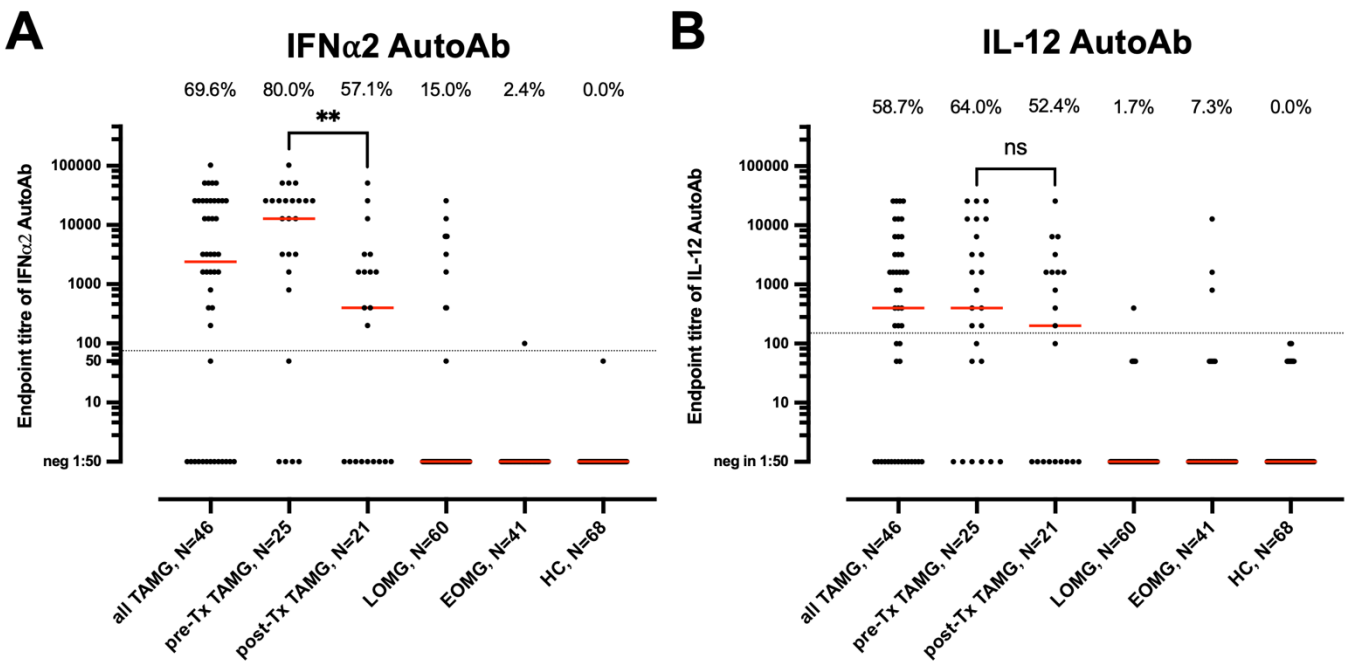


Figure 3.15: The endpoint titre distributions of autoantibodies to IFNα2 and IL-12 in each cohort. (a-b) The y-axis displayed the endpoint titres of autoantibodies to (a) IFNα2 and (b) IL-12, and the details of each cohort were mentioned below the x-axis. The statistical difference was evaluated by nonparametric Mann-Whitney test. The percentages of positive samples were quoted above each column. The medians were as red lines, and the cut-offs were dotted black lines.

Table 3.5: Summary of autoantibodies to IFNα2 and/or IL-12 in each cohort

	Autoantibodies to		
Sample cohort	**IFNα2**	**IL-12**	**IFNα2 & IL-12**
TAMG pre-Tx, N=25	20	16	14
LOMG, N=60	9	1	1
EOMG, N=41	1	3	0
HC, N=68	0	0	0
Sensitivity	80.0%	64.0%	56.0%
Specificity	94.1%	97.6%	100%
PPV	66.7%	80.0%	93.3%
NPV	96.4%	94.0%	92.9%

To understand if autoantibodies to IFNα2 and IL-12 disappear soon after patients' thymectomy, we screened the samples from 21 post-Tx TAMG patients. Surprisingly, around half of the post-Tx TAMG samples were with their endpoint titres of autoantibodies to IFNα2 and IL-12 above the cut-offs even years after patients' thymectomy, and none of the post-Tx patients were found recurrent thymoma (Figure 3.16). Although the percentage of positive samples having cytokine autoantibodies was lower in post-Tx TAMG cohort (Table 3.4), the presence of autoantibodies to IFNα2 and IL-12 after patients' thymectomy could inevitably complicate the prediction of recurrent thymoma among thymectomized aMG patients.

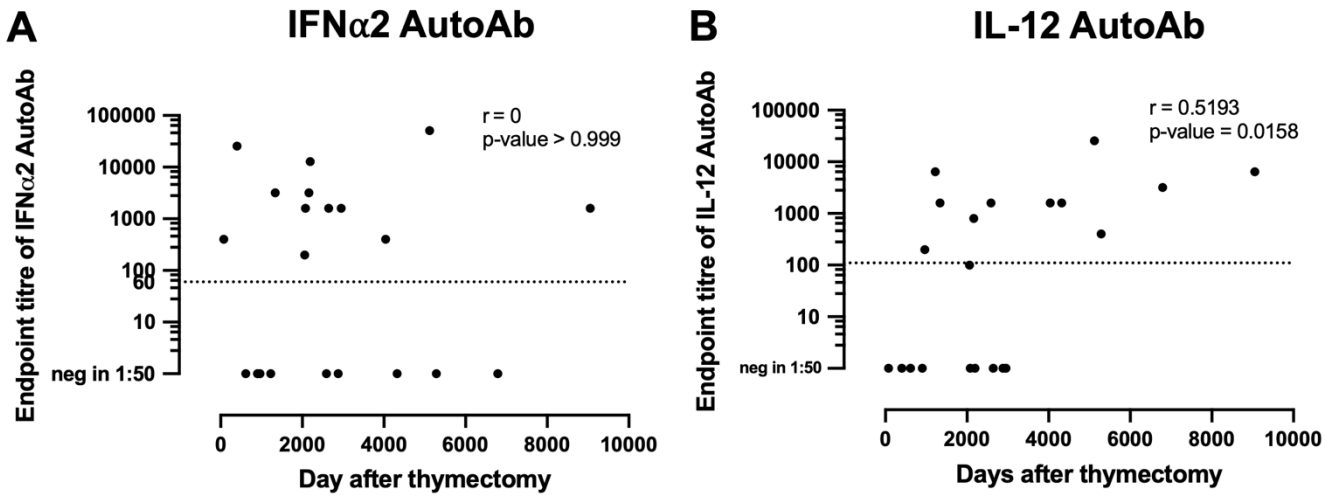


Figure 3.16: Regarding individual TAMG patients, their endpoint titres of autoantibodies to IFNα2 and IL-12 were above the cut-offs years after their thymectomy. (a-b) The y-axis displayed the endpoint titres of autoantibodies to (a) IFNα2 and (b) IL-12 when screening 21 post-Tx TAMG samples via the corresponding live CBAs, and the x-axis displayed the days after patient's thymectomy of each sample. The r and p-values were calculated via Spearman nonparametric correlation test. The cut-offs were as dotted black lines.

To further validate the utility of our live CBAs, we compared our live CBA results with the published LIPS data (Karner et al., 2016) to see if both assays agreed well with one another.

3.5.7. Live CBA and LIPS assays showed good correlation

We screened the same 25 plasma samples from thymoma patients (23 of them with MG) to detect autoantibodies to IFNα2, IL-6, IL-12, IL-17A, IL-17F, IL-22 and IL-23. Figure 3.17 displayed the percentage samples picked up by live CBAs and LIPS assays. Both assays were comparably capable to detect individual cytokine autoantibodies (Figure 3.18a, the detection of autoantibodies to monomeric IFNα2 for example), except some discrepancies results while detecting IL-12 autoantibodies (Figure 3.18b). There were 6 discrepant samples picked up by LIPS assay but not by our live CBA when detecting autoantibodies to heterodimeric IL-12.

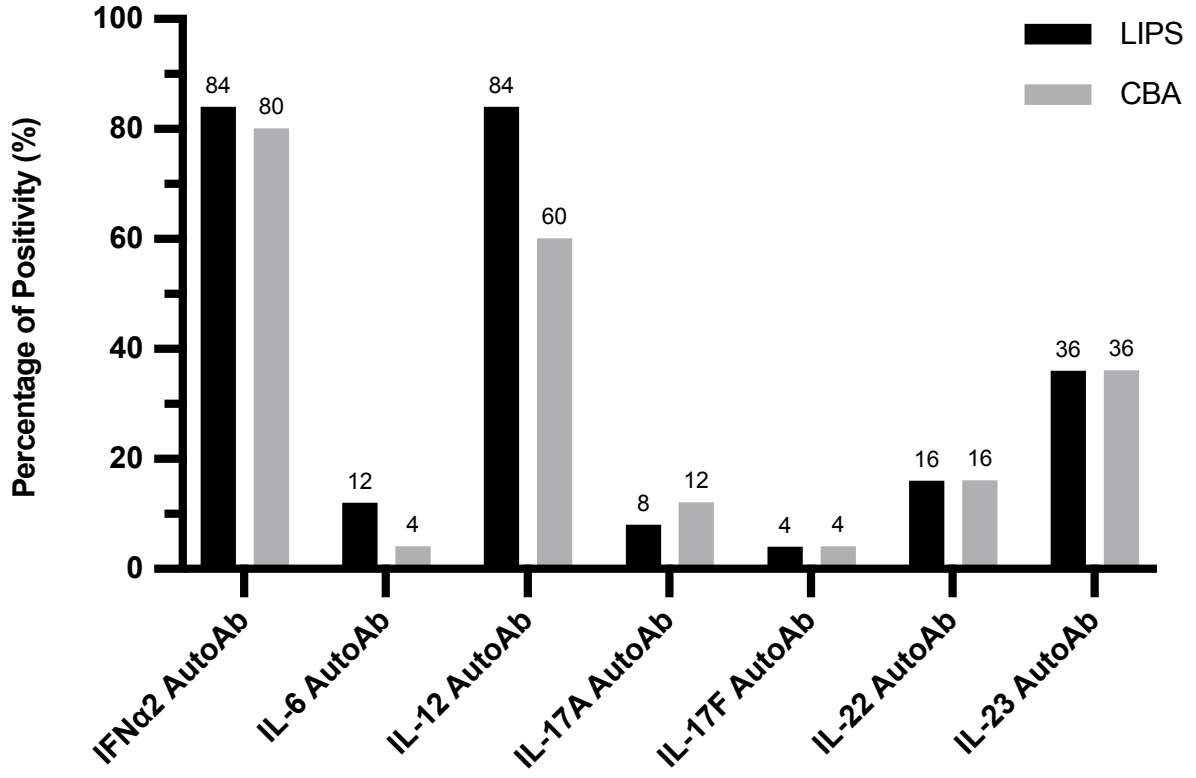


Figure 3.17: The percentage of samples picked up by live CBAs and LIPS assays. The percentage of samples picked up by individual live CBAs were plotted as grey columns, and the percentage of samples picked up by individual LIPS assays were plotted as black columns. The percentage of each assay was quoted above the columns.

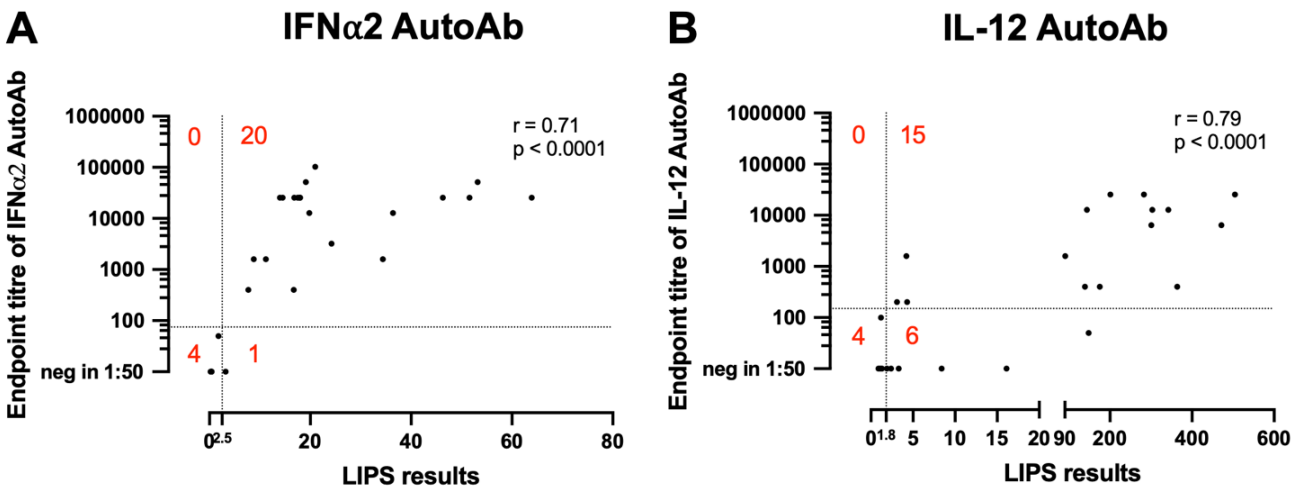
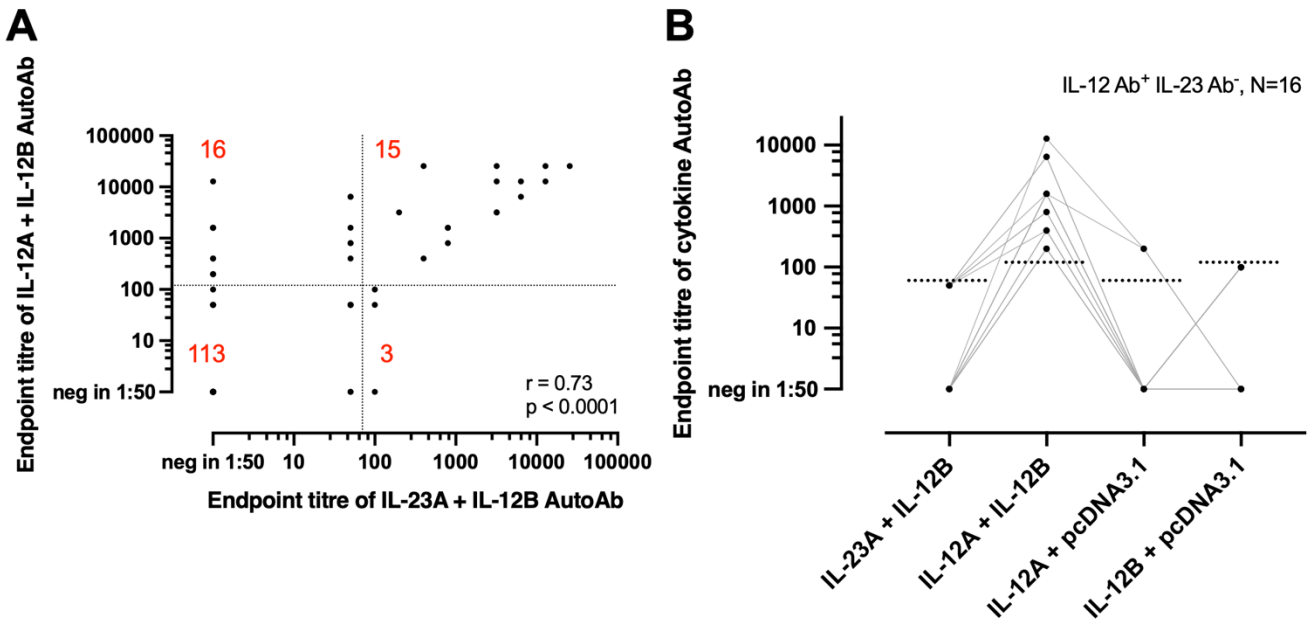


Figure 3.18: The correlations between live CBAs and LIPS assays for detecting autoantibodies to IFNα2 and IL-12. (a-b) The y-axis displayed the endpoint titres of autoantibodies to (a) IFNα2 and (b) IL-12, and the x-axis displayed the LIPS results. The number of samples in each quadrant were mentioned in red. The r and p-values were calculated via Spearman nonparametric correlation test. The cut-offs were as dotted black lines.

To defend our results, we would like to prove that our CBA could detect autoantibodies to both IL-12 heterodimer (IL-12A + IL-12B) and IL-12B homodimer. As Figure 3.19a, the endpoint titres of autoantibodies to IL-12 and IL-23 from 147 MG samples were plotted. According to the plot, 16 samples were picked up by live IL-12 CBA but not by live IL-23 CBA, suggesting those samples were without detectable autoantibodies to IL-12B homodimer; otherwise, those samples would appear at the first quadrant in Figure 3.20a. For those 16 samples, the conformational epitopes between IL-12A and IL-12B, and the IL-12A alone were the two possible targets for autoantibodies to bind. Therefore, those 16 samples were further tested to detect autoantibodies to IL-12A + IL-12B, IL-12B + IL-23A, IL-12A and IL-23A. All 16 samples were with autoantibodies

to IL-12A + IL-12B, 2/16 with autoantibodies to IL-12A alone, and none with autoantibodies to IL-12B alone or IL-12B + IL-23A (Figure 3.19b). The relatively low expression level of IL-12A compared to other cytokine targets (Figure 3.10) could explain why only 2/16 samples were picked up at the low endpoint titres of 200. Besides, we used commercial IL-23A polyclonal antibody to demonstrate the success of IL-23A expression on the surface of HEK cells (Figure 3.19c) because Figure 3.19a itself couldn't prove there was IL-23A specific autoantibodies among the 147 MG samples.



C

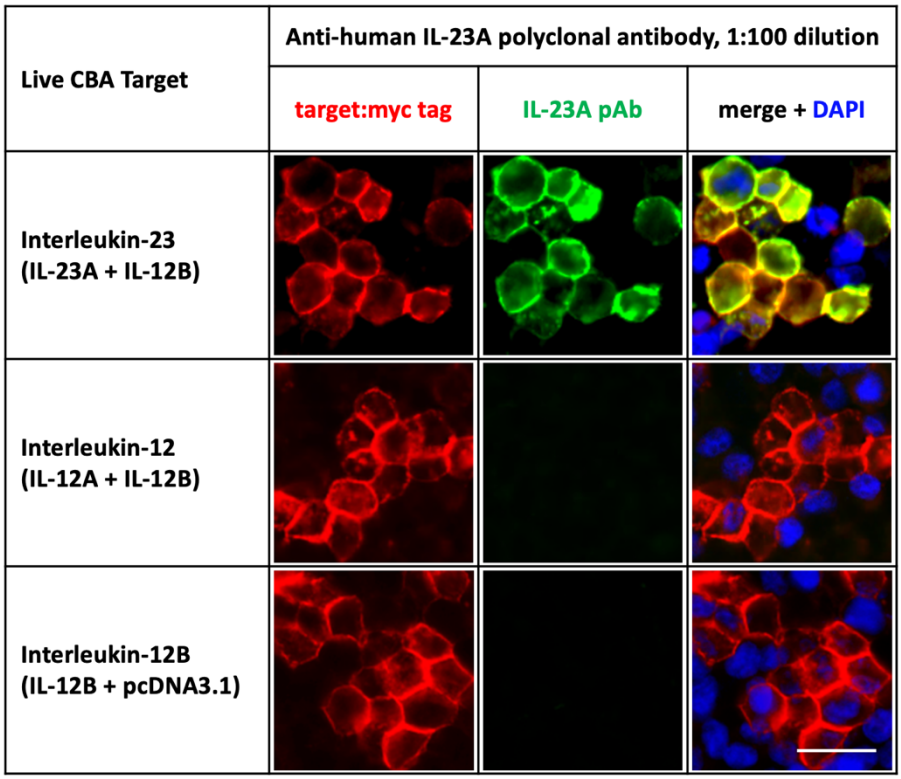


Figure 3.19: Our live IL-12 CBA recognized autoantibodies to either IL-12 heterodimer or IL-12B homodimer. (a) The y-axis displayed the endpoint titres of autoantibodies to IL-12 (IL-12A + IL-12B), and the x-axis displayed the endpoint titres of autoantibodies to IL-23 (IL-23A + IL-12B) when screen 147 MG samples. The number of samples in each quadrant are mentioned in red. The r and p-values were calculated via the Spearman nonparametric correlation test. The cut-offs are displayed as dotted black lines. (b) The 16 samples with autoantibodies to IL-12 but not to IL-23 were screened. The y-axis displayed the endpoint titres of autoantibodies to the targets mentioned below the x-axis. The gray lines linked the same samples, and the cut-offs of each CBA are displayed as dotted black line. (c) The images displayed the results of a commercial anti-IL-23A antibody screened at 1:100 dilution on IL-23, IL-12 and IL-12B CBA. The anti-myc tag antibody binding was in red, the anti-IL-23A antibody binding was in green, and the nuclei labelled by DAPI were in blue. Magnification x 400. Scale bar = 25 μm.

To summarize, the results in this chapter had demonstrated the robustness of our myc-tagged live CBAs to detect autoantibodies to soluble cytokines, especially our live IL-12 CBA, which was proved to detect autoantibodies to either IL-12 heterodimer or IL-12B homodimer.

3.6. Discussion

Beginning from a DsRed2-reporting cytokine surface expression platform, we have successfully establised a panel of myc-tagged, 36 flexible amino acids extended, surface-expressing live HEK293T CBAs to detect autoantibodies to IL-6, IL-12, IL-17A, IL-17F, IL-22, IL-23, IFNα2, IFNα8 and IFNω1 in the plasma or sera from MG patients with or without thymoma. Under myc-tagged cytokine expression system, we found 4% formadehyde fixation hindered the access of anti-myc tag antibody to myc tag, and the AF488 anti-human IgG (H+L) antibody non-specifically recognized DyLight 550 anti-myc tag antibody. To solve those issues, we optimized our myc-tagged live CBA by moving the fixation step to the end and using DyLight 488 anti-human IgG Fc antibody for secondary incubation. In addition, we identified the surface expression of each cytokine target varied perhaps due to the nature of their endogneous signal peptides.

Followingly, we screened 46 TAMG, 60 LOMG, 41 EOMG and 68 healthy control samples via our optimised myc-tagged live CBAs to detect individual cytokine autoantibodies. We found 3/68 healthy control samples with autoantibodies to IL-17F, IFNω1 or IL-22, respectively. Their antibody titres are above median plus 6 standard deviations of the endpoint titres from 68 healthy control samples, so we considered them having the correspoinding cytokine autoantibodies. Among all the TAMG patients (N=46), we found around 70% of them with IFNα2 autoantibodies, and around 60% of them with IL-12 autoantibodies. In addition, we found the endpoint titres between autoantibodies to IFNα2 and IFNα8 highly matched with one another, and both assays demenostrated lower background compared to our live IFNω1 CBA. By contrast, the endpoint titres of IFNα2 autoantibodies correalted weakly with IL-12 autoantibodies,

implying they were distinct biomarkers to predict the presence of thymoma. Therefore, we selected our live IFNα2 and IL-12 CBAs for further investigations.

Next, we found if only analyzing the pre-Tx TAMG cohort (N=25), the sensitivity of our live IFNα2 CBA increased from 60% to 80%, suggesting more samples in the pre-Tx TAMG cohort having autoantibodies to IFNα2. Although past studies didn't clearly state if the TAMG samples had been collected before patients' thymectomy (Buckley et al., 2001, Meager et al., 2003), in our study, we identified the pre-Tx TAMG samples were more representative to predict the presence of thymoma. Despite the increase of sensitivity, our live IFNα2 CBA was lack of specificity, with PPV = 66.7, because it picked up 9/60 (15%) LOMG samples with IFNα2 autoantibodies but without radilogically evident thymoma. On the other hand, our live IL-12 CBA was more specific, with PPV = 80%, to predict the presence of thymoma, and only 1/60 (1.7%) LOMG patient without radiologcially evident thymoma was found seropositive for IL-12 autoantibodies via our live CBA. Therefore, when analyzing the samples with autoantibodies to both IFNα2 and IL-12, we improved the PPV to 93.3%. However, the new analysis reduced the sensitivity to 56%.

Despite autoantibodies to IFNα and IL-12 being a good diagnostic marker to predict the presence of thymoma, their endpoint titres from most of the post-Tx patients were above the cut-offs years after patients' thymectomy and despite the immunosuppressive therapy often applied (Meager et al., 2003). We also identified this issue as shown in Figure 3.16. There were three possible reasons to explain this observation. Firstly, the pool of long-lived plasma cells, which were hard to be depleted by immunotherapy such as rituximab (Huang et al., 2010), had established before

patients' thymectomy, so the autoantibodies to IFNα and IL-12 could be continually produced for years. Secondly, the infection-triggered release of IFNα and IL-12 could activate the pre-existing memory B cells allowing them to produce the corresponding autoantibodies. Thirdly, the metastatic thymoma or newly formed malignant thymic tissue, which again triggered the autoimmune responses to IFNα and IL-12, were relatively hard to be identified by chest CT scan compared to a mature thymoma. Whichever reason fits, the remaining autoantibodies to IFNα and IL-12 could disturb the prediction of recurrent thymoma, so more regular CT scans, infection tests, e.g., C-reactive protein test or measuring the level of IFNα and IL-12 by ELISA, shall be implemented before drawing any clinical conclusion. Nevertheless, our myc-tagged live CBA panel was more useful to support clinicians finding the as yet undiagnosed thymoma rather than the recurrent thymoma. However, the longitudinal screening for autoantibodies to IFNα and IL-12 after patients' thymectomy is still recommended because Meager et al. suggested at the time of recurrence the titres of autoantibodies to IFNα and L-12 could dramatically raise about 5-16 times (Meager et al., 2003). Also, thymoma is associated with a range of autoimmune diseases such as Morvan's syndrome and Grave's disease, so the utility of our myc-tagged live CBA panel can be extended to other thymoma-associated diseases.

Last but not least, our live CBAs showed good correlation with the published LIPS assays for detecting cytokine autoantibodies. However, there were 6 out of 25 discreptant samples, tested positive by LIPS but negative by live CBA when detecting IL-12 autoantibodies. There are many possibilities to explain the discrpenant results we found. First, because the LIPS assays were performed 5 years ago, it is possible that the samples we screened via live CBAs had degraded in storage, thereby

generating the negative results observed in our live CBAs. Secondly, the difference in construct design between the two methods could generate discrepancies when expressing IL-12, a heterodimeric cytokine composed of IL-12A and IL-12B. In LIPS, the IL-12 subunits were cloned at the downstream of GLuc (185 amino acids, 19.9 kDa), but in our live CBAs the IL-12 subunits were cloned at the upstream of truncated C-terminal CASPR2 domain. Both assays require co-transfecting two DNA plamsmid individually containing IL-12A and IL-12B subunits, so it is likely that the difference in construct design could impact on the exposure of essential epitopes. However, we proved our live IL-12 CBA was able to detect autoantibodies to either IL-12 heterodimer or IL-12B homodimer (Figure 3.19). Thirdly, when detecting IL-12 autoantibodies, 3/6 LIPS positive but CBA negative samples were broader-line positive, i.e., just above the cut-off of IL-12 LIPS assay (Figure 3.18b). Because we didn't have the DNA contructs and relevent materials in our lab to repeat the LIPS experiments, otherwise it would be worth running live CBAs and LIPS assays simultaneously for fair comparsion. Besides, given the fact that LIPS assays hadn't been applied to screen the same 68 healthy sera and disease control sera (60 LOMG patients and 41 EOMG patients) as our live CBAs did, here we couldn't make direct comparsion to judge if our live CBAs are diagnostically superior to the LIPS assays for predicting the presence of thymoma. Future works to evaluate the specificity of LIPS assays will be required.

Chapter IV

Detection of onconeural autoantibodies in patients with paraneoplastic neurological syndromes

4.1. Introduction

4.1.1. Paraneoplastic neurological syndromes

Paraneoplastic neurological syndromes (PNS) are a range of rare but progressive autoimmune-mediated neuronal disorders associated with their corresponding malignancies, e.g., small-cell lung cancer (SCLC) associated with sensory neuronopathy, ovarian and breast cancers associated with paraneoplastic cerebellar degeneration, or thymoma associated with autoimmune myasthenia gravis (Dalmau and Rosenfeld, 2020, Yshii et al., 2020, Leypoldt and Wandinger, 2014, Dubey et al., 2020, Taverna et al., 2014, Sun et al., 2020, Bataller et al., 2004). In Vogrig et al.'s study in Northeastern Italy, the prevalence of PNS was 4.37 per 100,000, the median age was 68 years old, and PNS developed in 1 in every 334 cancer patients (Vogrig et al., 2020).

Patients with PNS have been reported having autoantibodies to intracellular onconeural or neuronal-surface antigens (Hoftberger et al., 2015). Those autoantibodies are highly associated with the corresponding tumours, and the patients normally develop PNS before their tumours become apparent. In neurology clinics, once the patients are suspected or diagnosed with PNS, screening for the corresponding autoantibodies should be initiated (Leypoldt and Wandinger, 2014). The presence or absence of relevant autoantibodies supports further predicting the probability and location of underlying cancer. Dubey et al. suggested if patients' testicular tumours had been early diagnosed and managed owing to the early detection of KLHL11 autoantibodies, they became less dependent on wheelchair (Dubey et al., 2020). Hence, the early detection of onconeural autoantibodies is critical to prognose and early manage the corresponding tumours. Table 4.1 summarizes the onconeural

autoantibodies investigated in my DPhil research along with their commonly associated classical PNS and tumours.

Table 4.1: Summary of onconeural autoantibodies investigated in our study

Antibody targets	Commonly associated PNS	Commonly associated tumour / Positive predictive value (PPV)
Hu antigen (HuD)	cerebellar degeneration/ataxia, chronic intestinal pseudo-obstruction, encephalomyelitis, limbic encephalitis, sensory neuronopathy	small-cell lung cancer (SCLC), neuroblastoma, neuroendocrine tumours / 85%
Yo antigens (CDR2, CDR2L)	cerebellar degeneration/ataxia	breast cancer, ovarian cancer / > 90%
Ri antigens (NOVA1)	cerebellar degeneration/ataxia, opsoclonus-myoclonus syndrome, rhombencephalitis	breast cancer, ovarian cancer, SCLC / > 70%
Ma antigens (Ma1, Ma2)	limbic encephalitis, rhombencephalitis	SCLC, testicular cancer / > 75%
CRMP5	cerebellar degeneration/ataxia, encephalomyelitis, limbic encephalitis, sensory neuronopathy	SCLC / 75%; thymoma / 15%
SOX1	Lambert-Eaton myasthenic syndrome, cerebellar degeneration	SCLC / > 90%; sensitivity = 67%, specificity = 95% for SCLC among LEMS patients
Amphiphysin	cerebellar degeneration/ataxia rhombencephalitis, limbic encephalitis, polyneuropathy, sensory neuronopathy, stiff-person syndrome	breast cancer, SCLC / 80%
KLHL11	limbic encephalitis, neuropathy, rhombencephalitis	testicular cancer / 80%

ZIC4	cerebellar degeneration/ataxia	SCLC / 90%

Regarding PNS pathology, it is attributed to the ectopic expression of onconeural antigens within the corresponding tumours where the antigens are captured by tissue-resident dendritic cells and then presented to antigen specific T cells for trigger autoimmune cascade (Pignolet et al., 2013). In patients with HuD-associated paraneoplastic encephalomyelitis, Szabo et al. found HuD expressed in both patients' CNS neurons and SCLC (Szabo et al., 1991). Despite patients typically demonstrating high titres of onconeural autoantibodies, these antibodies are not thought to be pathogenic, with evidence suggesting a role for cellular immunity in neuronal cell death (Rousseau et al., 2005, Gebauer et al., 2017).

4.1.2. The available methods to detecting onconeural autoantibodies

Among many commercially available methods to detect onconeural autoantibodies, line blots and fixed rodent cerebellar immunohistochemistry (IHC) are used more frequently (Ricken et al., 2018). The onconeural autoantibodies are defined as well-characterized if a recognizable IHC staining pattern appears after incubating with patients' sera or CSF. Then, the presence of onconeural autoantibodies is further identified by line blots. However, some pitfalls have been reported when applying them to detect onconeural autoantibodies. In 2019, Ruiz-Garcia et al. found line blots missed 18/71 (25.4%) of the samples identified having SOX1 autoantibodies by fixed cell-based assay (Ruiz-Garcia et al., 2019). A year later, the same team suggested if using line blots alone, especially when detecting autoantibodies to ZIC4 and Yo antigen, the PPVs were low to distinguish patients with or without PNS (Ruiz-Garcia et al., 2020). On the other hand, the staining pattern of fixed IHC may be masked by the concomitant

anti-nuclear autoantibodies, and it is hard to simultaneously detect multiple autoantibodies as the line blots (Ricken et al., 2018). Therefore, in order to make accurate diagnosis, it is recommeneded to combine the results from both line blots and fixed IHC.

4.2. Research Rationales

So far, live CBAs have been shown with good sensitivity and specificity to detect cell-surface anitgens, for instance AQP4, compared to ELISA, IIF and commercially avaialbe fixed CBA (Prain et al., 2019). Therefore, we developed live CBAs to detect onconeural autoantibodies by expressing the native onconeural antigens on the surface of HEK293T cells. This is an unique approach. To our knowledge, no other attempts have been made to express intracellular antigens on the surface of live HEK cells, so we were interested in seeing if our live CBAs could achieve better diagnostic accuracy. In this chapter, the development of live and permeabilized CBAs to detect onconeural autoantibodies is described, and the results of live CBAs and conventional methods (line blots and fixed IHC) to detect the identical oncoenrual antignes are compared. Besides, although fixed IHC is known to be more specific than commercial line blots for identifying patients without PNS and tumour, it is hard to perform in multiplex manner as line blots. In the end of this chapter, the results of our quadruplex coverslip-based live CBA are displayed as an in-lab alternative and a prologue of multiplex flow cytometry CBA development descirbed in Chapter V.

4.3. Study Aims

I. Develop eGFP-tagged live and permeabilized CBAs for detecting autoantibodies to onconeural antigens in patients with or without PNS and tumours

II. Compare our live CBA results with fixed IHC and line blots data from two international centers

III. Establish quadruplex coverslip-based live CBA for detecting autoantibodies to HuD, NOVA1, CDR2L and CRMP5 simultaneously

4.4. Methods

4.4.1. Samples

Samples were provided by collaborators at Institut d'Investigacions Biomèdiques August Pi i Sunyer, Barcelona and Mayo Clinic, Rochester. The Barcelona cohort consisted of 36 serum samples, including 15/36 sera from patients with both classical PNS and their corresponding tumours, 1/36 sera with classical PNS only, 4/36 sera with tumour only and 16/36 sera without both. Diagnostically, 17/36 sera were seropositive for the corresponding onconeural autoantibodies double identified by line blots and fixed IHC, and 19/36 sera were seropositive for the corresponding onconeural autoantibodies identified by line blots only. The demographic details of Barcelona samples were not provided. On the other hand, the Mayo Clinic cohort consisted of 33 sera and 21 CSF samples. Among those, 46/54 samples were seropositive for the corresponding onconeural autoantibodies double identified by fixed IHC and line blots (or western blots), 5/54 samples had anti-nuclear autoantibodies and 3/54 samples were from patients with hypogammaglobulinemia. In addition, the Mayo Clinic's samples with onconeural autoantibodies were endpoint titrated via IIF,

and the endpoint titres were reported by our collaborator at Mayo Clinic. However, the demographic and clinical details of Mayo Clinic samples were not provided. Besides, 90 healthy sera were screened to set the cut-offs of our live CBAs. Table 4.2 summarizes the serological profile of the sera and CSF samples from Barcelona and Mayo Clinic.

Table 4.2: Summary of the samples from Barcelona and Mayo Clinic

	Barcelona Cohort	**Mayo Clinic Cohort**
Sample size	Sera sample, N=36	Sera sample, N=33 CSF samples N=21
Serological profile	**Double identified seropositive by line blots and fixed IHC, N=17** CDR2/CDR2L Ab+, N=3 SOX1 Ab+, N=1 HuD Ab+, N=3 NOVA1 Ab+, N=1 Ma1/Ma2 Ab+, N=2 CRMP5 Ab+, N=4 Amphiphysin Ab+, N=3 **Identified seropositive by line blots only, N=19** CDR2 Ab+, N=5 SOX1 Ab+, N=4 (2 with ANA) HuD Ab+ N=1 (GAD Ab IHC+) NOVA1 Ab+, N=1 Ma2 Ab+, N=1 (with ANA) CRMP5 Ab+, N=2 Amphiphysin Ab+, N=1 ZIC4 Ab+, N=3 (2 with ANA) CDR2&ZIC4 Ab+, N=1	**Double identified seropositive by fixed IHC and line blots (or western blots), N=46** CDR2/CDR2L Ab+, N=10 SOX1 Ab+, N=10 HuD Ab+, N=9 NOVA1 Ab+, N=5 CRMP5 Ab+, N=9 HuD&PCA2 Ab+, N=1 HuD&CRMP5 Ab+, N=2 **Samples with ANA, N=5** **Samples from patients with hypogammaglobulinemia (HGG), N=3**

Clinical details	Samples from patients, • With PNS and tumour, N=15 • With PNS only, N=1 • With tumour only, N=4 • Without PNS and tumour, N=16 To note, PNS here means high or intermediate-risk PNS.	Not provided
Demographic details	Not provided	Not provided

4.4.2. Construct design

The cDNAs of HuD, CDR2, NOVA1, Ma1, Ma2, Amphiphysin and CRMP5 were synthesized by IDT gBlocks. On the other hand, and the cDNAs of CDR2L, ZIC4, KLHL11 and SOX1 were synthesized by GeneArt and accommodated in pMK-RQ vector. All the cDNAs were subcloned between Caspr2 signal sequence and C-terminal Caspr2, which was intracellularly linked to an eGFP, via HindIII (AAGCTT) and XhoI (CTCGAG) sites on pcDNA3.1 plasmid (Figure 4-1).

CGACTCACTATAGGGAGACCCAAGCTGGCTAGCCCACCATGCAGGCGGCTCCGCGCGCCGGC
TGCGGGGCAGCGCTCCTGCTGTGGATTGTCAGCAGCTGCCTCTGCAGAGCCTGGACGGCTAA
GCTTATGAGATTACTTCTTTTAAGGGAAATTGTCATTAATGAGTCAAGAAACTGCTCATTTA
TGATAATTAGCACCATGGAGCCTCAGGTGTCAAATGGTCCGACATCCAATACAAGCAATGGA
CCCTCCAGCAACAACAGAAACTGTCCTTCTCCCATGCAAACAGGGGCAACCACAGATGACAG
CAAAACCAACCTCATCGTCAACTATTTACCCCAGAATATGACCCAAGAAGAATTCAGGAGTC
TCTTCGGGAGCATTGGTGAAATAGAATCCTGCAAACTTGTGAGAGACAAAATTACAGGACAG
AGTTTAGGGTATGGATTTGTTAACTATATTGATCCAAAGGATGCAGAGAAAGCCATCAACAC
TTTAAATGGACTCAGACTCCAGACCAAAACCATAAAGGTCTCATATGCCCGTCCGAGCTCTG
CCTCAATCAGGGATGCTAACCTCTATGTTAGCGGCCTTCCCAAAACCATGACCCAGAAGGAA
CTGGAGCAACTTTTCTCGCAATACGGCCGTATCATCACCTCACGAATCCTGGTTGATCAAGT
CACAGGAGTGTCCAGAGGGGTGGGATTCATCCGCTTTGATAAGAGGATTGAGGCAGAAGAAG
CCATCAAAGGGCTGAATGGCCAGAAGCCCAGCGGTGCTACGGAACCGATTACTGTGAAGTTT
GCCAACAACCCCAGCCAGAAGTCCAGCCAGGCCCTGCTCTCCCAGCTCTACCAGTCCCCCAA
CCGGCGCTACCCAGGTCCACTTCACCACCAGGCTCAGAGGTTCAGGCTGGACAATTTGCTTA
ATATGGCCTATGGCGTAAAGAGGTTCTCCCCAATTACCATTGATGGAATGACAAGCCTTGTG

GGAATGAACATCCCTGGTCACACAGGAACTGGGTGGTGCATCTTTGTCTACAACCTGTCCCC
CGATTCCGATGAGAGTGTCCTCTGGCAGCTCTTTGGCCCCTTTGGAGCAGTGAACAACGTAA
AGGTGATTCGTGACTTCAACACCAACAAGTGCAAGGGATTCGGCTTTGTCACCATGACCAAC
TATGATGAGGCGGCCATGGCCATCGCCAGCCTCAACGGGTACCGCCTGGGAGACAGAGTGTT
GCAAGTTTCCTTTAAAACCAACAAAGCCCACAAGTCCGGACTCGAGGGACAAGGCCAAGCTA
TAAGAAATGGAGTCAACAGAAACTCGGCTATCATTGGAGGCGTCATTGCTGTGGTGATTTTC
ACCATCCTGTGCACCCTGGTCTTCCTGATCCGGTACATGTTCCGCCACAAGGGCACCTACCA
TACCAACGAAGCAAAGGGGGCGGAGTCGGCAGAGAGCGCGGACGCCGCCATCATGAACAACG
ACCCCAACTTCACAGAGACCATTGATGAAAGCAAAAAGGAATGGCTCATTTCCCGGGATCCA
CCGGTCGCCACCATGGTGAGCAAGGGCGAGGAGCTGTTCACCGGGGTGGTGCCCATCCTGGT
CGAGCTGGACGGCGACGTAAACGGCCACAAGTTCAGCGTGTCCGGCGAGGGCGAGGGCGATG
CCACCTACGGCAAGCTGACCCTGAAGTTCATCTGCACCACCGGCAAGCTGCCCGTGCCCTGG
CCCACCCTCGTGACCACCCTGACCTACGGCGTGCAGTGCTTCAGCCGCTACCCCGACCACAT
GAAGCAGCACGACTTCTTCAAGTCCGCCATGCCCGAAGGCTACGTCCAGGAGCGCACCATCT
TCTTCAAGGACGACGGCAACTACAAGACCCGCGCCGAGGTGAAGTTCGAGGGCGACACCCTG
GTGAACCGCATCGAGCTGAAGGGCATCGACTTCAAGGAGGACGGCAACATCCTGGGGCACAA
GCTGGAGTACAACTACAACAGCCACAACGTCTATATCATGGCCGACAAGCAGAAGAACGGCA
TCAAGGTGAACTTCAAGATCCGCCACAACATCGAGGACGGCAGCGTGCAGCTCGCCGACCAC
TACCAGCAGAACACCCCCATCGGCGACGGCCCCGTGCTGCTGCCCGACAACCACTACCTGAG
CACCCAGTCCGCCCTGAGCAAAGACCCCAACGAGAAGCGCGATCACATGGTCCTGCTGGAGT
TCGTGACCGCCGCCGGGATCACTCTCGGCATGGACGAGCTGTACAAGTAA

Figure 4.1: The design of HuD surface expression construct. The Caspr2 signal sequence is in red, the cDNA of HuD is in blue, the cDNA of C-terminal Caspr2 domain is in green, Kozak sequence is underlined, the restriction sites (HindIII: AAGCTT; XhoI: CTCGAG; XmaI: CCCGGG) are in yellow and the cDNA of eGFP is in green.

4.4.3. Cell-based Assay (CBA)

In Chapter II, the methods of cell seeding, transient transfection, and the details of DsRed2-reporting live CBA and eGFP-tagged permeabilized CBA were described. Here, the methods of eGFP-tagged simplex and quadruplex live CBAs are narrated, and Table 4.3 summarizes the methods of transient transfection applied in this chapter.

Table 4.3: Methods of transient transfection in 6- and 96-well plate

Materials	**6-well plate**	**96-well plate**
Seeding amount on day 1	860,000 cells per well	40,000 cells per well
Seeding volume on day 1	3 ml per well	150 µl per well

Plasmid DNA	3 µg per well	25.2 µg per plate
PEI	1.5 µl per well	12.6 µl per plate
Unsupplemented DMEM (mixed with DNA or PEI separately)	Per well: Filled up to 25 µl along with DNA or PEI before combining together	Per plate: Filled up to 500 µl along with DNA or PEI before combining together
Volume of allocated transfection mix	50 µl per well without aspirating the original media	Per plate: 14 ml of DMEM (with FBS and AA) was added to 1ml of transfection mix. After aspirating the original media, 150 µl of master mix was allocated to each well
Volume of supplemented DMEM culture media	3 ml per well	150 µl per well

4.4.3.1. eGFP-tagged simplex live CBAs

On day 3, the transfected HEK cells were incubated with sera diluted 1:20, CSF diluted 1:2 or commercial antibodies diluted as recommended in DMEM/20 mM HEPES/1% BSA at RT for one hour. Cells were then washed three times with DMEM/20 mM HEPES before fixed by PBS/4% formaldehyde at RT for 10 minutes. Following fixation, cells were washed twice with DMEM/20 mM HEPES and then incubated with anti-human IgG Fc DyLight 594 or anti-rabbit/mouse IgG (H+L) Alexa Fluor 568 secondary antibody (diluted 1:750 in DMEM/20 mM HEPES/1% BSA) at RT for 45 minutes. Cells were then washed twice with DMEM/20 mM HEPES and twice with PBS, after which cells were mounted with DAPI-supplemented mounting media and stored in 4°C fridge before being observed by fluorescent microscopes. Figure 4.2 provides a schematic of using eGFP-tagged live CBA to detect onconeural autoantibodies, with Table 4.4 summarizing the live CBA methodology applied to 24- and 96-well plate. The endpoint titre was defined as the reciprocal value of sample dilution given a CBA score of 1. In

this chapter, the cut-offs of sera samples were set above the highest endpoint titres of individual live CBAs when screening 90 healthy sera. As for CSF, the samples were picked up as long as the endpoint titres ≥ 2.

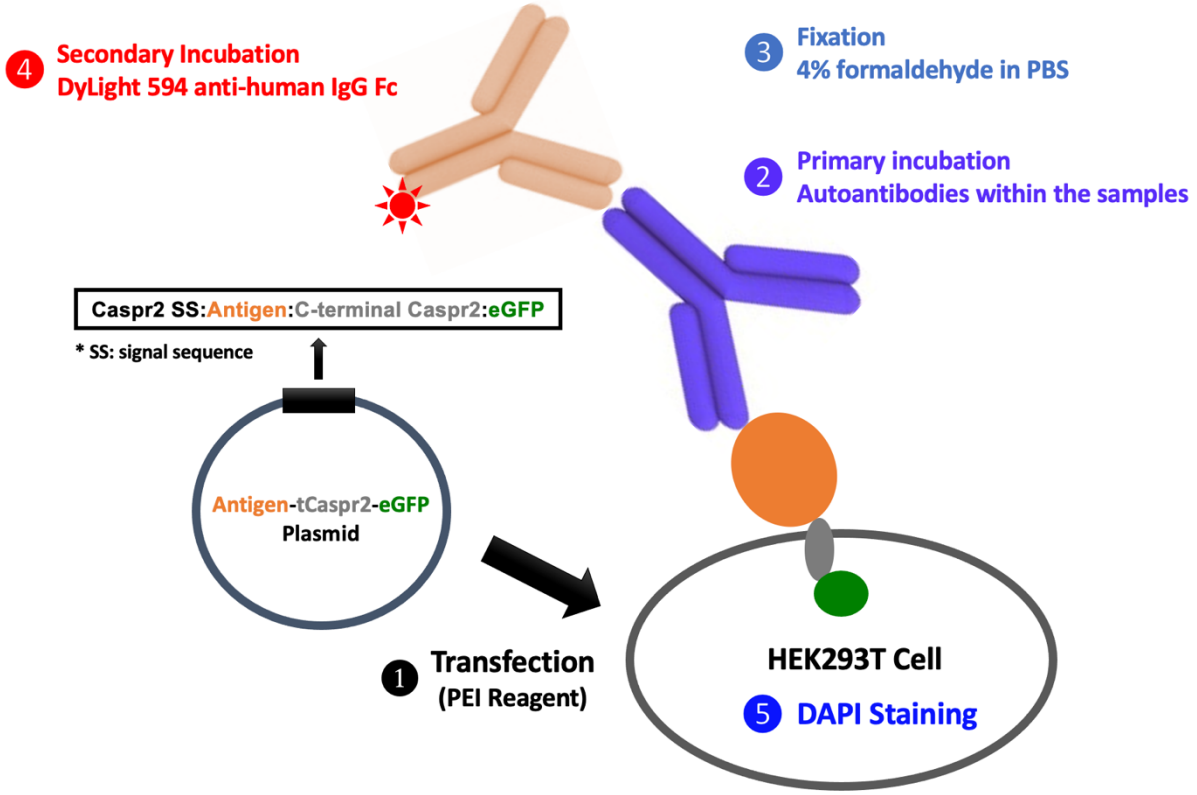


Figure 4.2: The eGFP-tagged simplex live CBA to detect onconeural autoantibodies. On day 2, the HEK293T cells were transfected with the plasmid to surface-express onconeural antigens above the plasma membrane. The targeted antigen was C-terminally tethered to a truncated Caspr2 C-terminal domain and an eGFP. On day 3 at RT, the transfected HEK cells were incubated with diluted blood samples, washed, fixed with 4% formaldehyde, washed, then incubated with 1:750 diluted DyLight 594 anti-human IgG Fc antibody. Lastly, the coverslips were mounted onto slides in mounting media supplement with DAPI.

Table 4.4: Methods of live CBA applied to 24- and 96-well plate

Experimental steps	**24-well plate**	**96-well plate**
1. Blood samples (desired dilution)	250 µl, at RT for an hour	60 µl, at RT for an hour
2. Washed twice with DMEM/20 mM HEPES	250 µl each	180 µl each

3. Fixation	250 µl, at RT for 10 minutes	150 µl, at RT for 10 minutes
4. Washed twice with DMEM/20 mM HEPES	250 µl each	180 µl each
5. Secondary antibodies (1:750 dilution)	250 µl, at RT for an hour	100 µl, at RT for an hour
6. Washed twice with DMEM/20 mM HEPES	250 µl each	180 µl each
7. Mounting	One drop of mounting media (supplemented 1:1000 diluted DAPI)	
8. Storage	Stored at 4°C	

4.4.3.2. eGFP-tagged live quadruplex CBAs

On day 1, individual PLL pre-coated coverslips were placed into each well in 24-well plate, and a water-proof marker pen was used to mark the top right corner of each coverslip. 80 µl of unsupplemented DMEM (w/o FBS and AA), 2 µg of plasmid DNA and 1 µl of PEI were mixed and incubated at RT for 15 minutes. Then, 1 µl of DNA-PEI mixtures, including individual plasmid DNAs, were added to the corresponding locations on each coverslip. Hence, as Figure 4.3, one coverslip could accommodate four different DNA-PEI mixture dots. After 15 minutes allowing the DNA-PEI mixture dots to dry, 170,000 of HEK293T cells were seeded out in supplemented DMEM (with FBS and AA) per well in 24-well plate, and the cells were incubated at 37°C with 5% CO_2 for 48 hours without media change. On day 3, the 24-well plate live CBA protocol was followed (Table 4.4).

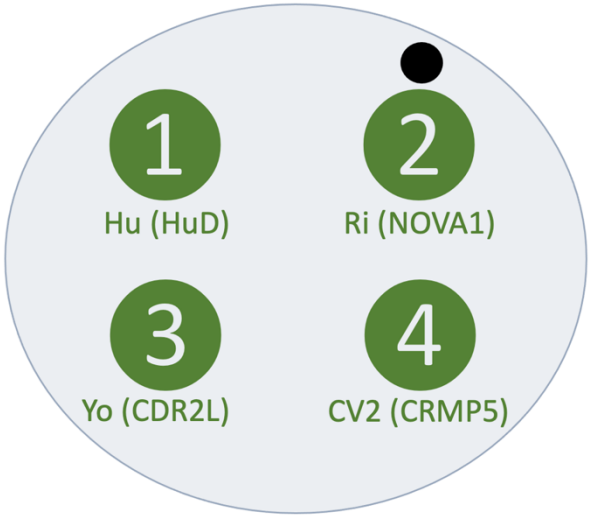


Figure 4.3: The eGFP-tagged quadruplex live CBA to detect onconeural autoantibodies. The image demonstrates the orientation of our eGFP-tagged quadruplex live CBA to detect autoantibodies to HuD, NOVA1, CDR2L and CRMP5. A water-proof black dot was marked at the top right corner of each coverslip.

4.5. Results

4.5.1. The eGFP-tagged live and permeabilized cell-based assays to detect onconeural autoantibodies

Live cell-based assays are specific, partly because the inside of the cells is not exposed to patient's serum or CSF. Due to the intracellular nature of onconeural antigens, we subcloned them between Caspr2 signal sequence and the C-terminal Caspr2 transmembrane domain to facilitate expression on the surface of HEK293T cells (Figure 4.2). We used commercial polyclonal antibodies against individual onconeural antigens to validate their surface expressions. HuD, NOVA1, CRMP5, CDR2L, ZIC4 and Amphiphysin were all detected by commercial antibody staining on the surface of HEK cells (Figure 4.4). However, Ma1, Ma2, CDR2L, SOX1 and KLHL11 were not detected on the cell surface, implying their expression had remained in cytosol (Figure 4.5). To detect Ma1, Ma2, CDR2, SOX1 and KLHL11, we applied the

permeabilized CBA protocol (Figure 2.2), and by doing so the commercial polyclonal antibodies could access those onconeural antigens (Figure 4.6). However, the relatively high assay background was a caveat compared to our live CBAs.

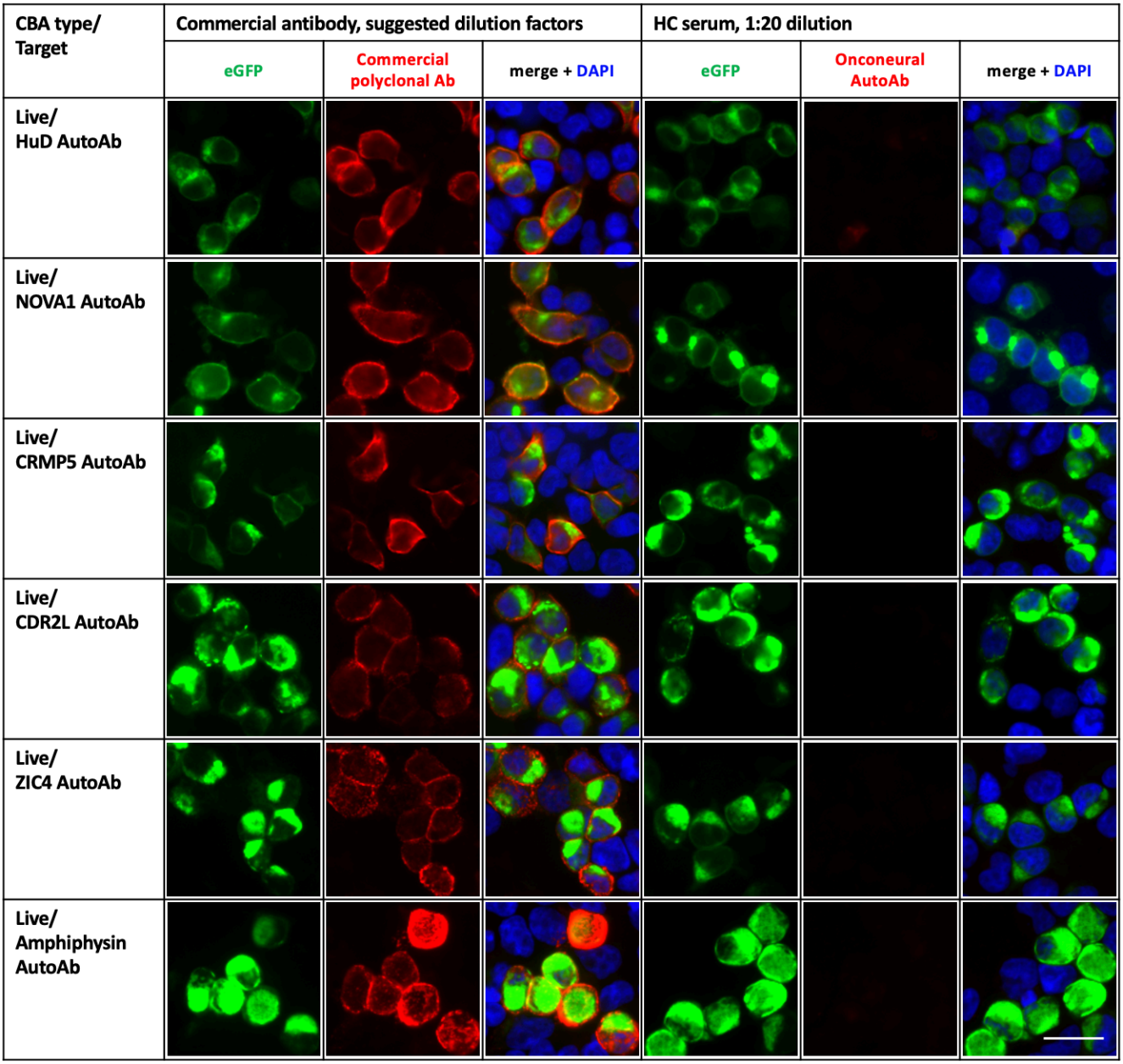


Figure 4.4: The eGFP-tagged live CBAs could detect the commercial antibodies to surface-expressing HuD, NOVA1, CRMP5, CDR2L, ZIC4 and Amphiphysin. When running individual eGFP-tagged live CBAs, the commercial antibodies targeting individual onconeural antigens were applied under the suggested dilution factors, and a healthy serum was screened under 1:20 dilution. The eGFP signal was in green, the secondary antibody binding was in red, and the nuclei labelled by DAPI were in blue. Magnification x 400. Scale bar = 25 μm.

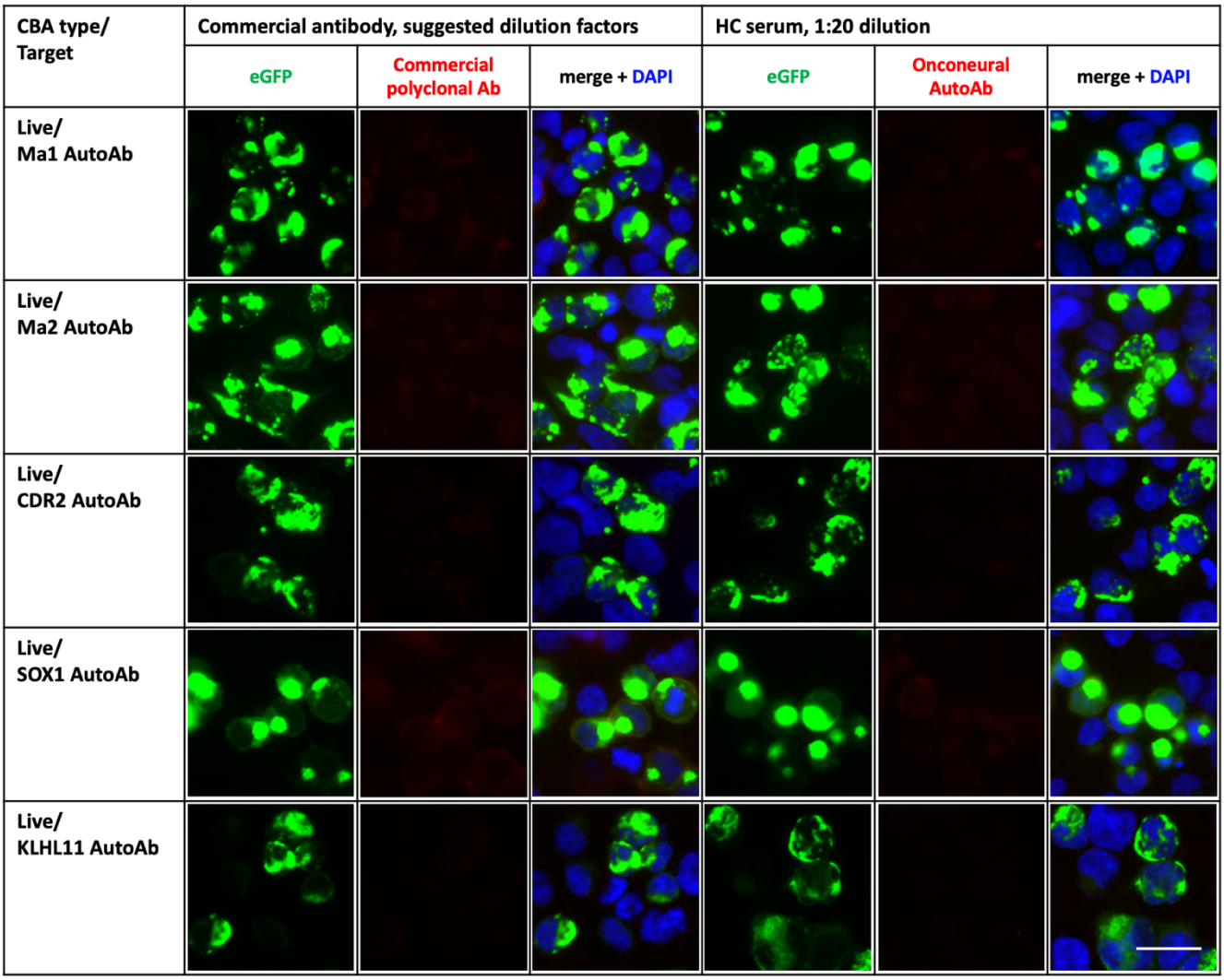


Figure 4.5: The eGFP-tagged live CBAs couldn't detect the commercial antibodies to intracellular Ma1, Ma2, CDR2, SOX1 and KLHL11. When running individual eGFP-tagged live CBAs, the commercial antibodies targeting individual onconeural antigens were applied under the suggested dilution factors, and a healthy serum was screened under 1:20 dilution. The eGFP signal was in green, the secondary antibody binding was in red, and the nuclei labelled by DAPI were in blue. Magnification x 400. Scale bar = 25 μm.

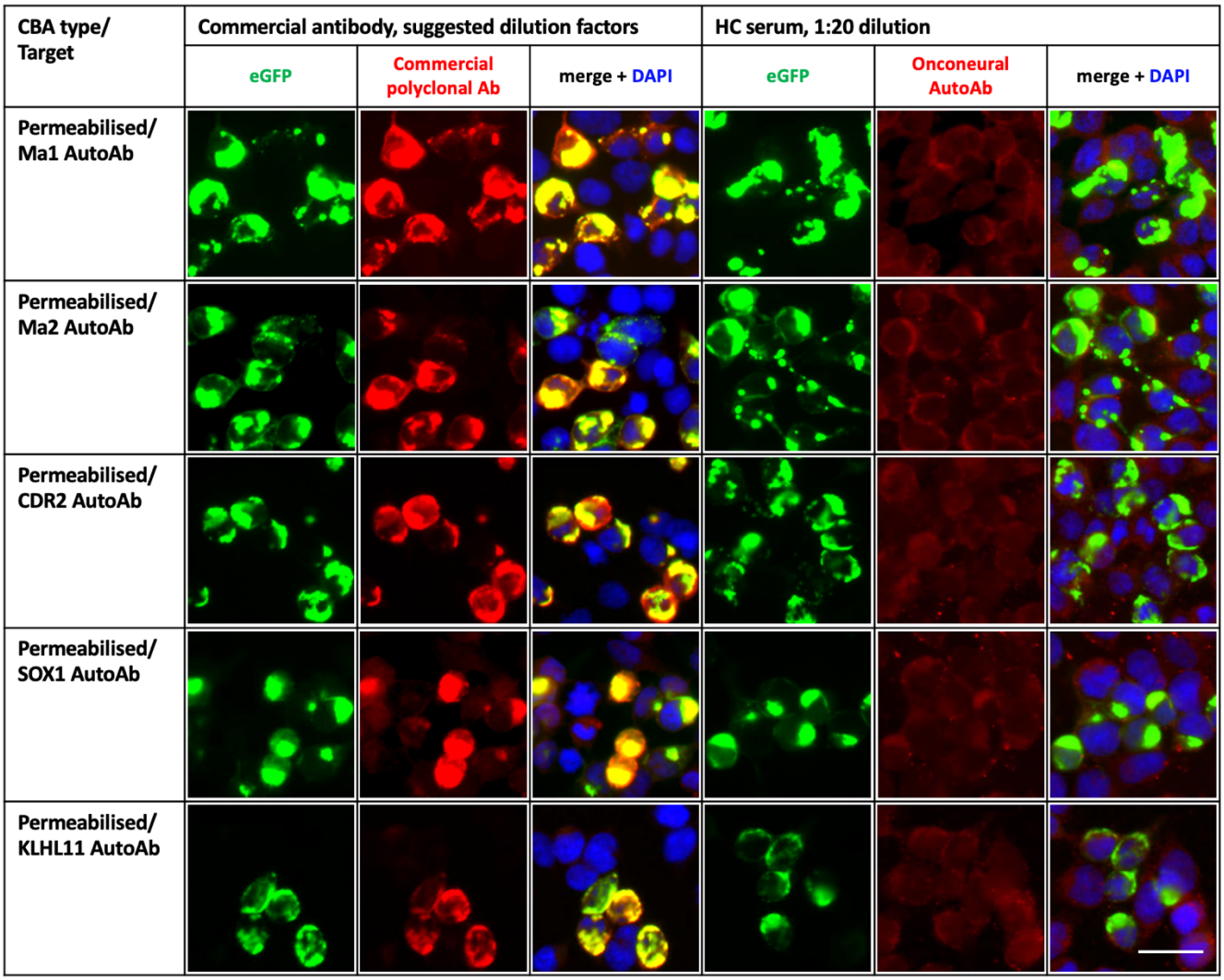


Figure 4.6: The eGFP-tagged permeabilized CBAs could detect the commercial antibodies to intracellular Ma1, Ma2, CDR2, SOX1 and KLHL11. When running individual eGFP-tagged permeabilized CBAs, the commercial antibodies targeting individual onconeural antigens were applied under the suggested dilution factors, and a healthy serum was screened under 1:20 dilution. The eGFP signal was in green, the secondary antibody binding was in red, and the nuclei labelled by DAPI were in blue. Magnification x 400. Scale bar = 25 μm.

Next, we compared two secondary antibodies: AF568 anti-human IgG (H+L) antibody and DyLight 594 anti-human IgG Fc antibody, to tell which produced lower background under the same dilution of 1:750. When screening 50 healthy sera and several patients' sera samples via live HuD and NOVA1 CBAs, DyLight 594 anti-human IgG Fc antibody produced lower CBA cut-offs than AF568 anti-human IgG (H+L) antibody (Figure 4.7). The result suggested DyLight 594 anti-human IgG Fc antibody was better than AF568 anti-human IgG (H+L) for our live CBAs, so we decided to use it for subsequent screens. However, despite using DyLight 594 anti-human IgG Fc antibody, the high background was still evident in our permeabilized CBAs. Figure 4.8 demonstrates the relatively high background in our permeabilized Ma1 CBA compared to our live NOVA1 CBA.

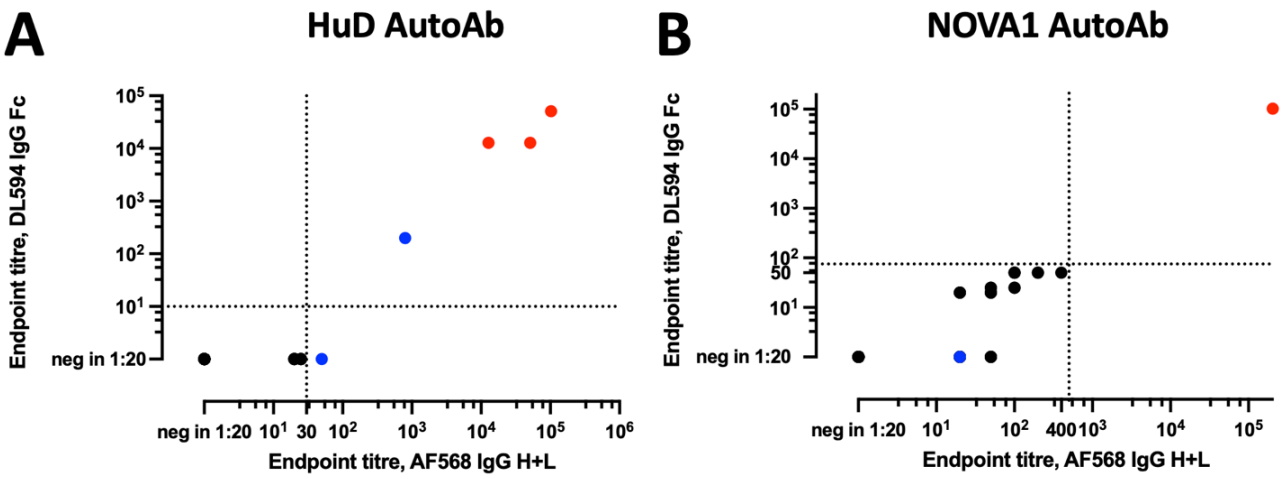


Figure 4.7: DyLight 594 anti-human IgG Fc antibody produced lower CBA cut-offs than AF568 anti-human IgG (H+L) antibody. (a-b) The endpoint tires of autoantibodies to (a) HuD and (b) NOVA1 were plotted. The y-axis displayed the endpoint titres with using DyLight 594 anti-human IgG Fc antibody, and the x-axis displayed endpoint titres with using AF568 anti-human IgG (H+L) antibody. The black dots were healthy sera, the blue dots were the sera identified seropositive for the corresponding autoantibodies by line blots only, and the red dots were the sera identified seropositive for the corresponding autoantibodies by line blots and fixed IHC. The cut-offs for each assay were as the dotted black lines.

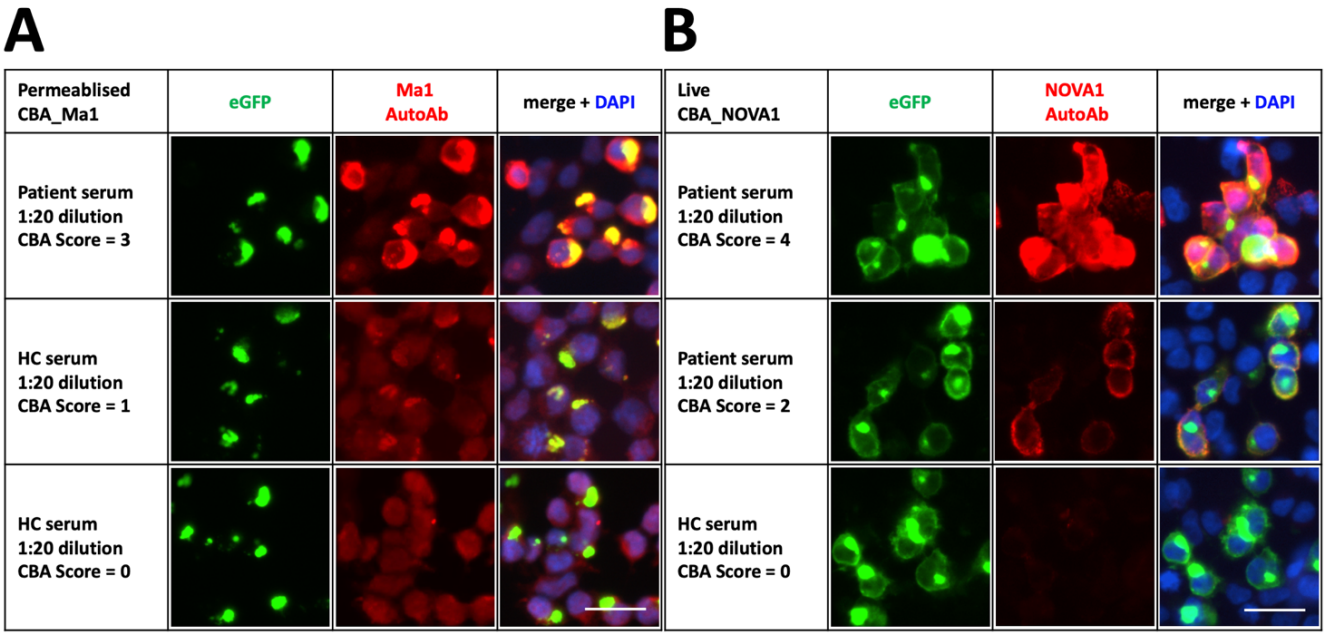


Figure 4.8: The high background noise in permeabilized Ma1 CBA was evident compared to live NOVA1 CBA despite applying DyLight 594 anti-human IgG Fc antibody. (a-b) The images of (a) permeabilized CBA to detect Ma1 autoantibodies and (b) live CBA to detect NOVA1 autoantibodies were displayed. The eGFP signal was in green, the secondary antibody binding was in red, and the nuclei labelled by DAPI were in blue. Magnification x 400. Scale bar = 25 µm.

Despite being imperfect, we were able to identify the patients with both PNS and tumours at a serum dilution of 1:20 using visual scores (Figure 4.9). Our permeabilized Ma1 and Ma2 CBAs picked up 2 samples, identified seropositive for Ma1 and Ma2 autoantibodies by fixed IHC and line blots, from patients with PNS and seminoma (Figure 4.9a-b). Also, our permeabilized Ma1 but not Ma2 CBA didn't pick up a false positive sample, identified seropositive for Ma2 autoantibodies by line blots only, from a patient without PNS and tumour. Next, our permeabilized CDR2 CBA picked up 3 samples, identified seropositive for CDR2/CDR2L autoantibodies by fixed IHC and line blots. However, only 2/3 samples were from patients with paraneoplastic cerebellar degeneration (PCD) and ovarian or breast cancer (Figure 4.9c). A patient with PCD but without ovarian or breast cancer was identified with CDR2/CDR2L autoantibodies by line blots, fixed IHC and our permeabilized CBA. Hence, it would have been useful

to follow this patient longitudinally because there may have been an as yet undiagnosed ovarian or breast cancer present. Besides, our permeabilized CDR2 CBA didn't pick up all the 6 samples identified CDR2 Ab+ by line blots only. 1/6 sample was from a patient with myasthenia gravis (MG, low-risk PNS) and thymoma, and 5/6 samples were from patients without PNS and tumour.

On the other hand, as Figure 4.9d, our permeabilized SOX1 CBA picked up a Barcelona serum sample from a patient with SCLC and Guillain-Barré syndrome spectrum disorder with brainstem encephalitis (GBS-BE). Also, 4 SOX1 Ab+ samples, identified seropositive by line blots only, weren't picked up by our permeabilized SOX1 CBA. Furthermore, we screened more serum samples from Mayo Clinic to expand the sample size. However, only 3/8 SOX1 Ab+ samples from Mayo Clinic were partially provided with the diagnoses of patients' PNS (1/8 with LEMS) and tumours (2/8 with SCLC). Although we couldn't make diagnostic conclusions with limited clinical details, those 8 SOX1 Ab+ samples were with similar 1:20 CBA visual scores compared to the Barcelona SOX1 Ab+ sample scored 3. Besides, both LEMS and SCLC were associated with SOX1 autoantibodies from past literatures (Berger et al., 2016). To conclude, at 1:20 sample dilution, our permeabilized Ma1, Ma2, CDR2 and SOX1 CBAs picked up all the 14 seropositive samples, identified by line blots and fixed IHC, but our permeabilized Ma2 CBA picked up a Ma2 Ab+ samples, identified by line blots only, from a patient without PNS and tumour.

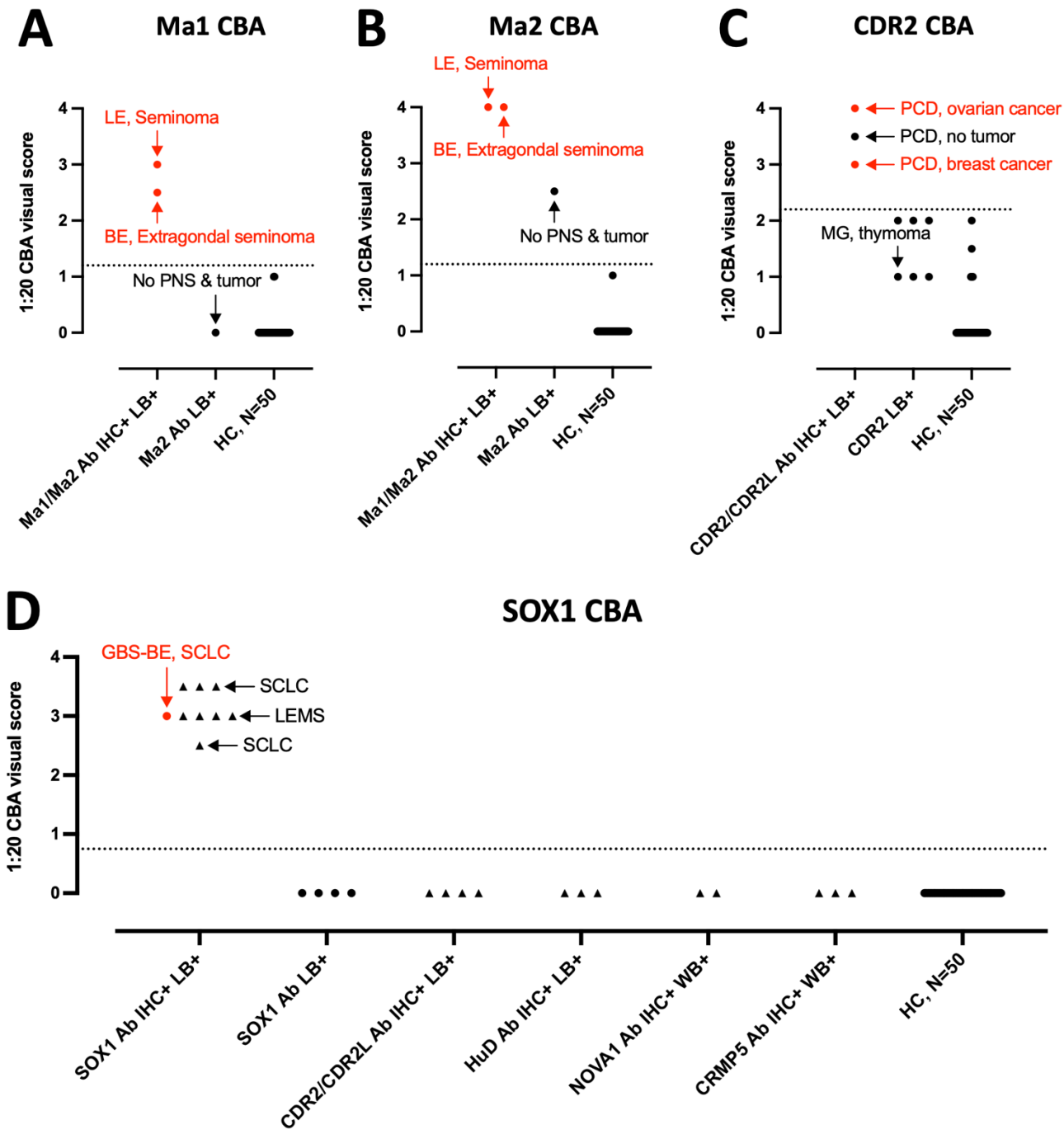


Figure 4.9: The permeabilized CBAs identified samples from patients with both PNS and tumours. (a-c) The y-axis displayed the 1:20 visual scores of each sample from Barcelona screened by permeabilized CBAs to detect autoantibodies to (a) Ma1, (b) Ma2 and (c) CDR2, and the sample cohorts were mentioned below the x-axis. The samples from patients with tumours and high- or intermediate-risk PNS were in red. The diagnoses of patients' PNS and tumours were mentioned as the arrows indicated. The cut-offs were as the dotted black lines. (d) The y-axis displayed the 1:20 visual scores of each sera sample screened by our permeabilized SOX1 CBA, and the sample cohorts were mentioned below the x-axis. The sample from a patient with GBS-BE and SCLC was in red. The diagnoses, if known, of patients' PNS and tumours were

mentioned as the arrows indicated. The samples from Barcelona and Mayo Clinic were shown as circles and triangles respectively. The cut-off was as the dotted black line. *Abbreviations: GBS-BE, Guillain-Barré syndrome spectrum disorder with brainstem encephalitis; LB, line blot; LE, limbic encephalitis; LEMS, Lambert-Eaton myasthenic syndrome; MG, myasthenia gravis; PCD, paraneoplastic cerebellar degeneration; PNS, paraneoplastic neurological syndrome; SCLC, small cell lung cancer; WB, western blots.*

Because our live CBAs produced lower background noise and owing to the limited sample volumes, from here, we only applied our live HuD, NOVA1, CDR2L, Amphiphysin, CRMP5 and ZIC4 CBAs to screen the samples from our collaborators in Barcelona and Mayo Clinic. Nevertheless, the concept of our permeabilized CBA would be revisited later in a better quantification fashion through flow cytometry. The developments of live and permeabilized flow cytometry CBAs (F-CBAs) and the results are described in Chapter V.

The following sections would display and interpret the screening results of Barcelona and Mayo Clinic cohorts. Because the clinical details of the serum and CSF samples from Mayo Clinic were very limited, we decided not to combine two cohorts together for the benefits of evaluating the diagnostic accuracy of individual live CBAs when screening Barcelona samples.

4.5.2. Live CBA results: Barcelona cohort

The 36 Barcelona serum samples and 90 healthy sera were screened by eGFP-tagged live CBAs for detecting autoantibodies to HuD, NOVA1, CDR2L, Amphiphysin, CRMP5 and ZIC4. The endpoint titres of individual live CBAs were plotted as Figure 4.10.

In our live HuD CBA, 5/126 samples were picked up as HuD Ab CBA+ (Figure 4.10a). 3/5 HuD Ab CBA+ samples were also identified seropositive by fixed IHC and line blots, 1/5 sample was picked up by line blots only, and the other one was picked up by live HuD CBA only. All the 5 HuD Ab CBA+ samples were from patients with PNS and tumour, but 2/5 samples were identified strong positive in CRMP5 autoantibodies by fixed IHC and line blots. In addition, our live HuD CBA didn't pick up a HuD Ab+ sample, identified by line blots only, from a patient with stiff-person syndrome (SPS, intermediate-risk PNS) but without tumour.

In our live NOVA1 CBA, 6/126 samples were picked up as NOVA1 Ab CBA+, but only 1/6 NOVA1 Ab CBA+ sample was also identified by fixed IHC and line blots (Figure 4.10b). The concordant sample was from a patient with brainstem encephalitis and ovarian cancer. The 5 discordant samples were reported endpoint titre ≤ 400 in our live NOVA1 CBA, and only 1/5 of them was from a patient without PNS and tumour. From the plot, there was more than 200-time difference between the endpoint titres of the true positive and the discordant samples, so it would be worth screening more samples to define a better cut-off. Besides, our live NOVA1 CBA didn't pick up a NOVA1 Ab+ sample, identified seropositive by line blots only, from a patient without PNS and tumour.

In our live CDR2L CBA, 4/126 samples were picked up as CDR2L Ab CBA+ (Figure 4.10c). 3/4 CDR2L Ab CBA+ samples were also identified seropositive by fixed IHC and line blots, and the other one was identified seropositive by line blots only. Compared to our permeabilized CDR2 CBA, our live CDR2L CBA picked up the identical 3 samples from patients with PCD, but one of them had not been diagnosed with ovarian or breast cancer yet. Additionally, our live CDR2L CBA picked up a CDR2 Ab+ sample, identified seropositive by line blots only, from a patient without PNS and tumour. However, the other 5 CDR2 Ab+ samples, identified seropositive by line blots only, weren't picked up by our live CDR2L CBA. Those samples were from a patient with MG and thymoma and from 4 patients without PNS and tumour.

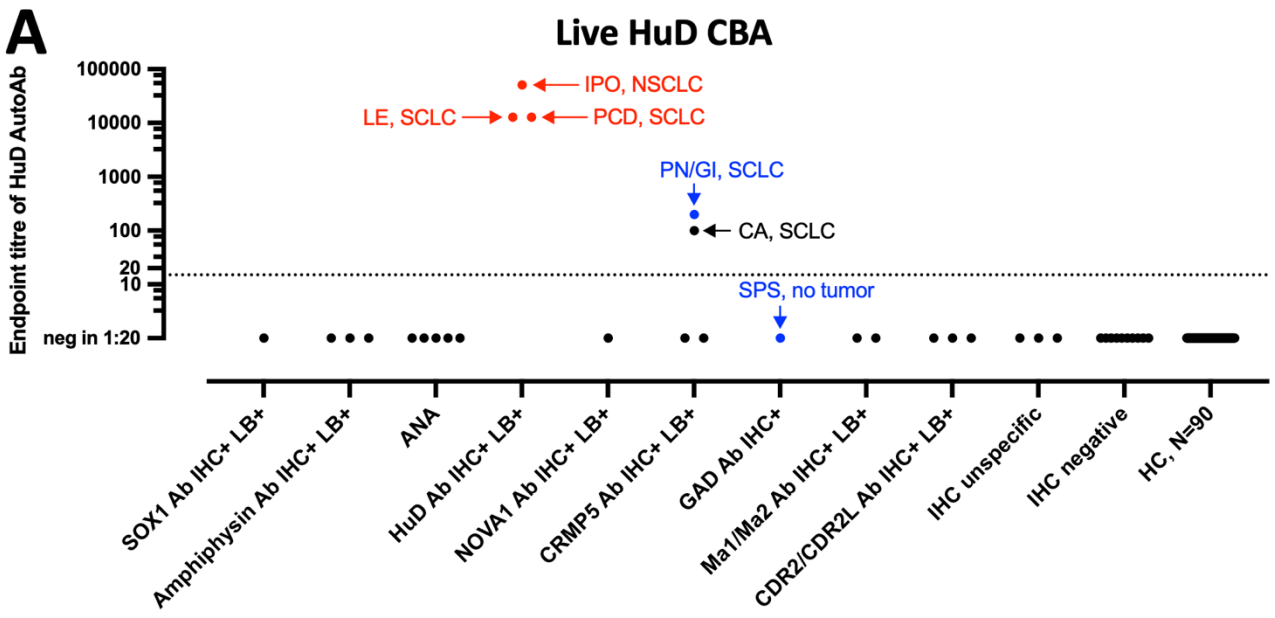
In our live Amphiphysin CBA, 3/126 samples were picked up as Amphiphysin Ab CBA+ (Figure 4.10d). All the 3 samples were also identified seropositive by fixed IHC and line blots, and from patients with PNS and tumours. In addition, our live Amphiphysin CBA didn’t pick up a Amphiphysin Ab+ sample, identified seropositive by line blots only, from a patient without PNS and tumour. So far, our live Amphiphysin CBA had shown no discordance result double identified Amphiphysin Ab+ by fixed IHC and line blots.

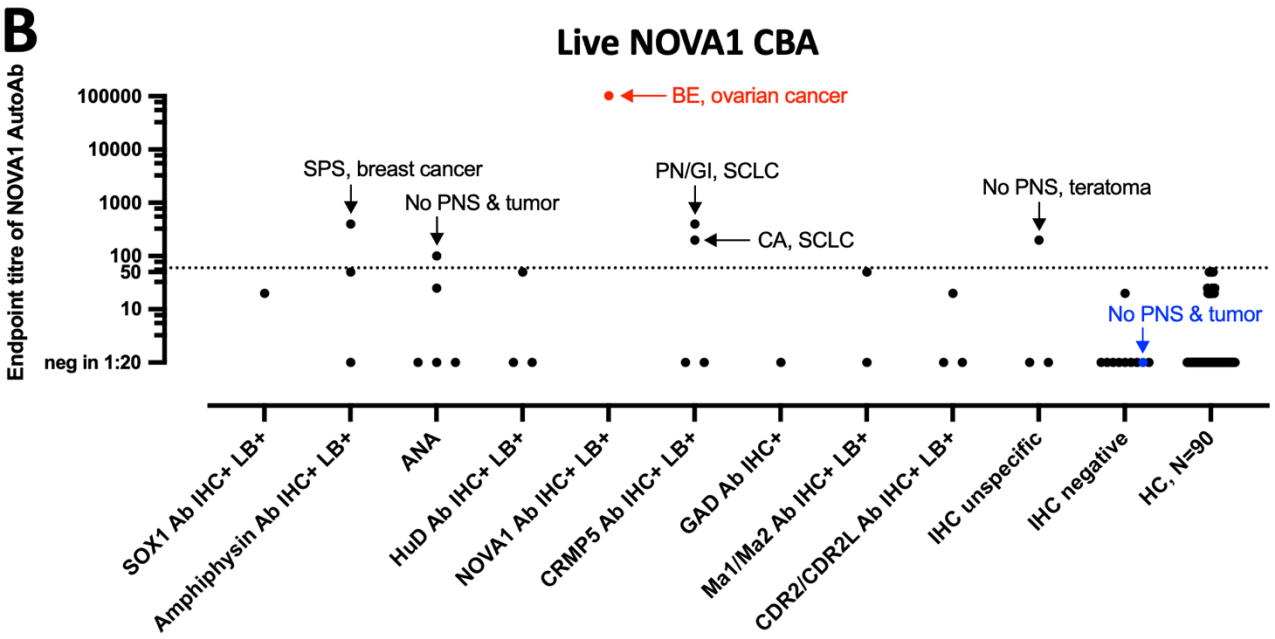
In our live CRMP5 CBA, 7/126 samples were picked up as CRMP5 Ab CBA+ (Figure 4.10e). 4/7 CRMP5 Ab CBA+ samples were also identified seropositive by fixed IHC and line blots, 2/7 samples were identified seropositive by line blots and the other one was picked up by our live CRMP5 CBA only. The 3/4 concordant samples were from patients with PNS and SCLC, but our live CRMP5 CBA picked up 1/4 concordant sample from a patient with MG and thymoma. Furthermore, our live CRMP5 CBA picked up 2 CRMP5 Ab+ samples, identified seropositive by line blots only, from

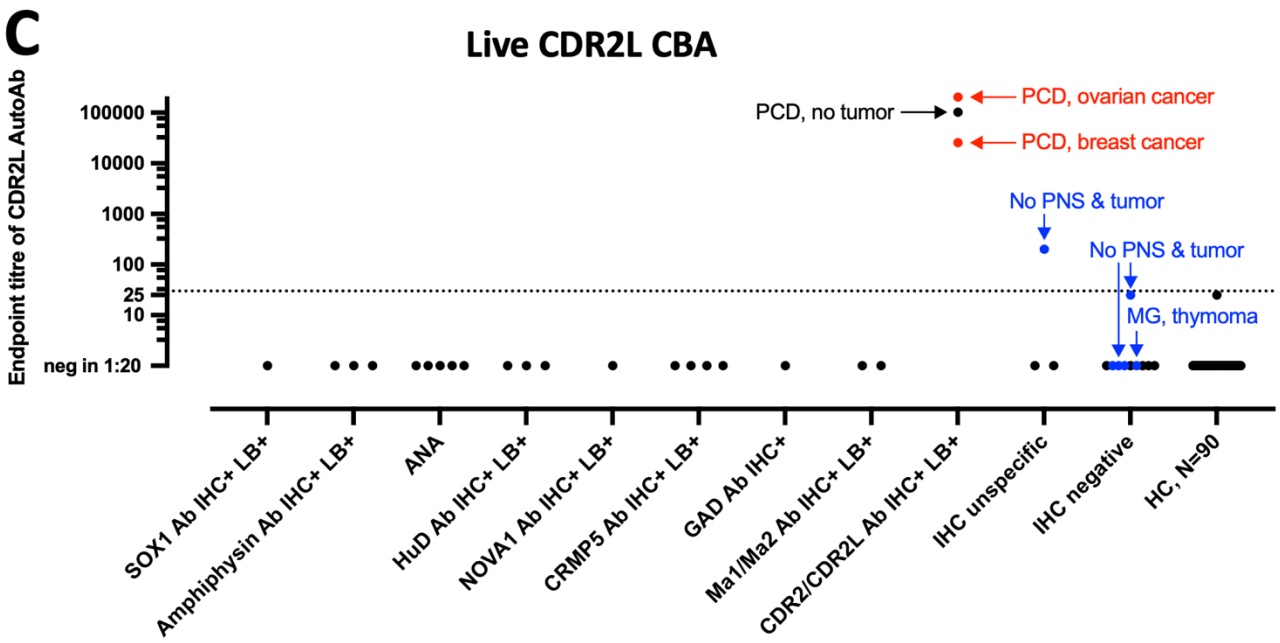
patients without PNS despite one of them diagnosed with melanoma. Besides, the sample picked up by our live CRMP5 CBA only with very low endpoint titre of CRMP5 autoantibodies equal to 20 and from a patient without PNS and tumour.

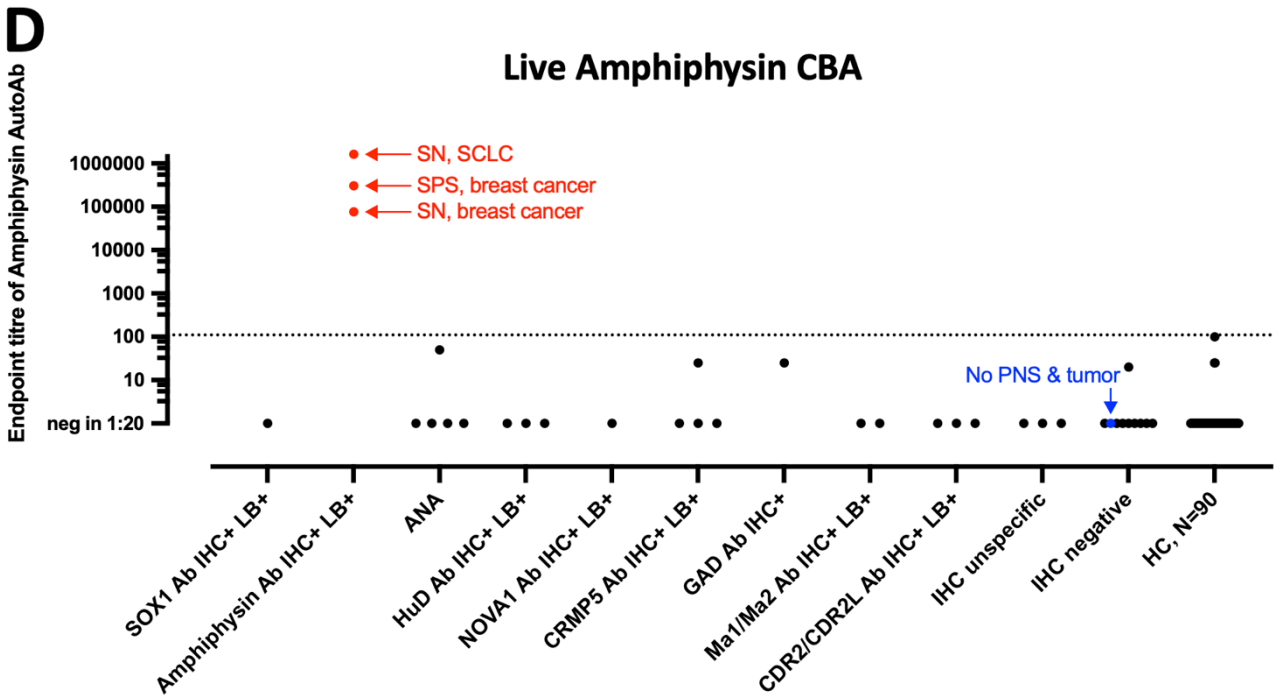
In our live ZIC4 CBA, 1/126 sample was picked up as ZIC4 Ab CBA+ (Figure 4.10f). 6/126 ZIC4 Ab+ samples, identified seropositive by line blots only, weren't picked up by our live ZIC4 CBA. Among the 6 ZIC Ab LB+ samples, 4/6 samples were from patients without PNS and tumour, 1/6 sample was from a patient without PNS but with teratoma and the other one was from a patient with PCD and breast cancer. The result implies line blots have poor specificity to predict patients' PNS and tumour. To note, there was no sample from Barcelona with ZIC4 IHC+ pattern, and the highest endpoint titre of ZIC4 autoantibodies tested by our live ZIC4 CBA was 200 from a patient with PCD and ovarian cancer. However, this patient was identified with CDR2/CDR2L autoantibodies by line blots and IHC. Therefore, we haven't been able to conclude the diagnostic accuracy of our live ZIC4 CBA so far.

To conclude, Table 4.5 summarizes the number of Barcelona samples picked up by our live CBAs in each sample cohort, and Table 4.6 summarizes the diagnostic accuracy of our live CBAs for detecting autoantibodies to HuD, NOVA1, CDR2L, Amphiphysin and CRMP5.


A
Live HuD CBA
Endpoint titre of HuD AutoAb
100000
10000
1000
100
20
10
neg in 1:20
IPO, NSCLC
LE, SCLC
PCD, SCLC
PN/GI, SCLC
CA, SCLC
SPS, no tumor
SOX1 Ab IHC+ LB+
Amphiphysin Ab IHC+ LB+
ANA
HuD Ab IHC+ LB+
NOVA1 Ab IHC+ LB+
CRMP5 Ab IHC+ LB+
GAD Ab IHC+
Ma1/Ma2 Ab IHC+ LB+
CDR2/CDR2L Ab IHC+ LB+
IHC unspecific
IHC negative
HC, N=90


B
Live NOVA1 CBA
Endpoint titre of NOVA1 AutoAb
100000
10000
1000
100
50
10
neg in 1:20
BE, ovarian cancer
SPS, breast cancer
No PNS & tumor
PN/GI, SCLC
CA, SCLC
No PNS, teratoma
No PNS & tumor
SOX1 Ab IHC+ LB+
Amphiphysin Ab IHC+ LB+
ANA
HuD Ab IHC+ LB+
NOVA1 Ab IHC+ LB+
CRMP5 Ab IHC+ LB+
GAD Ab IHC+
Ma1/Ma2 Ab IHC+ LB+
CDR2/CDR2L Ab IHC+ LB+
IHC unspecific
IHC negative
HC, N=90


C
Live CDR2L CBA
Endpoint titre of CDR2L AutoAb
100000
10000
1000
100
25
10
neg in 1:20
PCD, no tumor
PCD, ovarian cancer
PCD, breast cancer
No PNS & tumor
No PNS & tumor
MG, thymoma
SOX1 Ab IHC+ LB+
Amphiphysin Ab IHC+ LB+
ANA
HuD Ab IHC+ LB+
NOVA1 Ab IHC+ LB+
CRMP5 Ab IHC+ LB+
GAD Ab IHC+
Ma1/Ma2 Ab IHC+ LB+
CDR2/CDR2L Ab IHC+ LB+
IHC unspecific
IHC negative
HC, N=90


D
Live Amphiphysin CBA
Endpoint titre of Amphiphysin AutoAb
1000000
100000
10000
1000
100
10
neg in 1:20
SN, SCLC
SPS, breast cancer
SN, breast cancer
No PNS & tumor
SOX1 Ab IHC+ LB+
Amphiphysin Ab IHC+ LB+
ANA
HuD Ab IHC+ LB+
NOVA1 Ab IHC+ LB+
CRMP5 Ab IHC+ LB+
GAD Ab IHC+
Ma1/Ma2 Ab IHC+ LB+
CDR2/CDR2L Ab IHC+ LB+
IHC unspecific
IHC negative
HC, N=90

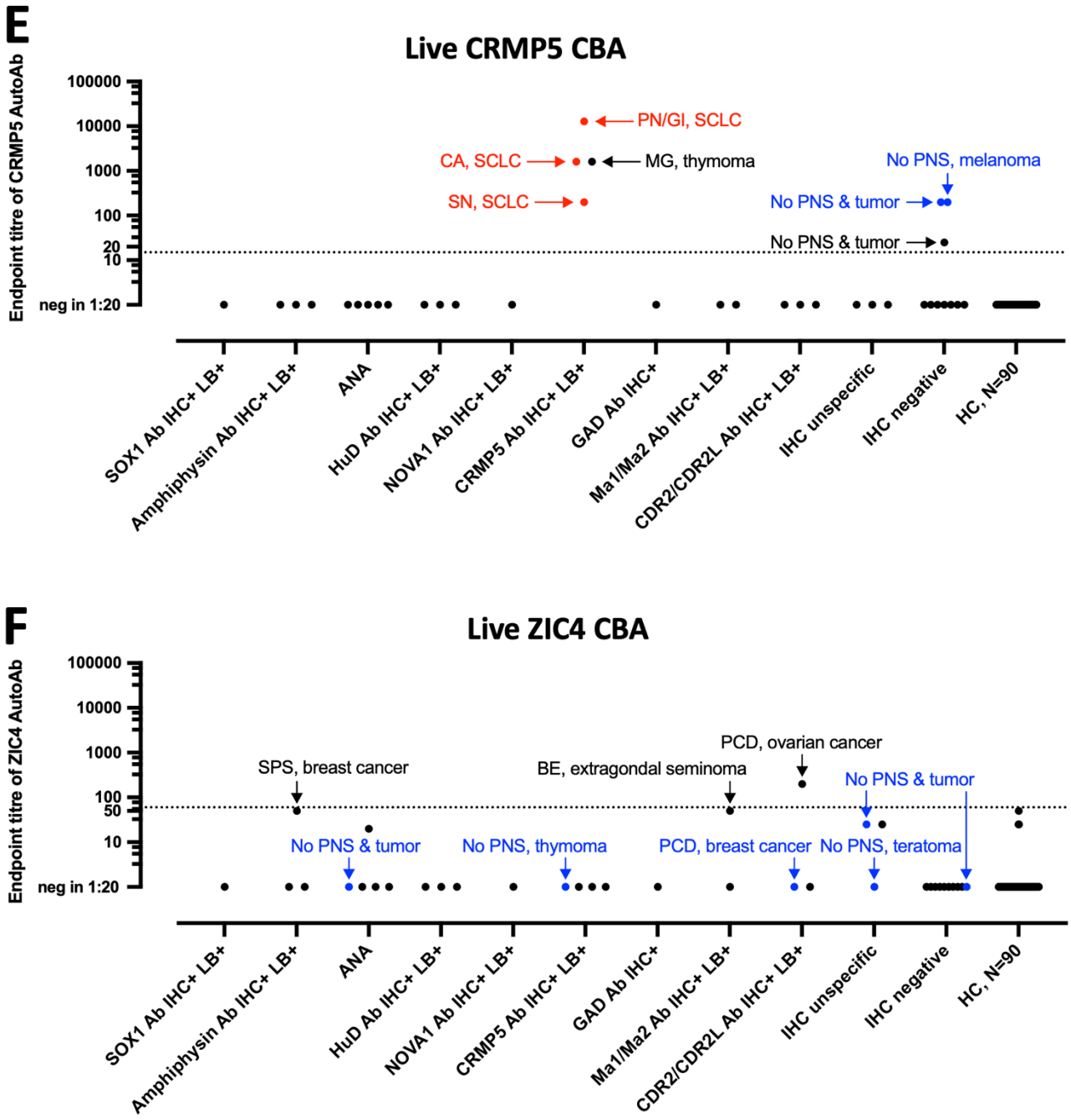


Figure 4.10: The results of eGFP-tagged live CBAs for detecting onconeural autoantibodies in Barcelona samples. (a-g) The 36 Barcelona serum samples and 90 healthy sera were screened by our eGFP-tagged live CBAs to detect autoantibodies to (a) HuD, (b) NOVA1, (c) CDR2L, (d) Amphiphysin, (e) CRMP5 and (f) ZIC4. The endpoint titres from individual live CBAs were plotted on the y-axis, and the sample cohorts were mentioned below the x-axis. The red dots indicated the samples were from patients diagnosed with high/intermediate-risk PNS, tumours and the corresponding autoantibodies identified by fixed IHC and line blots. The blue dots indicated the samples were identified seropositive for the autoantibodies, which we were screening, by line blots only. Among the live CBA+ or LB+ only samples, the

diagnoses of patients' PNS and tumours were mentioned as the arrow indicated. The cut-offs of individual live CBAs were as the dotted black lines. *Abbreviations: BE, brainstem encephalitis; CA, cerebellar ataxia; GI, gait instability; IPO, intestinal pseudo-obstruction; LE, limbic encephalitis; MG, myasthenia gravis (non-classical PNS); NSCLC, non-small cell lung cancer; PCD, paraneoplastic cerebellar degeneration; PN, peripheral neuropathy; PNS, paraneoplastic neurological syndrome; SCLC, small cell lung cancer; SN, sensory neuropathy; SPS, stiff-person syndrome.*

Table 4.5: Summary of the Barcelona samples picked up by eGFP-tagged live HuD, NOVA1, CDR2L, Amphiphysin and CRMP5 CBAs

	Live HuD CBA	**Live NOVA1 CBA**	**Live CDR2L CBA**	**Live Amphiphy -sin CBA**	**Live CRMP5 CBA**
SOX1 Ab IHC+ LB+, N=1	0/1 (0%)	0/1 (0%)	0/1 (0%)	0/1 (0%)	0/1 (0%)
Amphiphysin Ab IHC+ LB+, N=3	0/3 (0%)	1/3 (33.3%)	0/3 (0%)	3/3 (100%)	0/3 (0%)
ANA, N=5	0/5 (0%)	1/5 (20%)	0/5 (0%)	0/5 (0%)	0/5 (0%)
HuD Ab IHC+ LB+, N=3	3/3 (100%)	0/3 (0%)	3/3 (100%)	0/3 (0%)	0/3 (0%)
NOVA1 Ab IHC+ LB+, N=1	0/1 (0%)	1/1 (100%)	0/1 (0%)	0/1 (0%)	0/1 (0%)
CRMP5 Ab IHC+ LB+, N=4	2/4 (50%)	2/4 (50%)	0/4 (0%)	0/4 (0%)	4/4 (100%)
GAD Ab IHC+, N=1	0/1 (0%)	0/1 (0%)	0/1 (0%)	0/1 (0%)	0/1 (0%)
Ma1/Ma2 Ab IHC+ LB+, N=2	0/2 (0%)	0/2 (0%)	0/2 (0%)	0/2 (0%)	0/2 (0%)
CDR2/CDR2L Ab IHC+ LB+, N=3	0/3 (0%)	0/3 (0%)	3/3 (100%)	0/3 (0%)	0/3 (0%)
IHC unspecific, N=3	0/3 (0%)	1/3 (33.3%)	1/3 (33.3%)	0/3 (0%)	0/3 (0%)

IHC negative, N=10	0/10 (0%)	0/10 (0%)	0/10 (0%)	0/10 (0%)	3/10 (30%)
IHC-, LB+ in the autoantibody we screened	1/2 (50%)	0/1 (0%)	1/6 (16.6%)	0/1 (0%)	2/2 (100%)
HC, N=90	0/90 (0%)	0/90 (0%)	0/90 (0%)	0/90 (0%)	0/90 (0%)

Table 4.6: The diagnostic accuracy of our live CBAs for detecting onconeural autoantibodies in Barcelona samples

	Live HuD CBA	**Live NOVA1 CBA**	**Live CDR2L CBA**	**Live Amphiphy -sin CBA**	**Live CRMP5 CBA**
Sensitivity	100% (4/4)	100% (1/1)	100% (2/2)	100% (3/3)	100% (3/3)
Specificity	98.4% (121/123)	96.0% (120/125)	98.4% (122/124)	100% (123/123)	96.7% (119/123)
PPV	60% (3/5)	16.6% (1/6)	50% (2/4)	100% (3/3)	42.9% (3/7)
NPV	100% (121/121)	100% (120/120)	100% (122/122)	100% (123/123)	100% (119/119)

Next, we correlated the endpoint titres from our live CBAs with the line blots readouts to learn if both assays agreed with one another (Figure 4.11). When detecting HuD autoantibodies, both assays agreed to pick up 4 samples, but there were 2 low positive samples picked up by either live HuD CBA or line blots (Figure 4.11a). Next, our live NOVA1 CBA and line blots agreed to pick up a sample with high titre of NOVA1 autoantibodies, but the 5 samples picked up by our live NOVA1 CBA weren't picked up by line blots (Figure 4.11b). For detecting CDR2/CDR2L autoantibodies, both assays agreed to pick up 4 samples, and our live CDR2L CBA didn't pick up 5 samples, which were picked up by line blots using fixed CDR2 antigen (Figure 4.11c). As for detecting Amphiphysin autoantibodies, both assays agreed to pick up 3 samples, and our live Amphiphysin CBA didn't pick up one sample, which had a border-line positive line blot readout (Figure 4.11d). For detecting CRMP5 autoantibodies, there were 6 samples picked up by line blots and our live CRMP5 CBA, and our live CRMP5 CBA picked up one borderline positive sample, which wasn't picked up by line blots (Figure 4.11e). Lastly, our live ZIC4 CBA didn't pick up 6 samples, which were picked up by line blots only, and our live ZIC4 CBA picked up one sample that wasn't picked up by line blots (Figure 4.11f). There was no sample picked up by both live ZIC4 CBA and line blots when detecting ZIC4 autoantibodies. To conclude, the strong positive samples were picked up by both live CBAs and line blots, and our live CBAs didn't pick up 14 samples, which had been identified seropositive by line blots only (HuD Ab+, n=1, NOVA1 Ab+, n=1; CDR2 Ab+, n=5; Amphiphysin Ab+, n=1; ZIC4 Ab+, n=6).

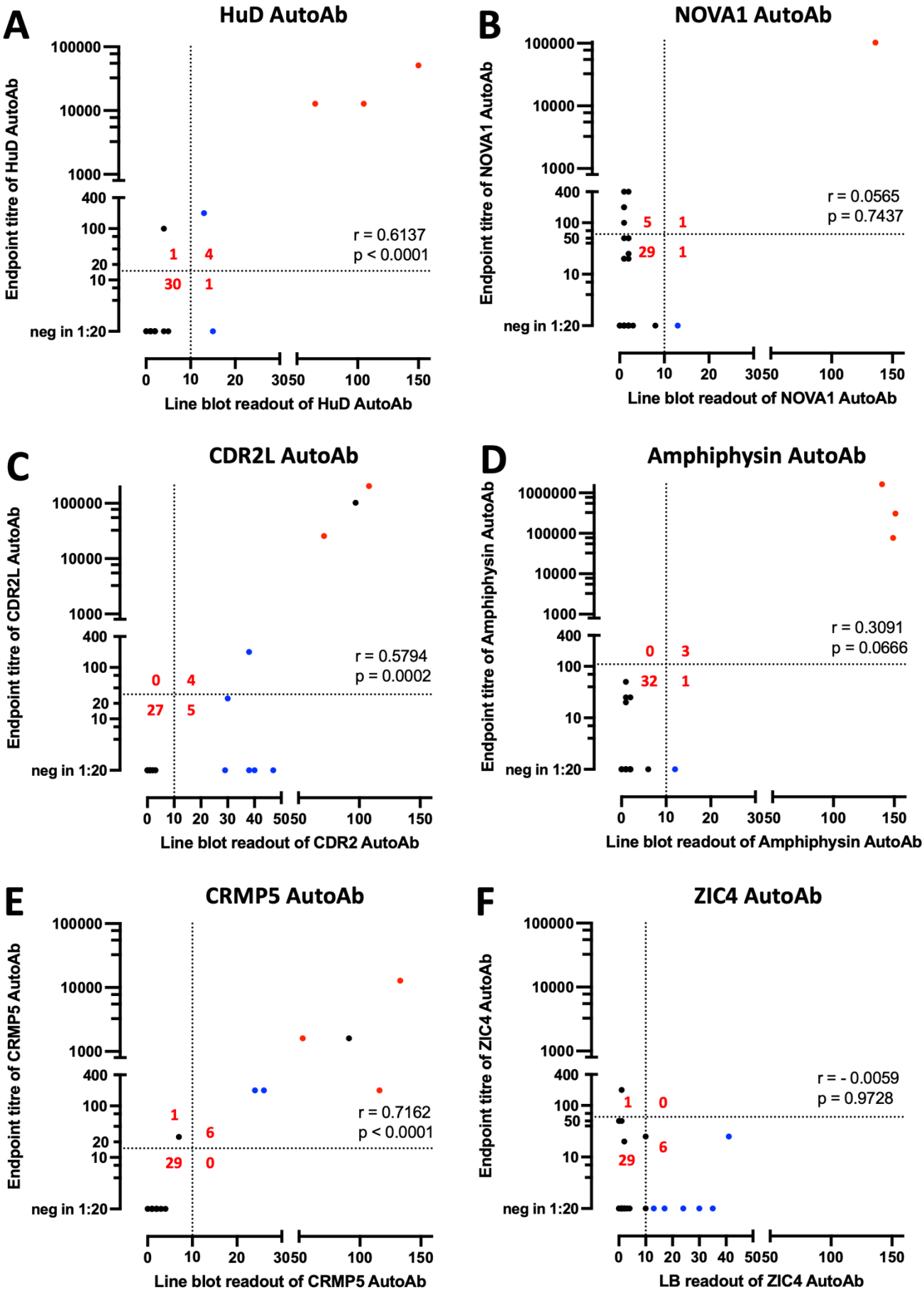

A
HuD AutoAb
Endpoint titre of HuD AutoAb
100000
10000
1000
400
100
20
10
neg in 1:20
1
4
30
1
r = 0.6137
p < 0.0001
0
10
20
3050
100
150
Line blot readout of HuD AutoAb
B
NOVA1 AutoAb
Endpoint titre of NOVA1 AutoAb
100000
10000
1000
400
100
50
10
neg in 1:20
5
1
29
1
r = 0.0565
p = 0.7437
0
10
20
3050
100
150
Line blot readout of NOVA1 AutoAb
C
CDR2L AutoAb
Endpoint titre of CDR2L AutoAb
100000
10000
1000
400
100
20
10
neg in 1:20
0
4
27
5
r = 0.5794
p = 0.0002
0
10
20
30
40
5050
100
150
Line blot readout of CDR2 AutoAb
D
Amphiphysin AutoAb
Endpoint titre of Amphiphysin AutoAb
1000000
100000
10000
1000
400
100
10
neg in 1:20
0
3
32
1
r = 0.3091
p = 0.0666
0
10
20
3050
100
150
Line blot readout of Amphiphysin AutoAb
E
CRMP5 AutoAb
Endpoint titre of CRMP5 AutoAb
100000
10000
1000
400
100
20
10
neg in 1:20
1
6
29
0
r = 0.7162
p < 0.0001
0
10
20
3050
100
150
Line blot readout of CRMP5 AutoAb
F
ZIC4 AutoAb
Endpoint titre of ZIC4 AutoAb
100000
10000
1000
400
100
50
10
neg in 1:20
1
0
29
6
r = - 0.0059
p = 0.9728
0
10
20
30
40
5050
100
150
LB readout of ZIC4 AutoAb

Figure 4.11: The correlations between the results from live CBAs and line blots. (a-f) The endpoint titres of live CBAs were plotted on the y-axis, and the line blots (LB) readout were plotted on the x-axis when screening 36 sera samples from Barcelona to detect autoantibodies to (a) HuD, (b) NOVA1, (c) CDR2L, (d) Amphiphysin, (e) CRMP5 and (f) ZIC4. The red dots indicated the samples were from patients diagnosed with high/intermediate-risk PNS, tumours and the corresponding autoantibodies identified by fixed IHC and line blots. The blue dots indicated the samples were identified seropositive for the autoantibodies, which we were screening, by line blots only. The number of samples in each quadrant was quoted in red, and the cut-offs of each assay were as the dotted black lines. The r and p-values were calculated via Spearman nonparametric correlation test.

4.5.3. Live CBA results: Mayo Clinic cohort

The 33 serum samples and 21 CSF samples from Mayo Clinic and 90 healthy sera were screened by our eGFP-tagged live CBAs for detecting autoantibodies to HuD, NOVA1, CDR2L, Amphiphysin, CRMP5 and ZIC4. The endpoint titres of individual live CBAs were plotted as Figure 4.12.

When detecting HuD autoantibodies, 14/141 samples were picked up as HuD Ab CBA+ (Figure 4.12a). 12/14 HuD Ab CBA+ samples were also identified seropositive by fixed IHC and line blots, and 2/14 HuD Ab CBA+ samples were SOX1 Ab+ identified by fixed IHC and line blots. According to the limited clinical details, a HuD Ab CBA+ sample was from a patient diagnosed with neuropathy and SCLC, and a SOX1 Ab IHC+ sample was from a patient diagnosed with SCLC.

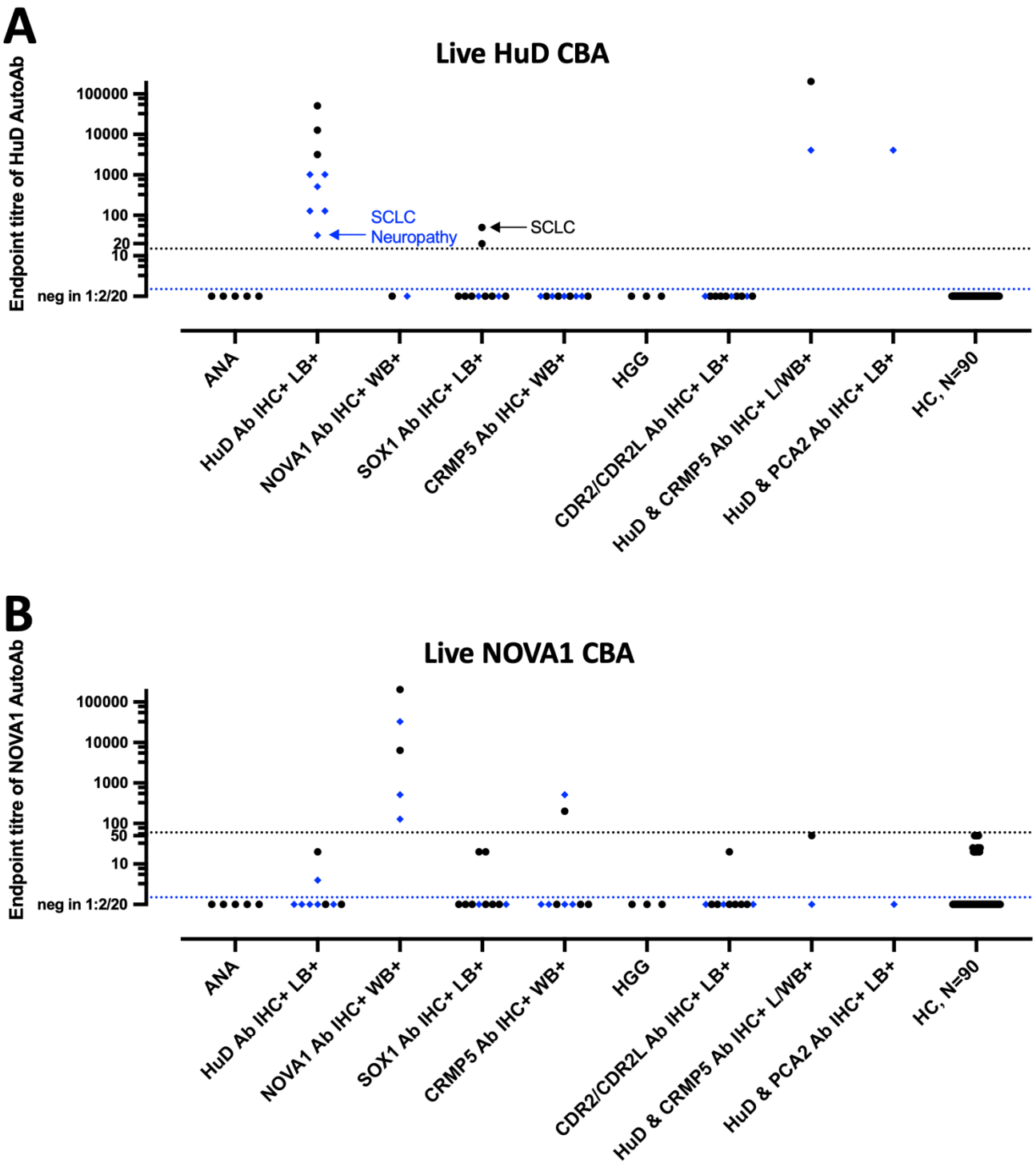
When detecting NOVA1 autoantibodies, 8/144 samples were picked up as NOVA1 Ab CBA+ (Figure 4.12b). 5/8 NOVA1 Ab CBA+ samples were also identified seropositive by fixed IHC and western blots. 2/8 and 1/8 NOVA1 Ab CBA+ samples were identified seropositive for autoantibodies to CRMP5 and HuD respectively by fixed IHC and line/western blots. Our live NOVA1 CBA still tended to pick up the samples with other

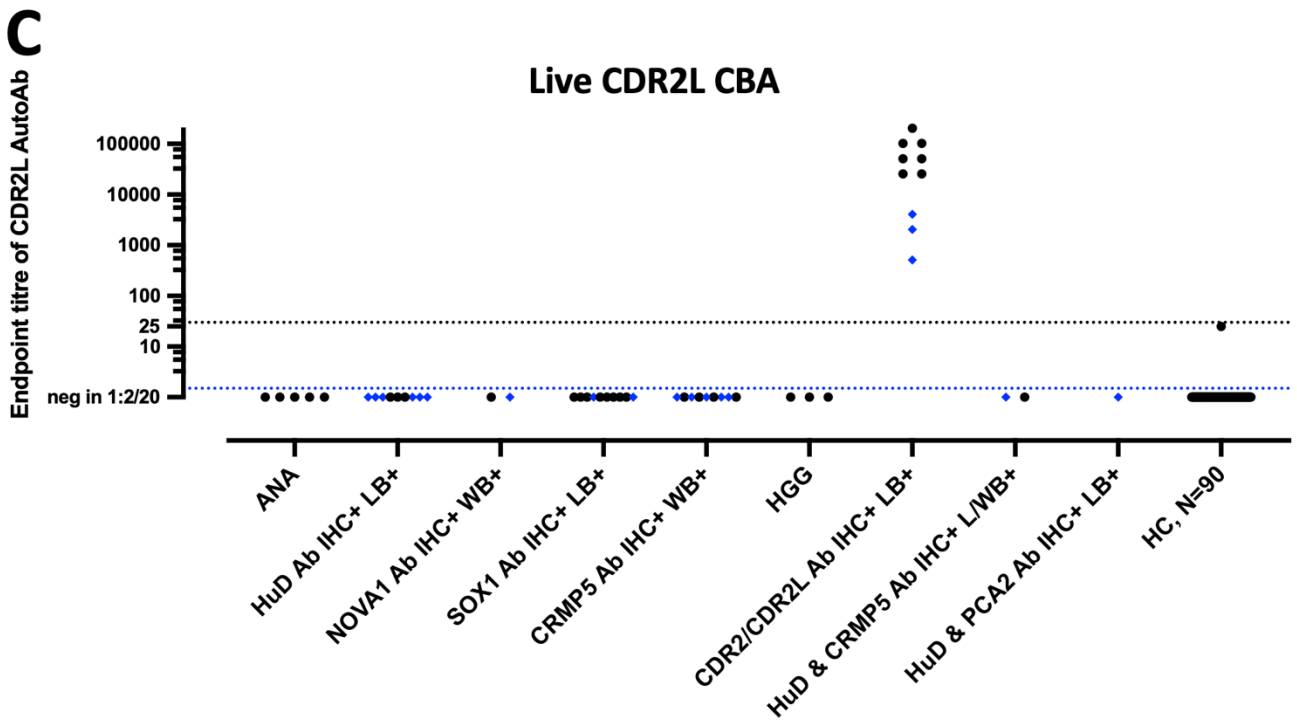
onconeural autoantibodies as we found in Barcelona screen. On the contrary, our live CDR2L CBA was a much cleaner assay, which picked up 10/141 samples as CDR2L Ab CBA+ and without picking up any sample not identified seropositive for CDR2/CDR2L Ab+ by fixed IHC and line blots (Figure 4.12c).

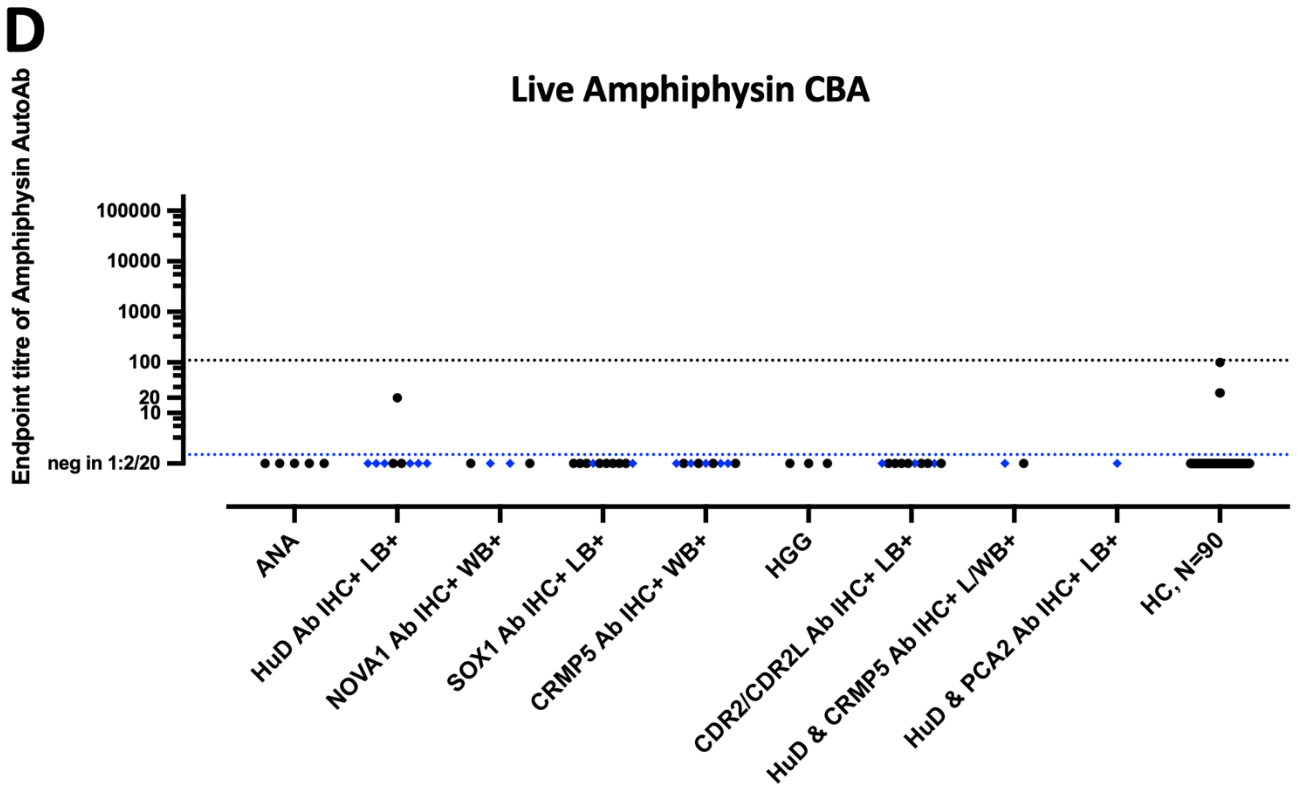
In terms of detecting Amphiphysin autoantibodies, because there was no sample from Mayo Clinic identified seropositive for Amphiphysin autoantibodies by fixed IHC and line blots, our live Amphiphysin CBA agreed with the fact and picked up nothing above the assay cut-off (Figure 4.12d). On the other hand, our live CRMP5 CBA was problematic because only 9/11 samples were picked up as CRMP5 Ab CBA+, but all the 11 CRMP5 Ab+ samples were identified seropositive by fixed IHC and western blots (Figure 4.12e). Besides, a CRMP5 Ab IHC+ WB+ sample was from a patient with SCLC but with a very low endpoint titre of CRMP5 autoantibodies equal to 25. The findings suggested there could be issues regarding epitope exposure in our live CRMP5 CBA.

Similar to Barcelona screen, our live ZIC4 CBA also picked up samples with autoantibodies to other onconeural antigens. Our live ZIC4 CBA picked up 9/141 samples as ZIC4 Ab CBA+ (Figure 4.12f). However, 5/9, 3/9 and 1/9 ZIC4 Ab CBA+ samples were identified seropositive for SOX1 Ab+, CRMP5 Ab+ and HuD & CRMP5 Ab+, respectively, by fixed IHC and line/western blots. Here, because we didn't have patients' clinical details, we couldn't judge the diagnostic accuracy of our live ZIC4 CBA.

To conclude, Table 4.7 summarizes the number of samples from Mayo Clinic picked up by individual live CBAs in each sample cohort for detecting autoantibodies to HuD, NOVA1, CDR2L, CRMP5 and ZIC4.




C
Live CDR2L CBA
Endpoint titre of CDR2L AutoAb
100000
10000
1000
100
25
10
neg in 1:2/20
ANA
HuD Ab IHC+ LB+
NOVA1 Ab IHC+ WB+
SOX1 Ab IHC+ LB+
CRMP5 Ab IHC+ WB+
HGG
CDR2/CDR2L Ab IHC+ LB+
HuD & CRMP5 Ab IHC+ L/WB+
HuD & PCA2 Ab IHC+ LB+
HC, N=90


D
Live Amphiphysin CBA
Endpoint titre of Amphiphysin AutoAb
100000
10000
1000
100
20
10
neg in 1:2/20
ANA
HuD Ab IHC+ LB+
NOVA1 Ab IHC+ WB+
SOX1 Ab IHC+ LB+
CRMP5 Ab IHC+ WB+
HGG
CDR2/CDR2L Ab IHC+ LB+
HuD & CRMP5 Ab IHC+ L/WB+
HuD & PCA2 Ab IHC+ LB+
HC, N=90

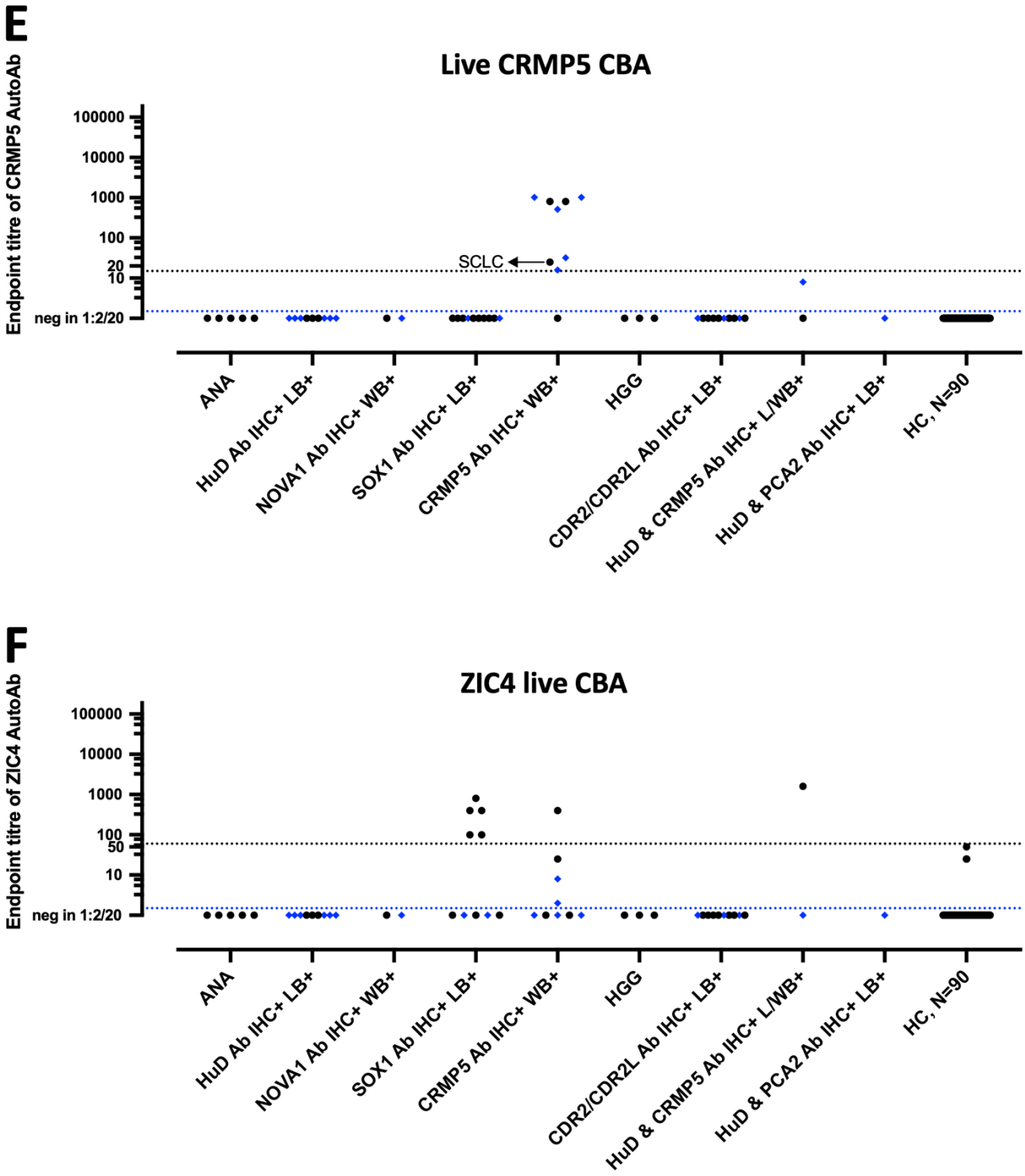


Figure 4.12: The results of live CBAs to detect onconeural autoantibodies in Mayo Clinic samples. (a-f) The 54 serum and CSF samples from Mayo Clinic and 90 healthy sera were screened by our live CBAs to detect autoantibodies to (a) HuD, (b) NOVA1, (c) CDR2L, (d) Amphiphysin, (e) CRMP5, (f) ZIC4. The endpoint titres from individual live CBAs were plotted on the y-axis, and the sample cohorts were mentioned below the x-axis. The black dots were the serum samples, and the blue diamonds were the CSF samples. The cut-offs of serum and CSF samples for each

assay were as the dotted black and dotted blue lines respectively. Abbreviation: ANA: anti-nuclear antibodies; *HGG: hypogammaglobulinemia. L/WB: line/western blots.*

Table 4.7: Summary of the Mayo Clinic samples picked up by eGFP-tagged live HuD, NOVA1, CDR2L, CRMP5 and ZIC4 CBAs

	Live HuD CBA	**Live NOVA1 CBA**	**Live CDR2L CBA**	**Live CRMP5 CBA**	**Live ZIC4 CBA**
ANA, N=5	0/5 (0%)	0/5 (0%)	0/5 (0%)	0/5 (0%)	0/5 (0%)
HuD Ab IHC+ LB+, N=9	9/9 (100%)	0/9 (0%)	0/9 (0%)	0/9 (0%)	0/9 (0%)
NOVA1 Ab IHC+ WB+, N=2-5	0/2 (0%)	5/5 (100%)	0/2 (0%)	0/2 (0%)	0/2 (0%)
SOX1 Ab IHC+ LB+, N=10	2/10 (20%)	0/10 (0%)	0/10 (0%)	0/10 (0%)	5/10 (50%)
CRMP5 Ab IHC+ WB+, N=9	0/9 (0%)	2/9 (22.2%)	0/9 (0%)	8/9 (88.9%)	3/9 (33.3%)
HGG, N=3	0/3 (0%)	0/3 (0%)	0/3 (0%)	0/3 (0%)	0/3 (0%)
CDR2/CDR2L Ab IHC+ LB+, N=10	0/10 (0%)	0/10 (0%)	10/10 (100%)	0/10 (0%)	0/10 (0%)
HuD & CRMP5 Ab IHC+ L/WB+, N=2	2/2 (100%)	0/2 (0%)	0/2 (0%)	1/2 (50%)	1/2 (50%)
HuD & PCA2 Ab IHC+ LB+, N=1	1/1 (100%)	0/1 (0%)	0/1 (0%)	0/1 (0%)	0/1 (0%)
HC, N=90	0/90 (0%)	0/90 (0%)	0/90 (0%)	0/90 (0%)	0/90 (0%)

Next, the endpoint titres from our live CBAs were correlated with the endpoint titres of IIF to understand if both assays agreed with one another (Figure 4.13). When detecting autoantibodies to HuD, NOVA1 and CDR2L, both assays correlated well with each other (p-value < 0.05) (Figure 4.13a-c). However, both assays correlated poorly (p-value = 0.85) to detect CRMP5 autoantibodies (Figure 4.13d). Because the experimental nature of IIF allowed CRMP5 autoantibodies access to intracellular CRMP5, the problem may fall to our side, i.e., the design of our CRMP5 construct might hinder the major CRMP5 epitopes. We would further discuss and investigate in this issue as a case study in Chapter V.

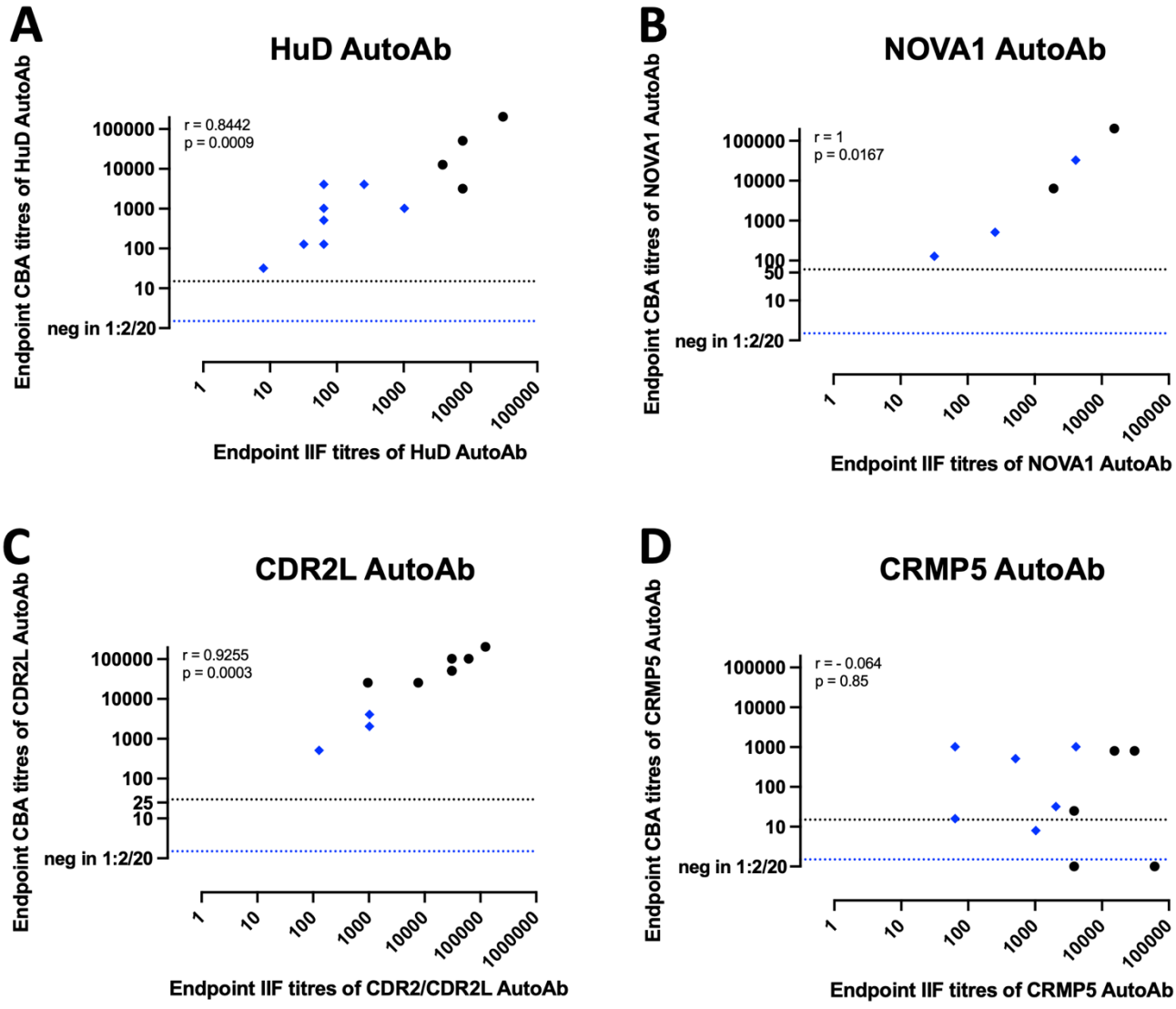


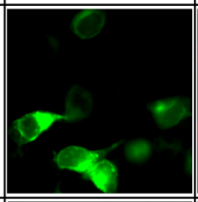
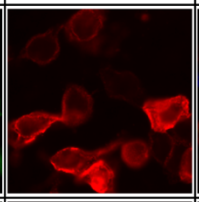
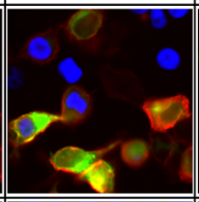
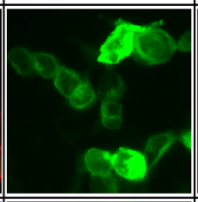
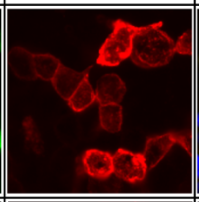
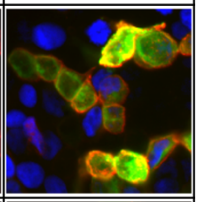
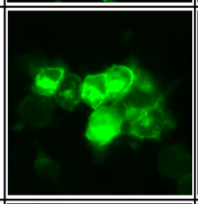
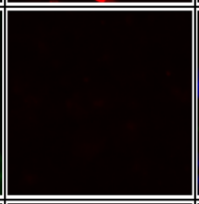
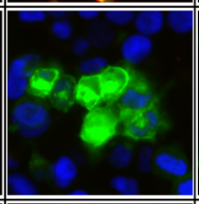
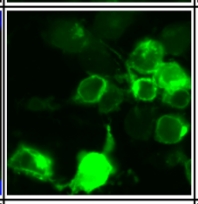
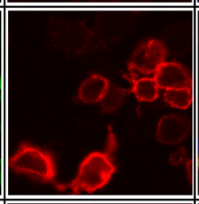
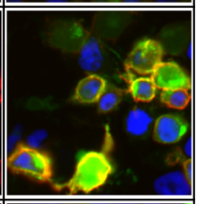
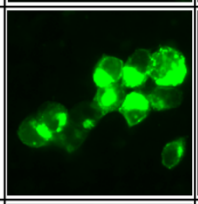
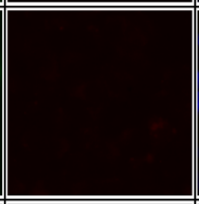
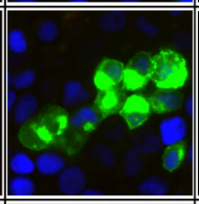
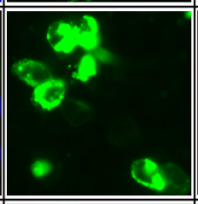
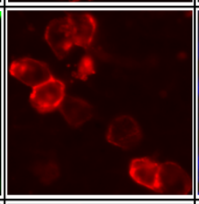
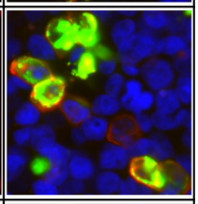
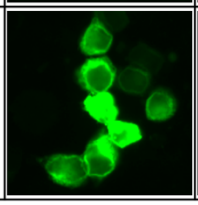
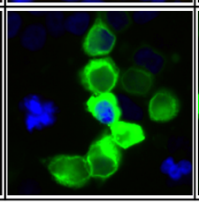
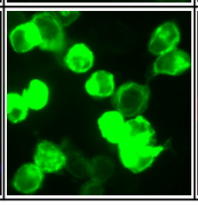
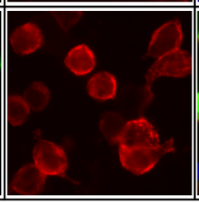
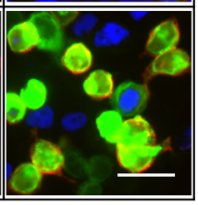
Figure 4.13: The correlations between the endpoint titres of live CBAs and IIFs from Mayo Clinic samples. (a-d) The CSF and serum samples with onconeural autoantibodies were screened by live CBAs and IIFs to detect autoantibodies to (a) HuD, (b) NOVA1, (c) CDR2L and (d) CRMP5. The endpoint titres of live CBAs and IIFs were plotted on the y-axis and x-axis respectively. The serum samples were as black dots, and the CSF samples were as blue diamonds. The cut-offs of serum and CSF samples for each assay were as the dotted black and dotted blue lines respectively. The r and p-values were calculated via Spearman nonparametric correlation test.

So far, we have established eGFP-tagged live and permeabilized CBA to detect our targeted onconeural autoantibodies, and we have screened two international cohorts via our live CBAs to demonstrate the utility of our assays. Now, we would like to establish a multiplex antibody detection platform for reducing assay time and manual errors when testing one sample in multiple wells.

4.5.4. The eGFP-tagged quadruplex live CBA to detect autoantibodies to HuD, NOVA1, CDR2L and CRMP5 simultaneously

As a pilot multiplex assay to detect onconeural autoantibodies, we accommodated the live HEK cells surface expressing HuD, NOVA1, CDR2L and CRMP5 at four different corners on a single coverslip (Figure 4.3.). Due to spatial separation, commercial antibodies to human HuD only recognized the area expressing HuD antigens (Figure 4.14a). This demonstrated the specificity of our quadruplex live CBA. In addition, the specific bindings were also demonstrated by incubating our quadruplex coverslip with the sera with known autoantibodies from a patient and a healthy doner (Figure 4.14b).

A

Quadraplex Live CBA Target	HuD Commercial Antibody, 1:100 dilution			HuD/NOVA1/CDR2L/CRMP5 Commercial Antibodies, 1:100 dilution		
	eGFP	Commercial polyclonal Ab	merge + DAPI	eGFP	Commercial polyclonal Ab	merge + DAPI
HuD AutoAb						
NOVA1 AutoAb						
CDR2L AutoAb						
CRMP5 AutoAb						

B

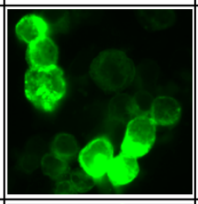
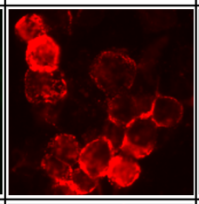
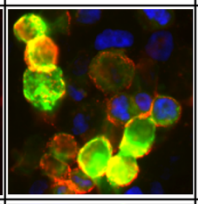
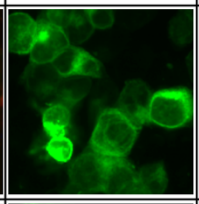
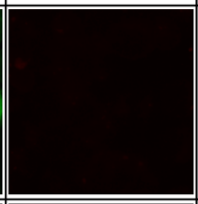
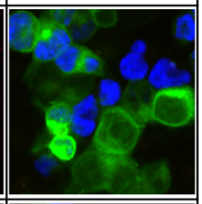
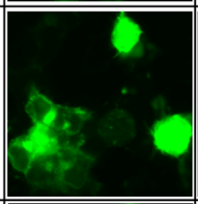
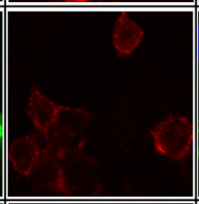
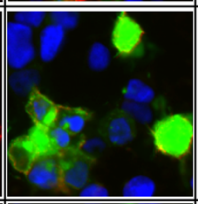
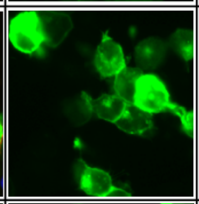
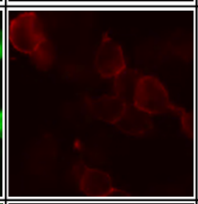
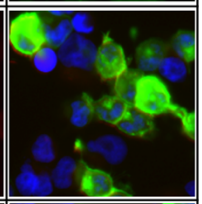
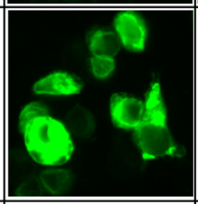
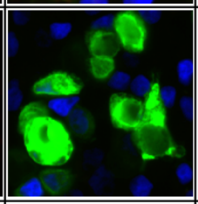
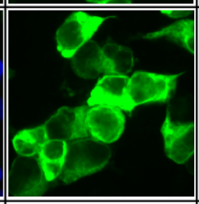
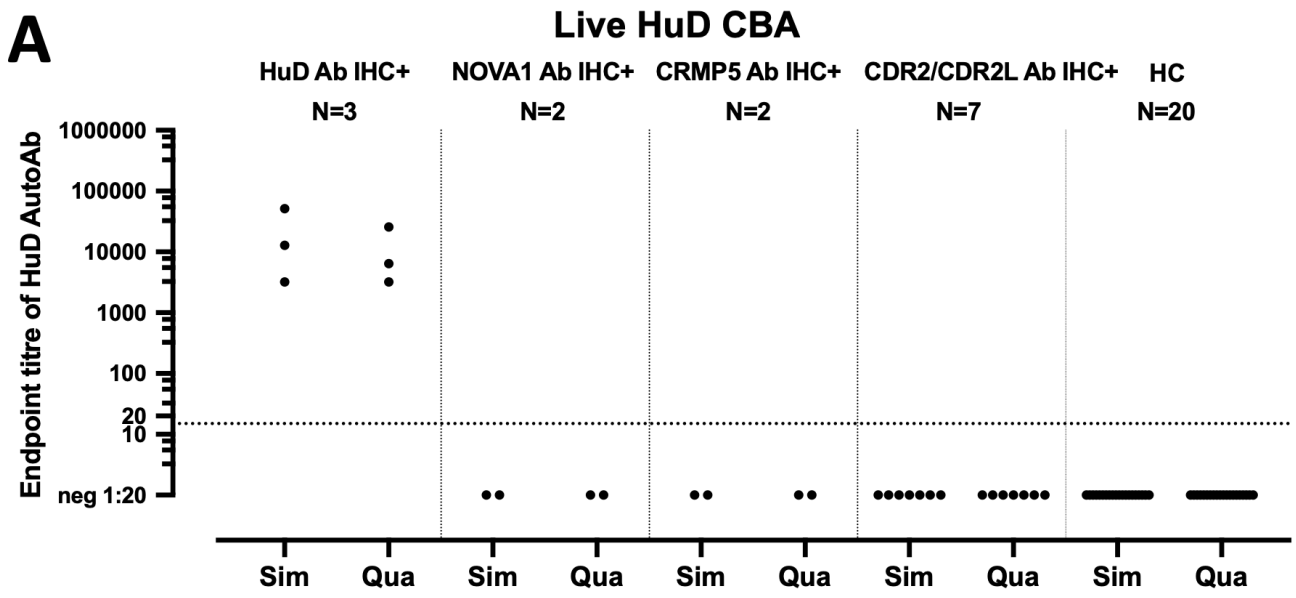
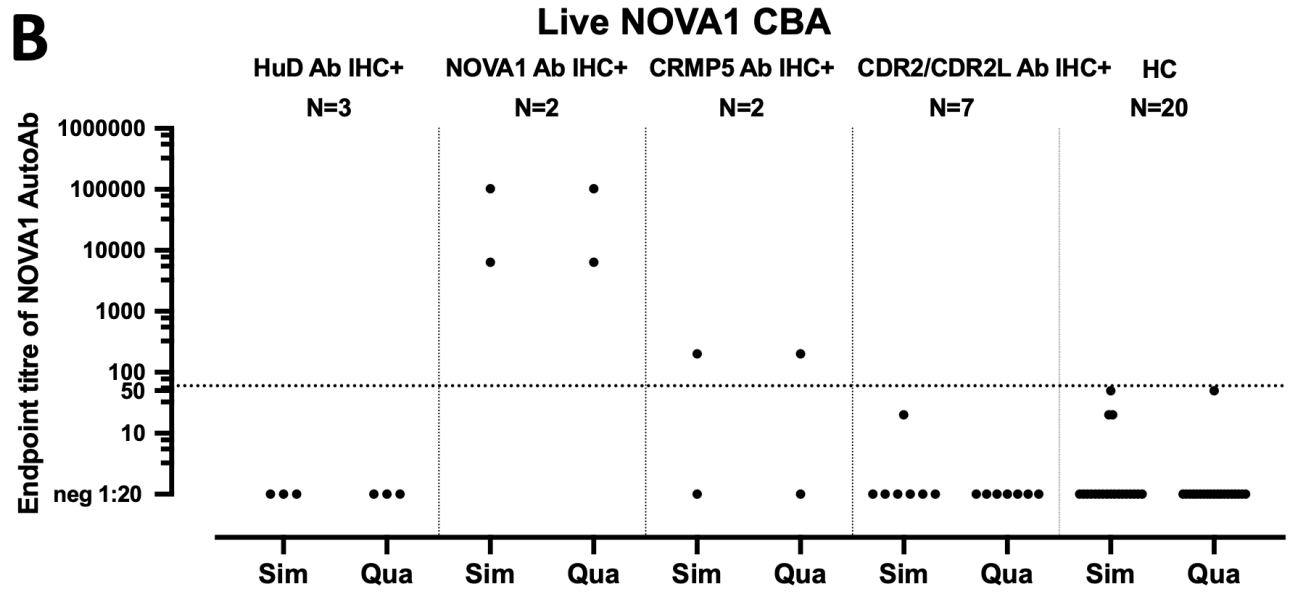
Quadraplex Live CBA Target	Patient serum with HuD Ab (endpoint titre = 204800) and NOVA1 Ab (endpoint titre = 100), 1:100 dilution			Healthy serum with NOVA1 Ab (endpoint titre = 50), 1:50 dilution		
	eGFP	human AutoAb	merge + DAPI	eGFP	human AutoAb	merge + DAPI
HuD AutoAb						
NOVA1 AutoAb						
CRMP5 AutoAb						
CDR2L AutoAb						

Figure 4.14: The eGFP-tagged quadruplex live CBA for detecting autoantibodies to HuD, NOVA1, CDR2L and CRMP5 simultaneously. (a) The commercial polyclonal antibodies to HuD, NOVA1, CDR2L and CRMP5 were applied at 1:100 dilution to verify the surface expression of each onconeural antigen on a single coverslip. The eGFP signal was in green, the secondary antibody binding was in red, and the nuclei labelled by DAPI were in blue. Magnification x 400. Scale bar = 25 μm. (b) The patient and healthy sera with known onconeural autoantibodies were screened by our eGFP-tagged quadruplex live CBA. The eGFP signal was in green, the secondary antibody binding was in red, and the nuclei labelled by DAPI were in blue. Magnification x 400. Scale bar = 25 μm.

Moreover, we validated the fidelity of our quadruplex live CBA by screening 14 Mayo Clinic samples and 20 healthy sera alongside our individual simplex live CBAs, following 24-well plate CBA protocol, for detecting autoantibodies to HuD, NOVA1, CDR2L and CRMP5. As Figure 4.15, every sample picked up by simplex live CBAs was also picked up by quadruplex live CBA with presenting comparable endpoint titres. Also, there was no statistical difference between the endpoint titres of CDR2L autoantibodies generated by simplex live CDR2L CBA and quadruplex live CBA (Figure 4.15c). In summary, our quadruplex live CBA worked nicely to increase assay efficiency and generate reproducible data when detecting onconeural autoantibodies in patients' serum samples.


A
Live HuD CBA
HuD Ab IHC+
N=3
NOVA1 Ab IHC+
N=2
CRMP5 Ab IHC+
N=2
CDR2/CDR2L Ab IHC+
N=7
HC
N=20
Endpoint titre of HuD AutoAb
1000000
100000
10000
1000
100
20
10
neg 1:20
Sim
Qua


B
Live NOVA1 CBA
HuD Ab IHC+
N=3
NOVA1 Ab IHC+
N=2
CRMP5 Ab IHC+
N=2
CDR2/CDR2L Ab IHC+
N=7
HC
N=20
Endpoint titre of NOVA1 AutoAb
1000000
100000
10000
1000
100
50
10
neg 1:20
Sim
Qua

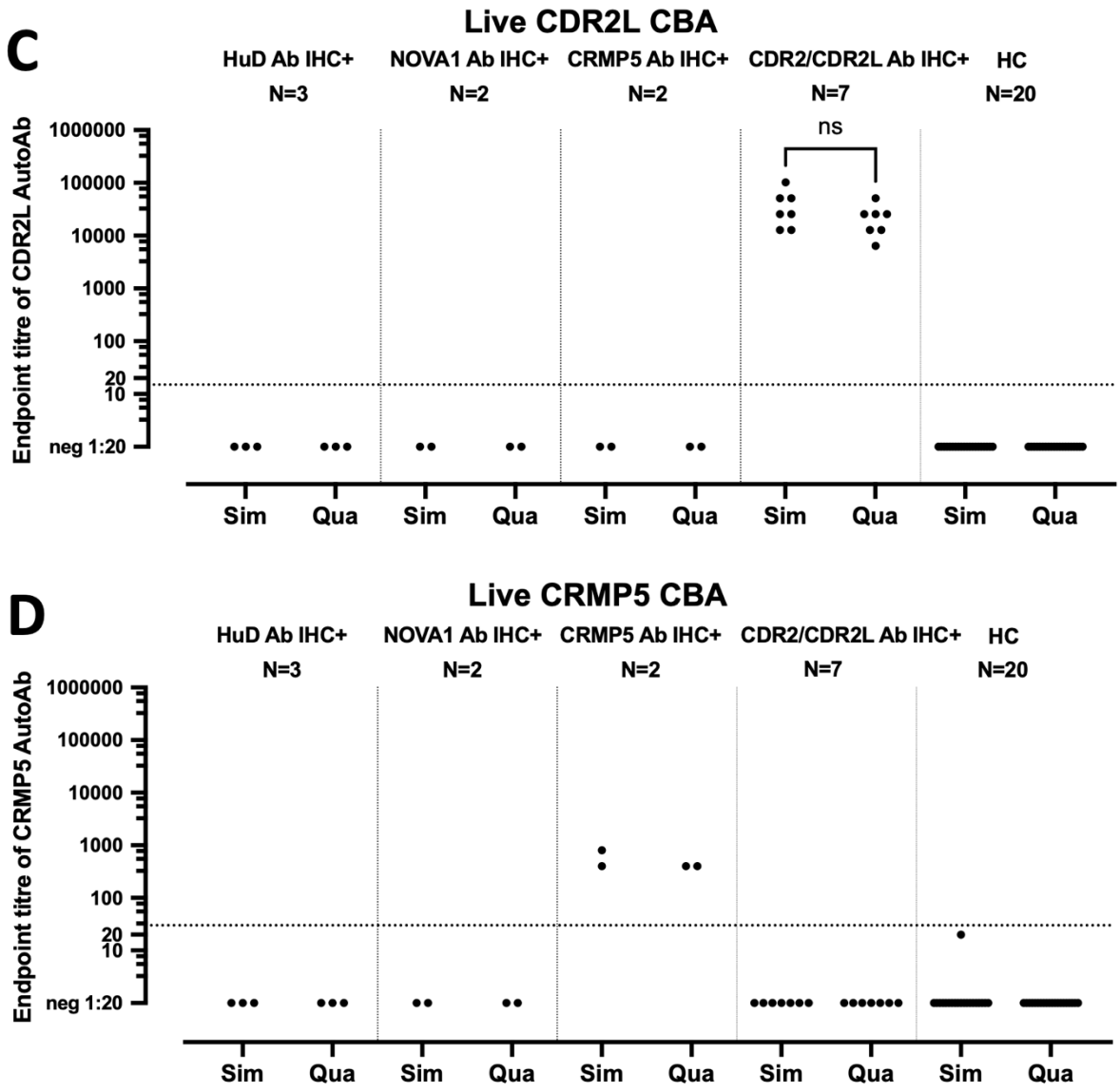


Figure 4.15: The quadruplex live CBA generated comparable endpoint titres compared to individual simplex live CBAs. (a-d) The endpoint titres of autoantibodies to (a) HuD, (b) NOVA1, (c) CDR2L and (d) CRMP5, measured by individual simplex live CBAs (Sim, 24-well plate CBA protocol) and quadruplex live CBA (Qua, 24-well plate CBA protocol), were plotted on the y-axis. The sample cohorts and sizes were mentioned above each column. The statistical difference was evaluated by nonparametric Wilcoxon test. The cut-offs were as the dotted black lines.

4.6. Discussion

To date, we have developed eGFP-tagged live CBAs to detect autoantibodies to HuD, NOVA1, NOVA2, CDR2L, Amphiphysin, CRMP5 and ZIC4, and eGFP-tagged permeabilized CBAs to detect autoantibodies to Ma1, Ma2, CDR2, SOX1 and KLHL11. We have also successfully developed a dot-transfected quadruplex live CBA method to detect autoantibodies to HuD, NOVA1, CDR2L and CRMP5 simultaneously on a single coverslip. The results of our CBAs agreed with all the IHC+ results, apart from not picking up 2 CRMP5 Ab+ serum samples identified seropositive by fixed IHC and western blots. This suggests our CRMP5 antigen was not expressing well on the cell surface. A past study reported the CRMP5 autoantibodies in two CSF samples recognized the C-terminal domain of CRMP5 (O'Donovan et al., 2020). Hence, the possible reason could be our C-terminal tethering cloning strategy hindered the access of autoantibodies to CRMP5 epitopes. There would be a case study in Chapter V describing how we improved CRMP5 assay with using the quantitative methodology of flow cytometry CBA (F-CBA).

As Table 4.5 summarized, our live CBAs picked up all the serum samples reported seropositive for the corresponding autoantibodies by fixed IHC and line blots, and our live CBAs didn't pick up 8/12 serum samples, which had been identified seropositive by line blots only (HuD Ab+, n=1, NOVA1 Ab+, n=1; CDR2 Ab+, n=5; Amphiphysin Ab+, n=1), from patients without high-risk PNS and tumours. Although our live CBAs showed comparable diagnostic accuracy to the fixed IHC for detecting onconeural autoantibodies, our live CBA was unfixed before sample incubation, which allowed native epitopes being recognized by the corresponding autoantibodies. Furthermore, we demonstrated our live CBAs were multiplexable on a single coverslip to detect

autoantibodies to HuD, NOVA1, CDR2L and CRMP5 simultaneously. This may prove superior to IHC for detection of multiple autoantibodies because the IHC patterns of cerebellar staining were similar, especially when comparing between HuD Ab+ and NOVA1 Ab+ samples (Greenlee et al., 2014). In Chapter V, a flow cytometry-based multiplex method would be introduced and demonstrated how to detect up to 8 different autoantibodies at once within the same well of 96-well plate.

Practically, the detection of autoantibodies to Hu, Ri, Yo, Ma, CRMP5, Amphiphysin, SOX1 and KLHL11 have been covered by our eGFP-tagged CBA platform. Regarding of Yo antigens, CDR2L was reported as the optimal antigen for diagnostic assays because Yo autoantibodies from PCD patients bound endogenous CDR2L but not endogenous CDR2 in CNS neurons (Krakenes et al., 2019). In addition, CDR2L but not CDR2 were found overexpressed in the ovarian tumours from PCD patients (Small et al., 2018). In our live CBA platform, CDR2L was not only successfully expressed above the cell membrane but also a better alternative to replace CDR2 attributed to the recommendations from the past studies.

Regarding Ma antigens, the patients diagnosed with Ma2 autoantibodies only are more likely to be subsequently found with testicular tumour or seminoma compared to the patients diagnosed with autoantibodies to both Ma1 and Ma2 (Hoffmann et al., 2008, Rosenfeld et al., 2001). However, the 2 Ma1 and Ma2 Ab+ serum samples, identified seropositive by line blots, fixed IHC and our permeabilized CBAs, were from patients diagnosed with seminoma and PNS. Hence, it would be good to increase the sample size of patients with autoantibodies to Ma1 and Ma2 before drawing any clinical conclusion. Similar to Ma2 autoantibodies, KLHL11 autoantibodies are also highly

associated with testicular tumour, but patients with KLHL11 autoantibodies are usually diagnosed with the distinct symptoms such as ataxia, vertigo, hearing loss and tinnitus under the umbrella of rhombencephalitis (Dubey et al., 2020). Although we proved that the permeabilized KLHL11 CBA worked by using commercial antibodies, we had no positive patient CSF or serum sample to validate its capability of binding patients' KLHL11 autoantibodies. In this chapter, our live CBAs demonstrate good fidelity with fixed IHC and more specific than commercial line blots to predict the corresponding tumours in PNS patients from Barcelona cohort. However, due to the limited clinical details in Mayo Clinic cohort, we couldn't make further conclusion if the 2 CRMP5 Ab IHC+ LB+ samples missed by our live CRMP5 CBA were false positive. More patient samples with sufficient clinical details will be required to validate our paraneoplastic CBA panel.

Chapter V

Flow cytometry cell-based assays to detect autoantibodies

5.1. Introduction

Flow cytometry is a well-developed quantitative technology to perform cellular phenotyping, cell cycle tracking, viability measurement, functional analysis and antibody detection (Saggau et al., 2021, Merkel et al., 2019, Lieschke et al., 2022, Amatoury et al., 2013, Schmid et al., 2007). To date, live flow cytometry CBA (F-CBA) has been applied to detect autoantibodies to AQP4 M1/M23 and MOG α1 isoforms in the sera from patients with autoimmune-mediated demyelinating diseases (Sugimoto et al., 2019, Lopez et al., 2022, Waters et al., 2016). In two multicenter studies, F-CBA was proven with higher sensitivity and comparable specificity to detect AQP4 M23 autoantibodies compared to in-house live CBA, commercial fixed CBA and tissue-based IIFs and ELISA (Waters et al., 2016, Waters et al., 2012). Besides, using anti-human IgG1 but not anti-human IgG (H+L) as the secondary antibody was shown to improve the assay specificity when detecting MOG α1 autoantibodies via F-CBA (Waters et al., 2015).

Furthermore, flow cytometry has been applied to simultaneously detect multiple antibody targets via the technology of fluorescent cell barcoding (FCB) (Krutzik et al., 2011). FCB can not only increase the assay efficiency but also minimize the pipetting error and staining variation. In the past, FCB has been achieved in several ways to quantify the bindings of multiple antibodies through flow cytometry. Krutzik et al. color-coded individual cell groups with different types and concentrations of amine-reactive dyes before combining them as a multiplex master mix (Krutzik and Nolan, 2006). On the other hand, Song et al. established the panel of fluorescence-barcoded stable cell lines expressing the fluorescent protein barcodes within the cytosol and the targeted antigens on the cell surface (Song et al., 2021). Compared to commercially matured

Luminex® technology, FCB is less costly, more in-lab manageable and flexible to be applied in F-CBA for multiplex purposes.

5.2. Research Rationales

As in Chapter IV, we had established quadruplex live CBA on a single coverslip, and the results showed consistency with our individual simplex live CBAs. Here, we would like to transfer the working knowledge from coverslip-based live CBA to F-CBA because flow cytometry has its strength to produce quantitative data and F-CBA is multiplexable with applying the concept of FCB. In addition, our multiplex live F-CBA could be a better alternative than fixed IHC due to 3 advantages. Firstly, the native epitopes are expressed above the surface of HEK cells for autoantibodies to access. Secondly, quantitative measurements rather than visual judgements allow us to generate objective results. Thirdly, because normally only the most intense IHC pattern is reported, it is likely to miss some weak binding autoantibodies when screening the samples with fixed IHC alone. Especially, the IHC patterns of HuD Ab+ and NOVA1 Ab+ samples are very similar. Inspired by Krutzik et al.'s method, the development of multiplex F-CBAs for detecting autoantibodies to onconeural antigens, AQP4 M23 or MOG α1 isoforms is described in this chapter.

5.3. Study Aims

1. Develop eGFP-tagged live and permeabilized F-CBAs to detect onconeural autoantibodies in the samples from patients with or without PNS and tumour
2. Optimise the multiplex method to detect multiple autoantibodies simultaneously via F-CBA
3. Apply the multiplex method to perform quadruplex live and permeabilized F-CBAs for detecting onconeural autoantibodies
4. Establish DsRed2-reporiting live F-CBA for detecting autoantibodies to AQP4 M23 and MOG α1 isoforms

5.4. Methods

5.4.1. Samples

For assessing our F-CBAs, the remaining 27 Barcelona serum samples, and the remaining 16 CSF and 33 serum samples from Mayo Clinic were used. Table 5.1 summarizes the details of the remaining samples from two international cohorts. An additional 20 sera samples were obtained from OUH Clinical Immunology Unit with HuD autoantibodies identified seropositive for HuD autoantibodies by indirect immunofluorescence and commercial line blots. However, there was no information suggested if those 20 samples were seropositive for other onconeural autoantibodies. On the other hand, we obtained 30 AQP4 M23 CBA+ sera, 26 MOG α1 CBA+ sera and 34 double negative serum samples from NMO and MOGAD Diagnostic Service. The AQP4 M23 Ab+ and MOG α1 Ab+ samples were determined as positive using the routine diagnostic CBA methods run in the Oxford Autoimmune Neurology Diagnostic Laboratory (method summarized in Table 5.2). Besides, 50 healthy sera were screen by our F-CBAs to set the cut-offs.

Table 5.1: Summary of the remaining samples from Barcelona and Mayo Clinic

	Barcelona Cohort	**Mayo Clinic Cohort**
Sample size	Sera sample, N=27	Sera sample, N=33 CSF samples N=16
Serological profile	**Double identified seropositive by line blots and fixed IHC, N=10** CDR2/CDR2L Ab+, N=3 SOX1 Ab+, N=1 HuD Ab+, N=2 Ma1/Ma2 Ab+, N=1 CRMP5 Ab+, N=1 Amphiphysin Ab+, N=2 **Identified seropositive by line blots only, N=17** CDR2 Ab+, N=3 SOX1 Ab+, N=4 (2 with ANA) HuD Ab+ N=1 (GAD Ab IHC+) NOVA1 Ab+, N=1 Ma2 Ab+, N=1 (with ANA) CRMP5 Ab+, N=2 Amphiphysin Ab+, N=1 ZIC4 Ab+, N=3 (2 with ANA) CDR2&ZIC4 Ab+, N=1	**Double identified seropositive by fixed IHC and line blots (or western blots), N=41** CDR2/CDR2L Ab+, N=10 SOX1 Ab+, N=10 HuD Ab+, N=8 NOVA1 Ab+, N=4 CRMP5 Ab+, N=7 HuD&PCA2 Ab+, N=1 HuD&CRMP5 Ab+, N=1 **Samples with ANA, N=5** **Samples from patients with hypogammaglobulinemia (HGG), N=3**
Clinical details	Samples from patients, • With PNS and tumour, N=8 • With PNS only, N=1 • With tumour only, N=4 • Without PNS and tumour, N=14 To note, PNS here means high or intermediate-risk PNS.	Not provided
Demographic details	Not provided	Not provided

Table 5.2: The diagnostic methods for detecting autoantibodies to AQP4 M23 and MOG α1 isoforms

	Live AQP4 M23 CBA	**Live MOG α1 CBA**
Substrate	Untagged AQP4 M23 isoform	Untagged MOG α1 isoform
First screen	• Sera dilution: 1:20 • Secondary antibody: AF568 goat anti-human IgG (H+L) (A21090, Invitrogen), 1:750 dilution	• Sera dilution: 1:20 • Secondary antibody: AF488 mouse anti-human IgG1 (A10631, Invitrogen), 1:750 dilution
Repeat screen (if first screen shows any signal)	• Sera endpoint titrated from 1:20 • Secondary antibody: Goat anti-human IgG Fc (31125, Invitrogen), 1:750 dilution • Tertiary antibody: AF568 donkey anti-goat IgG (H+L) (A11057, Invitrogen), 1:750 dilution	• Sera endpoint titrated from 1:20 • Secondary antibody: AF568 goat anti-human IgG (H+L), (A21090, Invitrogen), 1:750 dilution
Consider positive if (fulfilling all)	1. 1:20 H+L CBA visual score ≥ 0.5 2. 1:20 Fc CBA visual score ≥ 1	1. 1:20 IgG1 CBA visual score ≥ 1 2. H+L CBA endpoint titre ≥ 200

5.4.2. Construct design

The eGFP-tagged constructs cloned with onconeural antigens were described in chapter IV. The eGFP-tagged CRMP5 construct was modified by introducing a TAA stop codon before the cDNA of CRMP5 allowing native CRMP5 to be secreted extracellularly. Subsequently, the Caspr2 signal sequence before the cDNA of CRMP5 was removed to make the native CRMP5 expressed within the transfected HEK cells.

On the other hand, the cDNA clones of AQP4 M23 and MOG α1 isoforms were in pIRES2-DsRed2 vector where a DsRed2 gene, at the downstream of the targeted cDNA clones, was regulated by an internal ribosome entry site (IRES).

5.4.3. Flow cytometry CBA (F-CBA)

The method of simplex flow-CBA has been described in chapter II, so here the method of multiplex flow-CBA is described. In brief, each HEK293T cell population expressing individual targeted antigens was color-coded with live cell-labelling dyes before combing them as a multiplex master mix. Then, the following procedures were similar to our simplex F-CBA.

5.4.3.1. Methods for color-coding cells

For multiplex purposes, each cell population was color-coded with live cell-labelling solutions before the sample incubation in our multiplex live F-CBA, or before the fixation step in our multiplex permeabilized F-CBA. In a 15 ml Falcon tube, 10,000,000 transfected HEK cells were labelled with 10 ml working solution of each live cell-labelling dye, summarized in Table 5.3, at RT in dark for 20 minutes. Each dye was diluted in FACS buffer, consisting of 2-3% FBS and 2 mM EDTA in PBS. After labelling, the tube was centrifuged at 800 *xg* for 2 minutes to pellet the cells before aspirating the supernatant. Then, the cells were washed once with 10 mL FACS buffer before subsequent procedures.

Table 5.3: Summary of tested live cell-labelling dyes

Product Name	Company	Catalogue Number	Working Concentration
Draq-5	Thermo Scientific	62254	5 µM
WGA-AF647	Invitrogen	W32466	2.5 µg/ml
Hoechst 33342	Invitrogen	H3570	10 µM
CellTrace Violet	Invitrogen	C34557	5 µM
CellTrace Far Red	Invitrogen	C34564	1 µM

5.4.3.2. Methods for detecting multiple autoantibodies via F-CBA

Similar to simplex F-CBA, in our multiplex F-CBA, we introduced live cell-labelling dyes to color-code each cell population on the same day but before the antibody staining or fixation step. Below, the protocols of multiplex live and permeabilized F-CBAs are displayed, and Figure 5.1 illustrates the steps of our multiplex F-CBAs for detecting autoantibodies to surface-expressed and intracellular antigens, respectively.

Multiplex live F-CBA staining protocol

1. 10,000,000 transfected HEK cells were allocated into a 15 ml Falcon tube
2. The tube was centrifuged at 800 *xg* for 2 minutes to pellet the cells, and then the supernatant was aspirated
3. Of each cell group, the cells were resuspended by 10 ml of FACS buffer, containing live cell-labelling dye at ideal concentrations, and incubated in dark at RT for 20 minutes
4. Repeat step 2
5. The cells were washed once with 10 ml FACS buffer
6. Repeat step 2
7. The cells were resuspended by 10 ml of FACS buffer
8. 50,000 color-coded HEK cells per cell population per well were allocated into a 96-well conical buttom plate

9. The plate was centrifuged at 800 *xg* for 2 minutes to pellet the cells, and then the supernatant was flicked off
10. The cells were resuspended by 50 µl of blood sample (1:20 diluted sera or 1:4 diluted CSF), and incubated on ice in dark for 50 minutes
11. Repeat step 9
12. The cells were washed twice with 180 µl of FACS buffer (repeat step 9 between each wash)
13. Repeat step 9
14. The cells were resuspended by 50 µl of 1:200 diluted secondary antibody, and incubated on ice in dark for 30 minutes
15. Repeat step 9
16. The cells were washed twice with 180 µl of FACS buffer (repeat step 9 between each wash)
17. Repeat step 9
18. The cells were suspended by 80 µl of FACS buffer, containing 1:100 diluted 7-AAD viability dye
19. The cells were incubated at RT in dark for at least 10 minutes before acquired by BD LSRII

Multiplex permeabilized F-CBA staining protocol

1. 10,000,000 transfected HEK cells were allocated into a 15 ml Falcon tube
2. The tube was centrifuged at 800 *xg* for 2 minutes to pellet the cells, and then the supernatant was aspirated
3. The cells were resuspended by 10 ml of FACS buffer, containing 1:1000 diluted amine-reactive dye, and incubated in dark at RT for 20 minutes
4. Repeat step 2
5. The cells wash washed once with 10 ml of FACS buffer
6. Repeat step 2
7. The cells were resuspended by 10 ml of FACS buffer, containing live cell-labelling dye at ideal concentrations, and incubated in dark at RT for 20 minutes
8. Repeat step 2
9. The cells were washed once with 10 ml of FACS buffer
10. Repeat step 2

11. The cells were resuspended by 1.5 ml of Cyto-Fast™ Fix/Perm buffer, and incubated at RT in dark for 20 minutes
12. The tube was centrifuged at 500 *xg* for 5 minutes to pellet the cells, and then the supernatant was aspirated
13. The cells were washed once with 10 ml of 1X Cyto-Fast™ Perm/Wash buffer
14. Repeat step 12
15. The cells were resuspended by 10 ml of 10% normal serum in 1X Cyto-Fast™ Perm/Wash buffer, and incubated at RT in dark for 30 minutes
16. Repeat step 12
17. The cells were washed once with 10 ml of FACS buffer
18. Repeat step 12
19. The cells were resuspended by 10 ml of FACS buffer
20. 50,000 color-coded HEK cells per cell population per well were allocated into a 96-well conical buttom plate
21. The plate was centrifuged at 800 *xg* for 2 minutes to pellet the cells, and then the supernatant was flicked off
22. The cells were resuspended by 100 µl of blood sample (1:20 diluted sera or 1:4 diluted CSF), and incubated on ice in dark for 40 minutes
23. Repeat step 21
24. The cells were washed twice with 180 µl of FACS buffer (repeat step 21 between each wash)
25. Repeat step 21
26. The cells were resuspended by 100 µl of 1:200 diluted secondary antibody, and incubated on ice in dark for 30 minutes
27. Repeat step 21
28. The cells were washed twice with 180 µl of FACS buffer (repeat step 21 between each wash)
29. Repeat step 21
30. The cells were resuspended by 80 µl of FACS buffer before acquiring by BD LSRII

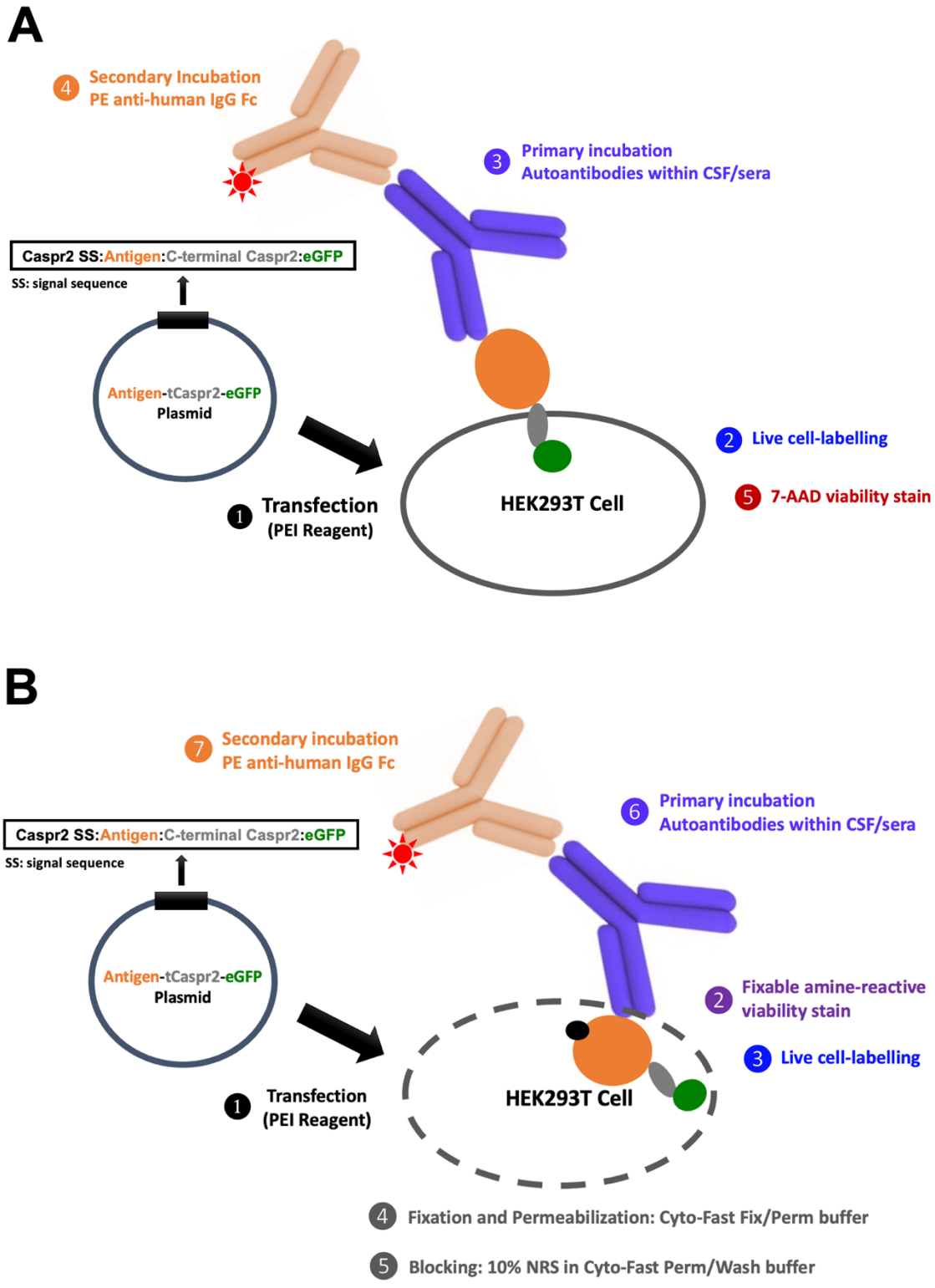

A
4 Secondary Incubation
PE anti-human IgG Fc
3 Primary incubation
Autoantibodies within CSF/sera
Caspr2 SS:Antigen:C-terminal Caspr2:eGFP
SS: signal sequence
Antigen-tCaspr2-eGFP
Plasmid
1 Transfection
(PEI Reagent)
HEK293T Cell
2 Live cell-labelling
5 7-AAD viability stain
B
7 Secondary incubation
PE anti-human IgG Fc
6 Primary incubation
Autoantibodies within CSF/sera
Caspr2 SS:Antigen:C-terminal Caspr2:eGFP
SS: signal sequence
Antigen-tCaspr2-eGFP
Plasmid
1 Transfection
(PEI Reagent)
HEK293T Cell
2 Fixable amine-reactive
viability stain
3 Live cell-labelling
4 Fixation and Permeabilization: Cyto-Fast Fix/Perm buffer
5 Blocking: 10% NRS in Cyto-Fast Perm/Wash buffer

Figure 5.1: Methods of multiplex live and permeabilized F-CBAs. (a) Multiplex live F-CBA was applied to detect multiple autoantibodies to surface-expressing antigens. One day after transfection, the cells were stained with fixable amine-reactive viability dye, then labelled with live cell-labelling dyes for multiplex purposes. Then, the cells were allocated into 96-well plates, incubated with diluted CSF/sera on ice, washed twice with FACS buffer and incubated with PE anti-human IgG Fc antibody on ice. After washing twice with FACS buffer, the cells were resuspended in 7-AAD added FACS buffer before acquired by BD LSRII cytometer. (b) Multiplex permeabilized F-CBA was applied to detect multiple autoantibodies to intracellular antigens. As image shows, some of our onconeural antigens, e.g., SOX1 wasn't successfully expressed on the surface of HEK cells despite with a Caspr2 signal peptide. Therefore, permeabilization step was required for SOX1 Ab to access SOX1. One day after transfection, the cells were stained with fixable amine-reactive viability dye, then labelled with live cell-labelling dyes for multiplex purposes. Next, the cells were fixed and permeabilized with Cyto-Fast Fix/Perm buffer, washed once with Cyto-Fast Perm/Wash buffer, blocked with 10% normal rat serum (NRS) in Cyto-Fast Perm/Wash buffer, washed once with FACS buffer, before allocating to 96-well plates. Then, the cells were incubated with diluted CSF/sera on ice, washed twice with FACS buffer and incubated with PE anti-human IgG Fc antibody on ice. After washing twice with FACS buffer, the cells were acquired by BD LSRII cytometer.

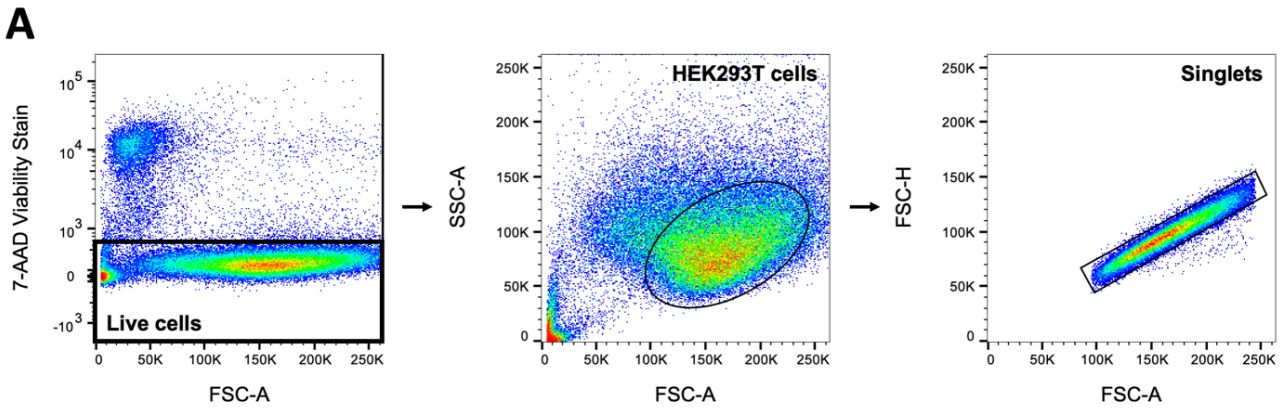
5.4.3.3. Strategies of gating and analysis

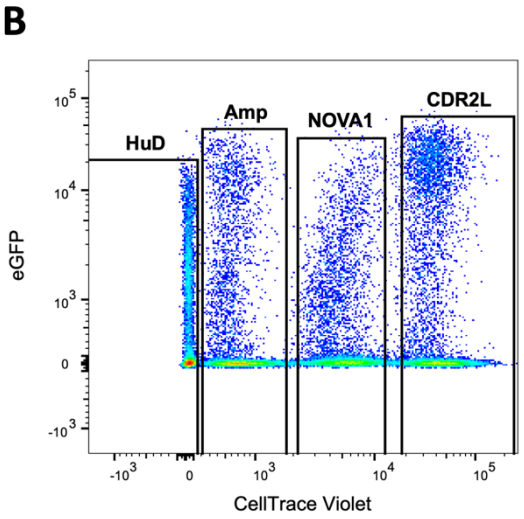
In Chapter II, the gating strategy was described to gate the results of DsRed2-reporting simplex F-CBAs in FlowJo. Here, the similar gating strategy was applied to gate the results of eGFP-tagged quadruplex live and permeabilized F-CBA (as demonstrated in Figure 5.2 and Figure 5.3). In this chapter, our eGFP-tagged live quadruplex F-CBA was used for simultaneously detecting autoantibodies to HuD, Amphiphysin, NOVA1 and CDR2L, and our permeabilized F-CBA was used for simultaneously detecting autoantibodies to untagged CRMP5, and eGFP-tagged SOX1, Ma1 and Ma2.

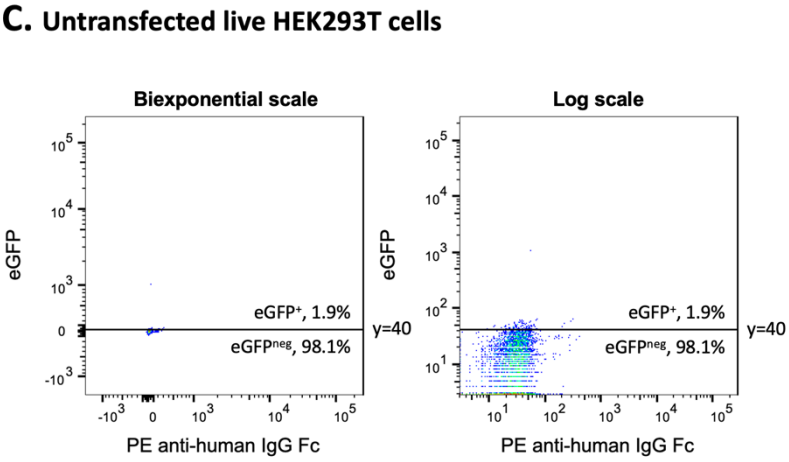
Figure 5.2 displayed the gating strategies to analyze multiplex live F-CBA to detect autoantibodies to HuD, Amphiphysin, NOVA1 and CDR2L. Here, 7-AAD viability dye was applied to distinguish live and dead cells, and same gating stream was followed

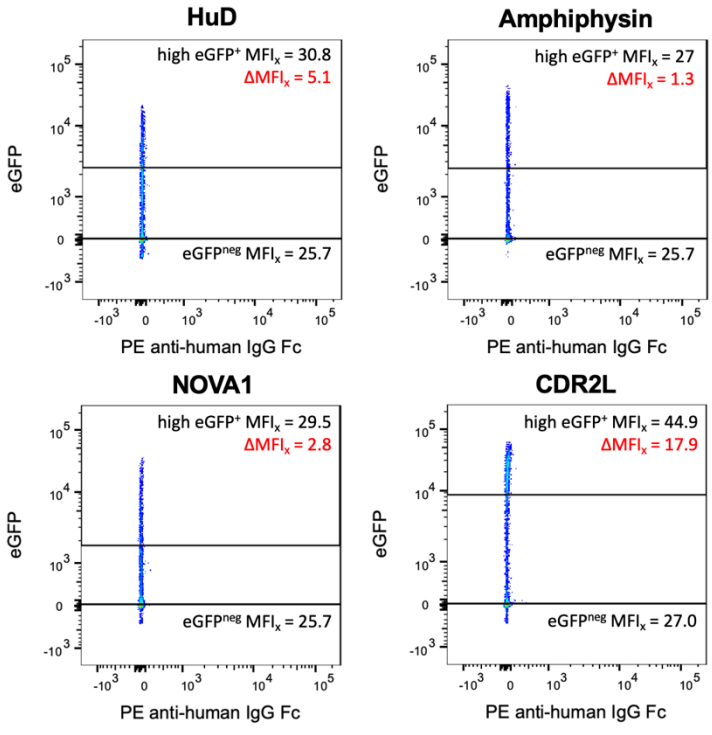
to gate on the singlets (Figure 5.2a). Next, the eGFP signal was plotted on the y-axis, and CellTrace Violet signal was plotted on the x-axis (Figure 5.2b). Because each HEK cell population had been color-coded with four concentrations of CellTrace Violet dye (0, 0.133, 0.83 and 5 μM), we could easily gate on individual populations for subsequent analysis. After gating on each population, their eGFP signals were plotted on the y-axis, and their secondary antibody signals were plotted on the x-axis. The $eGFP^{neg}$ gate was set as y=40 because 98.1% of the events from untransfected live HEK cells was below y=40 (Figure 5.2c). With using 2^{nd} Ab only control as reference, the high $eGFP^{+}$ threshold was set above the "median + 10 x MADP*" of fluorescence intensities on the y-axis in $eGFP^{+}$ population (Figure 5.2d). Then, the same gates were applied to every sample to quantify the MFI_x of $eGFP^{+}$ and high $eGFP^{+}$ populations, and then ΔMFI_x was calculated as "MFI_x (high $eGFP^{+}$) - MFI_x ($eGFP^{neg}$). Figure 5.3e presented the results when screening a patient serum seropositive for CDR2L autoantibodies only. With following the same gating strategies, Figure 5.3 demonstrated the gating steps and plots of our quadruplex permeabilized F-CBA when screening a patient serum having autoantibodies to Ma1 and Ma2.

The cut-off was set above "mean + 6 x standard deviation" of the ΔMFI_x from healthy sera. The signal-to-noise ratio was calculated as "average ΔMFI_x of the samples in targeted group ÷ (mean + 3 x standard deviation) of the ΔMFI_x from healthy sera". The serum samples above the cut-off were picked up, and the CSF samples above the average ΔMFI_x from healthy sera were picked up.


A
7-AAD Viability Stain
Live cells
FSC-A
SSC-A
HEK293T cells
FSC-A
FSC-H
Singlets
FSC-A


B
HuD
Amp
NOVA1
CDR2L
eGFP
CellTrace Violet


C. Untransfected live HEK293T cells
Biexponential scale
Log scale
eGFP
eGFP+, 1.9%
eGFPneg, 98.1%
y=40
PE anti-human IgG Fc


D. 2nd Ab only control
HuD
high eGFP+ MFIx = 30.8
ΔMFIx = 5.1
eGFPneg MFIx = 25.7
Amphiphysin
high eGFP+ MFIx = 27
ΔMFIx = 1.3
eGFPneg MFIx = 25.7
NOVA1
high eGFP+ MFIx = 29.5
ΔMFIx = 2.8
eGFPneg MFIx = 25.7
CDR2L
high eGFP+ MFIx = 44.9
ΔMFIx = 17.9
eGFPneg MFIx = 27.0
eGFP
PE anti-human IgG Fc

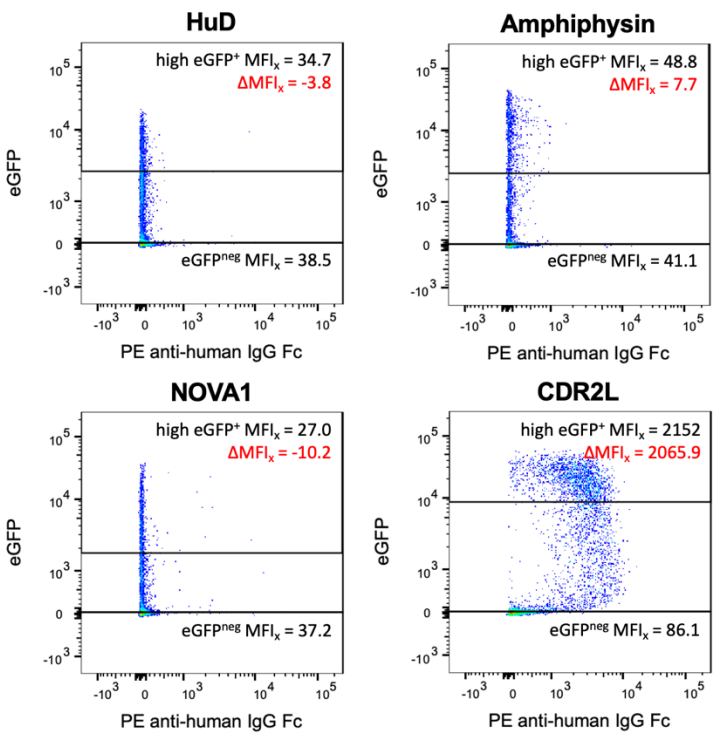
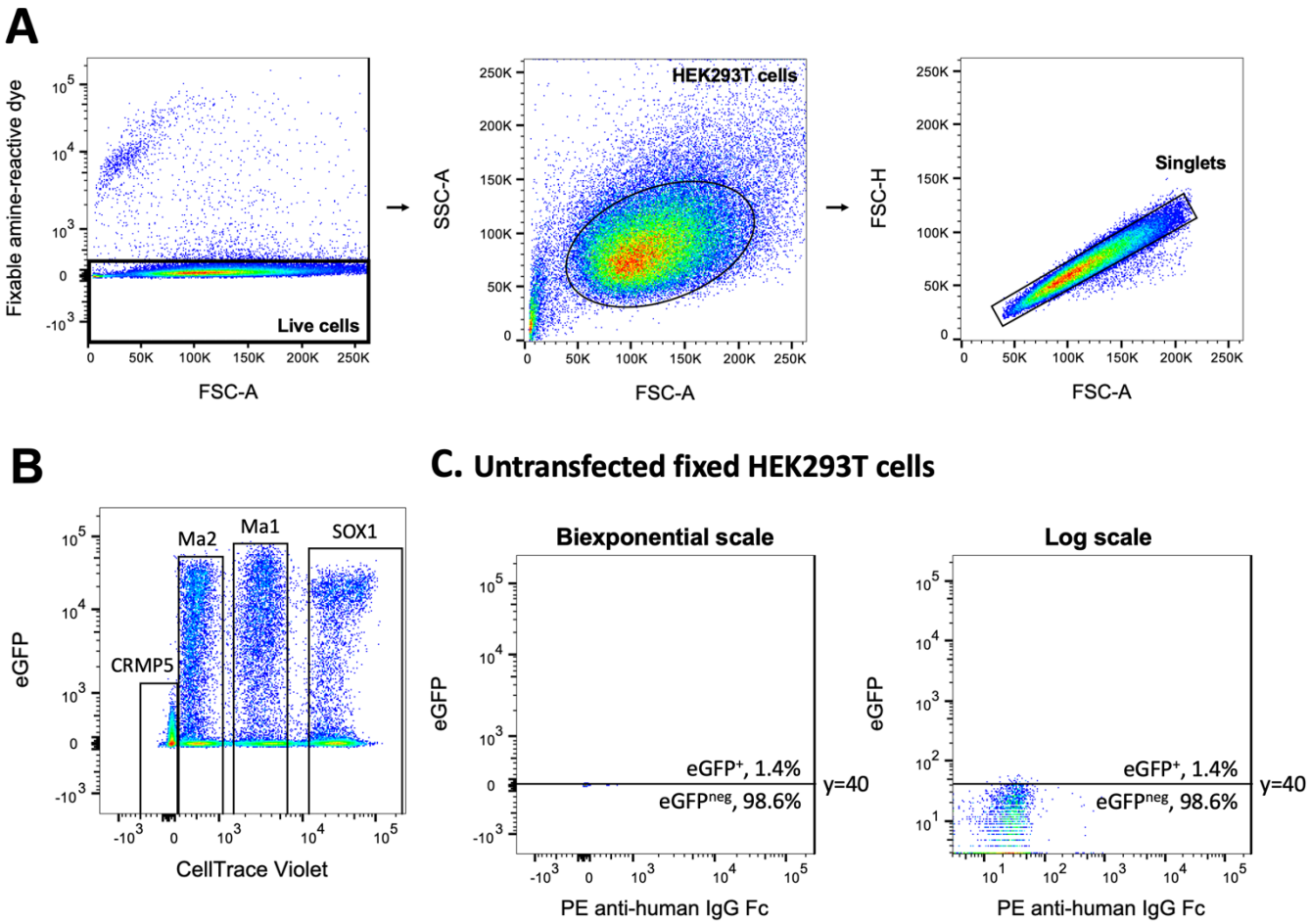

E. Serum with CDR2L Ab
HuD
high eGFP+ MFIx = 34.7
ΔMFIx = -3.8
eGFPneg MFIx = 38.5
Amphiphysin
high eGFP+ MFIx = 48.8
ΔMFIx = 7.7
eGFPneg MFIx = 41.1
NOVA1
high eGFP+ MFIx = 27.0
ΔMFIx = -10.2
eGFPneg MFIx = 37.2
CDR2L
high eGFP+ MFIx = 2152
ΔMFIx = 2065.9
eGFPneg MFIx = 86.1
eGFP
PE anti-human IgG Fc

Figure 5.2: The step-by-step gating strategies of eGFP-tagged quadruplex live F-CBA. (a) With using 7-AAD, the live cells population was gated on before plotting its SSC-A on the y-axis and its FSC-A on the x-axis. Next, the core of live HEK cell cloud was gated on before plotting its FSC-H on the y-axis and its FSC-A on the x-axis. Then, the singlets were gated on. (b) The eGFP signals of live singlets were plotted on the y-axis, and their CellTrace Violet signals were plotted on the x-axis before gating on each cell population surface-expressing eGFP-tagged HuD, Amphiphysin, NOVA1 and CDR2L respectively. (c) The singlets of the untransfected live HEK293T cells were plotted as eGFP signal on the y-axis and secondary antibody signal on the x-axis. The same sample was plotted in biexponential and log scales. The threshold was y=40, and the percentages of events in $eGFP^{neg}$ and $eGFP^{+}$ gates were quoted. (d) As a gating reference, the live singlets of secondary antibody only control was gated to define the high $eGFP^{+}$ population. (e) The same gate was applied when screening a patient serum with CDR2L autoantibodies only. The MFI_x of $eGFP^{neg}$ and high $eGFP^{+}$ populations were mentioned at the top right corner of each population, and the ΔMFI_x of each sample were quoted in red.



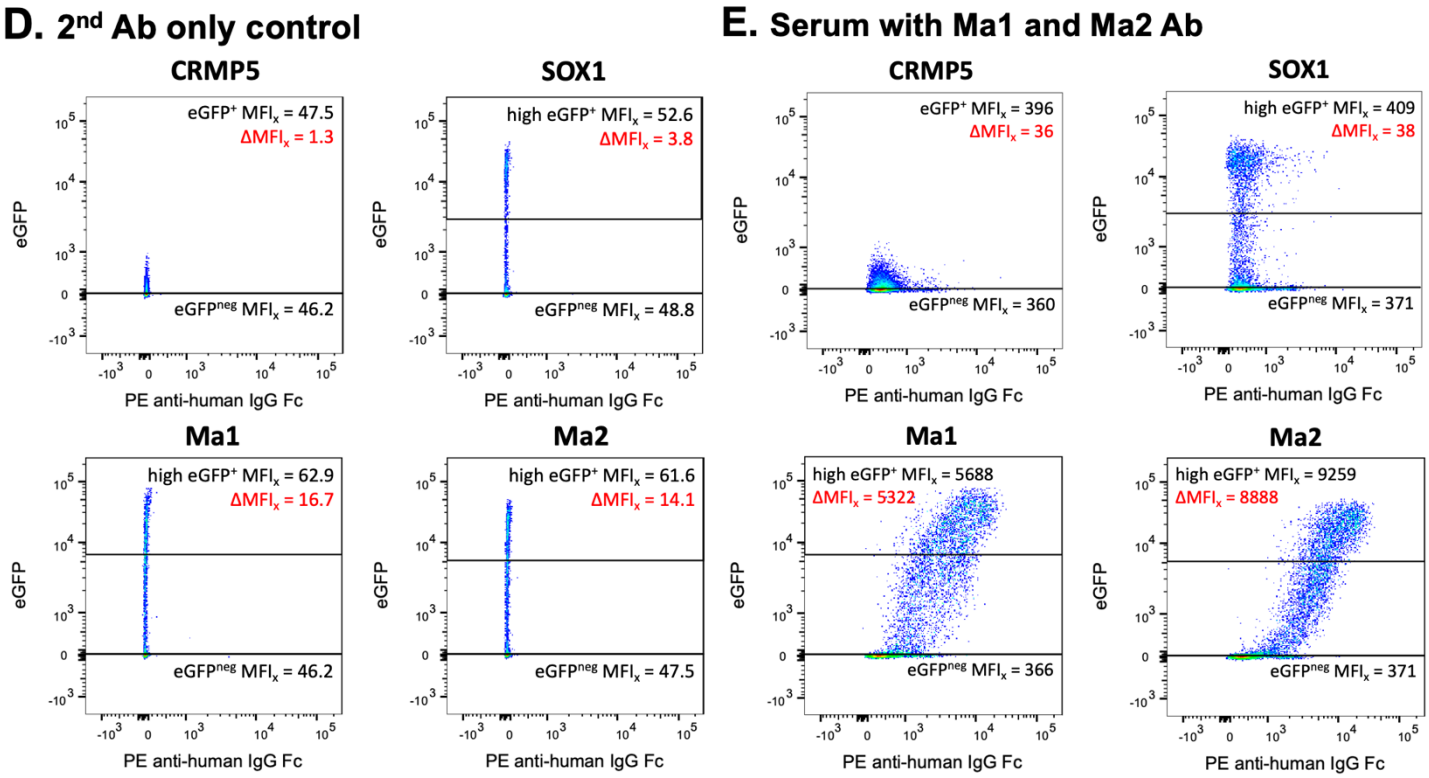


Figure 5.3: The step-by-step gating strategies of quadruplex permeabilized F-CBA. (a) With using Near-IR fixable amine-reactive dye, the live cells population was gated on before plotting its SSC-A on the y-axis and its FSC-A on the x-axis. Next, the core of live HEK cell cloud was gated on before plotting its FSC-H on the y-axis and its FSC-A on the x-axis. Then, the singlets were gated on. (b) The eGFP signals of live singlets were plotted on the y-axis, and their CellTrace Violet signals were plotted on the x-axis before gating on each cell population intracellular expressing untagged CRMP5, eGFP-tagged SOX1, Ma1 and Ma2 respectively. (c) The singlets of the untransfected fixed HEK293T cells were plotted as eGFP signal on the y-axis and secondary antibody signal on the x-axis. The same sample was plotted in biexponential and log scales. The threshold was y=40, and the percentages of events in $eGFP^{neg}$ and $eGFP^{+}$ gates were quoted. (d) As a gating reference, the live singlets of secondary antibody only control was gated to define the high $eGFP^{+}$ population. (e) The same gate was applied when screening a patient serum with Ma1 and Ma2 autoantibodies. The MFI_x of $eGFP^{neg}$, $eGFP^{+}$ and high $eGFP^{+}$ populations were mentioned at the top right or left corner of each population, and the ΔMFI_x of each sample were quoted in red.

5.5. Results

5.5.1. The simplex eGFP-tagged live F-CBA to detect HuD autoantibodies

As a pilot assay, we performed simplex live HuD F-CBA, and compared 2 secondary antibodies: DyLight 594 and PE anti-human IgG Fc antibodies at the same dilution of 1:100. The gated live HEK singlets were plotted as Figure 5.4, and PE anti-human IgG Fc antibody was more sensitive to detect HuD autoantibodies, i.e., the ΔMFI_x increased up to 4-time when screening 1:20 diluted patient serum samples with high and low titres of HuD autoantibodies (Figure 5.4a-b). However, our live HuD F-CBA was specific still with using PE anti-human IgG Fc as secondary antibody because the ΔMFI_x didn't increase when screening a patient serum with high titre of CDR2L autoantibodies and a healthy serum at 1:20 sample dilution (Figure 5.4c-d).

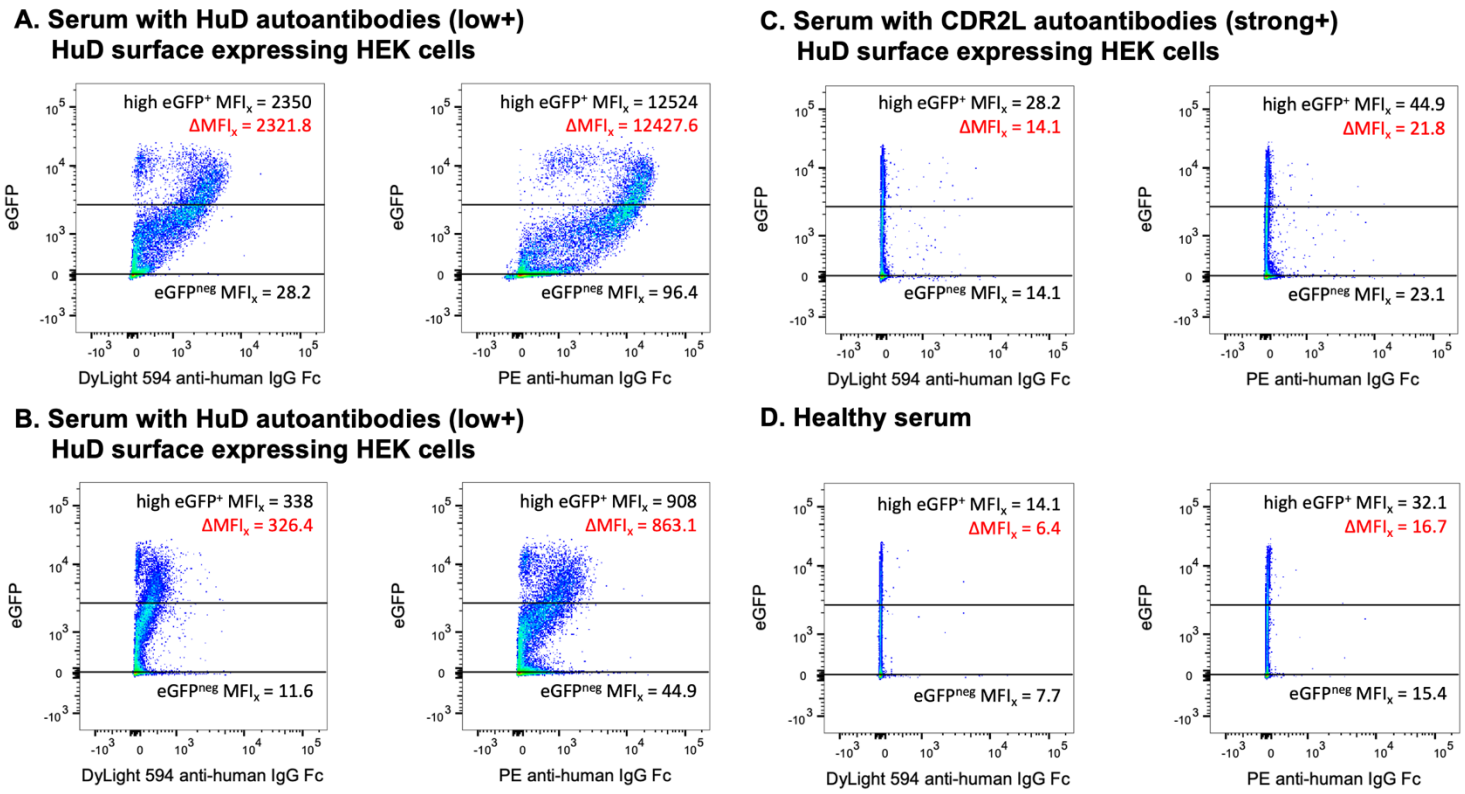


Figure 5.4: The simplex live F-CBA to detect HuD autoantibodies. (a-d) The live HEK cell singlets were plotted as their eGFP signals on the y-axis and their secondary antibody binding signals on the x-axis. As antibody target, HuD was expressed on the surface of HEK cells. The sera with (a) high titre (b) and low titre of HuD antibody, (c) a serum with CDR2L autoantibodies and (d) a healthy serum were screened at 1:20, and two secondary antibodies: DyLight 594 and PE anti-human IgG Fc antibody, were used at 1:100 dilution. The results of using DyLight 594 and PE anti-human IgG Fc as secondary antibody were plotted in the left and right columns, respectively. The MFI_x of $eGFP^{neg}$ and high $eGFP^{+}$ populations were mentioned at the top right corner of each gate, and the ΔxMFIs of each sample were quoted in red.

Moreover, we titrated both secondary antibodies from 1:100 to 1:1600 when screening a few patient and healthy serum samples at 1:20 sample dilution. As Figure 5.5a, PE anti-human IgG Fc antibody showed stronger signals than DyLight 594 anti-human IgG Fc antibody to detect HuD autoantibodies, and it can pick up two SOX1 Ab IHC+ sera, with low titres of HuD autoantibodies (CBA score = 20-50), more nicely. Under 1:100 dilution, the signal-to-noise ratio of PE anti-human IgG Fc antibody to pick up the sera with high (red) and low titres (blue) of HuD autoantibodies were 5.63- and 3.07-time higher than DyLight 594 anti-human IgG Fc antibody (Figure 5.5b). Although 1:100 dilution had better signal-to-noise ratio, we decided to use PE anti-human IgG Fc antibody at 1:200 dilution. It was because, apart from saving half of the antibody usage, 1:200 diluted PE anti-human IgG Fc antibody had demonstrated sufficient signal-to-nose ratios, which were 450 and 35, to pick up the samples with high or low titres of HuD autoantibodies.

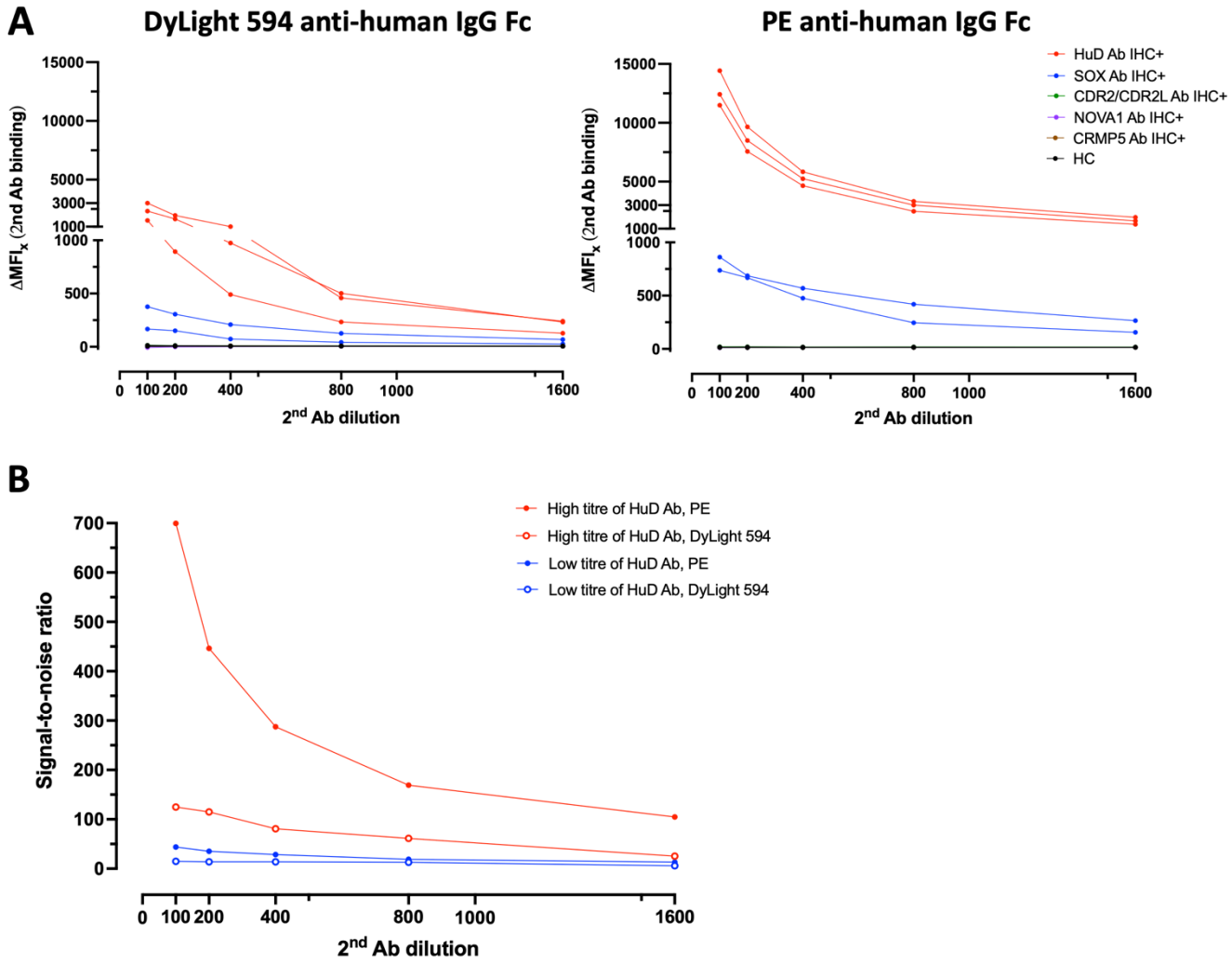
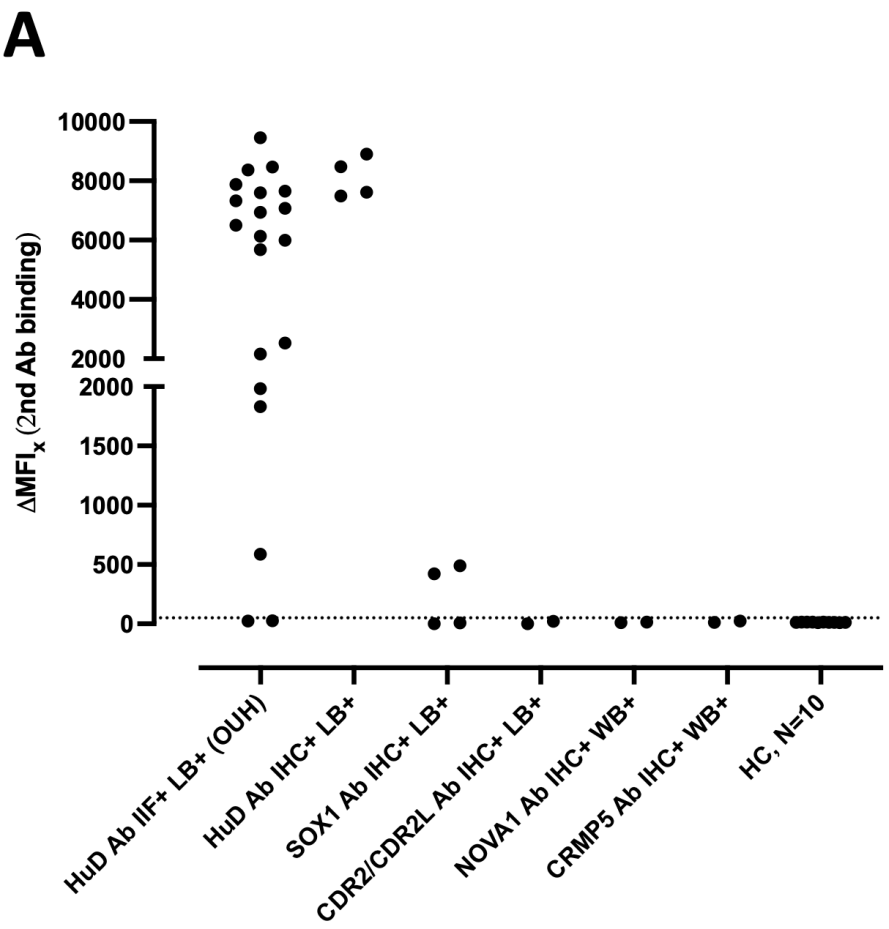


Figure 5.5: The titration results between using DyLight 594 or PE anti-human IgG Fc as secondary antibody. (a) The plots displayed the titration results of using DyLight 594 (left) or PE (right) anti-human IgG Fc as secondary antibody. The ΔMFI_x were plotted on the y-axis, and the dilutions of secondary antibody were plotted on the x-axis. 3 HuD Ab IHC+ sera, 2 SOX1 Ab IHC+ serum, 1 CDR2/CDR2L Ab IHC+ serum, 1 NOVA1 Ab IHC+ serum, 1 CRMP5 Ab IHC+ serum and 5 healthy sera were screed by our live HuD F-CBA. The sera were diluted at 1:20, and both secondary antibodies were titrated from 1:100 to 1:1600. The lines were color-coded to echo the samples, and the legends were mentioned at the top right corner. (b) The plot displayed the signal-to-noise ratio of our live HuD F-CBA when screening sera with high (red) and low (blue) titres of HuD autoantibodies with using DyLight 594 (hollow) and PE (solid) anti-human IgG Fc antibodies. The signal-to-noise ratios were calculated as "average ΔMFI_x of the samples in targeted group ÷ (mean + 3 x standard deviation) of the ΔMFI_x from healthy sera".

Next, we performed a pilot live HuD F-CBA screen on 34 serum samples from Mayo Clinic and OUH Clinical Immunology Unit, and 10 healthy sera. As Figure 5.6a, our live HuD F-CBA picked up 22/44 samples as HuD Ab CBA+, including 2/4 SOX1 Ab+ samples identified seropositive by fixed IHC and line blots from Mayo Clinic. However, we didn't pick up 2/20 HuD Ab+ samples, identified seropositive by indirect immunofluorescence (IIF) and line blots from OUH Clinical Immunology Unit. In addition, the ΔMFI_x from live HuD F-CBA showed good correlation (p-value < 0.001) with the 1:20 CBA visual scores from live HuD CBA when screening 24 HuD Ab+ samples identified seropositive by fixed IHC/IIF and line blots (Figure 5.6b).



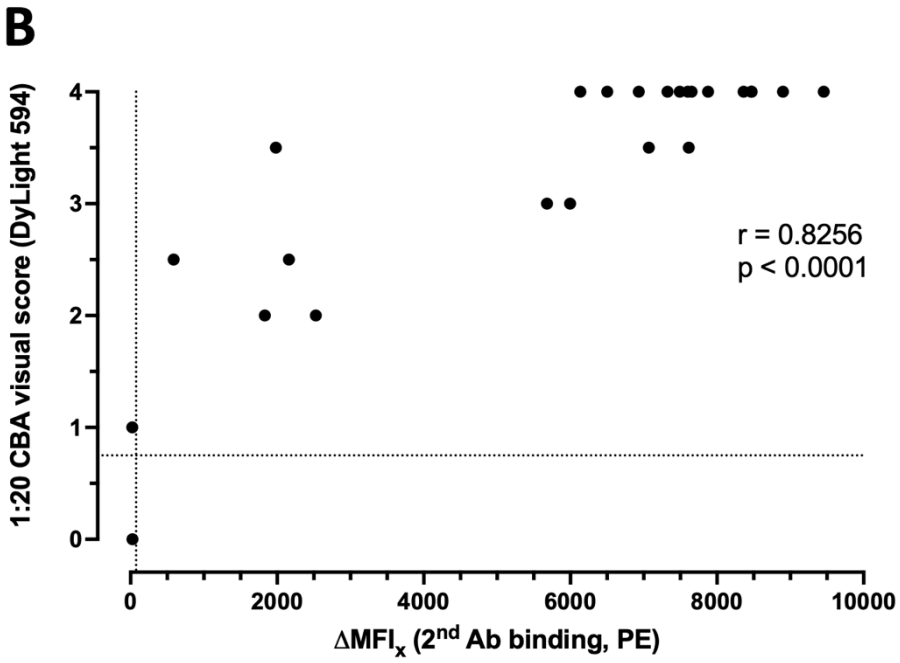
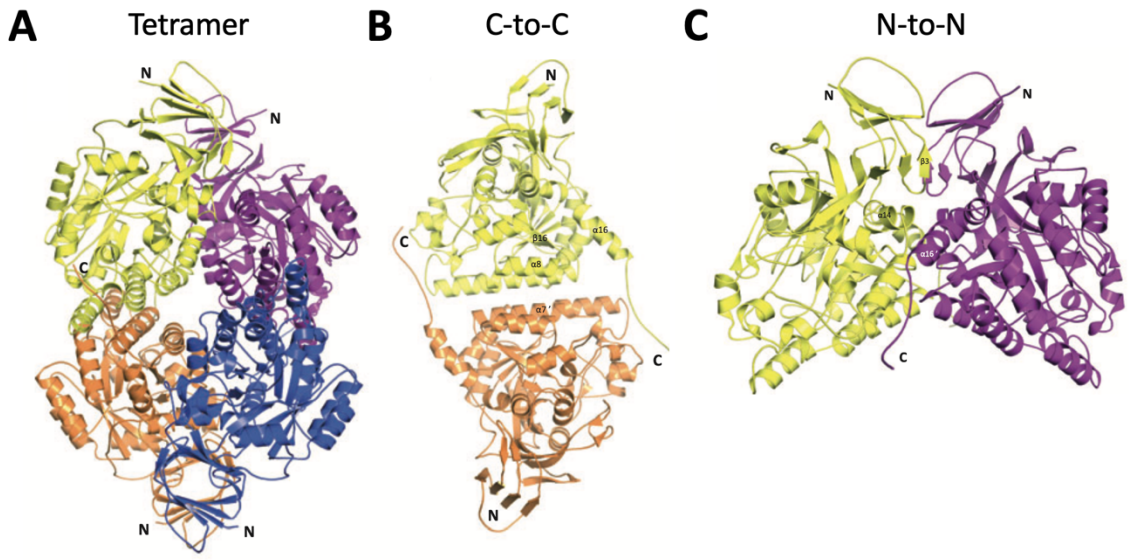


Figure 5.6: A pilot live HuD F-CBA screen to detect HuD autoantibodies. (a) 32 sera samples identified seropositive for onconeural autoantibodies (HuD Ab+, n=24 (20 from OUH Clinical Immunology Unit and 4 from Mayo Clinic); SOX1 Ab+, n=4; CDR2/CDR2L Ab+, n=2; NOVA1 Ab+, n=2) by IHC/IIF and line/western blots and 10 healthy sera were screened by our live HuD F-CBA for detecting HuD autoantibodies. The ΔMFI_x were plotted on the y-axis, and the sample cohorts were mentioned below the x-axis. The cut-off was as the dotted black line. (b) The ΔMFI_x from live HuD F-CBA using 1:200 diluted PE anti-human IgG Fc antibody and the 1:20 CBA visual scores from live HuD CBA using 1:750 diluted DyLight 594 anti-human IgG Fc antibody were correlated when screening 24 HuD Ab+ samples identified seropositive by fixed IHC/IIF and line/western blots. The cut-offs were as the dotted black lines, and the r and p-values were calculated via Spearman nonparametric correlation test.

5.5.2. Optimization of live CRMP5 F-CBA

As chapter IV indicated, our live CRMP5 CBA didn't pick up 2 CRMP5 Ab+ serum samples, which were identified seropositive by fixed IHC and western blots. In this section, the optimization steps to improve the signal of our CRMP5 F-CBA were elaborated.

From a past research, two CSF samples was reported to bind CRMP5 at its C-terminus and the C-to-C interface of CRMP5 homodimer (O'Donovan et al., 2020). However, our construct design, i.e., C-terminus of CRMP5 tethering to the truncated Caspr2 protein above the membrane (Figure 5.1a), may hinder the access of CRMP5 autoantibodies to the C-terminal epitopes of CRMP5. As displayed in Figure 5.7a-c, the crystal structure of CRMP5 homotetramer suggested CRMP5 could form homodimer through C-to-C or N-to-N interaction (Ponnusamy and Lohkamp, 2013). To expose the C-terminal epitopes of CRMP5, we modified CRMP5 construct by introducing a TAA stop codon after the cDNA of CRMP5 to achieve the extracellular secretion of CRMP5. To set up our new live CRMP5 F-CBA, on day 2, the co-transfection mixture was made up with 50% of original CRMP5 construct and 50% of modified CRMP5 construct. Then, on day 3, the secreted CRMP5 could form N-to-N homodimer with the membrane-anchored CRMP5, so that the C-terminal epitopes of CRMP5 were more accessible above the surface of HEK cells (Figure 5-7d).



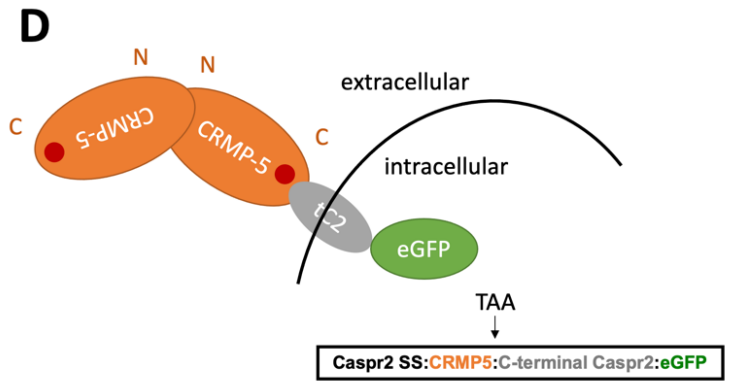


Figure 5.7: The strategy to expose the C-terminal epitopes of CRMP5. (a-c) The crystal structures were summarized from Ponnusamy and Lohkamp's publication in 2013 showing the 3D orientations of (a) CRMP5 homotetramer, (b) C-to-C and (c) N-to-N homodimers. (d) The cartoon image displayed the expression model of our live CRMP5 F-CBA. On day 2, the original and modified CRMP5 constructs were co-transfected into HEK cells in 1:1 ratio. The C-terminal epitopes of CRMP5 were as the red dots. Below was the illustration indicating where a TAA stop codon was introduced.

As Figure 5.8a, the bindings of CRMP5 autoantibodies were improved in new live CRMP5 F-CBA, but the high eGFP expressing cells still remained as weaker binders compared to medium eGFP expressing cells. To increase MFI_x readouts of $eGFP^+$ population, medium $eGFP^+$ threshold was set above the MFI_y of $eGFP^+$ population (Figure 5.8a). When screening 5 serum and 3 CSF CRMP5 Ab+ samples, identified seropositive by fixed IHC and western blots, our new live CRMP5 F-CBA picked up all the CSF samples as the original live CRMP5 F-CBA did, but serum sample 1 (red dot) was picked up by new live CRMP5 F-CBA but not by the original live CRMP5 F-CBA (Figure 5.8c). Despite improving the access of CRMP5 autoantibodies, our new live CRMP5 F-CBA was not optimal because it didn't pick up 3/5 CRMP5 Ab+ serum samples, for example serum sample 2 (purple dot), identified seropositive by fixed IHC and western blots (Figure 5.8b-c). Surprising, all the 3 CSF samples had higher ΔMFI_x when tested by the original live CRMP5 F-CBA than by the new CRMP5 F-CBA (Figure

5.8c). The finding implied CRMP5 autoantibodies in patients' sera and CSF samples may recognize different CRMP5 epitopes.

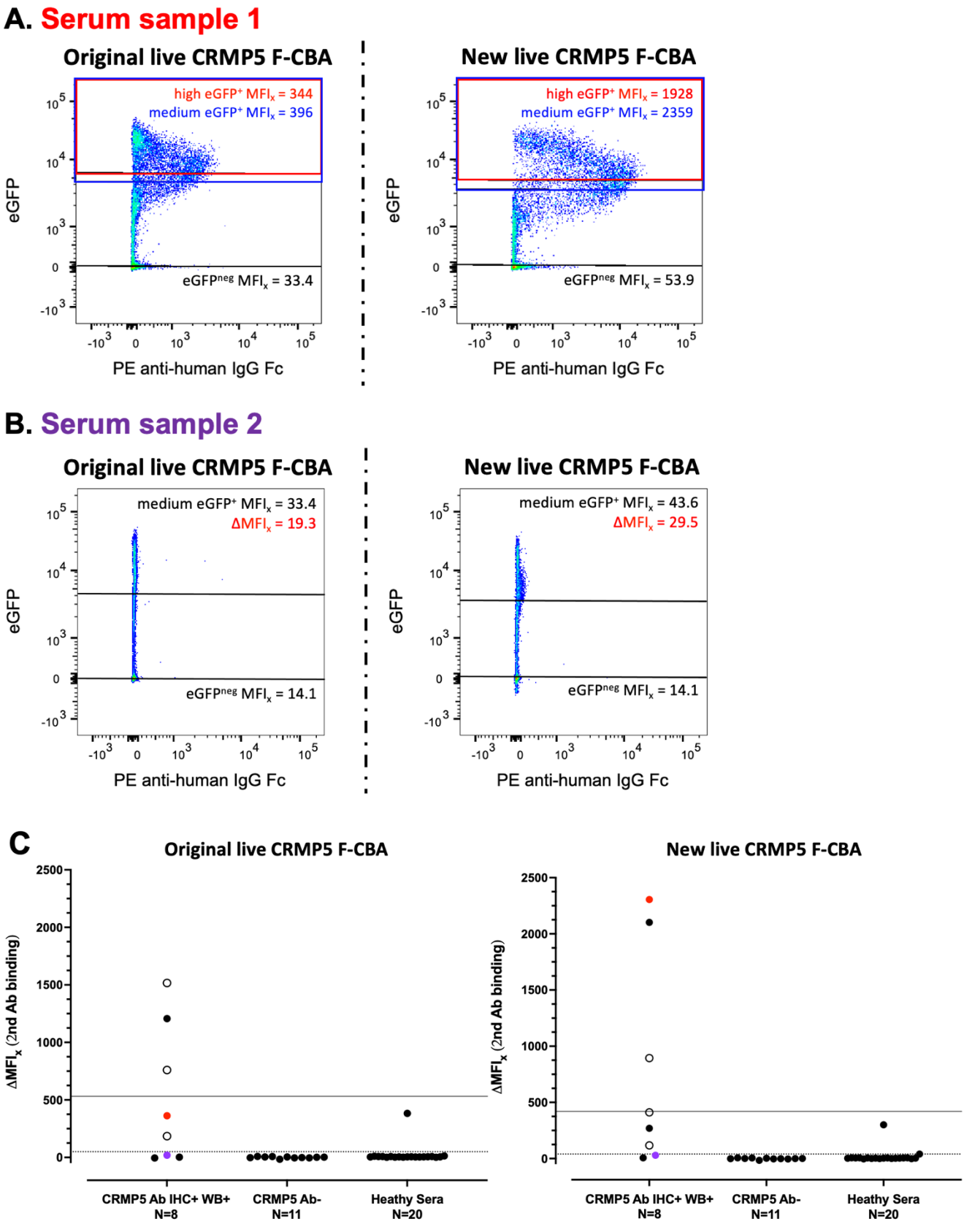


Figure 5.8: The new eGFP-tagged live CRMP5 F-CBA improved the bindings of CRMP5 autoantibodies. (a-b) When screening (a) serum sample 1 and (b) sample 2 by our original (left) and new live CRMP5 F-CBAs (right), the live singlets were plotted to quantify the MFI_x of medium and high $eGFP^+$, and $eGFP^{neg}$ populations. The eGFP signals were potted on the y-axis, and the secondary antibody binding signals were plotted on the x-axis. The MFI_x were color-coded in (a) and mentioned at the top right corner of each gate. The ΔMFI_x were mentioned in (b). (c) 5 serum and 3 CSF samples identified CRMP5 Ab+ by fixed IHC and line/western blots, 11 CRMP5 Ab- patient samples and 20 healthy sera were screened by our original and new CRMP5 F-CBA. The ΔMFI_x of each sample were plotted. Serum sample 1 and 2 were colour-coded in red and purple respectively. The CSF samples were as hollow dots. The cut-offs of serum and CSF samples were as the solid and dotted black lines respectively.

To further improve the access of CRMP5 autoantibodies, an untagged permeabilized CRMP5 F-CBA was developed, by removing the Caspr2 signal peptide from the modified CRMP5 construct, to intracellularly express naive CRMP5. However, the translation of eGFP tag wasn't completely depleted despite a TAA stop codon situating before the cDNA of C-terminal Caspr2 domain. In this case, the ΔMFI_x of our permeabilized CRMP5 F-CBA was quantified as "MFI_x ($eGFP^+$ population) - MFI_x ($eGFP^{neg}$ population)" (Figure 5.9a). This time, serum sample 2 (purple dot) was picked up by permeabilized CRMP5 F-CBA, but serum sample 3 (green dot) was the only CRMP5 Ab+ serum sample not picked up by our permeabilized CRMP5 F-CBA (Figure 5.9b-c). Although our new live CRMP5 F-CBA improved the access of CRMP5 autoantibodies in patients' serum samples, our permeabilized CRMP5 F-CBA was shown to be the better alternative to detect CRMP5 autoantibodies because it not only picked up all the CSF samples but also the 4/5 CRMP5 Ab+ serum samples, identified seropositive by fixed IHC and western blots (Figure 5.10). To note, the clinical details of the sample we missed will be required to judge the diagnostic accuracy between our CRMP5 CBA and conventional diagnostic practices (fixed IHC and line/western blots).

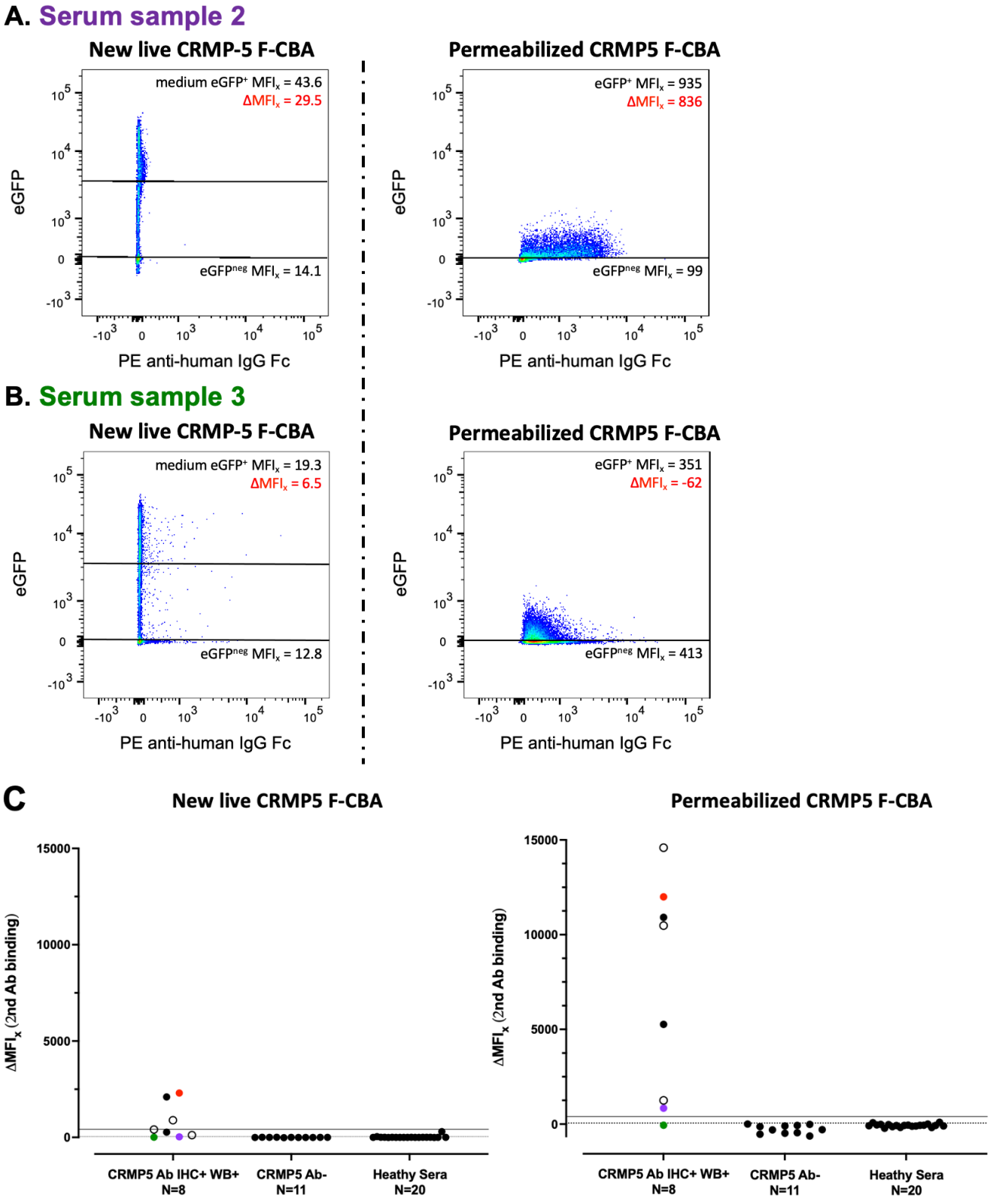


Figure 5.9: The permeabilized CRMP5 F-CBA further improved the access of CRMP5 autoantibodies to CRMP5. (a-b) When screening (a) serum sample 2 and (b) sample 3 by our new live CRMP5 F-CBA (left) and permeabilized CRMP5 F-CBA (right), the live singlets were plotted to quantify the MFI_x of medium $eGFP^+$, $eGFP^+$ and $eGFP^{neg}$ populations. The eGFP signals were potted on the y-axis, and the secondary

antibody binding signals were plotted on the x-axis. The MFI_x were mentioned at the top right corner of each gate, and the ΔMFI_x were mentioned in each plot. (c) The same CSF and serum samples, as Figure 5.8c, were screened by our new CRMP5 F-CBA and permeabilized CRMP5 F-CBA. The ΔMFI_x of each sample were plotted. Serum sample 1, 2 and 3 were colour-coded in red, purple and green respectively. The CSF samples were as hollow dots. The cut-offs of serum and CSF samples were as the solid and dotted black lines respectively.

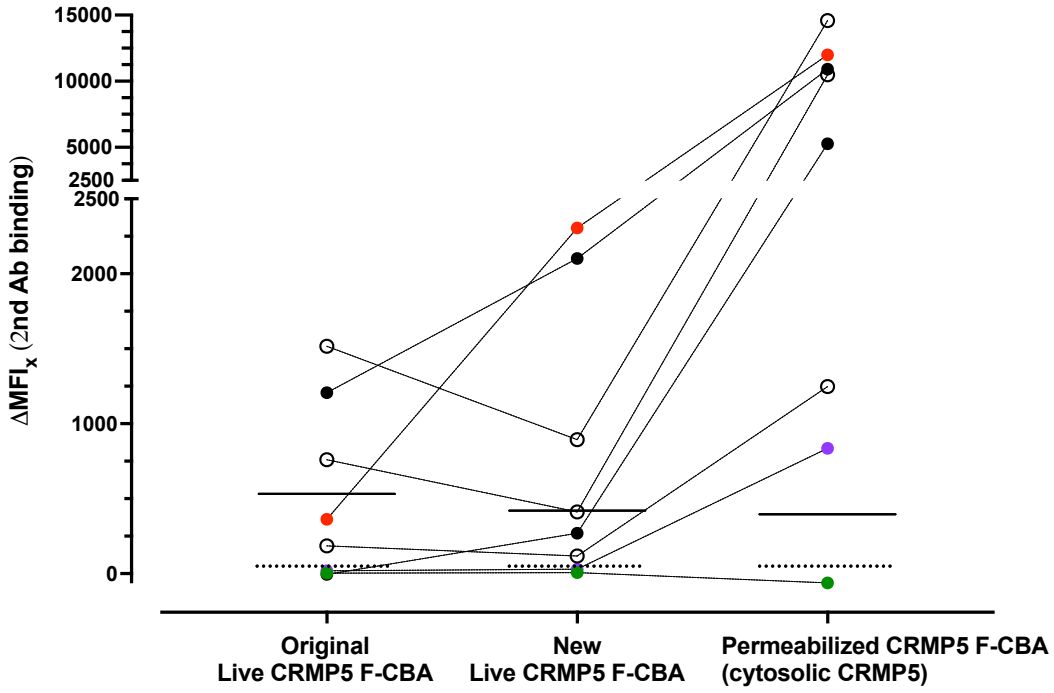


Figure 5.10: The permeabilized CRMP5 F-CBA was the optimal assay to detect CRMP5 autoantibodies. The plot combines the results from Figure 5.8c and 5.9c. The ΔMFI_x of each sample were plotted on the y-axis, and the types of CRMP5 F-CBA were mentioned below the x-axis. The ΔMFI_x from the sample samples were linked. The serum sample 1, 2 and 3 were colour-coded in red, purple and green respectively. The CSF samples were as hollow dots. The cut-offs of serum and CSF samples for each assay were as the solid and dotted black lines respectively.

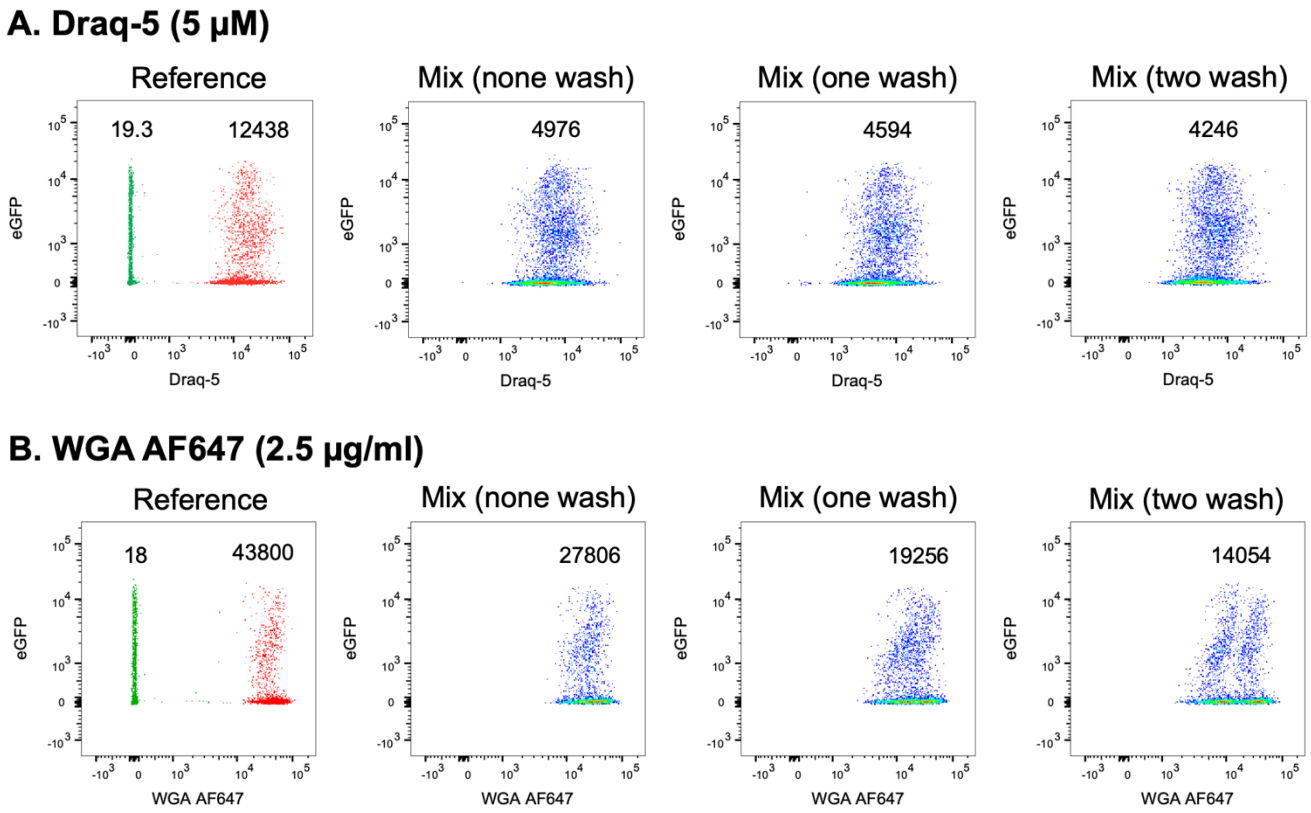
5.5.3. Development of live cell-labelling protocol for multiplex purposes

After introducing our simplex HuD and CRMP5 F-CBA, here the development of live cell-labelling protocol for multiplex purposes was described. To fit our needs, the suitable live cell-labelling dyes shall not only be detectable by flow cytometer with showing strong signals but also be sustainable to avoid leaking to the unstained cells.

Five live cell-labelling dyes including Draq-5, wheat germ agglutinin AF647 (WGA AF647), Hoechst 33342, CellTrace Violet and Far Red (CTV and CTFR) were tested for their sustainability. To achieve so, eGFP-tagged HuD surface-expressing cells were stained by individual live cell-labelling dyes at their working concentrations and washed zero to two times before combining with unstained cells (Figure 5.11). According to the results, although Draq-5 and WGA AF647 demonstrated strong signals in flow cytometer (MFI_x = 12438 and 43800), both dyes leaked into the unstained populations once the stained and unstained populations were mixed despite washing the stained population twice before combination (Figure 5.11a-b). In Draq-5 trial, there was an undistinguishable single population with a MFI_x equal to 4246 in two washes condition (Figure 5.11a). In WGA AF647 trial the unstained and stained populations were nearly separated with an overall MFI_x equal to 14054 in two washes condition (Figure 5.11b).

Alternatively, Hoechst 33342 and CellTrace dyes demonstrated better sustainability compared to Draq-5 and WGA AF647 (Figure 5.11 c-e). In Hoechst 33342 trial the unstained (MFI_x = 123) and stained population (MFI_x = 3554) were distinguishable in two washes condition (Figure 5.11c). In CTV trial, we applied the same voltage and channel as measuring Hoechst 33342. In two washes condition, the CTV-stained population (MFI_x = 19668) emitted stronger fluorescent signals than the Hoechst

33342-stained population (MFI_x =3554) (Figure 5.11c-d). Also, CTV in the stained population (MFI_x = 23932) didn't leak to the unstained population (MFI_x = 57.8) even without any wash before combination (Figure 5.11d). Lastly, in CTFR trial, although the stained (MFI_x = 82075) and unstained populations (MFI_x = 1788) were distinguishable in none washed condition, one wash condition was optimal because the MFI_x ratio between the stained (MFI_x = 67010) and unstained populations (MFI_x = 240) was 279, which was higher than the none wash (MFI_x ratio = 45.9) and two washes conditions (MFI_x ratio = 204) (Figure 5.11e). To conclude, CTV was shown to be the optimal candidate among those 5 live cell-labelling dyes due to its strong fluorescent signals and sustainable bindings to intracellular amine groups.



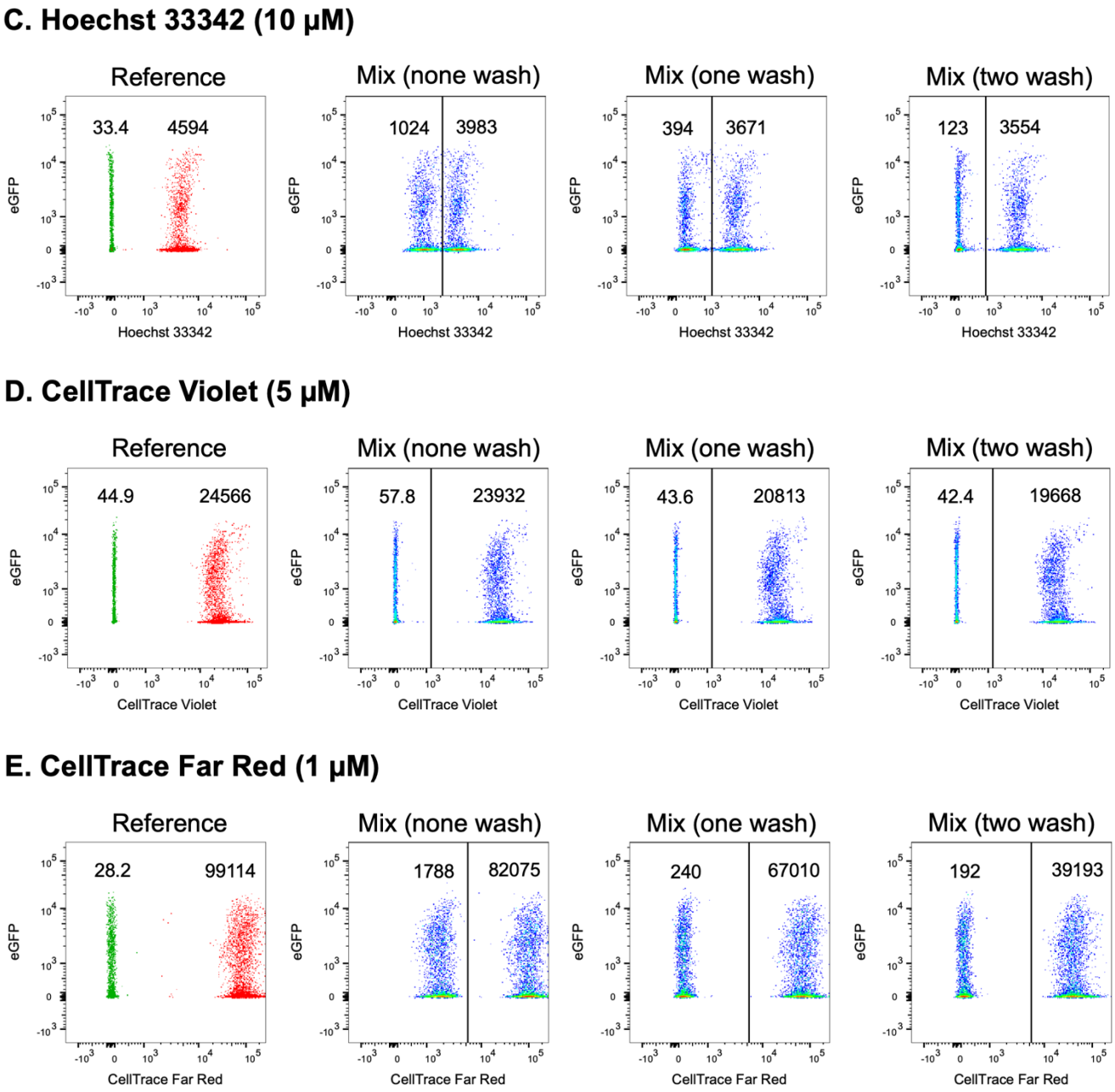


Figure 5.11: CellTrace Violet was the optimal live cell-labelling dye for multiplex purposes. (a-e) The eGFP-tagged HuD surface-expressing HEK cells were colored-coded with (a) Draq-5, (b) WGA AF647, (c) Hoechst 33342, (d) CTV and (e) CTFR at their recommended working concentrations (quoted in parentheses). The live singlets were plotted to display the results of combining the unstained and stained populations after zero to two washes (quoted in parentheses). The eGFP signals were plotted on the y-axis, and the signals of individual live cell-labelling dyes were plotted on the x-axis. In each row, the first plot showed the locations of unstained (green) and stained populations (red) before combining as reference, and the second to fourth plot displayed the results of combination after zero to two washes. In each plot, the MFI_x of individual cell populations were mentioned above.

Although CTFR was our second choice, we applied it with CTV to develop a 2x4 panel for octaplex live F-CBA. To achieve so, firstly we diluted the CTV working solution (5 μM) for 6- and 36-time, i.e., the diluted concentrations of 0.83 μM and 0.138 μM respectively, and four distinguishable cell populations appeared as each population was individually stained with 5 μM, 0.83 μM, 0.138 μM and 0 μM of CTV (Figure 5.12a). After figuring out the proper CTV titrations, each cell population were co-stained with CTV (5, 0.83, 0.138 and 0 μM) and CTFR (1 and 0 μM) and washed once before combining as an octaplex master mix. As Figure 5.11d-e, the signals of CTV and CTFR dropped after washes. In order to mimic the entire F-CBA staining procedure, the octaplex master mix was washed 6 more times in 96-well plate before acquisition. However, 6 out of 8 populations were blended together after the washes (Figure 5.12b). To resolve this issue, we used FBS-reduced FACS buffer (from 3% FBS reducing to 2% FBS) to dilute CTV and CTFR because the amine groups in FBS could pre-absorb amine-reactive CellTrace dyes, which then reduced the available dyes for cell-labelling. In FBS-reduced condition, each stained population accommodated more CTV and CTFR making them more tolerable to washes (Figure 5.12c). If necessary, we could further reduce the amount of FBS in FACS buffer for diluting CTV and CTFR so as to make each population even more separated from one another.

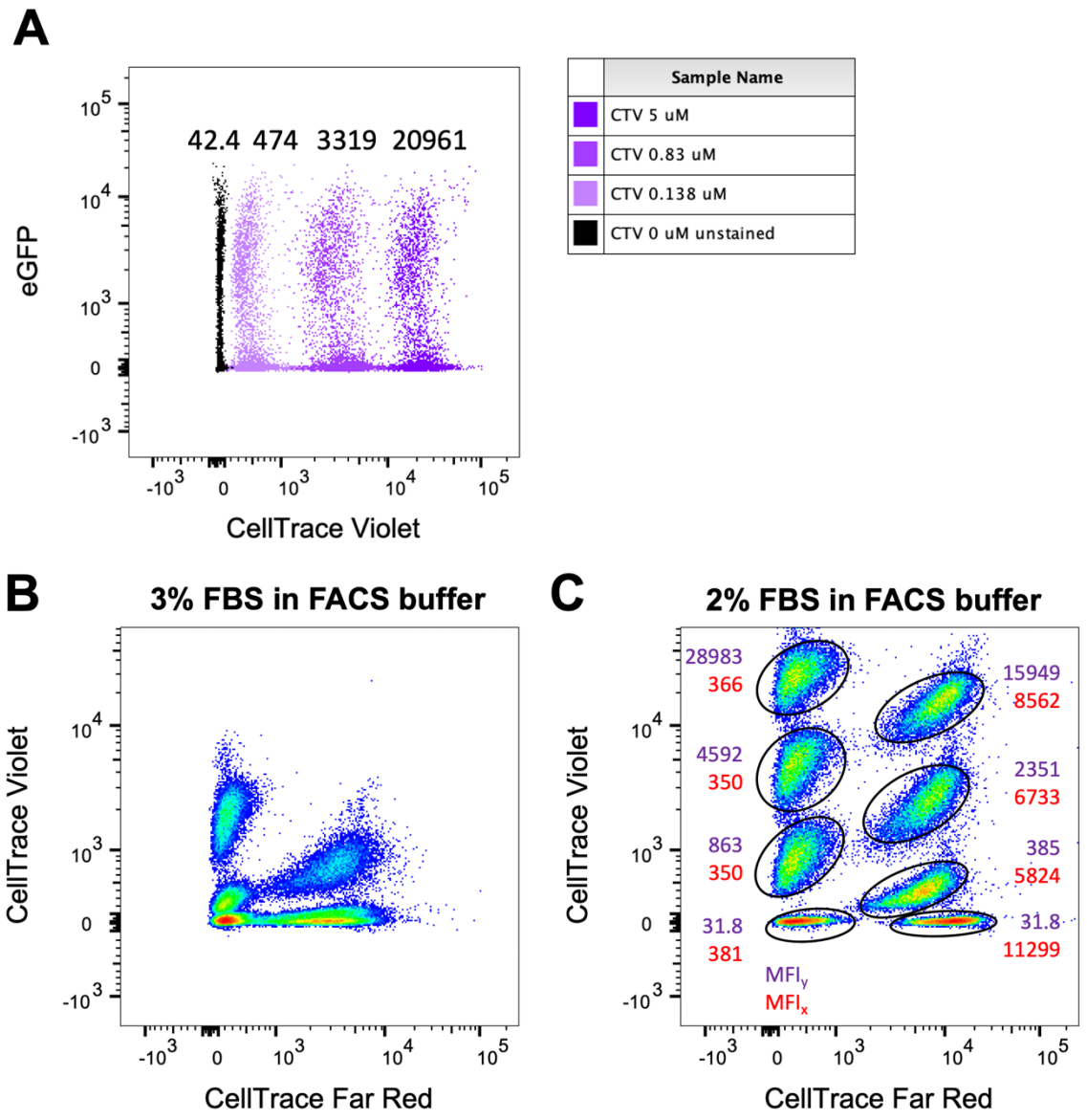


Figure 5.12: The octaplex live cell-labelling method was developed. (a) The eGFP-tagged HuD surface-expressing cells were stained with 5, 0.83, 0.1388 and 0 μM of CTV. With overlaying four scatter plots, the eGFP signals of live singlets were plotted on the y-axis, and the CTV signals of live singlets were plotted on the x-axis. The MFI_x of each population were mentioned above. (b-c) The scatter plots displayed the results between using (b) normal or (c) FBS-reduced FACS buffer to dilute CTV and CTFR for multiplex purposes. The CTV signals were plotted on the y-axis, and the CTFR signals were plotted on the x-axis. In (c), the MFI_x (red) and MFI_y (purple) were mentioned besides each cell population.

So far, a multiplex panel able to accommodate 8 different targeted antigens has been established and optimized with using CTV and CTFR together to color-code each population.

5.5.4. The eGFP-tagged quadruplex live F-CBA for simultaneously detecting autoantibodies to HuD, Amphiphysin, NOVA1 and CDR2L

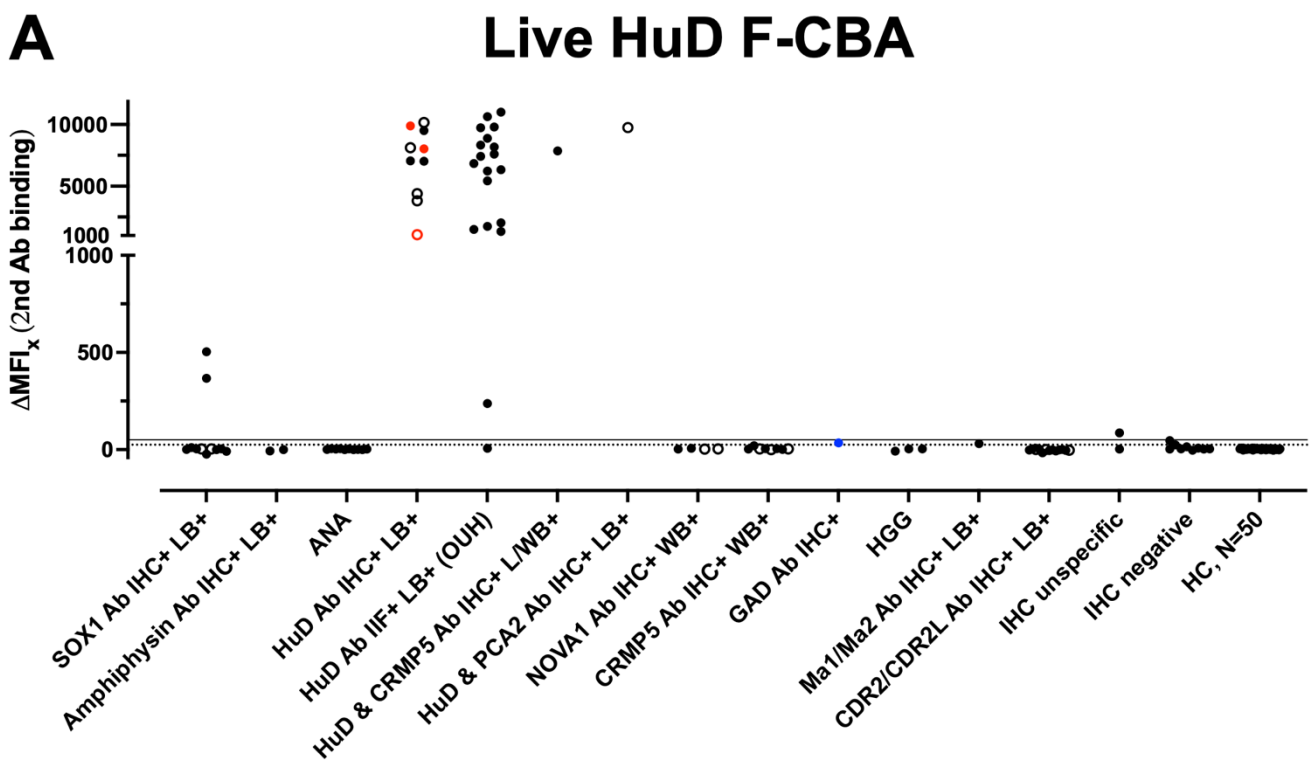
Next, we applied CTV alone to establish an eGFP-tagged quadruplex live F-CBA for screening the autoantibodies to surface-expressed HuD, Amphiphysin, NOVA1 and CDR2L within the same well of 96-well plate. As Figure 5.2, we screened and gated 60 serum and 16 CSF samples from Barcelona and Mayo Clinic, 19 serum samples from OUH Clinical Immunology Unit and 50 healthy sera. Our eGFP-tagged quadruplex live F-CBA was analyzed as 4 individual live F-CBAs for detecting autoantibodies to HuD, Amphiphysin, NOVA1 and CDR2L. The results of our quadruplex live F-CBA were plotted as Figure 5.13, and the number of samples picked up by individual live F-CBAs were summarized in Table 5.4

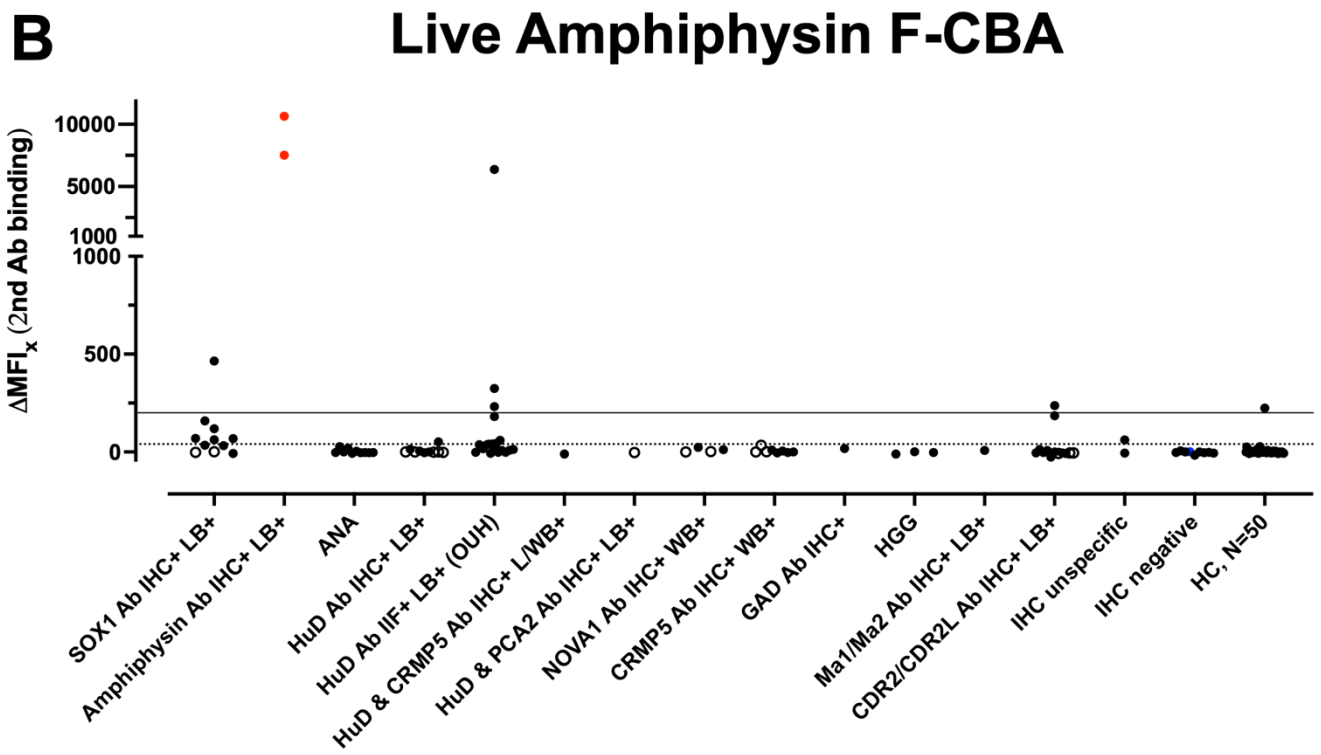
In our live HuD F-CBA, 33/145 samples were picked up as HuD Ab F-CBA+ (Figure 5.13a). We picked up 28/29 HuD Ab+ samples identified seropositive by fixed IHC/IIF and line/western blots, and 3/28 HuD Ab F-CBA+ samples were from the patients diagnosed with PNS and tumour (25/28 samples without clinical details). However, we didn't pick up 1/19 HuD Ab+ serum sample from OUH Clinical Immunology Unit, which hadn't been picked up by our live HuD CBA and simplex live HuD F-CBA as well (Figure 5.6). In addition, we picked up 2/11 SOX Ab+ samples, identified seropositive by fixed IHC and line blots, as our live HuD CBA did, but our live HuD F-CBA picked up 1/2 sample with unspecific IHC pattern. On the other hand, a GAD Ab+ serum sample, identified seropositive by fixed IHC only, and a HuD Ab+ serum sample, identified seropositive by line blots only, from patients without PNS and tumour weren't picked up by our live HuD F-CBA.

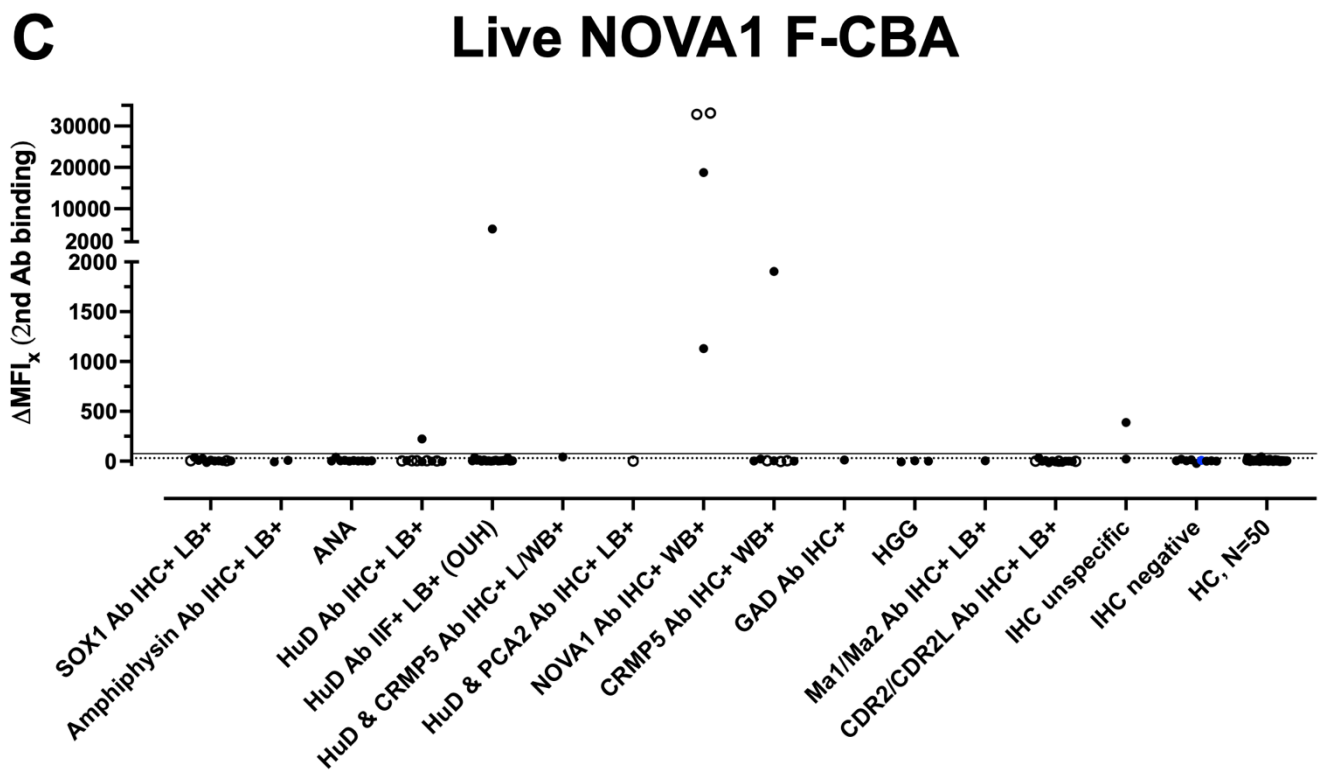
In our live Amphiphysin F-CBA, 8/145 samples were picked up as Amphiphysin Ab F-CBA+ (Figure 5.13b). We picked up all the 2 Amphiphysin Ab+ samples, identified seropositive by fixed IHC and line blots, from the patients diagnosed with PNS and tumour. However, we picked up 1/11 SOX1 Ab+ and 1/13 CDR2/CDR2L Ab+ samples, identified seropositive by fixed IHC and line blots, which hadn't been picked up by our live Amphiphysin CBA. In addition, 3/19 HuD Ab+ serum samples from OUH Clinical Immunology Unit, identified seropositive for HuD autoantibodies by fixed IIF and line blots, were picked up by our live Amphiphysin F-CBA (2 with $\Delta MFI_x < 500$ and 1 with $\Delta MFI_x = 6370$). Besides, one healthy serum was picked up as border-line positive by our live Amphiphysin F-CBA, and we didn't pick up a Amphiphysin Ab+ serum sample, identified seropositive by line blots only, from a patient without PNS and tumour.

In our live NOVA1 F-CBA, 8/145 samples were picked up as NOVA1 Ab F-CBA+ (Figure 5.13c). We picked up all the 4 NOVA1 Ab+ samples, identified seropositive by fixed IHC and western blots. Interestingly, both our live NOVA1 CBA and F-CBA picked up a CRMP5 Ab+ sample identified seropositive by fixed IHC and western blots, and a serum sample with unspecific IHC pattern from a patient diagnosed with teratoma but without PNS (Figure 4.10b). On the other hand, our live NOVA1 F-CBA picked up a HuD Ab+ sample, identified seropositive by fixed IHC and line blots, with $\Delta MFI_x = 223.3$, but our live NOVA1 CBA didn't pick it up. Among 19 HuD Ab+ serum samples from OUH Clinical Immunology Unit, identified seropositive by fixed IIF and line blots, we picked up a serum sample with high titre of NOVA1 autoantibodies ($\Delta MFI_x = 5077$). Besides, a NOVA Ab+ serum sample, identified seropositive by line blots only, from a patient without PNS and tumour wasn't picked up by our live NOVA1 F-CBA.

In our live CDR2L F-CBA, 14/145 samples were picked up as CDR2L Ab+ (Figure 5.13d). We picked up all the 13 CDR2L Ab+ samples, identified seropositive by fixed IHC and lines, and according to the clinical details we had, 2/13 CDR2L Ab F-CBA+ samples were from patients diagnosed with PNS and tumour. However, both our live CDR2L CBA and F-CBA picked up a CDR2 Ab+ sample (blue dot, IHC negative column), identified seropositive by line blots only, from a patient without PNS and tumour (Figure 4.10c). Nevertheless, our live CDR2L F-CBA was shown as the cleanest assay compared to the other three live F-CBAs, and it didn't pick up 3/4 CDR2 Ab+ samples, identified seropositive by line blots only, from 2 patients without PNS and tumour and a patient with MG and thymoma.




B
Live Amphiphysin F-CBA
ΔMFIx (2nd Ab binding)
10000
5000
1000
1000
500
0
SOX1 Ab IHC+ LB+
Amphiphysin Ab IHC+ LB+
ANA
HuD Ab IHC+ LB+
HuD Ab IIF+ LB+ (OUH)
HuD & CRMP5 Ab IHC+ L/WB+
HuD & PCA2 Ab IHC+ LB+
NOVA1 Ab IHC+ WB+
CRMP5 Ab IHC+ WB+
GAD Ab IHC+
HGG
Ma1/Ma2 Ab IHC+ LB+
CDR2/CDR2L Ab IHC+ LB+
IHC unspecific
IHC negative
HC, N=50


C
Live NOVA1 F-CBA
ΔMFIx (2nd Ab binding)
30000
20000
10000
2000
2000
1500
1000
500
0
SOX1 Ab IHC+ LB+
Amphiphysin Ab IHC+ LB+
ANA
HuD Ab IHC+ LB+
HuD Ab IIF+ LB+ (OUH)
HuD & CRMP5 Ab IHC+ L/WB+
HuD & PCA2 Ab IHC+ LB+
NOVA1 Ab IHC+ WB+
CRMP5 Ab IHC+ WB+
GAD Ab IHC+
HGG
Ma1/Ma2 Ab IHC+ LB+
CDR2/CDR2L Ab IHC+ LB+
IHC unspecific
IHC negative
HC, N=50

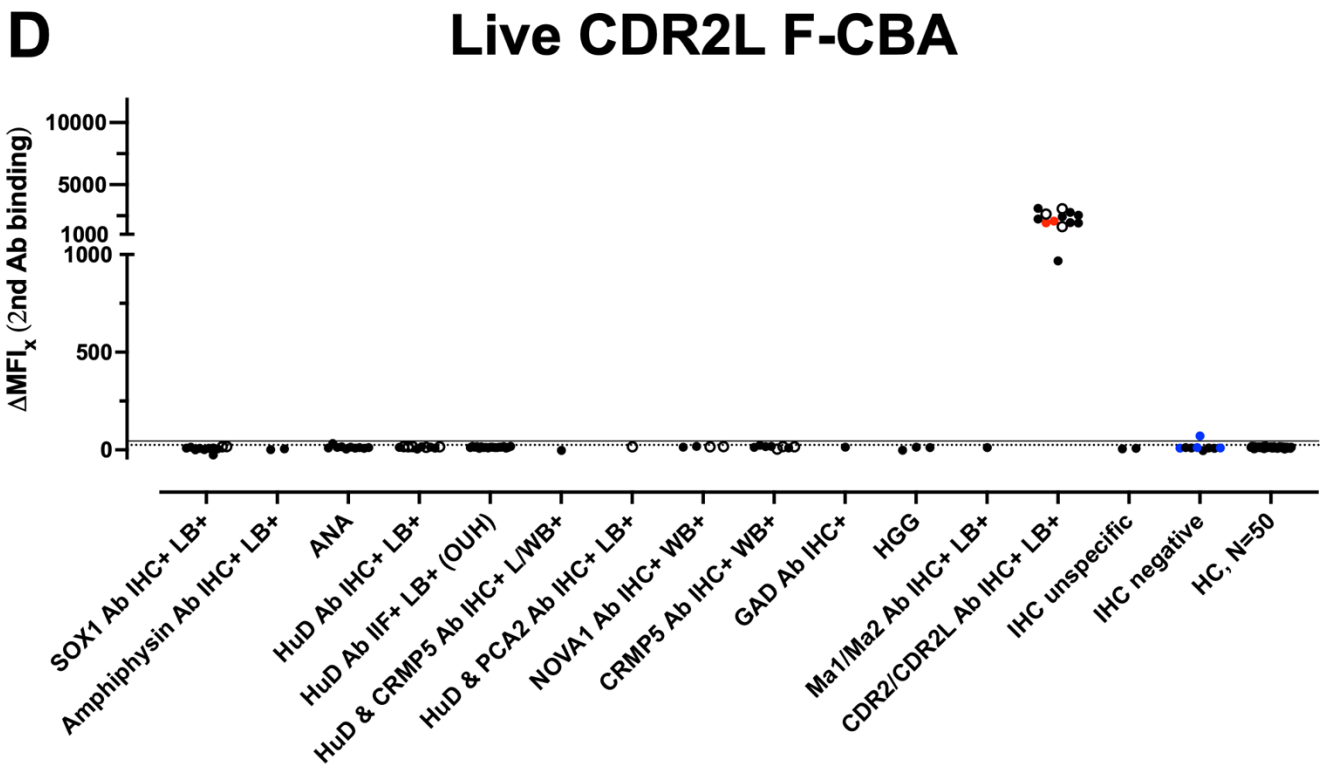


Figure 5.13: The results of quadruplex live F-CBA for detecting autoantibodies to HuD, Amphiphysin, NOVA1 and CDR2L. (a-d) 79 serum and 16 CSF samples from our collaborators, and 50 healthy sera were screened by our eGFP-tagged quadruplex live F-CBA for detecting autoantibodies to eGFP-tagged (a) HuD, (b) Amphiphysin, (c) NOVA1 and (d) CDR2L. The ΔMFI_x of each serum (solid dot) and CSF sample (hollow dot) were plotted on the y-axis, and the sample cohorts were mentioned below the x-axis. The red dots indicated the samples were from patients diagnosed with high/intermediate-risk PNS, tumours and the corresponding autoantibodies identified by fixed IHC/IIF and line/western blots. The blue dots indicated the samples were identified seropositive for the autoantibodies, which we were screening, by line blots only, and from patients without high-risk PNS, tumour or both. The cut-offs of serum and CSF samples were as the solid and dotted black lines respectively.

To assess the diagnostic consistency between live CBAs and F-CBAs, the 1:20 CBA visuals scores from our live CBAs were correlated with the ΔMFI_x from our live F-CBAs when detecting autoantibodies to HuD, Amphiphysin, NOVA1 and CDR2L (Figure 5.14). Our live HuD F-CBA showed good correlation with our live HuD CBA (p-value < 0.0001), except picking up a serum sample with unspecific IHC pattern from a patient without PNS and tumour (Figure 5.14a). Due to the limited amount of Amphiphysin

Ab+ samples identified seropositive by fixed IHC and line blots, the ΔMFI_x from our live Amphiphysin F-CBA correlated not significantly well (p-value = 0.0136) with the 1:20 visual scores from our live Amphiphysin CBA (Figure 5.14b). In addition, our live Amphiphysin F-CBA but not CBA picked up a CDR2/CDR2L Ab+ serum sample and a SOX1 Ab+ serum sample, identified seropositive by fixed IHC and line blots.

On the other hand, our live NOVA1 F-CBA showed good correlation with our live NOVA1 CBA (p-value < 0.0001), and both assays agreed to pick up the 6 samples with high titres of NOVA1 autoantibodies (Figure 5.14c). However, there was a HuD Ab+ serum sample (identified seropositive by fixed IHC and line blots) picked up by our live NOVA1 F-CBA but not by our live NOVA1 CBA. On the other way round, there was a serum sample with ANA IHC pattern picked up by our live NOVA1 CBA but not our live NOVA1 F-CBA. Lastly, our live CDR2L F-CBA also demonstrated good correlation (p-value < 0.0001) and 100% agreement with our live CDR2L CBA (Figure 5.14d). To conclude, because the results from our live CBAs and quadruplex live F-CBA demonstrated good correlation, we can rely on our quadruplex live F-CBA platform as a more efficient and quantitative alternative to implement routine diagnostic assays.

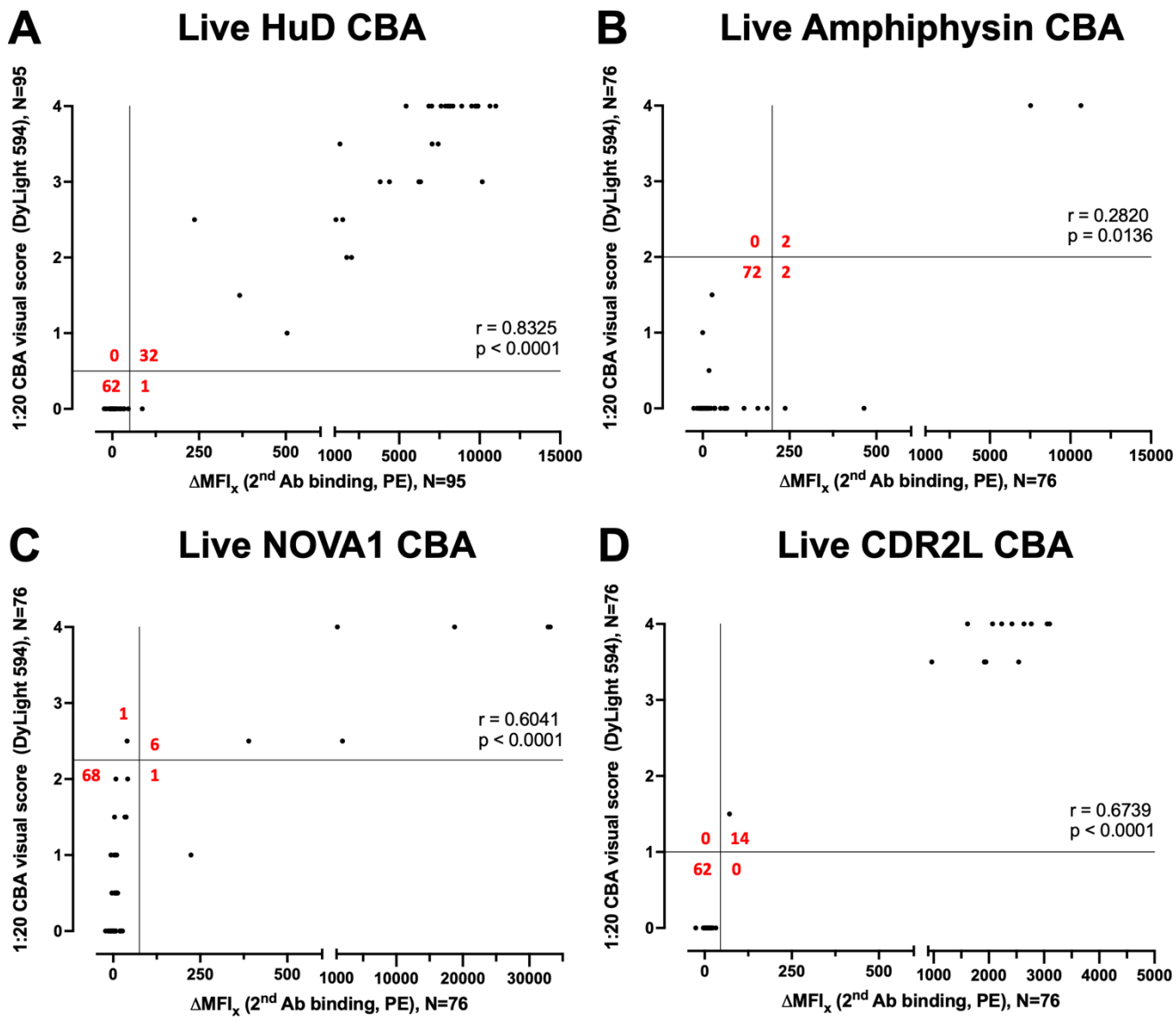


Figure 5.14: The ΔMFI_x from quadruplex live F-CBA correlated well with the 1:20 CBA visual scores from live CBAs for detecting autoantibodies to HuD, Amphiphysin, NOVA1 and CDR2L. (a) The 1:20 CBA visual scores from live CBAs for detecting autoantibodies to eGFP-tagged (a) HuD, (b) Amphiphysin, (c) NOVA1 and (d) CDR2L were plotted on the y-axis, and the ΔMFI_x from quadruplex live F-CBA for detecting autoantibodies to the same antigens were plotted on the x-axis when screening 60 serum and 16 CSF samples from Barcelona and Mayo Clinic. In HuD assays, additional 19 samples from OUH Clinical Immunology Unit were included for correlation. The 1:750 diluted DyLight 594 anti-human IgG Fc antibody and the 1:200 diluted PE anti-human IgG Fc antibody were used as the secondary antibodies for live CBAs and quadruplex live F-CBA respectively. The number of samples in each quadrant was quoted in red. The r and p-values were calculated via Spearman nonparametric correlation tests, and the cut-offs for serum samples were as the solid black lines.

Table 5.4: Summary of the samples picked up by quadruplex live F-CBA for detecting autoantibodies to HuD, Amphiphysin, NOVA1 and CDR2L

	Live HuD F-CBA (eGFP-tagged)	**Live Amphiphysin F-CBA (eGFP-tagged)**	**Live NOVA1 F-CBA (eGFP-tagged)**	**Live CDR2L F-CBA (eGFP-tagged)**
SOX1 Ab IHC+ LB+, N=11	2/11 (18.2%)	1/11 (9.1%)	0/11 (0%)	0/11 (0%)
Amphiphysin Ab IHC+ LB+, N=2	0/2 (0%)	2/2 (100%)	0/2 (0%)	0/2 (0%)
ANA, N=10	0/10 (0%)	0/10 (0%)	0/10 (0%)	0/10 (0%)
HuD Ab IIF+ LB+, N=19 (from OUH)	18/19 (94.7%)	3/19 (15.8%)	1/19 (5.3%)	0/19 (0%)
HuD Ab IHC+ LB+, N=10	10/10 (100%)	0/10 (0%)	1/10 (10%)	0/10 (0%)
HuD & CRMP5 Ab IHC+ L/WB+, N=1	1/1 (100%)	0/1 (0%)	0/1 (0%)	0/1 (0%)
HuD & PCA2 Ab IHC+ LB+, N=1	1/1 (100%)	0/1 (0%)	0/1 (0%)	0/1 (0%)
NOVA1 Ab IHC+ WB+, N=4	0/4 (0%)	0/4 (0%)	4/4 (100%)	0/4 (0%)
CRMP5 Ab IHC+ WB+, N=8	0/8 (0%)	0/8 (0%)	1/8 (12.5%)	0/8 (0%)
GAD Ab IHC+, N=1	0/1 (0%)	0/1 (0%)	0/1 (0%)	0/1 (0%)
HGG, N=3	0/3 (0%)	0/3 (0%)	0/3 (0%)	0/3 (0%)
Ma1/Ma2 Ab IHC+ LB+, N=1	0/1 (0%)	0/1 (0%)	0/1 (0%)	0/1 (0%)
CDR2/CDR2L Ab IHC+ LB+, N=13	0/13 (0%)	1/13 (7.7%)	0/13 (0%)	13/13 (100%)

IHC unspecific, N=2	1/2 (50%)	0/2 (0%)	1/2 (50%)	0/2 (0%)
IHC negative, N=9	0/9 (0%)	0/9 (0%)	0/9 (0%)	1/9 (11.1%)
IHC-, LB+ in the autoantibodies we screened	0/1 (0%)	0/1 (0%)	0/1 (0%)	1/4 (25%)
HC, N=50	0/50 (0%)	1/50 (2%)	0/50 (0%)	0/50 (0%)

5.5.5. The quadruplex permeabilized F-CBA for simultaneously detecting autoantibodies to CRMP5, SOX1, Ma1 and Ma2

Apart from live F-CBA, we also applied our quadruplex CTV color-coding panel to perform a quadruplex permeabilized F-CBA for screening the autoantibodies to intracellularly expressed CRMP5, SOX1, Ma1 and Ma2 in the same well of 96-well plate. Our permeabilized F-CBA was advantageous than our permeabilized CBA because the high background in $eGFP^{neg}$ population was subtracted and the diagnostic results were analyzed with using the ΔMFI_x. This can avoid any overscoring or subjective judgement attributed to the higher staining background in our permeabilized CBAs.

As Figure 5.3, we screened and gated 33 serum and 6 CSF samples from Barcelona and Mayo Clinic, 19 serum samples from OUH Clinical Immunology Unit and 50 healthy sera. Our quadruplex permeabilized F-CBA could be analyzed as 4 individual permeabilized F-CBAs for detecting autoantibodies to untagged CRMP5, eGFP-tagged SOX1, Ma1 and Ma2. The results of our quadruplex permeabilized F-CBA were

plotted as Figure 5.15, and the number of samples picked up by individual permeabilized F-CBAs were summarized in Table 5.5.

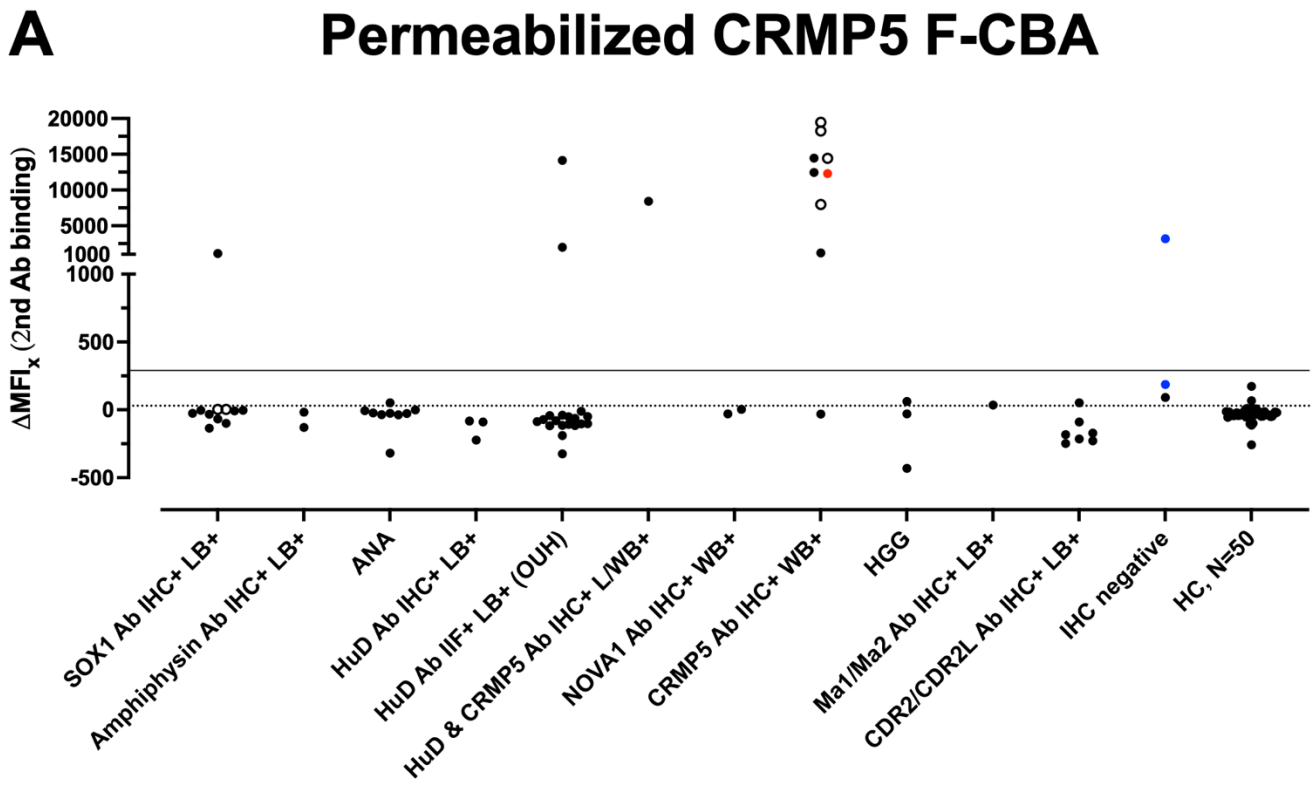
In our permeabilized CRMP5 F-CBA, 13/108 samples were picked up as CRMP5 Ab F-CBA+, including the 8/9 CRMP5 Ab+ samples and a HuD & CRMP5 Ab+ serum sample identified seropositive by fixed IHC and line/western blots (Figure 5.15a). According to the clinical details we had, 1/8 CRMP5 F-CBA+ sample were from a patient diagnosed with PNS and tumour. Likewise, the same CRMP5 Ab+ serum sample (as in Figure 5.9b) identified seropositive by fixed IHC and western blots wasn't picked up by our permeabilized CRMP5 F-CBA under quadruplex manner. In addition, our permeabilized CRMP5 F-CBA picked up 1/11 SOX1 Ab+ samples, identified seropositive by fixed IHC and line blots, from Mayo Clinic and 2/19 HuD Ab+ samples, identified seropositive by fixed IIF and line blots, from OUH Clinical Immunology Unit. Although our permeabilized CRMP5 F-CBA picked up 1/2 CRMP5 Ab+ sample, identified seropositive by line blots only, from a patient with melanoma but without PNS, it was an improvement compared to our live CRMP5 CBA, which picked up all the 2 CRMP5 Ab+ samples identified seropositive by line blots only (the other sample was from a patient without PNS and tumour).

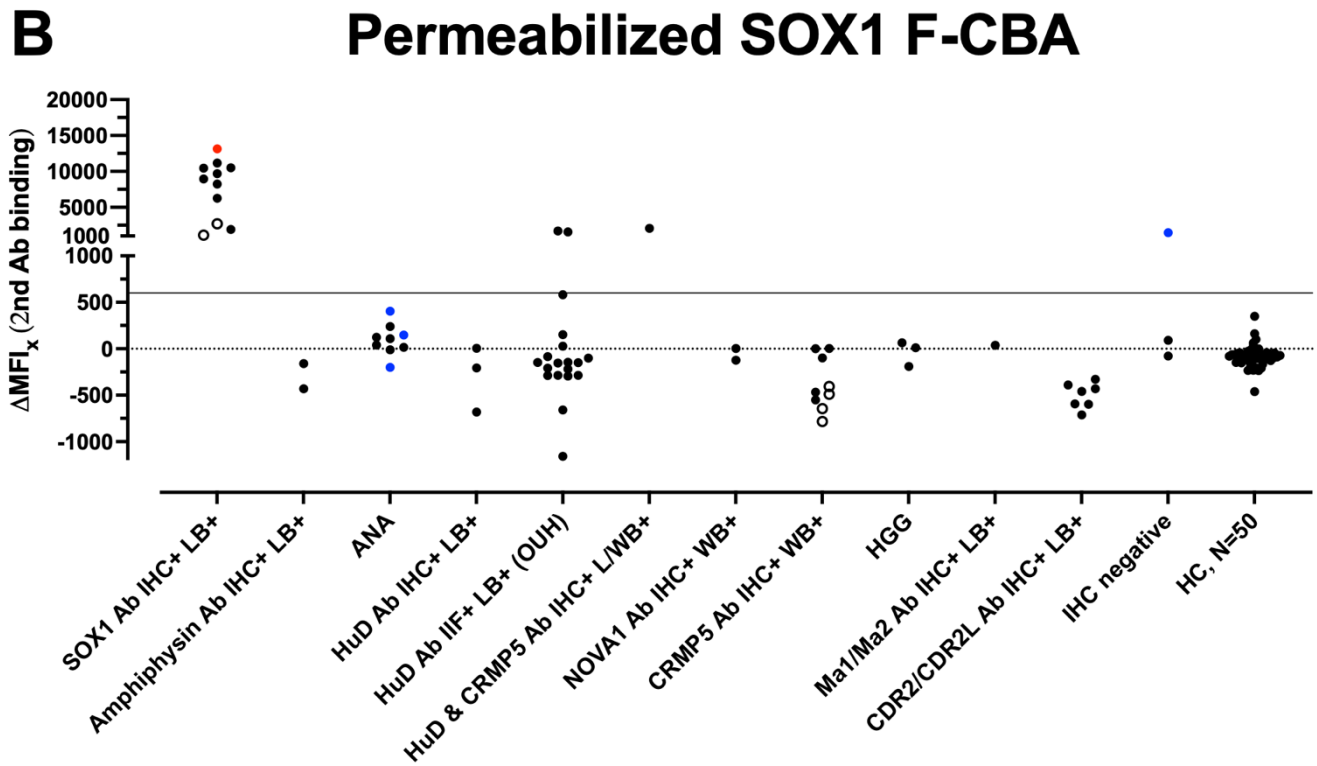
In our permeabilized SOX1 F-CBA, 15/98 samples were picked up as SOX1 Ab F-CBA+, including all the 11 SOX1 Ab+ samples identified seropositive by fixed IHC and line blots (Figure 5.15b). Our permeabilized SOX1 F-CBA didn't pick up 3/4 SOX1 Ab+ serum samples, identified seropositive by line blots only, from patients without PNS and tumour. In addition, our permeabilized SOX1 F-CBA picked up 2/19 HuD Ab+ serum samples, identified seropositive by fixed IIF and line blots, from OUH Clinical

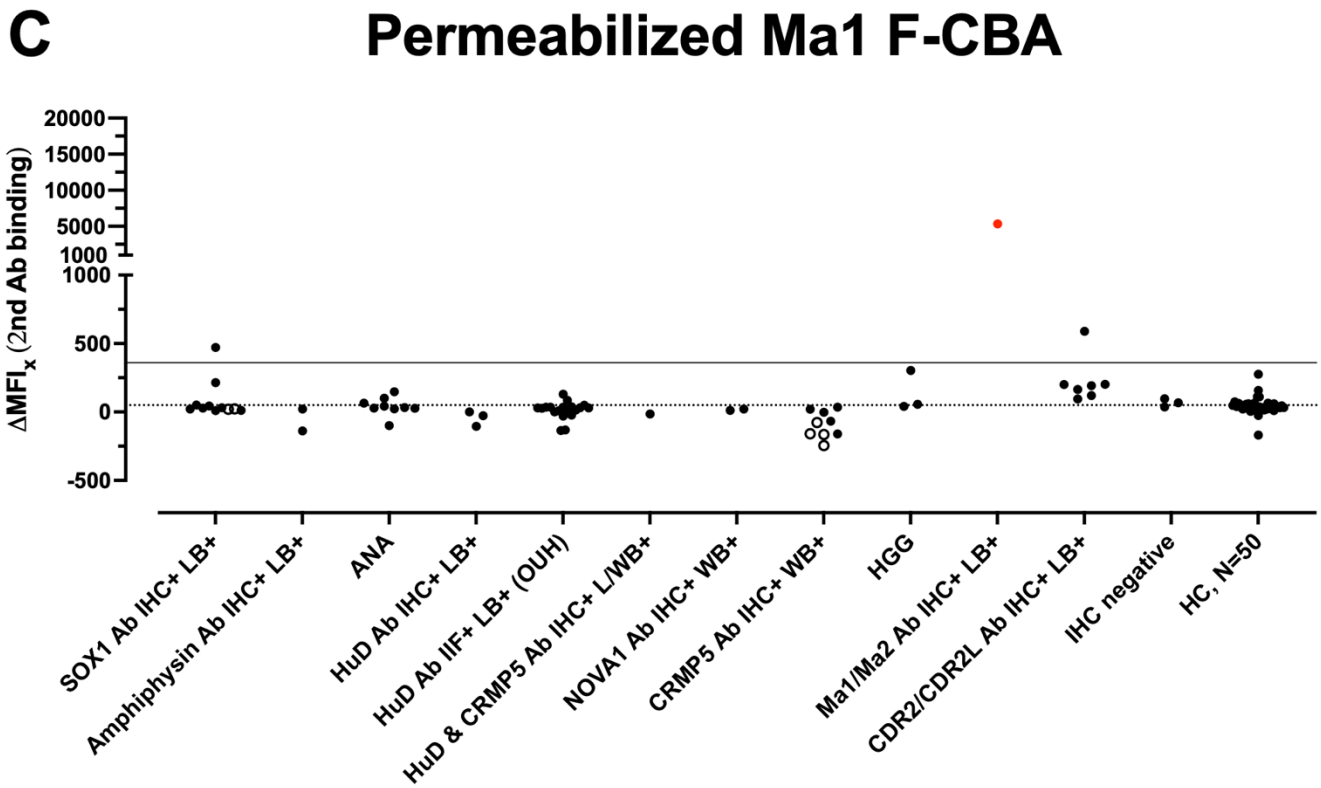
Immunology Unit and a HuD and CRMP5 Ab+ serum sample, identified seropositive by fixed IHC and line/western blots. However, we picked up a SOX1 Ab+ serum sample, identified seropositive by line blots only, from a patient without PNS and tumour.

In our permeabilized Ma1 and Ma2 F-CBAs, 5/98 samples were picked up as Ma1 or Ma2 Ab F-CBA+, and 1/98 sample was picked up as Ma1 and Ma2 Ab F-CBA+ (Figure 5.15c-d). The latter was from a patient with seminoma and limbic encephalitis, but the Ma2 Ab+ sample, identified seropositive by line blots only, was from a patient without PNS and tumour. Our permeabilized Ma1 F-CBA picked up 1/11 SOX1 Ab+ and 1/7 CDR2/CDR2L Ab+ serum samples, identified seropositive by fixed IHC and line blots, with $\Delta MFI_x \sim 500$. In addition, our permeabilized Ma2 F-CBA picked up 1/19 HuD Ab+ serum sample, identified seropositive by fixed IIF and line blots, from OUH Clinical Immunology Unit, with $\Delta MFI_x = 5521$.

To conclude, our quadruplex permeabilized F-CBA has identified all the patients diagnosed with PNS and tumours, and it didn't pick up 1/2 CRMP5 Ab+, 3/4 SOX1 Ab+ serum samples, identified seropositive by line blots only, from patients without PNS or tumour. In addition, our quadruplex permeabilized F-CBA identified additional antibody diagnoses to 9 serum samples, which had been originally identified seropositive for HuD Ab+ (N=5), HuD and CRMP5 Ab+ (N=1), SOX1 Ab+ (N=2) and CDR2/CDR2L Ab+ (N=1) by fixed IHC/IIF and line/western blots. However, there was no accessible clinical details for us to further interpret those 9 samples, from OUH Clinical Immunology Unit and Mayo Clinic, in a clinically useful manner.


A
Permeabilized CRMP5 F-CBA
ΔMFIx (2nd Ab binding)
20000
15000
10000
5000
1000
1000
500
0
-500
SOX1 Ab IHC+ LB+
Amphiphysin Ab IHC+ LB+
ANA
HuD Ab IHC+ LB+
HuD Ab IIF+ LB+ (OUH)
HuD & CRMP5 Ab IHC+ L/WB+
NOVA1 Ab IHC+ WB+
CRMP5 Ab IHC+ WB+
HGG
Ma1/Ma2 Ab IHC+ LB+
CDR2/CDR2L Ab IHC+ LB+
IHC negative
HC, N=50


B
Permeabilized SOX1 F-CBA
ΔMFIx (2nd Ab binding)
20000
15000
10000
5000
1000
1000
500
0
-500
-1000
SOX1 Ab IHC+ LB+
Amphiphysin Ab IHC+ LB+
ANA
HuD Ab IHC+ LB+
HuD Ab IIF+ LB+ (OUH)
HuD & CRMP5 Ab IHC+ L/WB+
NOVA1 Ab IHC+ WB+
CRMP5 Ab IHC+ WB+
HGG
Ma1/Ma2 Ab IHC+ LB+
CDR2/CDR2L Ab IHC+ LB+
IHC negative
HC, N=50


C
Permeabilized Ma1 F-CBA
ΔMFIx (2nd Ab binding)
20000
15000
10000
5000
1000
1000
500
0
-500
SOX1 Ab IHC+ LB+
Amphiphysin Ab IHC+ LB+
ANA
HuD Ab IHC+ LB+
HuD Ab IIF+ LB+ (OUH)
HuD & CRMP5 Ab IHC+ L/WB+
NOVA1 Ab IHC+ WB+
CRMP5 Ab IHC+ WB+
HGG
Ma1/Ma2 Ab IHC+ LB+
CDR2/CDR2L Ab IHC+ LB+
IHC negative
HC, N=50

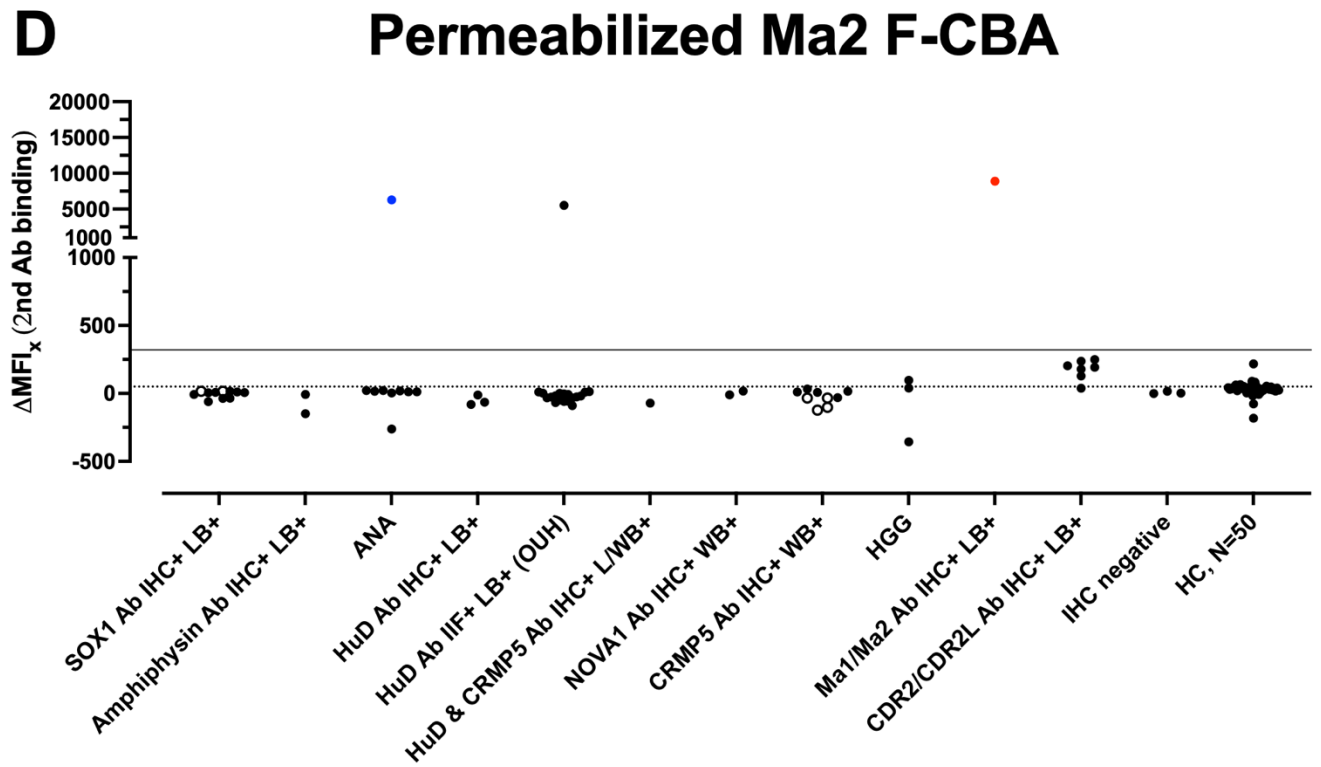

D
Permeabilized Ma2 F-CBA
ΔMFIx (2nd Ab binding)
20000
15000
10000
5000
1000
1000
500
0
-500
SOX1 Ab IHC+ LB+
Amphiphysin Ab IHC+ LB+
ANA
HuD Ab IHC+ LB+
HuD Ab IIF+ LB+ (OUH)
HuD & CRMP5 Ab IHC+ L/WB+
NOVA1 Ab IHC+ WB+
CRMP5 Ab IHC+ WB+
HGG
Ma1/Ma2 Ab IHC+ LB+
CDR2/CDR2L Ab IHC+ LB+
IHC negative
HC, N=50

Figure 5.15: The results of quadruplex permeabilized F-CBA for detecting autoantibodies to CRMP5, SOX1, Ma1 and Ma2. (a-d) 52 serum and 6 CSF samples from our collaborators, and 50 healthy sera were screened by our quadruplex live F-CBA for detecting autoantibodies to (a) untagged CRMP5, eGFP-tagged (b) SOX1, (c) Ma1 and (d) Ma2. The ΔMFI_x of each serum (solid dot) and CSF sample (hollow dot) were plotted on the y-axis, and the sample cohorts were mentioned below the x-axis. The red dots indicated the samples were from patients diagnosed with high/intermediate-risk PNS, tumours and the corresponding autoantibodies identified by fixed IHC/IIF and line/western blots. The blue dots indicated the samples were identified seropositive for the autoantibodies, which we were screening, by line blots only, and from patients without high-risk PNS, tumour or both. The cut-offs of serum and CSF samples were as the solid and dotted black lines respectively.

Table 5.5: Summary of the samples picked up by quadruplex permeabilized F-CBA for detecting autoantibodies to CRMP5, SOX1, Ma1 and Ma2

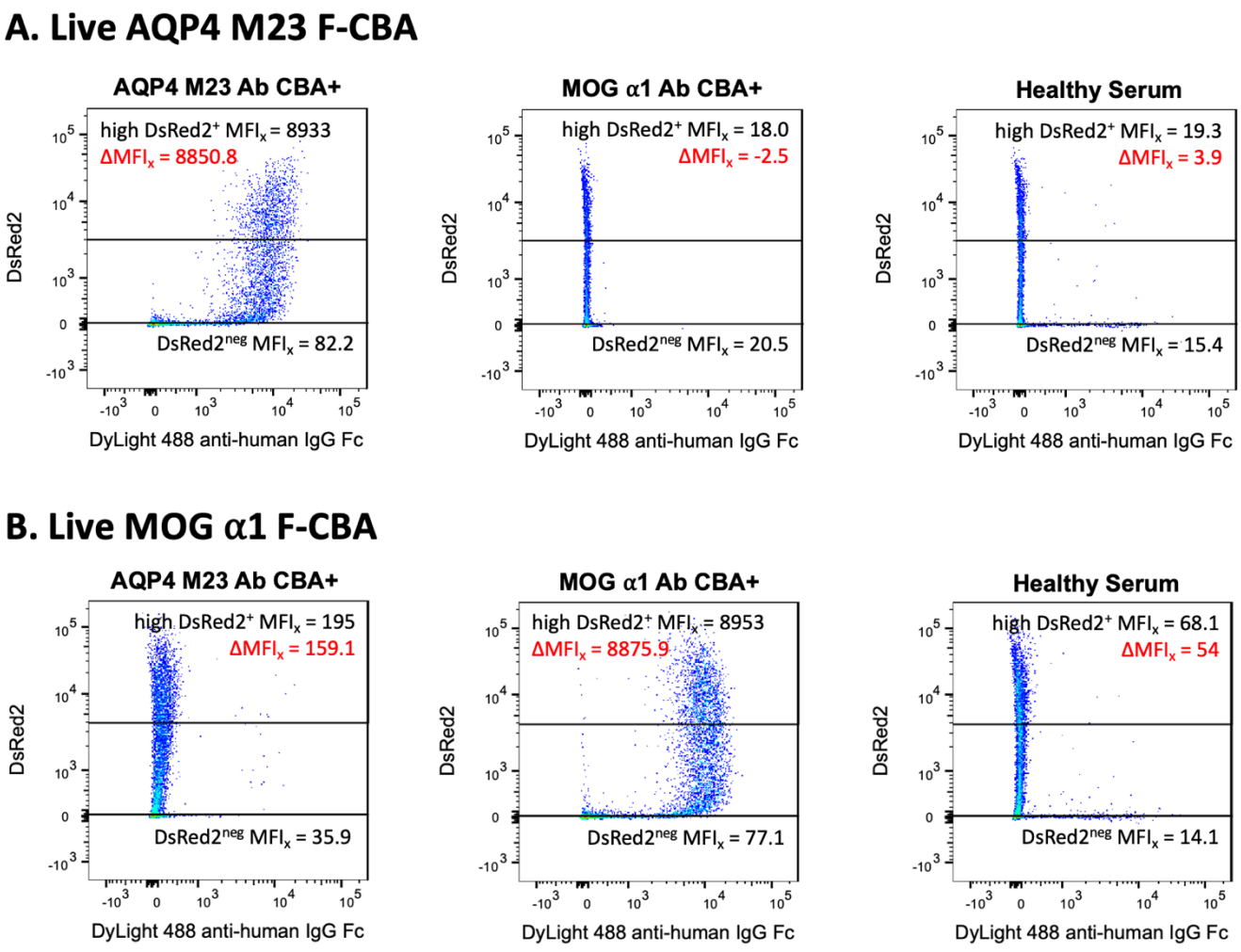
	Permeabilized CRMP5 F-CBA (untagged)	**Permeabilized SOX1 F-CBA (eGFP-tagged)**	**Permeabilized Ma1 F-CBA (eGFP-tagged)**	**Permeabilized Ma2 F-CBA (eGFP-tagged)**
SOX1 Ab IHC+ LB+, N=11	1/11 (9.1%)	11/11 (100%)	1/11 (9.1%)	0/11 (0%)
Amphiphysin Ab IHC+ LB+, N=2	0/2 (0%)	0/2 (0%)	0/2 (0%)	0/2 (0%)
ANA, N=9	0/9 (0%)	0/9 (0%)	0/9 (0%)	1/9 (11.1%)
HuD Ab IIF+ LB+, N=19 (from OUH)	2/19 (10.5%)	2/19 (10.5%)	0/19 (0%)	1/19 (5.3%)
HuD Ab IHC+ LB+, N= 3	0/3 (0%)	0/3 (0%)	0/3 (0%)	0/3 (0%)
HuD & CRMP5 Ab IHC+ L/WB+, N=1	1/1 (100%)	1/1 (100%)	0/1 (0%)	0/1 (0%)
NOVA1 Ab IHC+ WB+ N=2	0/2 (0%)	0/2 (0%)	0/2 (0%)	0/2 (0%)
CRMP5 Ab IHC+ WB+, N=9	8/9 (88.9%)	0/9 (0%)	0/9 (0%)	0/9 (0%)

HGG, N=3	0/3 (0%)	0/3 (0%)	0/3 (0%)	0/3 (0%)
Ma1/Ma2 Ab IHC+ LB+, N=1	0/1 (0%)	0/1 (0%)	1/1 (100%)	1/1 (100%)
CDR2/CDR2L Ab IHC+ WB+, N=7	0/7 (0%)	0/7 (0%)	1/7 (14.3%)	0/7 (0%)
IHC negative, N=3	1/3 (33.3%)	1/3 (33.3%)	0/3 (0%)	0/3 (0%)
IHC-, LB+ in the autoantibodies we screened	1/2 (50%)	1/4 (25%)	N/A	1/1 (100%)
HC, N=50	0/50 (0%)	0/50 (0%)	0/50 (0%)	0/50 (0%)

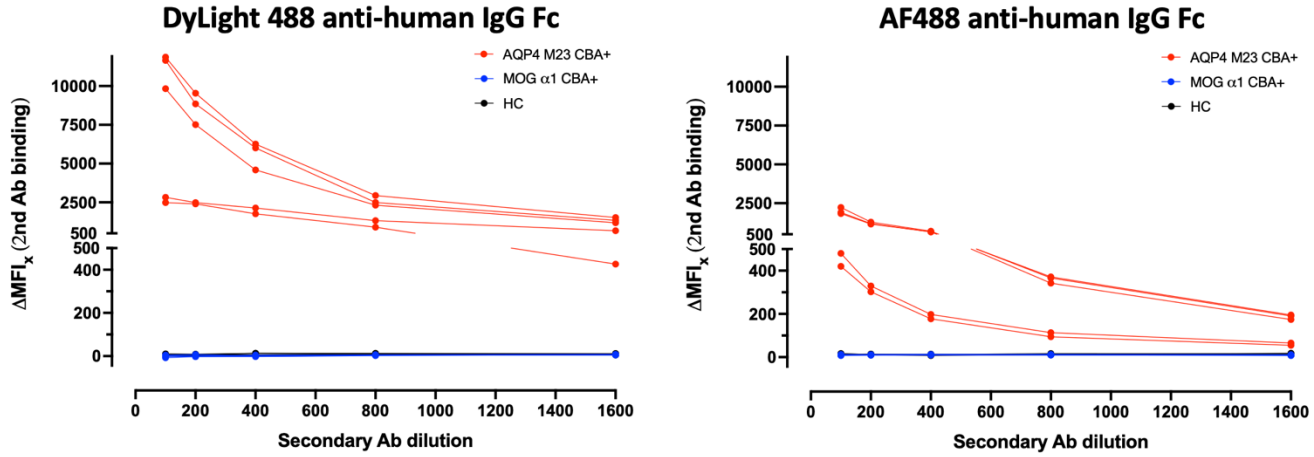
5.5.6. The DsRed2-reporting simplex live F-CBAs for detecting autoantibodies to AQP4 M23 and MOG α1 isoforms

After the success of developing F-CBAs to detect onconeural autoantibodies, we then established DsRed2-reporting simplex live F-CBAs for detecting autoantibodies to AQP4 M23 and MOG α1 isoforms in the serum samples from patients with autoimmune-mediated demyelinating diseases, e.g., NMOSD and MOGAD. With applying the gating strategy as described in Figure 2.4, our simplex live AQP4 M23 and MOG α1 CBAs could distinguish the AQP4 M23 Ab CBA+ and MOG α1 Ab CBA+ serum samples (Figure 5.16a-b). Next, at 1:20 serum dilution, we titrated two secondary antibodies - DyLight 488 and AF488 anti-human IgG Fc antibodies, from 1:100 to 1:1600 when screening 5 AQP4 M23 Ab CBA+ sera, 5 MOG α1 Ab CBA+ and 5 healthy sera. From the results, our live AQP4 M23 F-CBA had lower background compared to our live MOG α1 F-CBA, and AF488 anti-human IgG Fc antibody produced lower background compared to DyLight 488 anti-human IgG Fc antibody

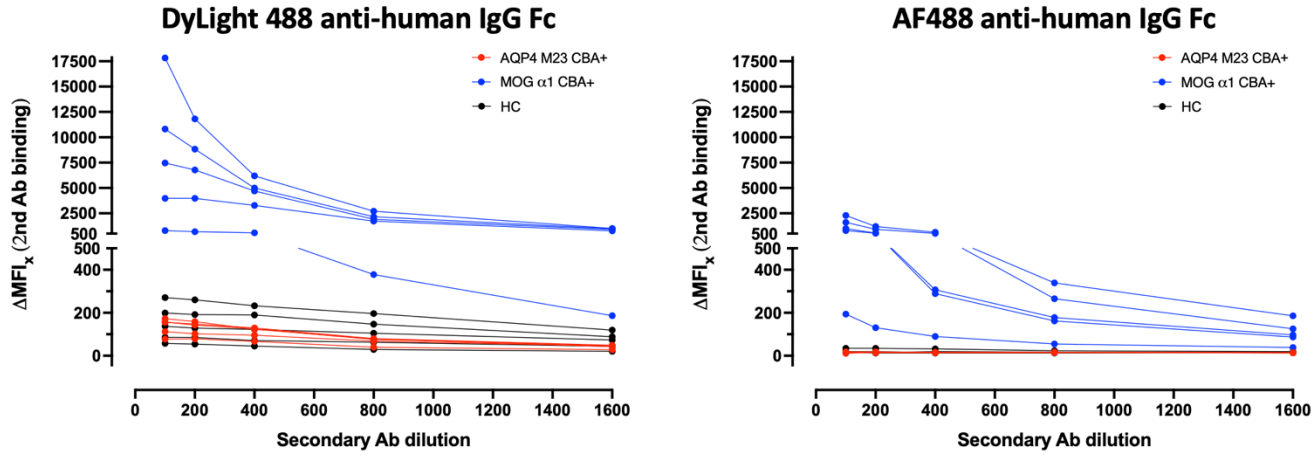
(Figure 5.16c-d). In addition, DyLight 488 anti-human IgG Fc antibody showed higher signal-to-noise ratio than AF488 anti-human IgG Fc antibody from 1:200 to 1:1600 dilution for detecting autoantibodies to AQP4 M23 and MOG α1 isoforms (Figure 5.16e). Except at 1:100 dilution, AF488 anti-human IgG antibody presented higher signal-to-noise ratio than DyLight 488 anti-human IgG Fc antibody to detect MOG α1 autoantibodies. After considerations, we decided to apply 1:200 diluted DyLight 488 anti-human IgG Fc antibody for secondary incubation step.



C. Live AQP4 M23 F-CBA



D. Live MOG α1 F-CBA



E

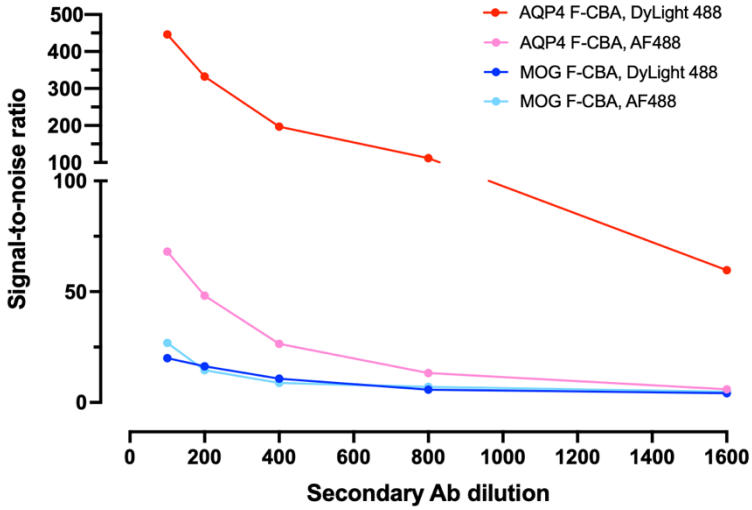


Figure 5.16: The DsRed2-reporting simplex live F-CBAs for detecting autoantibodies to AQP4 M23 and MOG α1 isoforms. (a-b) When screening the sera with autoantibodies to AQP4 M23 or MOG α1 isoform, and a healthy serum, the live singlets in our (a) live AQP4 M23 F-CBA and (b) live MOG α1 F-CBA were plotted. The DsRed2 signals were plotted on the y-axis, and the secondary antibody binding signals were plotted on the x-axis. The MFI_x were mentioned at the top right/left corners of each gate, and the ΔMFI_x in each plot were quoted in red. (c-d) The titration results of our (c) live AQP4 M23 F-CBA and (d) live MOG α1 F-CBA were plotted with using DyLight 488 (left) or AF488 (right) anti-human IgG Fc antibodies as secondary antibodies. The antibodies were titrated from 1:100 to 1:1600. The red lines were 5 AQP4 M23 Ab CBA+ sera, the blue lines were 5 MOG α1 Ab CBA+ sera and the black lines were 5 healthy sera. The ΔMFI_x were plotted on the y-axis, and the 2nd antibody dilutions were plotted on the x-axis. (e) The signal-to-noise ratios of each assay and titration were plotted on the y-axis, and the 2nd antibody dilutions were plotted on the x-axis. The assay types were color-coded with the legends.

With applying the decided setting, our live AQP4 M23 F-CBA picked up all the 28 serum samples in AQP4 M23 Ab CBA+ cohort, including the 7 samples with low titres of AQP4 M23 autoantibodies (hollow dots), and didn't pick up all the samples in MOG α1 Ab CBA+, double negative and healthy cohorts (Figure 5.17a). Also, our live AQP4 M23 F-CBA correlated well (p-value < 0.0001) with our live AQP4 M23 CBA when screening the same 28 AQP4 M23 Ab+ serum samples (Figure 5.17b).

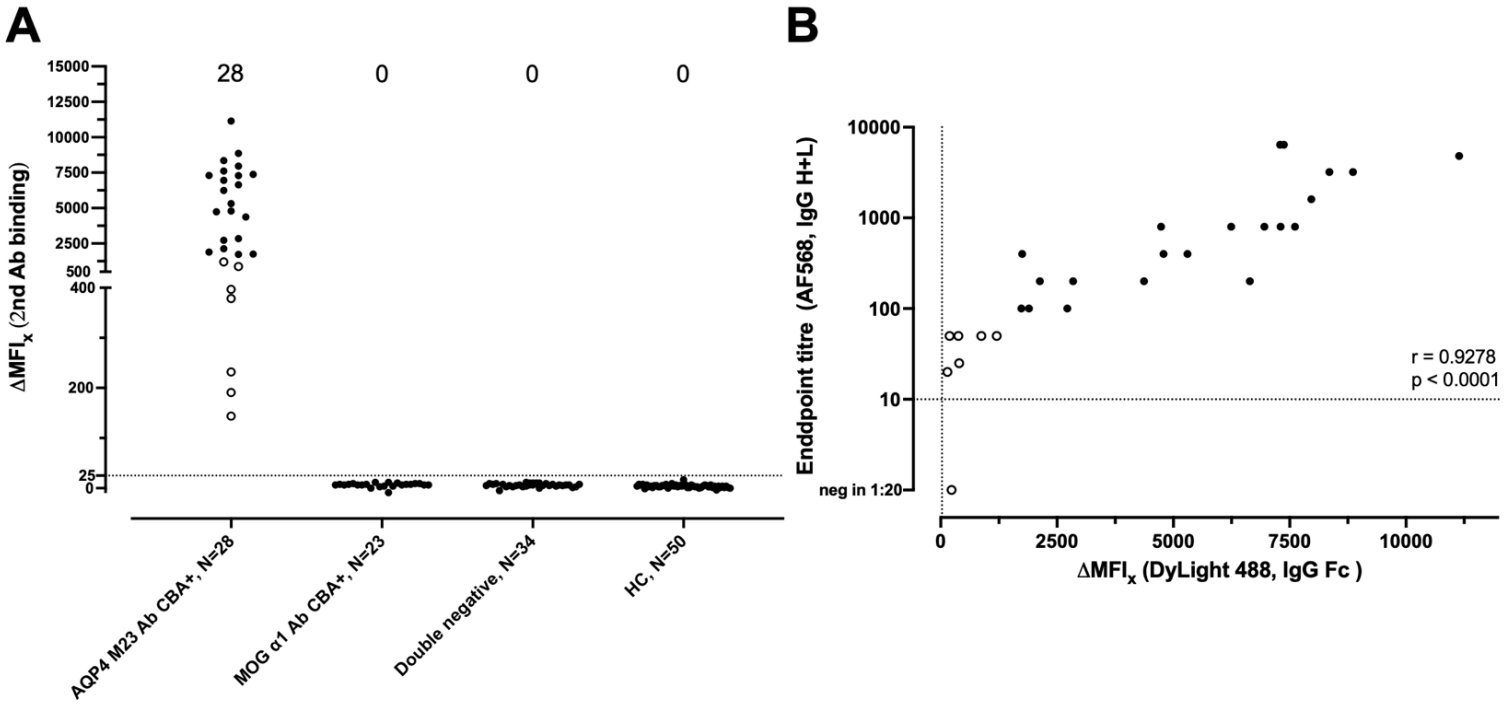


Figure 5.17: Live AQP4 M23 F-CBA was robust and correlated well with live AQP4 M23 CBA. (a) When screening 28 AQP4 M23 Ab CBA+ sera, 23 MOG α1 Ab CBA+ sera, 34 double negative sera and 50 healthy sera, the ΔMFI_x from live AQP4 M23 F-CBA were plotted on the y-axis, and the sample cohorts were mentioned below the x-axis. The hollow dots were the samples with the endpoint titres from live AQP4 M23 CBA ≦ 50. The cut-off was as the dotted black line. The number of samples above the cut-off in each cohort were quoted above. (b) Among the 28 AQP4 M23 Ab CBA+ samples, the endpoint titres from live AQP4 M23 CBA using 1:750 diluted AF568 anti-human IgG (H+L) antibody were plotted on the y-axis, and the ΔMFI_x from live AQP4 M23 F-CBA using 1:200 diluted DyLight 488 anti-human IgG Fc antibody were plotted on the x-axis. The hollow dots were the samples with the endpoint titres from live AQP4 M23 CBA ≦ 50. The r and p-values were calculated via Spearman nonparametric correlation test. The cut-offs were as the dotted black lines.

However, our live MOG α1 F-CBA was with problems. Although it didn't pick up all the 28 samples in AQP4 M23 Ab CBA+ cohort, there was an overlap of ΔMFI_x results between MOG α1 Ab CBA+ and double negative cohorts, i.e., we couldn't entirely distinguish them with the cut-off (Figure 5.18a). Therefore, we defined a high cut-off as "median + 3 x standard deviations" of the ΔMFI_x from the samples in double negative cohort. By doing so, the 18 samples above the cut-off in double negative cohorts stayed below the high cut-off. To reduce the background, we transfected the cells with less amount of DsRed2-reporting MOG α1 plasmid (1:8 diluted with DsRed2 only plasmid) to reduce the level of MOG α1 expression on the surface of HEK cells. As Figure 5.18b, although the overall background was reduced, the high cut-off was still required to not pick up any sample in double negative cohort.

Despite correlating well with the endpoint titres from live MOG α1 CBA, there were some samples with medium to low titres of MOG-IgG1 (blue and grey dots) distributed between the cut-off and high cut-off of our live MOG F-CBAs (Figure 5.18c-d). Surprisingly, 2 sample with low titres of MOG-IgG1 (grey dots) had the top 2 highest ΔMFI_x in double negative cohort. Because the secondary antibody we used was

specific to IgG Fc, it was possible that other MOG-IgG subclasses contributed to the total MOG IgG binding. Nevertheless, when applying high cut-off, we didn't pick up all the samples with medium to low titres of MOG-IgG1 (blue and grey dots) but only pick up the samples with high titres of MOG-IgG1 (blue dots).

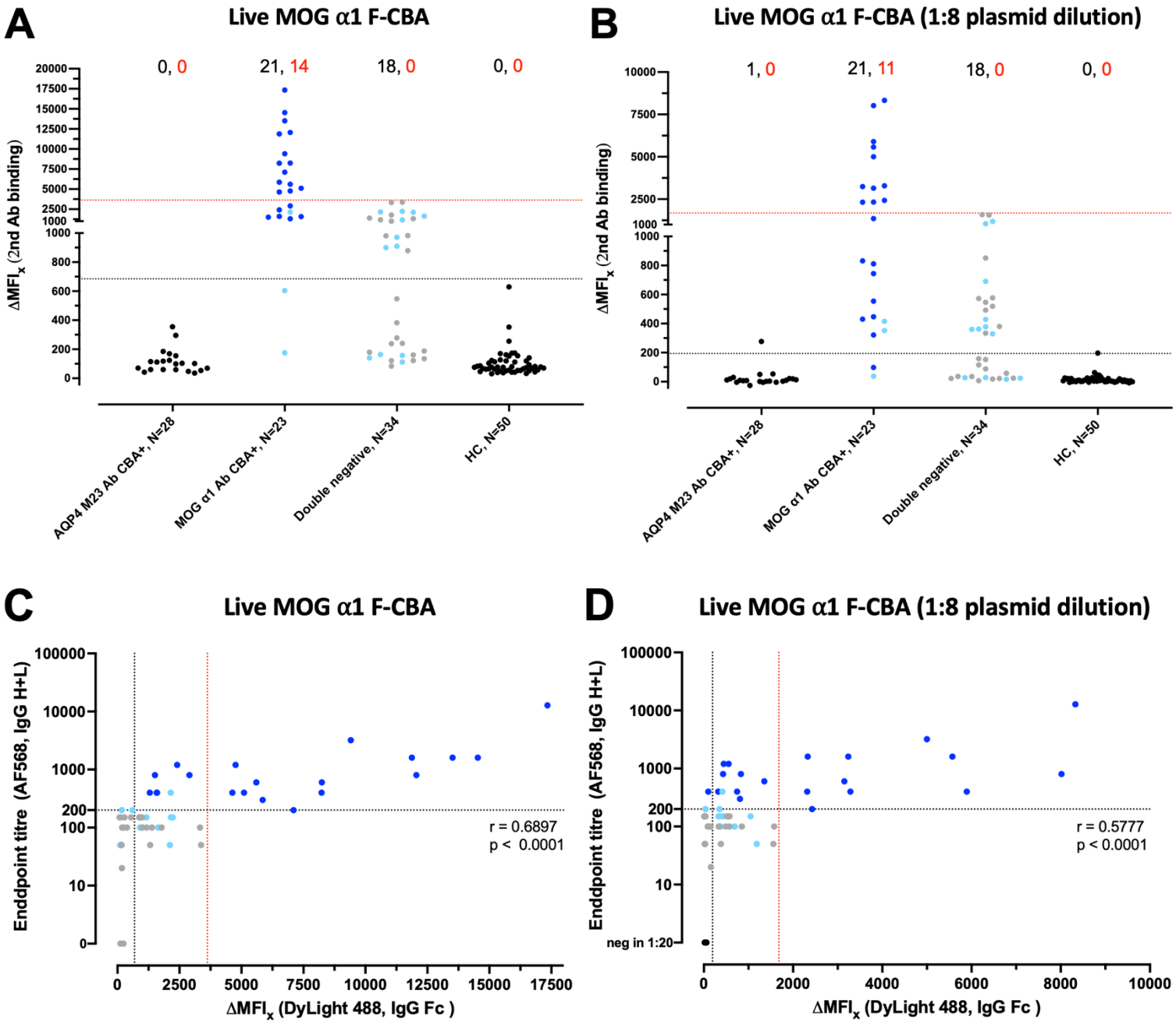
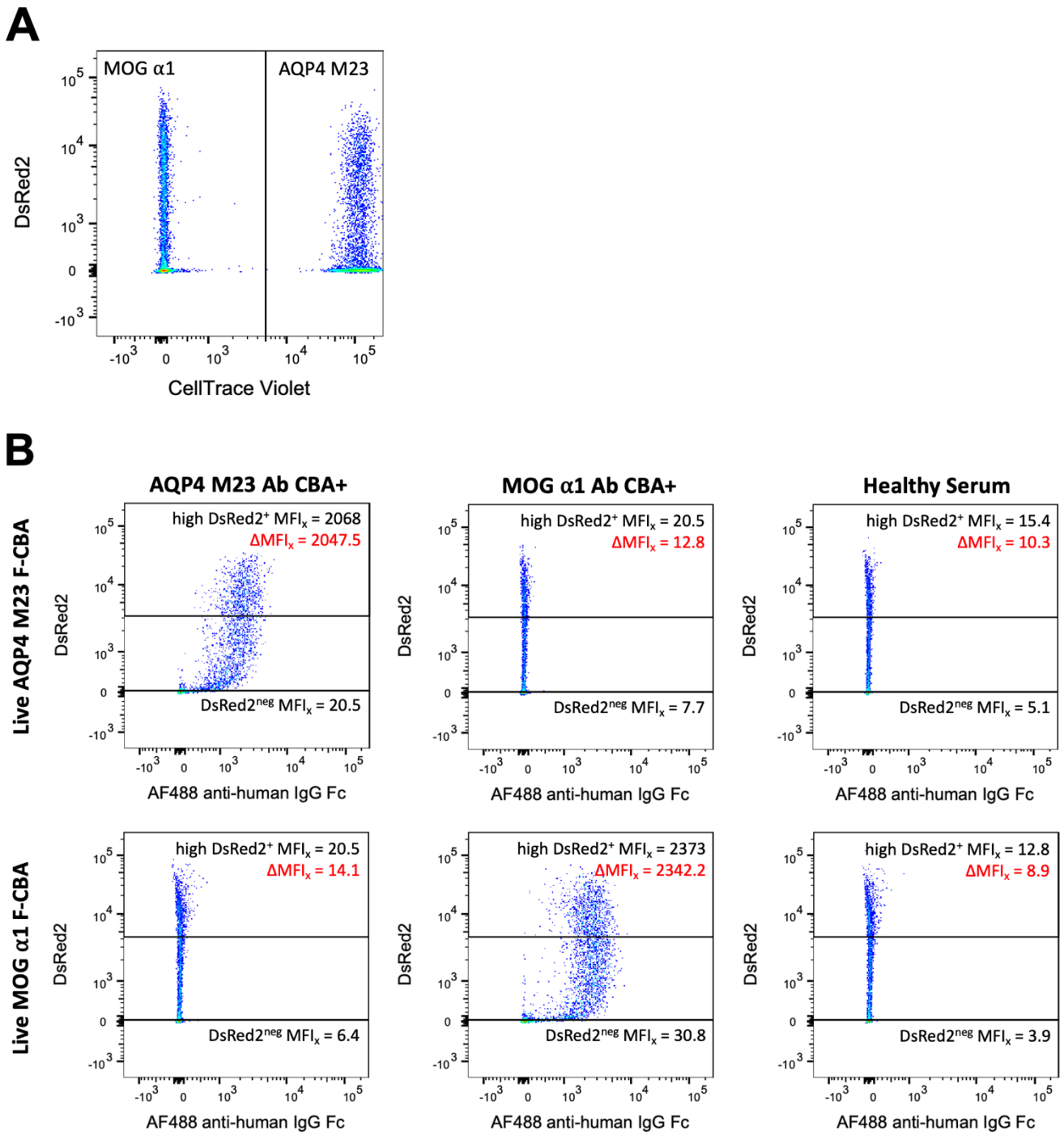


Figure 5.18: Live MOG α1 F-CBAs couldn't distinguish the samples between MOG α1 Ab CBA+ and double negative cohorts with the cut-offs. (a-b) When screening the same cohorts as Figure 5.17, the ΔMFI_x from (a) normal and (b) 1:8 plasmid-diluted live MOG α1 F-CBAs were plotted on the y-axis, and the sample cohorts were mentioned below the x-axis. The dark blue, light blue and grey dots indicated the samples with 1:20 CBA visual scores ≥ 2, between 1-1.75 and < 1, respectively, in live MOG α1 IgG1 CBA. The cut-offs and high cut-offs were as the dotted black and red lines, respectively. The number of samples above the cut-offs and high cut-offs in each cohort were quoted above in black and red, respectively. (c-d) Among the 23 MOG α1 Ab CBA+ and 34 double negative samples, the endpoint titres from live MOG α1 CBA using 1:750 diluted AF568 anti-human IgG (H+L) antibody were plotted on the y-axis, and the ΔMFI_x from live MOG α1 F-CBA using 1:200 diluted DyLight 488 anti-human IgG Fc antibody were plotted on the x-axis. The dark blue, light blue and grey dots indicated the samples with 1:20 CBA visual scores ≥ 2, between 1-1.75 and < 1, respectively, in live MOG α1 IgG1 CBA. The cut-offs and high cut-offs were as the black and red lines, respectively. The r and p-values were calculated via Spearman nonparametric correlation test.

Alternatively, 1:100 diluted AF488 anti-human IgG Fc antibody was used to reduce the background because Figure 5.16e suggested it had higher signal-to-nose ratio at 1:100 dilution for detecting MOG α1 autoantibodies compared to DyLight 488 anti-human IgG Fc antibody.

This time, we color-coded AQP4 M23 expressing HEK cells with 5 μM of CTV and kept MOG α1 expressing cells unstained in order to perform a duplex F-CBA (Figure 5.19a). Similar to simplex live F-CBAs, our duplex live F-CBA could distinguish AQP4 M23 Ab+ and MOG α1 Ab+ serum samples (Figure 5.19b). However, when using 1:100 diluted AF488 anti-human IgG antibody, our duplex live F-CBA didn't pick up 3/28 serum samples in AQP4 M23 Ab CBA+ cohort (Figure 5.19c). Although the background of live MOG F-CBA was further reduced, the high cut-off was still required to achieve better distinction between MOG α1 Ab CBA+ and double negative cohorts (Figure 5.19d). However, this time, the high cut-off picked up 1/34 samples in double

negative cohort, and that sample was one of the two samples with the top 2 highest ΔMFI_x in double negative cohort but with low titre of MOG-IgG1 (1:20 CBA visual score < 1). The similar finding made us suspect if the total MOG-IgG binding was solely contributed by MOG-IgG1 or not.



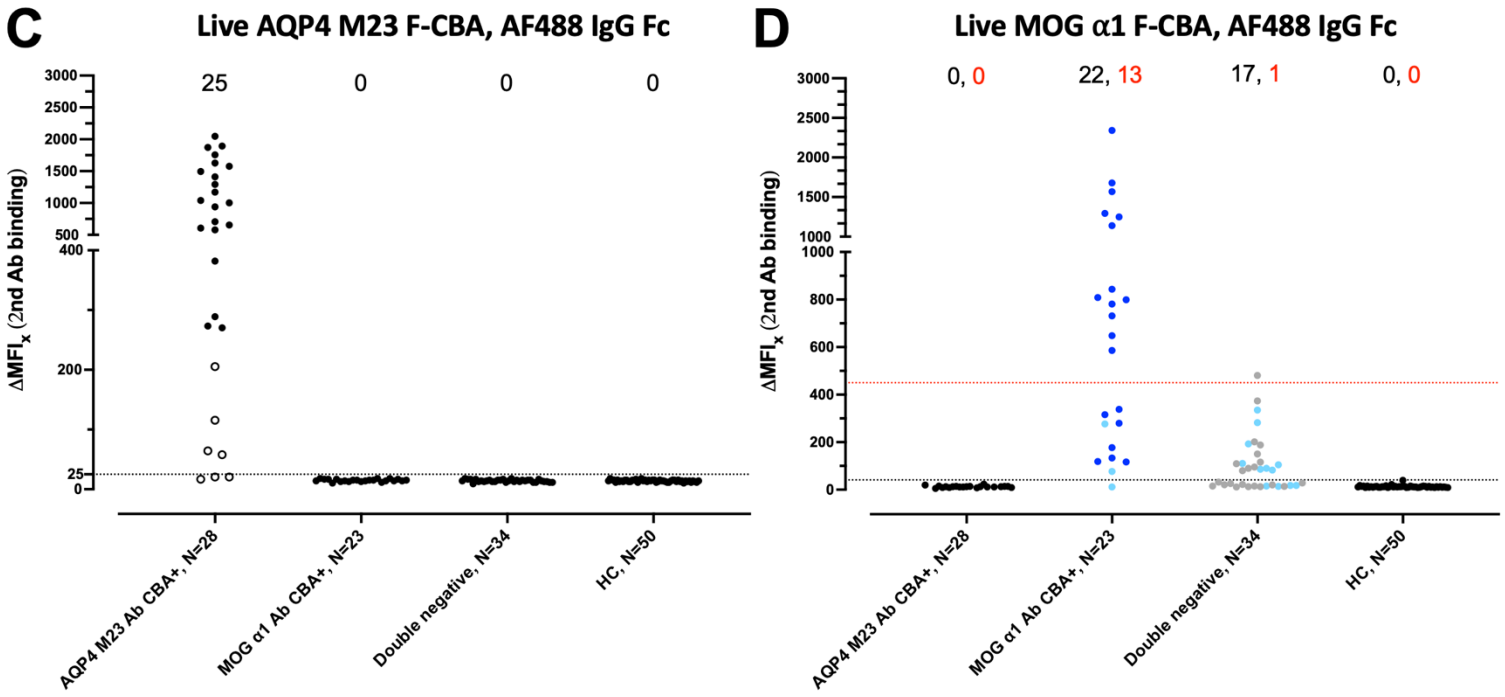


Figure 5.19: The Duplex live F-CBA for simultaneously detecting autoantibodies to AQP4 M23 and MOG α1 isoforms. (a) The live singlets of our duplex live F-CBA were plotted. The DsRed2 signals were plotted on the y-axis, and the CTV signals were plotted on the x-axis. (b) As the AQP4 M23 and MOG α1 expressing HEK cells were gated, their DsRed2 signals were plotted on the y-axis, and their secondary antibody binding signals were plotted on the x-axis. The top row was live AQP4 M23 F-CBA, and the bottom row was live MOG α1 F-CBA. Our duplex live F-CBA was applied to screen a AQP4 M23 Ab+ serum, a MOG α1 Ab+ serum and a healthy serum. The MFI_x were mentioned at the top right corners of each gate, and the ΔMFI_x of each sample were quoted in red. (c-d) When screening the same cohorts as Figure 5.17, the ΔMFI_x from (c) live AQP4 M23 and (d) live MOG α1 F-CBAs using 1:100 diluted anti-human IgG Fc antibody were plotted on the y-axis, and the sample cohorts were mentioned below the x-axis. The dark blue, light blue and grey dots indicated the samples with 1:20 CBA visual scores ≥ 2, between 1-1.75 and < 1, respectively, in live MOG α1 IgG1 CBA. The cut-off and high cut-off were as the dotted black and red lines, respectively. The number of samples above the cut-off and high cut-off in each cohort were quoted in black and red, respectively.

To testify our guess, we then applied 1:100 diluted AF488 anti-human IgG1 for the secondary incubation of our live duplex F-CBA, which was the identical secondary antibody used in our diagnostic lab for running live MOG α1 CBA. From the live AQP4 M23 F-CBA results, our duplex live F-CBA using 1:100 diluted AF488 anti-human IgG1 antibody didn't pick up 2/28 samples in AQP4 M23 Ab CBA+ cohort (Figure 5.20a). In addition, the same 2 samples with low titres of MOG-IgG1 identified by live MOG α1 CBA (grey dots) were still having the top 2 highest ΔMFI_x in double negative cohort (Figure 5.20b). This time, because we applied anti-human IgG1 antibody for secondary incubation, the possibility of MOG-IgG antibody binding contributed by other Ig subclasses could be excluded. Therefore, the discrepancy was more likely due to the manual error. Furthermore, the results of duplex live F-CBA between using AF488 anti-human IgG Fc and IgG1 antibody at 1:100 dilution were highly correlated with one another for detecting MOG α1 autoantibodies (Figure 5.20c). The results suggested MOG-IgG1 antibody was predominant in patients' serum samples, and either AF488 anti-human IgG Fc or IgG1 secondary antibody could pick up the binding of MOG-IgG antibody on the surface of HEK cells.

To conclude, using either AF488 anti-human IgG Fc or IgG1 antibody at 1:100 dilution for our duplex live F-CBA was not ideal because the assays didn't pick up 2-3 samples with low titres of AQP4 M23 autoantibodies. Therefore, using DyLight 488 anti-human IgG Fc shall be a better option for live AQP4 M23 F-CBA. On the other hand, our simplex live MOG α1 F-CBA using 1:200 diluted anti-human IgG Fc antibody picked up the most sample in live MOG α1 Ab CBA+ group (14/23) above the high cut-off compared to other settings we tried. Also, we proved that the predominant MOG-IgG subclass, which anti-human IgG Fc antibody recognized, was MOG-IgG1.

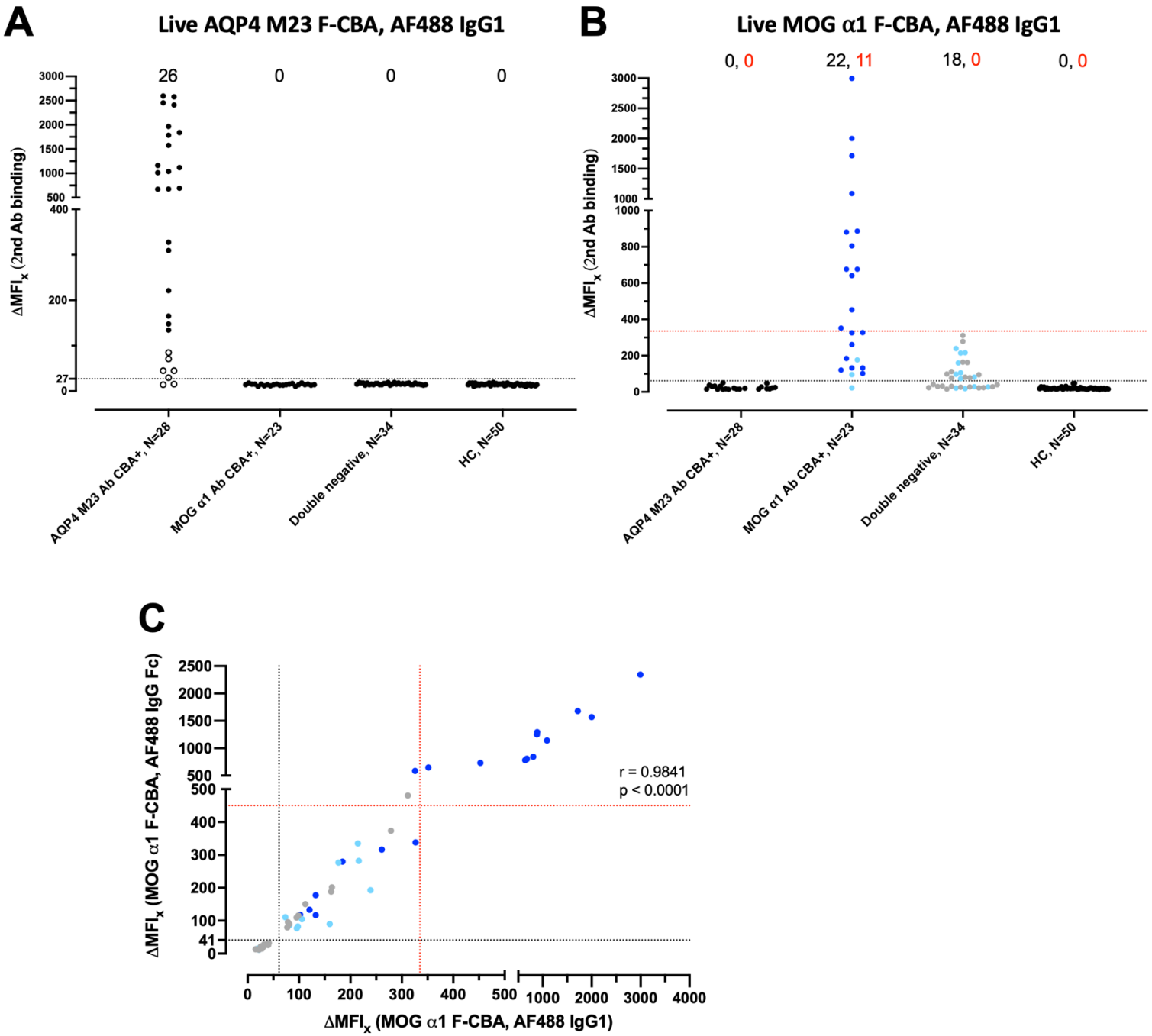


Figure 5.20: Our duplex live F-CBA presented similar results with using 1:100 diluted AF488 anti-human IgG1 antibody. (a-b) When screening the same cohorts as Figure 5.17, the ΔMFI_x from (a) live AQP4 M23 and (d) live MOG α1 F-CBAs using 1:100 diluted anti-human IgG1 antibody were plotted on the y-axis, and the sample cohorts were mentioned below the x-axis. The dark blue, light blue and grey dots indicated the samples with 1:20 CBA visual scores ≥ 2, between 1-1.75 and < 1, respectively, in live MOG α1 IgG1 CBA. The cut-off and high cut-off were as the dotted black and red lines, respectively. The number of samples above the cut-off and high cut-off in each cohort were quoted in black and red, respectively. (c) Among the 23 MOG α1 Ab CBA+ and 34 double negative samples, the ΔMFI_x from live MOG α1 F-

CBA using 1:100 diluted AF488 anti-human IgG Fc antibody were plotted on the y-axis, the ΔMFI_x from live MOG α1 F-CBA using 1:100 diluted AF488 anti-human IgG1 antibody were plotted on the x-axis. The dark blue, light blue and grey dots indicated the samples with 1:20 CBA visual scores ≥ 2, between 1-1.75 and < 1, respectively, in live MOG α1 IgG1 CBA. The cut-offs and high cut-offs were as the black and red lines, respectively. The r and p-values were calculated via Spearman nonparametric correlation test.

5.6. Discussion

In this chapter, we developed multiplex flow cytometry diagnostic assays to detect onconeural autoantibodies found in patients with PNS and tumours, as well as AQP4 and MOG autoantibodies found in patients with autoimmune-mediated demyelinating diseases. We transferred our eGFP-tagged live and permeabilized CBAs, described in Chapter IV, to flow cytometry platform for quantifying the binding of onconeural autoantibodies, and we applied the same idea to establish DsRed2-reporting live F-CBA for quantifying the bindings of autoantibodies to AQP4 M23 and MOG α1 isoforms.

Our pilot live HuD F-CBA picked up 22/24 samples from Mayo Clinic and OUH Clinical Immunology Unit as HuD Ab F-CBA+, and the ΔMFI_x from live HuD F-CBA showed good correlations with the endpoint titres from live HuD CBA. However, both assays didn't pick up 2/20 HuD Ab+ samples, identified seropositive by fixed IIF and line blots, from OUH. On the other hand, our live CRMP5 CBA was problematic as discussed in Chapter IV. When correlating the endpoint titres from live CRMP5 CBA with the endpoint titres from fixed IIF for detecting CRMP5 autoantibodies, the correlation was poor (Figure 4.13d) even though CRMP5 was proved being successfully expressed on the surface of HEK cells (Figure 4.4). We thought the membrane tethered CRMP5 may have difficulty forming multimeric structures so as to expose its C-terminal epitopes.

Therefore, we developed a new live CRMP5 F-CBA by adding soluble CRMP5 to membrane tethered CRMP5, and we found the access of CRMP5 autoantibodies was improved. Interestingly, when tested by our new CRMP5 F-CBA, the ΔMFI_x of 3/5 serum samples increased, but the ΔMFI_x of all the 3 CSF samples decreased compared to the ΔMFI_x in our original CRMP5 F-CBA (Figure 5.10). This finding implied the CRMP5 autoantibodies in patients' sera and CSF may recognize different CRMP5 epitopes. Next, because our new live CRMP5 F-CBA still didn't pick up 3/5 CRMP5 Ab+ serum samples, identified seropositive by fixed IHC and western blots, from Mayo Clinic, we developed an untagged permeabilized CRMP5 F-CBA, which made CRMP5 autoantibodies access to the native cytosolic CRMP5. The incomplete depletion of eGFP could be explained by a small proportion of translation bypassing the stop codon because the termination efficiency is known to depend on several factors, including the distance between the ribosome at the termination site and the poly-A binding proteins at the 3'-end (Dabrowski et al., 2015). Nevertheless, our permeabilized CRMP5 F-CBA picked up 4/5 CRMP5 Ab+ serum samples and all the 3 CRMP5 Ab+ CSF samples, identified seropositive by fixed IHC and western blots, from Mayo Clinic. To understand why our permeabilized CRMP5 F-CBA still missed a CRMP5 Ab+ serum sample, a larger PNS patient cohort with clinical details will be required to further investigate the head-to-head utility of our permeabilized CRMP5 F-CBA and fixed IHC.

Furthermore, we evaluated 5 live cell-labelling dyes, chose the suitable one and optimized the live cell-labelling protocol for multiplex purposes. Then, we established quadruplex live and permeabilized F-CBAs for simultaneously detecting autoantibodies to the surface-expressed onconeural antigens (HuD, Amphiphysin,

NOVA1 and CDR2L) or intracellularly expressed onconeural antigens (CRMP5, Ma1, Ma2 and SOX1) in the same well. Both quadruplex F-CBAs identified all the patients diagnosed with high/intermediate-risk PNS, tumours, and autoantibodies to HuD (N=3), Amphiphysin (N=2), CDR2L (N=2), CRMP5 (N=1), SOX1 (N=1) or Ma1 & Ma2 (N=1). In addition, our quadruplex live F-CBA correlated well with our individual live CBAs. In this chapter, our multiplex F-CBAs were demonstrated as a reliable, quantitative, and more efficient alternative to conventional CBAs, fixed IHC/IIF and line/western blots for detecting onconeural autoantibodies in the serum or CSF samples from patients diagnosed with PNS. However, apart for the samples from Barcelona, which were provided with clinical details, we couldn't make any clinical interpretation from the samples derived from Mayo Clinic and OUH Clinical Immunology Unit.

In terms of live AQP4 and MOG F-CBAs, our live AQP4 M23 F-CBA picked up all the 28 samples in AQP4 M23 Ab CBA+ cohort using 1:200 diluted DyLight 488 anti-human IgG Fc secondary antibody, and not picked up any sample in the control cohorts. However, the MOG F-CBA highlighted difficulties that have been found throughout the world. Our team had developed a live MOG α1 CBA using AF488 anti-human IgG1 secondary antibody that specifically identifies a non-MS demyelinating patient cohort (Waters et al., 2015). However, the clinical specificity was lost when IgG (H+L) secondary antibody was used in live MOG α1 CBA. In our live F-CBA, although we couldn't easily distinguish the samples between MOG α1 Ab CBA+ and double negative cohorts with the cut-off, the high cut-off was shown to be useful to make a clear distinction between the two. However, because we didn't have any clinical details for the samples from MOGAD clinics, we wouldn't be able to tell if the datapoints sitting between cut-off and high cut-off were true positive or true negative of the disease. In

the future, if those samples are identified as true positive after we receive their clinical details from the clinicians, we can then conclude our live F-CBA is more sensitive than live CBA currently applied in our diagnostic lab to detect MOG α1 autoantibodies. Besides, we also proved that the predominant MOG-IgG subclass in the samples we screen was MOG-IgG1, and the discrepant results between live MOG α1 F-CBA and CBA might be attributed to manual errors or different testing dates.

On the other hand, we also developed a live duplex F-CBA in an attempt to simultaneously detect autoantibodies to AQP4 M23 and MOG α1 isoforms by flow cytometry for generating automatic quantification of antibody levels and reducing the workload in detecting autoantibodies to both targets that are most often requested together. Although the background of live MOG F-CBA was reduced when using 1:100 diluted AF488 anti-human IgG Fc antibody, we didn't pick up 3/28 samples in AQP4 Ab CBA+ cohort. Again, the clinical details of those missed samples are required to judge if they are true negative or not. Also, further optimizations will be required to find the balance when simultaneously detecting autoantibodies to AQP4 M23 and MOG α1 isoforms in the same well. Nevertheless, we have developed a duplex live F-CBA platform, which is promising to be applied for efficiently identifying the samples, sent from NMOSD and MOGAD clinics, as either AQP4 M23 or MOG α1 Ab F-CBA+.

Chapter VI
General Discussion

Accurate autoantibody assays are key to help early disease diagnosis, instigate approved therapies or tumour screening which reduce patient morbidity and mortality. Many studies have demonstrated superiority of live CBAs to other antibody detection systems that include fixed CBAs, ELISA, FIPA and IHC. The aim of this thesis was to develop accurate live cell-based assays to detect autoantibodies in autoimmune-mediated neurological diseases, in patients with paraneoplastic neurological syndromes that have strong associations with specific cancers, and to detect antibodies to cytokines that predict the presence of a cancer in people with MG. Once individual tests were optimized, an attempt was made to multiplex the assays to improve test efficiency via CBA or flow cytometry. The data in the previous chapters highlights the success in developing and improving these different test systems. Here I discuss the key findings, strengths and imitations of my DPhil research and suggest future the next steps.

6.1. Summary and discussion of key findings

6.1.1. Myc-tagged, surface expressed cytokines in live CBAs detect autoantibodies and predict the presence of thymoma

In chapter III, we successfully developed a myc-tagged live CBA platform to detect autoantibodies to soluble cytokines, including IL-6, IL-12, IL17A, IL-17F, IL-22, IL-23, IFNα2, IFNα8 and IFNω1. We added the myc-tag to allow a direct measure of surface expression of each antigen. This approach supersedes the cytosolic DsRed2 reporter which informs on cells transfection but not on surface expression. While optimizing our myc-tagged live CBAs, we identified two issues. Firstly, we found that 4% formaldehyde appeared to destroy the myc-epitope, which was not recognized by the DyLight 550 anti-myc tag monoclonal antibody. In addition, the alexafluor488 anti-

human IgG (H+L) antibody non-specifically bound to DyLight 550 anti-myc tag monoclonal antibody. To resolve these issues, the fixation step was moved to the end of the assay and a DyLight 488 anti-human IgG Fc antibody, which did not cross-react, was applied with DyLight 550 anti-myc tag monoclonal antibody after sample incubation.

All tests had the same myc-tag. Data from the anti-myc tag antibody suggested that the different cytokines reproducibly expressed on the surface of the HEK cells at different levels. Likely, the different signal sequences impacted on surface expression, and this is worth future investigation. Nevertheless, we screened 68 healthy sera for antibodies to all the cytokines by CBA to generate a test cut-off. Of note, we found 3 healthy sera with relatively high endpoint titres of autoantibodies to IL-17F, IL-22 and IFNω1 respectively (endpoint titres = 1600 - 3200). Although some cytokine auto-antibodies were reported in both disease and healthy cohorts, they were much lower titres and less prevalent in healthy cohorts, e.g., autoantibodies to IFNα were found in 29.4% of patient with rheumatoid arthritis but only in 1.4% of healthy individuals (von Stemann et al., 2017, Cappellano et al., 2012, Meager et al., 2003). In our case, those 3 datapoints were excluded as the outliers for the determination of the test cut-off because their endpoint titres of the corresponding cytokine autoantibodies were higher than “median + 6 x standard deviation” of the 68 healthy sera we screened.

Next, the plasma or sera samples from 46 TAMG patients, 60 LOMG patients and 41 EOMG patients were screened by our live CBAs for detecting autoantibodies to IL-6, IL-12, IL-17A, IL-17F, IL-22, IL-23, IFNα2, IFNα8 and IFNω1. To predict the presence of thymoma, our live IFNα2, IFNα8, IFNω1 and IL-12 CBAs were more sensitive

compared to the others. Also, if only analyzing the pre-thymectomy TAMG cohort, the sensitivities of our live CBAs increased. These data suggest that the thymoma is breaking tolerance to a number of cytokines, particularly IFNα2, IFNα8, IFNω1 and IL-12. Previous studies reported an association between thymoma and neutralizing autoantibodies to IFNα and IL-12, and Shiono et al. found that the thymoma cells from > 40% patients seropositive for autoantibodies to IFNα or IL-12 could spontaneously produce the corresponding autoantibodies (Shiono et al., 2003, Meager et al., 1997, Meager et al., 2003). The finding implied *in situ* autoimmunization happened and perhaps germinal center formed within patients' thymoma. In addition, Meager et al. reckoned the selective autoimmunization happened due to the dendritic cells (DC) providing the source of IFNα and IL-12 in patients' thymoma where the microenvironment is inflammatory and autoimmunogenic. And because DC can develop from pre-T or pre-NK cell progenitor in thymus, the abnormal DC generated within the grossly thymopoietic thymoma, then circulating to periphery, might be a reason to explain why the autoantibodies to IFNα and IL-12 could persist years after patients' thymectomy. However, due to the persistence of antibody titres, our live CBAs are useful for prediction of the presence of a thymoma but lack power to identify aMG patients with recurrent thymoma.

The endpoint titres from the live CBAs agreed well with the published results generated by the LIPS assays for autoantibodies to monomeric IFNα2 and IL-12. Some borderline positive results against heterodimeric IL-12 on the LIPS assay were not reproducible by live CBA. Differences in construct design where the tag is at opposite ends of the cytokines, the difference in timing of the assays (the LIPS was performed on fresh sera, live CBA on the same sera after years of storage at freezer), or simple false-positive

test results by LIPS may explain the discrepant test results. Regardless, the live IL-12 CBA was robust enough to detect the autoantibodies to either IL-12 heterodimer or IL-12B homodimer. However, the same disease and healthy controls screened by our live CBAs shall also be screened by LIPS assays for us to evaluate the specificity of LIPS assays.

6.1.2. Live eGFP-tagged CBAs were superior to line blots for antibody detection in PNS patients

In chapter IV, an eGFP-tagged live CBA platform was established for detecting autoantibodies to onconeural antigens, including HuD, NOVA1, CDR2L, CRMP5, Amphiphysin, SOX1, CDR2, KLHL11, Ma1 and Ma2. The targeted onconeural antigens are expressed within neuro-glial cells, so each target was cloned between a Caspr2 signal peptide and a Caspr2 transmembrane domain in order to express them above the surface of HEK cells. HuD, NOVA1, CDR2L, CRMP5, and Amphiphysin were successfully surface expressed and detectable via our live CBA method. On the other hand, permeabilized CBAs were applied instead for detecting autoantibodies to the intracellularly expressed SOX1, CDR2, KLHL11, Ma1 and Ma2.

The surface expression of SOX1, CDR2, KLHL11, Ma1 and Ma2 could possibly be hindered by the intracellular interactions between our targets and HEK endogenous molecules, or they may form multimers that have difficulty expressing on the cell surface. For instance, CDR2 was found to sequester c-myc and downregulate its activity to inhibit programmed cell death (Okano et al., 1999, Wang et al., 2011). Ma1 and Ma2 were reported to form heterodimer with modulator-of-apoptosis-1' (MOAP-1), and MOAP-1 is ubiquitously expressed in many human tissues including HEK cells

(Pang et al., 2018, Lee et al., 2016b). SOX1 is a transcription factor that binds strongly to DNA with its high-mobility group (HMG) domain, and it is a known tumour suppressor that binds to β-catenin with its HMG domain in order to antagonize the WNT/β-catenin pathway (Jagga et al., 2021, Tsao et al., 2012). On the other hand, KLHL-11 is a member of E3 ubiquitin ligases within BTB-Kelch family, and the BTB domain allows KLHL-11 to form homodimer with one another (Canning et al., 2013). In summary, we speculate that interactions of the target proteins either with themselves, or with other proteins within the HEK cell prevent their surface expression.

Nevertheless, our live and permeabilized CBAs were capable of identifying onconeural autoantibodies in sera from patients with both high/intermediate-risk PNS and tumours. In addition, our CBAs demonstrated comparable diagnostic accuracy to fixed IHC but more specific compared to commercial line blots. Also, our live CBAs can be multiplexed, and a quadruplex assay to simultaneously detect autoantibodies to HuD, NOVA1, CDR2L and CRMP5 was developed as a proof of principle. Also, there was no loss of test accuracy with the quadruplex live CBA when compared to the simplex coverslip-based live CBAs. Therefore, our CBA method is a rapid alternative compared to fixed IHC and commercial line blots for detecting autoantibodies to multiple onconeural antigens.

6.1.3. The F-CBAs were developed to quantify autoantibody binding under simplex and multiplex settings

In Chapter V, flow cytometry diagnostic assays were developed for quantifying the autoantibodies not only to onconeural antigens in patients with PNS and tumour but also to AQP4 M23 and MOG α1 isoforms in patients with autoimmune-mediated

demyelinating diseases, e.g., NMOSD and MOGAD. The pilot live HuD F-CBA demonstrated that PE anti-human IgG Fc antibody was found more sensitive than DyLight 594 anti-human IgG Fc antibody at the same secondary antibody dilution. In addition, the live HuD F-CBA demonstrated excellent correlation (p-value < 0.0001) with the live HuD CBA.

The CRMP5 assay did not work well in the beginning. The endpoint titres on the live assay were poor and did not correlate to the IIF end-point titres sent with the samples (p-value = 0.85). We thought that the dimer formation of this target was impeded by the C-terminal tail attaching CRMP5 to the membrane. We co-transfected soluble CRMP5 and membrane linked CRMP5 to allow for some flexibility with dimer formation. This improved the assay but there was still discrepant data between this antigen specific test and the antigen agnostic IIF. Interestingly, we found the CRMP5 autoantibodies in patients' CSF samples showed stronger binding (higher ΔMFI_x) when tested by our original live CRMP5 F-CBA than by our new live CRMP5 F-CBA, which improved the accessibility of C-terminal CRMP5 epitopes. Subsequently, an untagged permeabilized CRMP5 F-CBA was developed to cytosolicly express the native CRMP5. Although it was shown to be the most robust assay to detect CRMP5 autoantibodies, it still didn't pick up a CRMP5 Ab+ serum sample identified seropositive by fixed IHC and western blots. Perhaps the fixed IIF and western blot may produce additional or different targets for autoantibodies to recognize. A larger patient cohort with clinical details will be required for further investigations.

After generating individual assays, we attempted to make our F-CBA multiplexable. Inspired by Krutzik et al.'s publication in 2011, our multiplex F-CBA method was

established by applying CellTrace dyes to color-code each cell population expressing different targeted antigens. Compared to other live cell-labelling dyes, CellTrace dyes, especially CTV, demonstrated strong fluorescent signals and sustainable binding to intracellular amine groups without leaking to unstained population. Unlike the cell impermeant amine-reactive dyes Krutzik et al. used previously, the CellTrace dyes are cell permeant, so they are compatible to our live F-CBA method by being able to label the intracellular amines in live HEK cells. By using CTV and CTFR together, the octaplex panel was demonstrated under flow cytometry without leakage of the dye to other populations once mixed. Then, the FCB color-coding technology was applied to set up a live and a permeabilized quadruplex F-CBA for simultaneously detecting autoantibodies to "HuD, NOVA1, CDR2L and Amphiphysin" and "SOX1, Ma1, Ma2 and CRMP5", respectively. The ΔMFI_x from our quadruplex live F-CBA correlated well ($p < 0.01$) with the 1:20 CBA visual scores from our individual live CBAs for detecting onconeural autoantibodies. Importantly, both our quadruplex live and permeabilized F-CBAs also picked up all the samples from patients with high/intermediate-risk PNS and tumours. Therefore, our quadruplex F-CBA was a more efficient and quantitative alternative to our simplex live CBAs, which demonstrated good diagnostic accuracy as described in Chapter IV.

Additionally, the DsRed2-reporting F-CBAs were established for detecting autoantibodies to AQP4 M23 and MOG α1 isoforms as an alternative to the routine live CBAs performed in our diagnostic lab. When using DyLight 488 anti-human IgG Fc secondary antibody, our live F-CBA showed high signal-to-noise ratio, more than 300 times background, to detect AQP4 M23 autoantibodies. However, our live MOG α1 F-CBA had higher background and relying on the original cut-off couldn't avoid picking

up any sample in the CBA double negative cohort. The newly defined high cut-off was required to achieve this. The background of our live MOG α1 F-CBA was reduced when transfecting the cells with 8-times diluted MOG plasmid, or when using AF488 anti-human IgG Fc or IgG1 secondary antibody in our duplex live F-CBA. However, we didn't pick up 2-3/28 samples identified seropositive for AQP4 M23 autoantibodies by live AQP4 M23 CBA when using 1:100 diluted AF488 anti-human IgG Fc or IgG1 as the secondary. If aiming to be applied as a routine diagnostic test, further optimizations for our live duplex F-CBA will be required to not only reduce the background for detecting MOG α1 autoantibodies but also pick up all the sample in AQP4 M23 Ab CBA+ cohort. Also, the live MOG CBA itself needs to be further investigated in order to understand why such a high background exists in healthy individuals or in individuals with other neuroimmunological diseases. Last but not least, we will require clinical details for every sample we screens before judging if they are true positive or true negative of the disease.

6.2. Research Limitations

The major limitation of my DPhil research, particularly in paraneoplastic project, is the small sample size due to the rarity of patients with PNS. In addition, we have not yet unblinded our collaborators to the data, hence there is a lack of clinical details. With more time, longitudinal screens may have been useful to determine any clinical association with titres, but the likelihood of this is low based on previous publications showing a lack of clinical association using CBA endpoint titres. Furthermore, the treatment details of the patients donating their blood samples were mostly unsure although the samples from Prof. Leite and Dr. Ambrose's clinics were collected at patients' first visit to avoid any therapeutic effects. Practically, if the patients have been

treated with immunosuppressants, it is possible for us to underestimate their autoantibodies titres. All in all, our studies and analyses could be more representative if we were provided with the clinical and treatment details for every sample we screens from our collaborators in US, Spain and NHS.

6.3. Future Avenues

If I have more time in the lab, the most important future work is to further evaluate the issue surrounding the surface expression those onconeural antigens, which were unsuccessfully expressed on the surface of HEK cells. This is because our live CBAs demonstrated lower backgrounds than our permeabilized CBAs. Therefore, here, I propose some possible methods to achieve the surface expression of those onconeural antigens, and the main idea is to avoid our targeted antigens forming multimeric structure with the corresponding intracellular molecules. The first method is to mutate their binding domains if known. This method can be applied to surface express KLHL-11 and SOX1 since past studies have unveiled their intracellular binding domains. Secondly, we can rely on CRISPR-Cas9 lentivirus-based gene editing technology to knockout their well-understood intracellular binding partners within HEK cells. This method is suitable to surface express CDR2 and Ma1/Ma2 because c-myc and MOAP-1 were known as their intracellular binding partners, respectively.

If the aforementioned methods don't work out, we can only express the truncated forms of our targeted antigens, only retaining their major epitopes. Removing binding domains may allow better surface expression, but it also may reduce the test accuracy by missing antibody epitopes, or by generating new epitopes as we mutate or modify the targets. These suggestions are limited by the lack of knowledge on the antibody

epitopes in many of these diseases. We have known the antibody target HuD since 1991. Despite technical advances, we still do not know the epitope. Recent data suggested a short peptide near the C-terminus of the protein, but only 30% of HuD positive sera precipitated this epitope (O'Donovan et al., 2020). There is still lots to learn about these targets that may facilitate future assay designs.

Furthermore, the longitudinal screening for the samples collected from sequential patient visits will be worth doing to understand the changes of antibody titre before and after the removal of tumour. For PNS patients, this may be an indicator to tell if the tumour is completely removed. Although we had found the endpoint titres of autoantibodies to IFNα and IL-12 could remain high years after patients' thymectomy, the samples we had tested were from different TAMG patients, i.e., the cross-sectional analysis. Therefore, a longitudinal study to understand the antibody profile of TAMG patients pre- and post-Tx can be done next. In addition, the longitudinal screen can answer if the antibody titre changes before and after patients' therapeutic interventions, e.g., immunosuppressant, IVIg etc.

As proposed, the future avenues of my DPhil studies are promising and supported by enough background knowledge. And especially the works to surface express all the onconeural antigens and multiplex all of them using flow cytometry haven't been completed so far, our prospective works may hopefully lead to a scientific breakthrough in this field.

Appendix

7.1. The cDNA clones of cytokine targets

7.1.1. Interleukin-6 (IL-6)

BC015511.1:50-688 Homo sapiens interleukin 6 (interferon, beta 2), mRNA (cDNA clone MGC:9215 IMAGE:3884652), complete cds

>IL-6_639bp

ATGAACTCCTTCTCCACAAGCGCCTTCGGTCCAGTTGCCTTCTCCCTGGGGCTGCTCCTGGT
GTTGCCTGCTGCCTTCCCTGCCCCAGTACCCCCAGGAGAAGATTCCAAAGATGTAGCCGCCC
CACACAGACAGCCACTCACCTCTTCAGAACGAATTGACAAACAAATTCGGTACATCCTCGAC
GGCATCTCAGCCCTGAGAAAGGAGACATGTAACAAGAGTAACATGTGTGAAAGCAGCAAAGA
GGCACTGGCAGAAAACAACCTGAACCTTCCAAAGATGGCTGAAAAAGATGGATGCTTCCAAT
CTGGATTCAATGAGGAGACTTGCCTGGTGAAAATCATCACTGGTCTTTTGGAGTTTGAGGTA
TACCTAGAGTACCTCCAGAACAGATTTGAGAGTAGTGAGGAACAAGCCAGAGCTGTGCAGAT
GAGTACAAAAGTCCTGATCCAGTTCCTGCAGAAAAAGGCAAAGAATCTAGATGCAATAACCA
CCCCTGACCCAACCACAAATGCCAGCCTGCTGACGAAGCTGCAGGCACAGAACCAGTGGCTG
CAGGACATGACAACTCATCTCATTCTGCGCAGCTTTAAGGAGTTCCTGCAGTCCAGCCTGAG
GGCTCTTCGGCAAATGTAG

7.1.2. Interleukin-12A (IL-12A)

BC104984.1:154-915 Homo sapiens interleukin 12A (natural killer cell stimulatory factor 1, cytotoxic lymphocyte maturation factor 1, p35), mRNA (cDNA clone MGC:132644 IMAGE:8143987), complete cds

>IL-12A_762bp

ATGTGGCCCCCTGGGTCAGCCTCCCAGCCACCGCCCTCACCTGCCGCGGCCACAGGTCTGCA
TCCAGCGGCTCGCCCTGTGTCCCTGCAGTGCCGGCTCAGCATGTGTCCAGCGCGCAGCCTCC
TCCTTGTGGCTACCCTGGTCCTCCTGGACCACCTCAGTTTGGCCAGAAACCTCCCCGTGGCC
ACTCCAGACCCAGGAATGTTCCCATGCCTTCACCACTCCCAAAACCTGCTGAGGGCCGTCAG
CAACATGCTCCAGAAGGCCAGACAAACTCTAGAATTTTACCCTTGCACTTCTGAAGAGATTG
ATCATGAAGATATCACAAAAGATAAAACCAGCACAGTGGAGGCCTGTTTACCATTGGAATTA
ACCAAGAATGAGAGTTGCCTAAATTCCAGAGAGACCTCTTTCATAACTAATGGGAGTTGCCT
GGCCTCCAGAAAGACCTCTTTTATGATGGCCCTGTGCCTTAGTAGTATTTATGAAGACTTGA
AGATGTACCAGGTGGAGTTCAAGACCATGAATGCAAAGCTTCTGATGGATCCTAAGAGGCAG
ATCTTTCTAGATCAAAACATGCTGGCAGTTATTGATGAGCTGATGCAGGCCCTGAATTTCAA
CAGTGAGACTGTGCCACAAAAATCCTCCCTTGAAGAACCGGATTTTTATAAAACTAAAATCA

AGCTCTGCATACTTCTTCATGCTTTCAGAATTCGGGCAGTGACTATTGATAGAGTGATGAGC
TATCTGAATGCTTCCTAA

7.1.3. Interleukin-12B (IL-12B)

BC067501.1:5-991 Homo sapiens interleukin 12B (natural killer cell stimulatory factor 2, cytotoxic lymphocyte maturation factor 2, p40), mRNA (cDNA clone MGC:79359 IMAGE:6971873), complete cds

>IL-12B_987bp

ATGTGTCACCAGCAGTTGGTCATCTCTTGGTTTTCCCTGGTTTTTCTGGCATCTCCCCTCGT
GGCCATATGGGAACTGAAGAAAGATGTTTATGTCGTAGAATTGGATTGGTATCCGGATGCCC
CTGGAGAAATGGTGGTCCTCACCTGTGACACCCCTGAAGAAGATGGTATCACCTGGACCTTG
GACCAGAGCAGTGAGGTCCTAGGCTCTGGCAAAACCCTGACCATCCAAGTCAAAGAGTTTGG
AGATGCTGGCCAGTACACCTGTCACAAAGGAGGCGAGGTTCTAAGCCATTCGCTCCTGCTGC
TTCACAAAAAGGAAGATGGAATTTGGTCCACTGATATTTTAAAGGACCAGAAAGAACCCAAA
AATAAGACCTTTCTAAGATGCGAGGCCAAGAATTATTCTGGACGTTTCACCTGCTGGTGGCT
GACGACAATCAGTACTGATTTGACATTCAGTGTCAAAAGCAGCAGAGGCTCTTCTGACCCCC
AAGGGGTGACGTGCGGAGCTGCTACACTCTCTGCAGAGAGAGTCAGAGGGGACAACAAGGAG
TATGAGTACTCAGTGGAGTGCCAGGAGGACAGTGCCTGCCCAGCTGCTGAGGAGAGTCTGCC
CATTGAGGTCATGGTGGATGCCGTTCACAAGCTCAAGTATGAAAACTACACCAGCAGCTTCT
TCATCAGGGACATCATCAAACCTGACCCACCCAAGAACTTGCAGCTGAAGCCATTAAAGAAT
TCTCGGCAGGTGGAGGTCAGCTGGGAGTACCCTGACACCTGGAGTACTCCACATTCCTACTT
CTCCCTGACATTCTGCGTTCAGGTCCAGGGCAAGAGCAAGAGAGAAAAGAAAGATAGAGTCT
TCACGGACAAGACCTCAGCCACGGTCATCTGCCGCAAAAATGCCAGCATTAGCGTGCGGGCC
CAGGACCGCTACTATAGCTCATCTTGGAGCGAATGGGCATCTGTGCCCTG CAGTTAG

7.1.4. Interleukin-17A (IL-17A)

BC066251.1:44-511 Homo sapiens interleukin 17A, mRNA (cDNA clone MGC:79361 IMAGE:6971875), complete cds

>IL-17A_468bp

ATGACTCCTGGGAAGACCTCATTGGTATCACTGCTACTGCTGCTGAGCCTGGAGGCCATAGT
GAAGGCAGGAATCACAATCCCACGAAATCCAGGATGCCCAAATTCTGAGGACAAGAACTTCC
CCCGGACTGTGATGGTCAACCTGAACATCCATAACCGGAATACCAATACCAATCCCAAAAGG
TCCTCAGATTACTACAACCGATCCACCTCACCTTGGAATCTCCACCGCAATGAGGACCCTGA
GAGATATCCCTCTGTGATCTGGGAGGCAAAGTGCCGCCACTTGGGCTGCATCAACGCTGATG
GGAACGTGGACTACCACATGAACTCTGTCCCCATCCAGCAAGAGATCCTGGTCCTGCGCAGG

GAGCCTCCACACTGCCCCAACTCCTTCCGGCTGGAGAAGATACTGGTGTCCGTGGGCTGCAC
CTGTGTCACCCCGATTGTCCACCATGTGGCCTAA

7.1.5. Interleukin-17F (IL-17F)

BC070124.1:72-563 Homo sapiens interleukin 17F, mRNA (cDNA clone MGC:88102

IMAGE:30417554), complete cds

>IL-17F_492bp

ATGACAGTGAAGACCCTGCATGGCCCAGCCATGGTCAAGTACTTGCTGCTGTCGATATTGGG
GCTTGCCTTTCTGAGTGAGGCGGCAGCTCGGAAAATCCCCAAAGTAGGACATACTTTTTTCC
AAAAGCCTGAGAGTTGCCCGCCTGTGCCAGGAGGTAGTATGAAGCTTGACATTGGCATCATC
AATGAAAACCAGCGCGTTTCCATGTCACGTAACATCGAGAGCCGCTCCACCTCCCCCTGGAA
TTACACTGTCACTTGGGACCCCAACCGGTACCCCTCGGAAGTTGTACAGGCCCAGTGTAGGA
ACTTGGGCTGCATCAATGCTCAAGGAAAGGAAGACATCTCCATGAATTCCGTTCCCATCCAG
CAAGAGACCCTGGTCGTCCGGAGGAAGCACCAAGGCTGCTCTGTTTCTTTCCAGTTGGAGAA
GGTGCTGGTGACTGTTGGCTGCACCTGCGTCACCCCTGTCATCCACCGTGTGCAGTAA

7.1.6. Interleukin-22 (IL-22)

BC070261.1:69-608 Homo sapiens interleukin 22, mRNA (cDNA clone MGC:88248

IMAGE:30416027), complete cds

>IL-22_540bp

ATGGCCGCCCTGCAGAAATCTGTGAGCTCTTTCCTTATGGGGACCCTGGCCACCAGCTGCCT
CCTTCTCTTGGCCCTCTTGGTACAGGGAGGAGCAGCTGCGCCCATCAGCTCCCACTGCAGGC
TTGACAAGTCCAACTTCCAGCAGCCCTATATCACCAACCGCACCTTCATGCTGGCTAAGGAG
GCTAGCTTGGCTGATAACAACACAGACGTTCGTCTCATTGGGGAGAAACTGTTCCACGGAGT
CAGTATGAGTGAGCGCTGCTATCTGATGAAGCAGGTGCTGAACTTCACCCTTGAAGAAGTGC
TGTTCCCTCAATCTGATAGGTTCCAGCCTTATATGCAGGAGGTGGTGCCCTTCCTGGCCAGG
CTCAGCAACAGGCTAAGCACATGTCATATTGAAGGTGATGACCTGCATATCCAGAGGAATGT
GCAAAAGCTGAAGGACACAGTGAAAAAGCTTGGAGAGAGTGGAGAGATCAAAGCAATTGGAG
AACTGGATTTGCTGTTTATGTCTCTGAGAAATGCCTGCATTTGA

7.1.7. Interleukin-23A (IL-23A)

BC067511.1:34-603 Homo sapiens interleukin 23, alpha subunit p19, mRNA (cDNA clone MGC:79390 IMAGE:6971850), complete cds

>IL-23A_570bp

ATGCTGGGGAGCAGAGCTGTAATGCTGCTGTTGCTGCTGCCCTGGACAGCTCAGGGCAGAGC
TGTGCCTGGGGGCAGCAGCCCTGCCTGGACTCAGTGCCAGCAGCTTTCACAGAAGCTCTGCA
CACTGGCCTGGAGTGCACATCCACTAGTGGGACACATGGATCTAAGAGAAGAGGGAGATGAA
GAGACTACAAATGATGTTCCCCATATCCAGTGTGGAGATGGCTGTGACCCCCAAGGACTCAG
GGACAACAGTCAGTTCTGCTTGCAAAGGATCCACCAGGGTCTGATTTTTTATGAGAAGCTGC
TAGGATCGGATATTTTCACAGGGGAGCCTTCTCTGCTCCCTGATAGCCCTGTGGGCCAGCTT
CATGCCTCCCTACTGGGCCTCAGCCAACTCCTGCAGCCTGAGGGTCACCACTGGGAGACTCA
GCAGATTCCAAGCCTCAGTCCCAGCCAGCCATGGCAGCGTCTCCTTCTCCGCTTCAAAATCC
TTCGCAGCCTCCAGGCCTTTGTGGCTGTAGCCGCCCGGGTCTTTGCCCATGGAGCAGCAACC
CTGAGTCCCTAA

7.1.8. Interferon alpha 2 (IFNα2)

BC074937.2:45-611 Homo sapiens interferon, alpha 2, mRNA (cDNA clone MGC:125764 IMAGE:40029595), complete cds

>IFNα2_567bp

ATGGCCTTGACCTTTGCTTTACTGGTGGCCCTCCTGGTGCTCAGCTGCAAGTCAAGCTGCTC
TGTGGGCTGTGATCTGCCTCAAACCCACAGCCTGGGTAGCAGGAGGACCTTGATGCTCCTGG
CACAGATGAGGAGAATCTCTCTTTTCTCCTGCTTGAAGGACAGACATGACTTTGGATTTCCC
CAGGAGGAGTTTGGCAACCAGTTCCAAAAGGCTGAAACCATCCCTGTCCTCCATGAGATGAT
CCAGCAGATCTTCAATCTCTTCAGCACAAAGGACTCATCTGCTGCTTGGGATGAGACCCTCC
TAGACAAATTCTACACTGAACTCTACCAGCAGCTGAATGACCTGGAAGCCTGTGTGATACAG
GGGGTGGGGGTGACAGAGACTCCCCTGATGAAGGAGGACTCCATTCTGGCTGTGAGGAAATA
CTTCCAAAGAATCACTCTCTATCTGAAAGAGAAGAAATACAGCCCTTGTGCCTGGGAGGTTG
TCAGAGCAGAAATCATGAGATCTTTTTCTTTGTCAACAAACTTGCAAGAAAGTTTAAGAAGT
AAGGAATGA

7.1.9. Interferon alpha 8 (IFNα8)

BC104830.1:30-599 Homo sapiens interferon, alpha 8, mRNA (cDNA clone MGC:132490 IMAGE:8143833), complete cds

>IFNα8_570bp

ATGGCCTTGACTTTTTATTTACTGGTGGCCCTAGTGGTGCTCAGCTACAAGTCATTCAGCTC
TCTGGGCTGTGATCTGCCTCAGACTCACAGCCTGGGTAACAGGAGGGCCTTGATACTCCTGG
CACAAATGCGAAGAATCTCTCCTTTCTCCTGCCTGAAGGACAGACATGACTTTGAATTCCCC
CAGGAGGAGTTTGATGATAAACAGTTCCAGAAGGCTCAAGCCATCTCTGTCCTCCATGAGAT
GATCCAGCAGACCTTCAACCTCTTCAGCACAAAGGACTCATCTGCTGCTTTGGATGAGACCC
TTCTAGATGAATTCTACATCGAACTTGACCAGCAGCTGAATGACCTGGAGTCCTGTGTGATG
CAGGAAGTGGGGGTGATAGAGTCTCCCCTGATGTACGAGGACTCCATCCTGGCTGTGAGGAA
ATACTTCCAAAGAATCACTCTATATCTGACAGAGAAGAAATACAGCTCTTGTGCCTGGGAGG
TTGTCAGAGCAGAAATCATGAGATCCTTCTCTTTATCAATCAACTTGCAAAAAAGATTGAAG
AGTAAGGAATGA

7.1.10. Interferon omega 1 (IFNω1)

BC117290.1:38-625 Homo sapiens interferon, omega 1, mRNA (cDNA clone MGC:150899 IMAGE:40125841), complete cds

>IFNω1_588bp

ATGGCCCTCCTGTTCCCTCTACTGGCAGCCCTAGTGATGACCAGCTATAGCCCTGTTGGATC
TCTGGGCTGTGATCTGCCTCAGAACCATGGCCTACTTAGCAGGAACACCTTGGTGCTTCTGC
ACCAAATGAGGAGAATCTCCCCTTTCTTGTGTCTCAAGGACAGAAGAGACTTCAGGTTCCCC
CAGGAGATGGTAAAAGGGAGCCAGTTGCAGAAGGCCCATGTCATGTCTGTCCTCCATGAGAT
GCTGCAGCAGATCTTCAGCCTCTTCCACACAGAGCGCTCCTCTGCTGCCTGGAACATGACCC
TCCTAGACCAACTCCACACTGGACTTCATCAGCAACTGCAACACCTGGAGACCTGCTTGCTG
CAGGTAGTGGGAGAAGGAGAATCTGCTGGGGCAATTAGCAGCCCTGCACTGACCTTGAGGAG
GTACTTCCAGGGAATCCGTGTCTACCTGAAAGAGAAGAAATACAGCGACTGTGCCTGGGAAG
TTGTCAGAATGGAAATCATGAAATCCTTGTTCTTATCAACAAACATGCAAGAAAGACTGAGA
AGTAAAGATAGAGACCTGGGCTCATCTTGA

7.2. The cDNA clones of onconeural antigens

7.2.1. HuD

Homo sapiens HUD4 mRNA, complete cds; GenBank: AY033996.1:43-1194

>HuD_1152bp

ATGAGATTACTTCTTTTAAGGGAAATTGTCATTAATGAGTCAAGAAACTGCTCATTTATGAT
AATTAGCACCATGGAGCCTCAGGTGTCAAATGGTCCGACATCCAATACAAGCAATGGACCCT
CCAGCAACAACAGAAACTGTCCTTCTCCCATGCAAACAGGGGCAACCACAGATGACAGCAAA
ACCAACCTCATCGTCAACTATTTACCCCAGAATATGACCCAAGAAGAATTCAGGAGTCTCTT
CGGGAGCATTGGTGAAATAGAATCCTGCAAACTTGTGAGAGACAAAATTACAGGACAGAGTT
TAGGGTATGGATTTGTTAACTATATTGATCCAAAGGATGCAGAGAAAGCCATCAACACTTTA
AATGGACTCAGACTCCAGACCAAAACCATAAAGGTCTCATATGCCCGTCCGAGCTCTGCCTC
AATCAGGGATGCTAACCTCTATGTTAGCGGCCTTCCCAAAACCATGACCCAGAAGGAACTGG
AGCAACTTTTCTCGCAATACGGCCGTATCATCACCTCACGAATCCTGGTTGATCAAGTCACA
GGAGTGTCCAGAGGGGTGGGATTCATCCGCTTTGATAAGAGGATTGAGGCAGAAGAAGCCAT
CAAAGGGCTGAATGGCCAGAAGCCCAGCGGTGCTACGGAACCGATTACTGTGAAGTTTGCCA
ACAACCCCAGCCAGAAGTCCAGCCAGGCCCTGCTCTCCCAGCTCTACCAGTCCCCCAACCGG
CGCTACCCAGGTCCACTTCACCACCAGGCTCAGAGGTTCAGGCTGGACAATTTGCTTAATAT
GGCCTATGGCGTAAAGAGGTTCTCCCCAATTACCATTGATGGAATGACAAGCCTTGTGGGAA
TGAACATCCCTGGTCACACAGGAACTGGGTGGTGCATCTTTGTCTACAACCTGTCCCCCGAT
TCCGATGAGAGTGTCCTCTGGCAGCTCTTTGGCCCCTTTGGAGCAGTGAACAACGTAAAGGT
GATTCGTGACTTCAACACCAACAAGTGCAAGGGATTCGGCTTTGTCACCATGACCAACTATG
ATGAGGCGGCCATGGCCATCGCCAGCCTCAACGGGTACCGCCTGGGAGACAGAGTGTTGCAA
GTTTCCTTTAAAACCAACAAAGCCCACAAGTCCTGA

7.2.2. CDR2

Homo sapiens cerebellar degeneration related protein 2 (CDR2), mRNA; NCBI Reference Sequence: NM_001802.2:311-1675

>CDR2_1365bp

ATGCTGGCGGAAAACCTGGTAGAGGAGTTTGAGATGAAGGAGGACGAGCCGTGGTACGACCA
CCAGGACCTCCAGCAAGATCTTCAACTTGCTGCTGAGCTTGGGAAGACATTACTGGATCGGA
ACACAGAGTTGGAGGACTCTGTTCAGCAGATGTATACAACCAATCAGGAGCAGTTACAGGAA
ATTGAGTATCTGACGAAGCAAGTGGAACTTCTACGGCAGATGAACGAACAACATGCAAAGGT
TTATGAACAATTAGACGTCACAGCAAGGGAACTGGAAGAAACAAATCAAAAGCTAGTTGCTG
ACAGCAAGGCCTCACAGCAAAAGATTCTGAGCCTGACTGAAACGATTGAATGCCTGCAAACC
AACATTGATCACCTCCAGAGCCAAGTGGAGGAGCTGAAGTCATCTGGCCAAGGGAGAAGGAG
CCCGGGAAAGTGTGACCAGGAGAAACCGGCACCCAGCTTTGCATGTCTGAAGGAGCTGTATG

ACCTCCGCCAACACTTCGTGTATGATCATGTGTTCGCTGAGAAGATCACTTCCTTGCAAGGT
CAGCCAAGCCCTGATGAAGAGGAAAATGAGCACTTGAAAAAAACAGTGACAATGTTGCAGGC
CCAGCTGAGCCTGGAGCGGCAGAAGCGGGTGACTATGGAGGAGGAATATGGGCTCGTGTTAA
AGGAGAACAGTGAACTGGAGCAGCAGCTGGGGGCCACAGGTGCCTACCGAGCACGGGCGCTG
GAACTAGAGGCCGAGGTGGCAGAGATGCGACAGATGTTGCAGTCAGAGCATCCATTTGTGAA
TGGAGTTGAGAAGCTGGTGCCAGACTCTCTGTATGTTCCTTTCAAAGAGCCCAGCCAGAGCC
TGCTGGAAGAGATGTTCCTGACTGTGCCGGAATCACATAGAAAGCCTCTCAAGCGCAGCAGC
AGTGAGACGATCCTCAGCAGCTTGGCAGGGAGTGACATCGTGAAGGGCCACGAGGAGACCTG
CATCAGGAGGGCCAAGGCTGTGAAACAGAGGGGCATCTCCCTTCTGCACGAAGTGGACACGC
AGTACAGCGCCCTGAAGGTGAAGTATGAAGAGTTGCTGAAGAAGTGCCAAGAGGAACAGGAC
TCCCTGTCACACAAGGCTGTGCAGACCTCCAGGGCTGCAGCCAAGGACCTGACTGGAGTGAA
CGCCCAGTCTGAGCCTGTTGCCAGCGGCTGGGAACTGGCCTCTGTCAACCCAGAGCCCGTGA
GTTCCCCTACAACACCTCCAGAATACAAAGCGTTGTTTAAGGAGATCTTTAGTTGCATCAAG
AAAACTAAGCAGGAAATAGATGAACAGAGAACAAAATACCGATCACTCTCCTCTCATTCTTA
A

7.2.3. CDR2L

Homo sapiens cerebellar degeneration related protein 2 like (CDR2L), mRNA; NCBI

Reference Sequence: NM_014603.3:413-1810

>CDR2L_1398bp

ATGCGGAGAGCCGCCGGGATGGAGGACTTCTCCGCGGAGGAAGAGGAGTCCTGGTACGACCA
GCAGGACCTGGAGCAGGACTTGCACCTAGCTGCGGAGCTGGGGAAGACTCTGCTGGAGAGGA
ACAAGGAGCTGGAGGGGTCCCTGCAGCAGATGTACTCCACCAATGAGGAACAGGTGCAGGAG
ATCGAGTACCTAACCAAGCAGCTGGACACGCTGCGGCACGTGAACGAGCAGCACGCCAAAGT
CTATGAGCAGCTGGACCTGACAGCCCGGGACCTGGAGCTGACCAACCACAGGCTGGTGCTGG
AGAGTAAGGCTGCCCAGCAGAAGATCCATGGGCTGACGGAGACCATTGAGCGCCTCCAGGCT
CAGGTGGAGGAGCTGCAGGCCCAGGTGGAGCAACTGAGAGGCCTGGAACAGCTGCGAGTGCT
CCGGGAGAAGCGGGAACGCAGGCGTACCATCCACACCTTCCCCTGCCTCAAGGAGCTGTGCA
CCAGCCCCCGGTGCAAGGATGCTTTCCGCCTACACAGTTCCTCCCTGGAGCTGGGCCCGCGG
CCCCTGGAGCAGGAGAACGAGCGGCTGCAGACCCTGGTGGGGGCGCTGCGCTCCCAGGTGAG
CCAGGAGCGGCAGCGCAAGGAGCGGGCGGAGCGCGAGTACACCGCGGTGCTGCAGGAGTACT
CGGAGCTGGAGCGCCAGCTGTGCGAGATGGAGGCCTGTCGCCTGCGTGTGCAGGAGCTGGAG
GCCGAGCTGCTGGAGCTGCAGCAGATGAAGCAGGCCAAGACCTACCTACTGGGTCCGGACGA
CCACCTGGCCGAGGCCCTGCTCGCACCCCTCACGCAGGCCCCTGAGGCCGACGATCCCCAGC
CCGGCCGCGGGGACGACTTGGGCGCCCAGGACGGGGTCTCCTCACCGGCAGCCTCTCCAGGC
CACGTGGTGCGCAAGAGCTGCAGCGACACTGCGCTCAACGCCATCGTGGCCAAAGACCCAGC
CAGCCGGCACGCGGGCAACCTCACACTGCACGCCAACAGCGTGCGCAAGCGGGGCATGTCCA
TCCTGCGGGAGGTGGACGAGCAGTACCACGCGCTGCTGGAGAAGTACGAGGAGCTGCTGAGC
AAGTGCCGGCAGCACGGGGCCGGAGTGCGGCACGCCGGCGTGCAGACCTCGCGCCCCATCTC
CCGGGACAGCTCGTGGAGGGACCTGCGCGGGGGTGAGGAGGGCCAGGGTGAGGTCAAGGCAG

GAGAGAAGAGCCTGAGCCAGCACGTGGAGGCCGTGGACAAGCGGCTGGAACAGAGCCAGCCC
GAGTACAAGGCGCTCTTCAAAGAGATCTTCTCCAGGATCCAGAAGACCAAGGCTGACATCAA
CGCCACCAAAGTCAAGACGCACAGCAGCAAGTGA

7.2.4. NOVA1

Human onconeural ventral antigen-1 (Nova-1) mRNA, complete cds; GenBank: U04840.1:61-1593

>NOVA1_1533bp

ATGATGGCGGCAGCTCCCATCCAGCAGAACGGGACCCACACTGGGGTTCCCATAGACCTGGA
CCCGCCGGACTCGCGGAAAAGGCCGCTGGAAGCCCCCCCTGAAGCCGGCAGCACCAAGAGGA
CCAATACGGGCGAAGACGGCCAGTATTTTCTAAAGGTTCTCATACCTAGTTATGCTGCTGGA
TCTATAATTGGGAAGGGAGGACAGACAATTGTTCAGTTGCAAAAAGAAACTGGAGCCACCAT
CAAGCTGTCTAAGCTGTCTAAGTCCAAAGATTTTTACCCAGGTACTACTGAGCGAGTGTGCT
TGATCCAGGGAACGGTTGAAGCACTGAATGCAGTTCATGGATTCATTGCAGAAAAAATTCGA
GAAATGCCCCAAAATGTGGCCAAGACAGAACCAGTCAGCATTCTACAACCCCAGACCACCGT
TAATCCAGATCGCATCAAACAAACATTGCCATCTTCCCCAACTACCACCAAGTCCTCTCCAT
CTGATCCCATGACCACCTCCAGAGCTAATCAGGTAAAGATTATAGTTCCCAACAGCACAGCA
GGTCTGATAATAGGGAAGGGAGGTGCTACTGTGAAGGCTGTAATGGAGCAGTCAGGGGCTTG
GGTGCAGCTTTCCCAGAAACCTGATGGGATCAACTTGCAAGAGAGGGTTGTCACTGTGAGTG
GAGAACCTGAACAAAACCGAAAAGCTGTTGAACTTATCATCCAGAAGATACAAGAGGATCCA
CAAAGTGGCAGCTGTCTCAATATCAGTTATGCCAATGTGACAGGTCCAGTGGCAAATTCCAA
TCCAACCGGATCTCCTTATGCAAACACTGCTGAAGTGTTACCAACTGCTGCAGCAGCTGCAG
GGCTATTAGGACATGCTAACCTTGCTGGCGTTGCAGCCTTTCCAGCAGTTTTATCTGGCTTC
ACAGGCAATGACCTGGTGGCCATCACCTCTGCACTTAATACATTAGCCAGCTATGGATATAA
TCTCAACACTTTAGGTTTAGGTCTCAGTCAAGCAGCAGCAACAGGGGCTTTGGCTGCAGCAG
CTGCCAGTGCCAACCCAGCAGCAGCAGCAGCCAATTTATTGGCCACCTATGCCAGTGAAGCC
TCAGCCAGTGGCAGCACAGCTGGTGGTACGGCGGGGACATTTGCATTAGGTAGCCTGGCTGC
TGCTACTGCTGCAACCAATGGATATTTTGGAGCTGCTTCTCCCCTAGCTGCCAGTGCCATTC
TAGGAACAGAAAAGTCCACAGATGGATCCAAGGATGTAGTTGAAATAGCAGTGCCAGAAAAC
TTAGTTGGTGCAATACTTGGCAAAGGAGGGAAAACATTAGTGGAATACCAGGAGTTGACTGG
TGCAAGGATACAGATCTCCAAAAAAGGAGAATTCGTACCTGGCACAAGGAATCGGAAGGTAA
CCATTACTGGAACACCAGCTGCAACACAGGCTGCTCAATATTTAATTACACAAAGGATCACA
TATGAGCAAGGAGTTCGGGCTGCCAATCCTCAGAAAGTGGGTTGA

7.2.5. Ma1

Homo sapiens PNMA family member 1 (PNMA1), mRNA; NCBI Reference Sequence:

NM_006029.5:746-1807

>Ma1_1062bp

ATGGCGATGACACTGTTGGAAGACTGGTGCCGGGGGATGGATGTGAACTCCCAGAGAGCTCT
GTTAGTCTGGGGCATCCCAGTGAACTGTGATGAGGCTGAAATCGAAGAGACCCTCCAGGCTG
CGATGCCCCAGGTCTCCTACCGAATGCTTGGGAGAATGTTCTGGAGGGAAGAAAATGCGAAA
GCAGCCTTATTAGAGCTCACTGGCGCTGTAGATTACGCCGCGATCCCCAGGGAGATGCCGGG
CAAAGGAGGGGTCTGGAAAGTGTTATTTAAGCCCCCAACTTCTGATGCTGAATTTTTAGAAA
GATTGCACCTCTTCCTAGCTAGAGAGGGGTGGACCGTGCAAGATGTTGCCCGTGTCCTTGGG
TTTCAGAACCCTACTCCGACCCCGGGCCCAGAGATGCCAGCAGAGATGCTAAACTATATTTT
GGATAATGTTATTCAGCCTCTTGTTGAGTCCATATGGTACAAGAGGCTGACACTTTTCTCGG
GGAGGGACATCCCAGGGCCTGGAGAGGAAACCTTTGATCCCTGGCTGGAGCACACTAATGAG
GTCCTAGAGGAGTGGCAGGTGTCCGATGTAGAAAAGAGGCGGCGGTTGATGGAGAGTCTTAG
AGGCCCCGCCGCTGATGTTATTCGCATCCTTAAGTCCAACAACCCCGCGATAACCACTGCCG
AATGCCTGAAGGCGCTTGAGCAGGTGTTTGGGAGCGTTGAGAGCTCTAGGGATGCCCAGATC
AAATTTCTGAACACTTATCAGAACCCGGGAGAAAAATTGTCTGCTTATGTCATTCGTCTGGA
GCCTCTGCTACAGAAGGTGGTAGAGAAGGGGGCCATTGATAAAGATAATGTGAACCAGGCCC
GCCTAGAGCAGGTCATTGCCGGGGCCAACCACAGCGGGGCCATCCGAAGGCAGCTGTGGCTT
ACCGGGGCTGGGGAAGGGCCAGCCCCAAACCTCTTTCAGTTGCTGGTGCAGATCCGTGAGGA
GGAAGCCAAGGAGGAGGAGGAGGAGGCTGAGGCCACCCTTCTGCAGTTAGGCCTGGAAGGGC
ACTTCTGA

7.2.6. Ma2

Homo sapiens PNMA family member 2 (PNMA2), mRNA; NCBI Reference Sequence:

NM_007257.6:676-1770

>Ma2_1095bp

ATGGCGCTGGCACTGTTAGAGGACTGGTGCAGGATAATGAGTGTGGATGAGCAGAAGTCACT
GATGGTTACGGGGATACCGGCGGACTTTGAGGAGGCTGAGATTCAGGAGGTCCTTCAGGAGA
CTTTAAAGTCTCTGGGCAGGTATAGACTGCTTGGCAAGATATTCCGGAAGCAGGAGAATGCC
AATGCTGTCTTACTAGAGCTTCTGGAAGATACTGATGTCTCGGCCATTCCCAGTGAGGTCCA
GGGAAAGGGGGGTGTCTGGAAGGTGATCTTTAAGACCCCTAATCAGGACACTGAGTTTCTTG
AAAGATTGAACCTGTTTCTAGAAAAAGAGGGGCAGACGGTCTCGGGTATGTTTCGAGCCCTG
GGGCAGGAGGGCGTGTCTCCAGCCACAGTGCCCTGCATCTCACCAGAATTACTGGCCCATTT
GTTGGGACAGGCAATGGCACATGCGCCTCAGCCCCTGCTACCCATGAGATACCGGAAACTGC
GAGTATTCTCAGGGAGTGCTGTCCCAGCCCCAGAGGAAGAGTCCTTTGAGGTCTGGTTGGAA

CAGGCCACGGAGATAGTCAAAGAGTGGCCAGTAACAGAGGCAGAAAAGAAAAGGTGGCTGGC
GGAAAGCCTGCGGGGCCCTGCCCTGGACCTCATGCACATAGTGCAGGCAGACAACCCGTCCA
TCAGTGTAGAAGAGTGTTTGGAGGCCTTTAAGCAAGTGTTTGGGAGCCTAGAGAGCCGCAGG
ACAGCCCAGGTGAGGTATCTGAAGACCTATCAGGAGGAAGGAGAGAAGGTCTCAGCCTATGT
GTTACGGCTAGAAACCCTGCTCCGGAGAGCGGTGGAGAAACGCGCCATCCCTCGGCGTATTG
CGGACCAGGTCCGCCTGGAGCAGGTCATGGCTGGGGCCACTCTTAACCAGATGCTGTGGTGC
CGGCTTAGGGAGCTGAAGGATCAGGGCCCGCCCCCCAGCTTCCTTGAGCTAATGAAGGTAAT
ACGGGAAGAAGAGGAGGAAGAGGCCTCCTTTGAGAATGAGAGTATCGAAGAGCCAGAGGAAC
GAGATGGCTATGGCCGCTGGAATCATGAGGGAGACGACTGA

7.2.7. Amphiphysin

Homo sapiens amphiphysin (AMPH), transcript variant 1, mRNA; NCBI Reference Sequence: NM_001635.4:23-2110

>Amphiphysin_2088bp

ATGGCCGACATCAAGACGGGCATCTTCGCCAAGAACGTCCAGAAGCGACTCAACCGCGCGCA
GGAAAAGGTCCTCCAAAAGCTGGGGAAAGCTGATGAGACAAAAGACGAACAGTTCGAAGAAT
ATGTCCAGAACTTCAAACGGCAAGAAGCAGAGGGTACCAGACTTCAGCGAGAACTCCGAGGA
TATTTAGCAGCAATCAAAGGCATGCAGGAGGCCTCCATGAAGCTCACAGAGTCGCTGCATGA
AGTCTATGAGCCTGACTGGTATGGGCGGGAAGATGTGAAAATGGTTGGTGAGAAATGTGATG
TGCTGTGGGAAGACTTCCATCAAAAACTCGTGGATGGGTCCTTGCTAACACTGGATACCTAC
CTGGGGCAATTTCCTGACATAAAGAATCGCATCGCCAAGCGCAGCAGGAAGCTAGTGGACTA
TGACAGTGCCCGCCACCATCTGGAAGCTCTGCAGAGCTCCAAGAGGAAGGATGAGAGTCGAA
TCTCTAAGGCAGAAGAAGAATTTCAGAAAGCACAGAAAGTGTTTGAAGAGTTTAACGTTGAC
TTACAAGAAGAGTTACCATCATTATGGTCAAGACGAGTTGGATTTTATGTTAATACTTTCAA
AAACGTCTCCAGCCTTGAAGCCAAGTTTCATAAGGAAATTGCGGTGCTTTGCCACAAACTGT
ATGAAGTGATGACAAAACTGGGTGACCAGCACGCCGACAAGGCCTTCACCATCCAAGGAGCG
CCCAGTGATTCGGGTCCTCTCCGCATTGCAAAGACACCATCACCGCCTGAGGAGCCTTCACC
CCTCCCGAGCCCGACAGCAAGTCCAAATCATACATTAGCACCTGCGTCTCCCGCACCAGCAC
GGCCTCGGTCACCTTCACAGACAAGGAAAGGGCCTCCTGTCCCACCTCTACCTAAAGTCACC
CCGACAAAGGAACTGCAGCAGGAGAACATCATCAGTTTCTTTGAGGACAACTTTGTTCCAGA
AATCAGTGTGACAACACCTTCCCAGAATGAAGTCCCTGAGGTGAAGAAAGAGGAGACTTTGC
TGGATCTGGACTTTGATCCTTTCAAGCCCGAGGTGACACCTGCAGGTTCTGCTGGAGTGACC
CACTCACCCATGTCTCAGACATTGCCCTGGGACCTATGGACGACAAGCACTGATTTGGTACA
GCCGGCTTCTGGTGGTTCATTTAATGGATTCACACAGCCCCAGGATACTTCATTATTCACAA
TGCAGACAGACCAGAGTATGATCTGCAACTTGGCTGAATCTGAACAGGCTCCACCCACAGAG
CCAAAAGCAGAGGAGCCTCTGGCTGCTGTCACACCTGCCGTTGGTCTGGACCTTGGAATGGA
CACTCGGGCTGAGGAGCCAGTGGAGGAGGCAGTGATCATACCTGGAGCTGATGCTGATGCAG
CTGTTGGAACCTTGGTGTCAGCAGCTGAGGGGGCCCCAGGAGAGGAAGCAGAGGCGGAGAAG
GCCACTGTCCCTGCCGGGGAAGGAGTAAGTTTAGAGGAGGCCAAAATTGGAACTGAAACCAC
TGAGGGTGCAGAGAGTGCCCAACCTGAAGCAGAGGAGCTCGAAGCAACAGTGCCTCAGGAGA

AGGTCATTCCTTCGGTGGTCATAGAGCCTGCCTCCAACCATGAAGAGGAAGGAGAAAACGAA
ATAACTATAGGTGCAGAGCCCAAGGAGACCACCGAGGACGCGGCTCCTCCGGGCCCCACCAG
CGAGACACCGGAGCTGGCTACGGAGCAGAAGCCTATCCAGGACCCTCAGCCCACGCCTTCTG
CACCAGCCATGGGGGCTGCTGACCAGCTAGCATCTGCAAGGGAGGCCTCTCAGGAATTGCCT
CCTGGCTTTCTCTACAAGGTGGAAACACTGCATGATTTTGAGGCAGCAAATTCTGATGAACT
TACCTTACAAAGGGGTGATGTGGTGCTGGTGGTCCCCTCAGATTCAGAAGCTGATCAGGATG
CAGGCTGGCTGGTGGGAGTGAAGGAATCAGACTGGCTTCAGTACAGAGACCTTGCCACCTAC
AAAGGCCTCTTTCCAGAGAACTTCACCCGACGCTTAGATTAG

7.2.8. CRMP5

Homo sapiens dihydropyrimidinase like 5 (DPYSL5), transcript variant 1, mRNA; NCBI

Reference Sequence: NM_020134.4:128-1822

>CRMP5_1695bp

ATGCTTGCCAACTCAGCCAGCGTGAGGATCCTCATCAAGGGAGGCAAGGTGGTGAACGATGA
CTGCACCCACGAGGCTGACGTCTACATCGAGAATGGCATCATCCAGCAGGTGGGCCGCGAGC
TCATGATCCCTGGCGGGGCCAAGGTGATTGATGCCACAGGAAAACTGGTGATCCCTGGTGGC
ATCGACACCAGCACCCACTTCCACCAGACCTTCATGAATGCCACGTGCGTGGACGACTTCTA
CCATGGGACCAAGGCAGCACTCGTCGGAGGCACCACCATGATCATCGGCCACGTCCTGCCCG
ACAAGGAGACCTCCCTTGTGGACGCTTATGAGAAGTGCCGAGGTCTGGCCGACCCCAAGGTC
TGCTGTGATTACGCCCTCCACGTGGGGATCACCTGGTGGGCACCCAAGGTGAAAGCAGAAAT
GGAGACACTGGTGAGGGAGAAGGGTGTCAACTCGTTCCAGATGTTCATGACCTACAAGGACC
TGTACATGCTTCGAGACAGTGAGCTGTACCAAGTGTTGCACGCTTGCAAGGACATTGGGGCA
ATCGCCCGCGTCCATGCTGAAAATGGGGAGCTTGTGGCCGAGGGTGCTAAGGAGGCACTGGA
TTTGGGGATCACAGGCCCAGAAGGAATCGAGATCAGCCGTCCAGAGGAGCTGGAAGCTGAAG
CCACTCATCGTGTTATCACCATTGCAAACAGGACTCACTGTCCAATCTACCTGGTCAACGTG
TCCAGTATCTCGGCTGGTGACGTTATCGCAGCTGCTAAGATGCAAGGGAAGGTTGTGCTGGC
GGAGACCACCACTGCACATGCCACGCTGACAGGCTTACACTACTACCACCAGGACTGGTCCC
ACGCGGCTGCCTATGTCACGGTGCCTCCCCTGAGACTGGACACCAACACCTCAACCTACCTC
ATGAGCCTGCTGGCCAATGACACTCTGAACATCGTGGCATCAGATCACCGGCCTTTCACCAC
AAAGCAGAAAGCTATGGGCAAGGAAGACTTCACCAAGATCCCACATGGAGTGAGTGGCGTGC
AGGACCGCATGAGCGTCATCTGGGAGAGAGGAGTGGTTGGAGGAAAGATGGATGAGAACCGT
TTTGTGGCCGTTACCAGTTCCAACGCAGCTAAGCTTCTGAACCTGTATCCCCGCAAGGGCCG
CATTATTCCCGGAGCCGATGCTGATGTGGTGGTGTGGGACCCAGAAGCCACAAAGACCATCT
CAGCCAGCACGCAGGTCCAGGGAGGAGACTTCAACCTGTATGAGAACATGCGCTGCCACGGC
GTGCCACTGGTCACCATCAGCCGGGGGCGCGTCGTGTATGAGAACGGCGTCTTCATGTGCGC
CGAGGGCACCGGCAAGTTCTGTCCCCTGAGGTCCTTCCCAGACACTGTCTACAAGAAGCTGG
TCCAGAGAGAGAAGACTTTAAAGGTTAGAGGAGTGGACCGCACTCCCTACCTGGGGGATGTC
GCTGTTGTCGTGCACCCTGGGAAAAAAGAGATGGGAACCCCACTCGCAGACACTCCTACCCG
GCCCGTCACCCGGCATGGGGGCATGAGGGACCTTCACGAATCCAGCTTCAGCCTCTCTGGCT

CTCAGATCGATGACCATGTTCCAAAGCGAGCTTCAGCTCGGATCCTCGCTCCTCCCGGAGGC
AGGTCGAGTGGCATTTGGTAA

7.2.9. ZIC4

Homo sapiens Zic family member 4, mRNA (cDNA clone MGC:167949 IMAGE:9020326), complete cds; GenBank: BC136339.1:99-1103

>ZIC4_1005bp

ATGAGATACAAGACATCCTTGGTGATGAGGAAACGATTACGGCTTTACCGAAACACTCTTAA
AGAGTCAAGTAGCAGCTCTGGACACCATGGCCCCCAGCTCACCGCCGCCTCCAGCCCCTCGG
TGTTCCCGGGCCTCCACGAGGAGCCTCCCCAGGCCTCCCCCAGCCGTCCTTTGAATGGACTC
CTGCGTCTGGGGCTCCCTGGAGACATGTACGCGCGGCCGGAGCCCTTCCCGCCAGGGCCTGC
GGCCCGCAGCGACGCCCTGGCAGCTGCCGCGGCCCTGCATGGCTACGGGGGCATGAACCTGA
CGGTGAACCTCGCTGCGCCCCACGGTCCTGGCGCTTTCTTCCGCTACATGCGCCAGCCCATC
AAACAGGAGCTCATCTGCAAGTGGCTGGCGGCCGACGGCACCGCGACCCCGAGCCTCTGCTC
CAAAACTTTCAGCACCATGCACGAGCTGGTCACGCACGTCACCGTGGAGCACGTCGGCGGCC
CGGAACAGGCCAACCACATTTGCTTCTGGGAGGAGTGTCCGCGCCAGGGAAAGCCCTTCAAA
GCCAAATACAAACTTGTAAATCACATCCGCGTGCACACGGGCGAGAAGCCCTTCCCTTGTCC
TTTCCCGGGGTGTGGGAAGGTCTTTGCTAGATCAGAAAATCTCAAAATACACAAACGAACTC
ACACAGGCGAGAAGCCCTTCAGATGCGAGTTCGAGGGCTGCGAGCGGCGCTTCGCCAACAGC
AGCGACCGTAAGAAGCATTCGCACGTGCACACTAGCGACAAGCCATACACGTGCAAGGTGCG
GGGCTGCGACAAGTGCTACACGCACCCCAGCTCGCTGCGTAAGCACATGAAGGTGCACGGGC
GCTCGCCGCCGCCCAGCTCTGGCTACGATTCGGCTACACCGTCTGCCCTCGTGTCGCCCTCG
TCGGACTGCGGCCACAAGTCCCAGGTGGCCTCCTCGGCGGCGGTGGCGGCGCGTACCGCCGA
CTTGAGCGAATGA

7.2.10. SOX1

Homo sapiens SRY-box transcription factor 1 (SOX1), mRNA; NCBI Reference Sequence: NM_005986.3:511-1686

>SOX1_1176bp

ATGTACAGCATGATGATGGAGACCGACCTGCACTCGCCCGGCGGCGCCCAGGCCCCCACGAA
CCTCTCGGGCCCCGCCGGGGCGGGCGGCGGCGGGGGCGGAGGCGGGGGCGGCGGCGGCGGCG
GGGGCGCCAAGGCCAACCAGGACCGGGTCAAACGGCCCATGAACGCCTTCATGGTGTGGTCC
CGCGGGCAGCGGCGCAAGATGGCCCAGGAGAACCCCAAGATGCACAACTCGGAGATCAGCAA
GCGCCTGGGGGCCGAGTGGAAGGTCATGTCCGAGGCCGAGAAGCGGCCGTTCATCGACGAGG
CCAAGCGGCTGCGCGCGCTGCACATGAAGGAGCACCCGGATTACAAGTACCGGCCGCGCCGC
AAGACCAAGACGCTGCTCAAGAAGGACAAGTACTCGCTGGCCGGCGGGCTCCTGGCGGCCGG

CGCGGGTGGCGGCGGCGCGGCTGTGGCCATGGGCGTGGGCGTGGGCGTGGGCGCGGCGGCCG
TGGGCCAGCGCCTGGAGAGCCCAGGCGGCGCGGCGGGCGGCGGCTACGCGCACGTCAACGGC
TGGGCCAACGGCGCCTACCCCGGCTCGGTGGCGGCGGCGGCGGCGGCCGCGGCCATGATGCA
GGAGGCGCAGCTGGCCTACGGGCAGCACCCGGGCGCGGGCGGCGCGCACCCGCACGCGCACC
CCGCGCACCCGCACCCGCACCACCCGCACGCGCACCCGCACAACCCGCAGCCCATGCACCGC
TACGACATGGGCGCGCTGCAGTACAGCCCCATCTCCAACTCGCAGGGCTACATGAGCGCGTC
GCCCTCGGGCTACGGCGGCCTCCCCTACGGCGCCGCGGCCGCCGCCGCCGCCGCTGCGGGCG
GCGCGCACCAGAACTCGGCCGTGGCGGCGGCGGCGGCGGCGGCGGCCGCGTCGTCGGGCGCC
CTGGGCGCGCTGGGCTCTCTGGTGAAGTCGGAGCCCAGCGGCAGCCCGCCCGCCCCAGCGCA
CTCGCGGGCGCCGTGCCCCGGGGACCTGCGCGAGATGATCAGCATGTACTTGCCCGCCGGCG
AGGGGGGCGACCCGGCGGCGGCAGCAGCGGCCGCGGCGCAGAGCCGGCTGCACTCGCTGCCG
CAGCACTACCAGGGCGCGGGCGCGGGCGTGAACGGCACGGTGCCCCTGACGCACATCTAG

7.2.11. KLHL11

Homo sapiens kelch like family member 11 (KLHL11), mRNA; NCBI Reference Sequence: NM_018143.3:54-2180

>KLHL11_2127bp

ATGGCGGCTGCGGCAGTGGCGGCGGCGGCGGCGGCGGCCGCGGCTGCATCTCTTCAGGTACT
GGAGATGGAGAGCATGGAGACGGCCGCCGCCGGCTCGGCAGGACTGGCCGCCGAGGTCCGAG
GCAGCGGCACGGTGGACTTCGGGCCTGGGCCGGGGATCTCTGCAATGGAGGCGAGCGGGGGC
GATCCGGGCCCAGAAGCCGAGGATTTCGAGTGCAGCTCTCACTGCTCAGAGCTGTCCTGGCG
GCAGAACGAGCAGCGGCGCCAGGGCCTCTTCTGCGACATTACCCTGTGCTTCGGCGGGGCTG
GAGGCCGCGAGTTCCGGGCCCACCGCTCGGTACTGGCTGCCGCCACCGAGTACTTCACGCCC
CTGCTCTCGGGCCAGTTTTCCGAGTCCCGCTCGGGACGGGTGGAGATGCGCAAGTGGAGCTC
CGAGCCGGGGCCCGAACCCGACACAGTGGAAGCCGTAATCGAGTACATGTACACCGGGCGCA
TCCGCGTCAGCACGGGCAGCGTGCACGAGGTGCTGGAGTTGGCCGACAGGTTCCTACTCATT
CGTTTAAAAGAATTTTGTGGAGAATTTCTCAAGAAAAAACTTCATCTCTCAAATTGTGTGGC
AATTCATAGCTTAGCACACATGTACACCCTGAGCCAACTTGCTCTGAAGGCTGCTGATATGA
TACGGAGAAATTTCCACAAAGTGATTCAGGATGAAGAATTTTATACGTTACCTTTCCATCTC
ATTAGAGACTGGCTTTCAGATTTGGAAATTACAGTTGATTCTGAAGAGGTTCTCTTTGAAAC
CGTTTTGAAATGGGTTCAGAGAAATGCTGAAGAGAGAGAGAGATACTTTGAAGAACTTTTTA
AATTGCTCAGGTTGTCCCAGATGAAACCTACCTACCTTACTCGACATGTCAAACCAGAGAGG
CTGGTAGCCAATAATGAAGTTTGTGTCAAGTTGGTCGCTGACGCAGTGGAGAGACATGCTCT
GAGAGCTGAGAATATACAATCTGGCACATGCCAGCACCCCACTTCTCATGTGTCACTATTGC
CTCGTTATGGGCAAAACATGGATGTGATCATGGTTATTGGAGGTGTGTCAGAAGGAGGGGAC
TATTTAAGTGAATGTGTGGGATACTTTGTTGATGAGGACAGATGGGTAAATCTGCCACATAT
TCATAATCACCTCGATGGACATGCTGTTGCAGTAACAGAATCCTACGTGTATGTTGCTGGAT
CAATGGAGCCAGGGTTTGCTAAAACTGTAGAAAGGTATAACCCAAATTTGAATACATGGGAA
CATGTTTGTAGTCTGATGACAAGAAAGCATTCTTTTGGACTAACAGAAGTCAAAGGGAAGCT
CTATAGCATTGGAGGACATGGCAACTTTAGTCCTGGTTTTAAAGATGTGACTGTTTATAATC

CTGAGCTTGATAAATGGCACAACTTGGAATCGGCACCAAAGATTCTTCGAGATGTCAAAGCA
CTAGCCATTGAAGACCGGTTTGTATACATTGCCGCCCGCACTCCTGTAGACCGGGACACTGA
AGATGGATTAAAGGCTGTAATTACTTGCTATGATACAGAGACTCGACAGTGGCAAGATGTGG
AATCTTTGCCGCTTATTGACAATTACTGCTTTTTCCAAATGTCTGTGGTCAATTCAAACTTT
TATCAGACAGCATCATGTTGTCCCAAGAGTTATTGTTTAGAAAACGAAGAGGCAGTAAGAAA
AATTGCCAGCCAAGTGTCTGATGAGATCCTTGAAAGCTTGCCTCCAGAAGTCCTAAGCATCG
AAGGAGCAGCCATTTGCTATTACAAAGATGATGTCTTCATTATAGGAGGCTGGAAAAACAGT
GATGATATTGATAAACAGTATCGGAAAGAAGCCTACCGATATTGTGCGGAGAGGAAGAGGTG
GATGCTTCTTCCTCCTATGCCACAACCTCGTTGTAGAGCCACTGCTTGTCACGTGAGGATCC
CATACCGGTACTTGCATGGCACACAGAGATACCCTATGCCTCAAAACCTGATGTGGCAGAAG
GACCGCATCAGACAGATGCAAGAGATACATCGTCACGCCCTGAACATGAGGCGAGTGCCAAG
CTCTCAGATTGAATGCTAG

7.3. The cDNA clones of AQP4 and MOG isoforms

7.3.1. AQP4 M23 isoform

Homo sapiens aquaporin 4 (AQP4), transcript variant 1, mRNA; NCBI Reference Sequence: NM_001364286.1:181-1086

>AQP4 M23_906bp

ATGGTGGCTTTCAAAGGGGTCTGGACTCAAGCTTTCTGGAAAGCAGTCACAGCGGAATTTCT
GGCCATGCTTATTTTTGTTCTCCTCAGCCTGGGATCCACCATCAACTGGGGTGGAACAGAAA
AGCCTTTACCGGTCGACATGGTTCTCATCTCCCTTTGCTTTGGACTCAGCATTGCAACCATG
GTGCAGTGCTTTGGCCATATCAGCGGTGGCCACATCAACCCTGCAGTGACTGTGGCCATGGT
GTGCACCAGGAAGATCAGCATCGCCAAGTCTGTCTTCTACATCGCAGCCCAGTGCCTGGGGG
CCATCATTGGAGCAGGAATCCTCTATCTGGTCACACCTCCCAGTGTGGTGGGAGGCCTGGGA
GTCACCATGGTTCATGGAAATCTTACCGCTGGTCATGGTCTCCTGGTTGAGTTGATAATCAC
ATTTCAATTGGTGTTTACTATCTTTGCCAGCTGTGATTCCAAACGGACTGATGTCACTGGCT
CAATAGCTTTAGCAATTGGATTTTCTGTTGCAATTGGACATTTATTTGCAATCAATTATACT
GGTGCCAGCATGAATCCCGCCCGATCCTTTGGACCTGCAGTTATCATGGGAAATTGGGAAAA
CCATTGGATATATTGGGTTGGGCCCATCATAGGAGCTGTCCTCGCTGGTGGCCTTTATGAGT
ATGTCTTCTGTCCAGATGTTGAATTCAAACGTCGTTTTAAAGAAGCCTTCAGCAAAGCTGCC
CAGCAAACAAAAGGAAGCTACATGGAGGTGGAGGACAACAGGAGTCAGGTAGAGACGGATGA
CCTGATTCTAAAACCTGGAGTGGTGCATGTGATTGACGTTGACCGGGGAGAGGAGAAGAAGG
GGAAAGACCAATCTGGAGAGGTATTGTCTTCAGTATGA

7.3.2. MOG α1 isoform

Homo sapiens myelin oligodendrocyte glycoprotein (MOG), transcript variant alpha1, mRNA; NCBI Reference Sequence: NM_206809.4:119-862

>MOG α1_744bp

ATGGCAAGCTTATCAAGACCCTCTCTGCCCAGCTGCCTCTGCTCCTTCCTCCTCCTCCTCCT
CCTCCAAGTGTCTTCCAGCTATGCAGGGCAGTTCAGAGTGATAGGACCAAGACACCCTATCC
GGGCTCTGGTCGGGGATGAAGTGGAATTGCCATGTCGCATATCTCCTGGGAAGAACGCTACA
GGCATGGAGGTGGGGTGGTACCGCCCCCCCTTCTCTAGGGTGGTTCATCTCTACAGAAATGG
CAAGGACCAAGATGGAGACCAGGCACCTGAATATCGGGGCCGGACAGAGCTGCTGAAAGATG
CTATTGGTGAGGGAAAGGTGACTCTCAGGATCCGGAATGTAAGGTTCTCAGATGAAGGAGGT
TTCACCTGCTTCTTCCGAGATCATTCTTACCAAGAGGAGGCAGCAATGGAATTGAAAGTAGA
AGATCCTTTCTACTGGGTGAGCCCTGGAGTGCTGGTTCTCCTCGCGGTGCTGCCTGTGCTCC
TCCTGCAGATCACTGTTGGCCTCATCTTCCTCTGCCTGCAGTACAGACTGAGAGGAAAACTT
CGAGCAGAGATAGAGAATCTCCACCGGACTTTTGATCCCCACTTTCTGAGGGTGCCCTGCTG
GAAGATAACCCTGTTTGTAATTGTGCCGGTTCTTGGACCCTTGGTTGCCTTGATCATCTGCT
ACAACTGGCTACATCGAAGACTAGCAGGGCAATTCCTTGAAGAGCTACGAAATCCCTTCTGA

7.4. Summary of primer sequences

Table 7.1: The primer pairs for restriction enzyme-based cloning

Amplifying target	Primer sequence	Annealing temperature
IL-6, FP	GATCGCTAGCCCACCATGAACTCCTTCTCCACAAGCG	64°C
IL-6, RP	GATCGTCGACCATTTGCCGAAGAGCCCT	
IL-12A, FP	GATCGCTAGCCCACCATGTGGCCCCCTGGGTCAG	66°C
IL-12A, RP	GATCGTCGACGGAAGCATTCAGATAGCTCATCACTC	
IL-12B, FP	GATCGCTAGCCCACCATGTGTCACCAGCAGTTGGTCATC	68°C
IL-12B, RP	GATCGTCGACACTGCAGGGCACAGATGCC	
IL-17A, FP	GATCAGATCTCCACCATGACTCCTGGGAAGACCTCATTGG	57°C

IL-17A, RP	GATCGTCGACGGCCACATGGTGGACAATCG	
IL-17F, FP	GATCAGATCTCCACCATGACAGTGAAGACCCTGCATGG	57°C
IL-17F, RP	GATCGTCGACCTGCACACGGTGGATGACAGG	
IL-23A, FP	GATCGCTAGCCCACCATGCTGGGGAGCAGAGCT	64°C
IL-23A, RP	GATCGTCGACGGGACTCAGGGTTGCTGCT	
IFNα2, FP	GATCGCTAGCCCACCATGGCCTTGACCTTTGCTTTAC	66°C
IFNα2, RP	GATCGTCGACTTCCTTACTTCTTAAACTTTCTTGCAAG	
IFNα8, FP	GATCGCTAGCCCACCATGGCCTTGACTTTTTATTTACTG	63°C
IFNα8, RP	GATCGTCGACTTCCTTACTCTTCAATCTTTTTTGC	
IFNω1, FP	GATCGCTAGCCCACCATGGCCCTCCTGTTCC	60°C
IFNω1, RP	GATCGTCGACAGATGAGCCCAGGTCTCTATC	
Onconeural cloning, FP	GCAGAGCCTGGACGGCTAAGC	61°C
Onconeural cloning, RP	GCTTGGCCTTGTCCCTCGAGTCC	

* FP, forward primer; RP, reverse primer; NheI site is in blue, SalI site is in yellow, BglII site is in green and XhoI site is in pink.

Table 7.2: The primer pairs for site-directed mutagenesis (SDM)

Aim	**Primer sequence**	**Annealing temperature**
Introduce a Glycine-Glycine-Serine 4 repeats linker extension into IL-22 CBA construct	FP: GGTGGTAGTGGTGGTAGTGGACAAGGCCAAGCTATAAG	64°C
	RP: GAAATGCCTGCATTGTCGACGGTGGTAGTGGTGGTAGT	

Introduce a XbaI restriction site before the cDNA of DsRed2	FP: TCTAGAGCCTCCTCCGAGAACGTC	65°C
	RP: CATGGTTGTGGCCATATTATCATC	
Introduce a myc tag to the position I of IL-22 36 flexible aa extended CBA construct	FP: AGCGAAGAAGATCTGGGTGGCAGTGCTGATAATG	64°C
	RP: AATCAGTTTCTGTTCGTCGACAATGCAGGCATTT	
Introduce a myc tag to the position II of IL-22 36 flexible aa extended CBA construct	FP: AGCGAAGAAGATCTGGGAGGGAGCGCCGACAAC	69°C
	RP: AATCAGTTTCTGTTCACTGCCACCATTGTCAGCATTATC	
Introduce a myc tag to the position III of IL-22 36 flexible aa extended CBA construct	FP: AGCGAAGAAGATCTGGGACAAGGCCAAGCTATAAGAAATGG	69°C
	RP: AATCAGTTTCTGTTCGCTCCCTCCGTTGTCGGC	
Modify myc tag from EQKLISEEDL to EGGGGGEEDL	FP: TGGTGGTGAAGAAGATCTGGGAGGG	62°C
	RP: CCACCACCTTCACTGCCACCATTGTC	
Introduce a stop codon (TAA) after the cDNA of CRMP5	FP: TAAGGACTCGAGGGACAAGGC	67°C
	RP: CCAAATGCCACTCGACCTG	
Delete Caspr2 signal sequence before the cDNA of CRMP5	FP: ATGCTTGCCAACTCAGCC	67°C
	RP: GGTGGGCTAGCCAGCTTG	

Table 7.3: The primer pairs for Sanger sequencing

Name	Primer sequence
pIRES2-DsRed2 FP (within CMV promoter)	GGGCGGTAGGCGTGTACGGTGG
pIRES2-DsRed2 RP (after truncated C-terminal Caspr2)	CAAACGCACACCGGCCTTATTCC
DsRed2_seq	GTCGAGGTTAAAAAAACGTCTAGGCC
IRES_seq	TAACGTTACTGGCCGAAGCCGCTT
CMVF_pCDNA3	CAACGGGACTTTCCAAAATG
EGFP_Nrev	CGTCGCCGTCCAGCTCGACCAG
Onconeural, FP	GCAGAGCCTGGACGGCTAAGC
Onconeural, RP	GCTTGGCCTTGTCCCTCGAGTCC

References

AL-DIWANI, A., THEORELL, J., DAMATO, V., BULL, J., MCGLASHAN, N., GREEN, E., KIENZLER, A. K., HARRISON, R., HASSANALI, T., CAMPO, L., BROWNE, M., EASTON, A., SOLEYMANI MAJD, H., TENAKA, K., IORIO, R., DALE, R. C., HARRISON, P., GEDDES, J., QUESTED, D., SHARP, D., LEE, S. T., NAUEN, D. W., MAKUCH, M., LENNOX, B., FOWLER, D., SHEERIN, F., WATERS, P., LEITE, M. I., HANDEL, A. E. & IRANI, S. R. 2022. Cervical lymph nodes and ovarian teratomas as germinal centres in NMDA receptor-antibody encephalitis. *Brain,* 145**,** 2742-2754.

AMATOURY, M., MERHEB, V., LANGER, J., WANG, X. M., DALE, R. C. & BRILOT, F. 2013. High-throughput flow cytometry cell-based assay to detect antibodies to N-methyl-D-aspartate receptor or dopamine-2 receptor in human serum. *J Vis Exp***,** e50935.

ATABAKHSH, E. 2019. Accelerating High-Throughput Screening with FirePlex. *Journal of Biomolecular Techniques: JBT,* 30**,** S3.

BATALLER, L., WADE, D. F., GRAUS, F., STACEY, H. D., ROSENFELD, M. R. & DALMAU, J. 2004. Antibodies to Zic4 in paraneoplastic neurologic disorders and small-cell lung cancer. *Neurology,* 62**,** 778-82.

BENDTZEN, K. & SVENSON, M. 2011. Enzyme Immunoassays and Radioimmunoassays for Quantification of Anti-TNF Biopharmaceuticals and Anti-Drug Antibodies. *Detection and Quantification of Antibodies to Biopharmaceuticals: Practical and Applied Considerations***,** 81-101.

BERGER, B., DERSCH, R., RUTHARDT, E., RASIAH, C., RAUER, S. & STICH, O. 2016. Prevalence of anti-SOX1 reactivity in various neurological disorders. *J Neurol Sci,* 369**,** 342-346.

BERNARD, C., FRIH, H., PASQUET, F., KEREVER, S., JAMILLOUX, Y., TRONC, F., GUIBERT, B., ISAAC, S., DEVOUASSOUX, M., CHALABREYSSE, L., BROUSSOLLE, C., PETIOT, P., GIRARD, N. & SEVE, P. 2016. Thymoma associated with autoimmune diseases: 85 cases and literature review. *Autoimmun Rev,* 15**,** 82-92.

BERRIH-AKNIN, S. & LE PANSE, R. 2014. Myasthenia gravis: a comprehensive review of immune dysregulation and etiological mechanisms. *J Autoimmun,* 52**,** 90-100.

BERRIH-AKNIN, S. 2016. Role of the thymus in autoimmune myasthenia gravis. *Clinical and Experimental Neuroimmunology,* 7**,** 226-237.

BERZERO, G., KARANTONI, E., DEHAIS, C., DUCRAY, F., THOMAS, L., PICARD, G., ROGEMOND, V., CANDELIER, G., CAMDESSANCHÉ, J.-P. & ANTOINE, J.-C. 2018. Early intravenous immunoglobulin treatment in paraneoplastic neurological syndromes with onconeural antibodies. *Journal of Neurology, Neurosurgery & Psychiatry,* 89**,** 789-792.

BIEN, C. G., VINCENT, A., BARNETT, M. H., BECKER, A. J., BLUMCKE, I., GRAUS, F., JELLINGER, K. A., REUSS, D. E., RIBALTA, T., SCHLEGEL, J., SUTTON, I., LASSMANN, H. & BAUER, J. 2012. Immunopathology of autoantibody-associated encephalitides: clues for pathogenesis. *Brain,* 135**,** 1622-38.

BINKS, S., UY, C., HONNORAT, J. & IRANI, S. R. 2022. Paraneoplastic neurological syndromes: a practical approach to diagnosis and management. *Pract Neurol,* 22**,** 19-31.

BLAES, F. 2021. Pathogenesis, diagnosis and treatment of paraneoplastic neurologic syndromes. *Expert Rev Neurother,* 21**,** 675-686.

BLAES, F., STRITTMATTER, M., MERKELBACH, S., JOST, V., KLOTZ, M., SCHIMRIGK, K. & HAMANN, G. F. 1999. Intravenous immunoglobulins in the therapy of paraneoplastic neurological disorders. *Journal of neurology,* 246**,** 299-303.

BORISOW, N., MORI, M., KUWABARA, S., SCHEEL, M. & PAUL, F. 2018. Diagnosis and Treatment of NMO Spectrum Disorder and MOG-Encephalomyelitis. *Front Neurol,* 9**,** 888.

BUCKLEY, C., NEWSOM–DAVIS, J., WILLCOX, N. & VINCENT, A. 2001. Do titin and cytokine antibodies in MG patients predict thymoma or thymoma recurrence? *Neurology,* 57**,** 1579-1582.

BUDHRAM, A., NICOLLE, M. W. & YANG, L. 2018. The Positive Predictive Value of Onconeural Antibody Testing: A Retrospective Review. *Can J Neurol Sci,* 45**,** 577-579.

BURBELO, P. D., BROWNE, S. K., SAMPAIO, E. P., GIACCONE, G., ZAMAN, R., KRISTOSTURYAN, E., RAJAN, A., DING, L., CHING, K. H., BERMAN, A., OLIVEIRA, J. B., HSU, A. P., KLIMAVICZ, C. M., IADAROLA, M. J. & HOLLAND, S. M. 2010. Anti-cytokine autoantibodies are associated with opportunistic infection in patients with thymic neoplasia. *Blood,* 116**,** 4848-58.

CANNING, P., COOPER, C. D. O., KROJER, T., MURRAY, J. W., PIKE, A. C. W., CHAIKUAD, A., KEATES, T., THANGARATNARAJAH, C., HOJZAN, V., MARSDEN, B. D., GILEADI, O., KNAPP, S., VON DELFT, F. & BULLOCK, A. N. 2013. Structural basis for Cul3 protein assembly with the BTB-Kelch family of E3 ubiquitin ligases. *J Biol Chem,* 288**,** 7803-7814.

CAPPELLANO, G., ORILIERI, E., WOLDETSADIK, A. D., BOGGIO, E., SOLURI, M. F., COMI, C., SBLATTERO, D., CHIOCCHETTI, A. & DIANZANI, U. 2012. Anti-cytokine autoantibodies in autoimmune diseases. *American journal of clinical and experimental immunology,* 1**,** 136.

CHAN, K. H., KWAN, J. S., HO, P. W., HO, J. W., CHU, A. C. & RAMSDEN, D. B. 2010. Aquaporin-4 autoantibodies in neuromyelitis optica spectrum disorders: comparison between tissue-based and cell-based indirect immunofluorescence assays. *Journal of neuroinflammation,* 7**,** 1-9.

CLUDTS, I., MEAGER, A., THORPE, R. & WADHWA, M. 2010. Detection of neutralizing interleukin-17 antibodies in autoimmune polyendocrinopathy syndrome-1 (APS-1) patients using a novel non-cell based electrochemiluminescence assay. *Cytokine,* 50**,** 129-37.

DABROWSKI, M., BUKOWY-BIERYLLO, Z. & ZIETKIEWICZ, E. 2015. Translational readthrough potential of natural termination codons in eucaryotes--The impact of RNA sequence. *RNA Biol,* 12**,** 950-8.

DALMAU, J., GEIS, C. & GRAUS, F. 2017. Autoantibodies to Synaptic Receptors and Neuronal Cell Surface Proteins in Autoimmune Diseases of the Central Nervous System. *Physiol Rev,* 97**,** 839-887.

DALMAU, J. & GRAUS, F. 2018. Antibody-Mediated Encephalitis. *N Engl J Med,* 378**,** 840-851.

DALMAU, J., GRAUS, F., CHEUNG, N. K. V., ROSENBLUM, M. K., HO, A., CAÑETE, A., DELATTRE, J. Y., THOMPSON, S. J. & POSNER, J. B. 1995. Major histocompatibility proteins, anti-Hu antibodies, and paraneoplastic encephalomyelitis in neuroblastoma and small cell lung cancer. *Cancer,* 75**,** 99-109.

DALMAU, J. & ROSENFELD, M. R. 2020. Paraneoplastic Neurologic Syndromes. *Abeloff's Clinical Oncology.*

DARNELL, R. B. & POSNER, J. B. 2003. Paraneoplastic syndromes involving the nervous system. *New England Journal of Medicine,* 349**,** 1543-1554.
DAY, G. S., LAIQ, S., TANG-WAI, D. F. & MUNOZ, D. G. 2014. Abnormal neurons in teratomas in NMDAR encephalitis. *JAMA Neurol,* 71**,** 717-24.
DE JONGSTE, A. H., VAN GELDER, T., BROMBERG, J. E., DE GRAAF, M. T., GRATAMA, J. W., SCHREURS, M. W., HOOIJKAAS, H. & SILLEVIS SMITT, P. A. 2015. A prospective open-label study of sirolimus for the treatment of anti-Hu associated paraneoplastic neurological syndromes. *Neuro Oncol,* 17**,** 145-50.
DECHELOTTE, B., MUNIZ-CASTRILLO, S., JOUBERT, B., VOGRIG, A., PICARD, G., ROGEMOND, V., PINTO, A. L., LOMBARD, C., DESESTRET, V., FABIEN, N. & HONNORAT, J. 2020. Diagnostic yield of commercial immunodots to diagnose paraneoplastic neurologic syndromes. *Neurol Neuroimmunol Neuroinflamm,* 7.
DOS PASSOS, G. R., OLIVEIRA, L. M., DA COSTA, B. K., APOSTOLOS-PEREIRA, S. L., CALLEGARO, D., FUJIHARA, K. & SATO, D. K. 2018. MOG-IgG-Associated Optic Neuritis, Encephalitis, and Myelitis: Lessons Learned From Neuromyelitis Optica Spectrum Disorder. *Front Neurol,* 9**,** 217.
DUBEY, D., WILSON, M. R., CLARKSON, B., GIANNINI, C., GANDHI, M., CHEVILLE, J., LENNON, V. A., EGGERS, S., DEVINE, M. F., MANDEL-BREHM, C., KRYZER, T., HINSON, S. R., KHAZAIE, K., HALES, C., KATTAH, J., PAVELKO, K. D., ANDREWS, P., EATON, J. E., JITPRAPAIKULSAN, J., MILLS, J. R., FLANAGAN, E. P., ZEKERIDOU, A., LEIBOVICH, B., FRYER, J., TORRE, M., KAUFMAN, C., THORESON, J. B., SAGEN, J., LINNOILA, J. J., DERISI, J. L., HOWE, C. L., MCKEON, A. & PITTOCK, S. J. 2020. Expanded Clinical Phenotype, Oncological Associations, and Immunopathologic Insights of Paraneoplastic Kelch-like Protein-11 Encephalitis. *JAMA Neurol,* 77**,** 1420-1429.
ELKON, K. & CASALI, P. 2008. Nature and functions of autoantibodies. *Nat Clin Pract Rheumatol,* 4**,** 491-8.
ENGELS, E. A. 2010. Epidemiology of thymoma and associated malignancies. *Journal of Thoracic Oncology,* 5**,** S260-S265.
GEBAUER, C., PIGNOLET, B., YSHII, L., MAURE, E., BAUER, J. & LIBLAU, R. 2017. CD4+ and CD8+ T cells are both needed to induce paraneoplastic neurological disease in a mouse model. *Oncoimmunology,* 6**,** e1260212.
GILHUS, N. E., TZARTOS, S., EVOLI, A., PALACE, J., BURNS, T. M. & VERSCHUUREN, J. 2019. Myasthenia gravis. *Nat Rev Dis Primers,* 5**,** 30.
GILHUS, N. E. & VERSCHUUREN, J. J. 2015. Myasthenia gravis: subgroup classification and therapeutic strategies. *The Lancet Neurology,* 14**,** 1023-1036.
GOZZARD, P. & MADDISON, P. 2010. Which antibody and which cancer in which paraneoplastic syndromes? *Practical neurology,* 10**,** 260-270.
GRAUS, F., DALMOU, J., RENE, R., TORA, M., MALATS, N., VERSCHUUREN, J., CARDENAL, F., VINOLAS, N., GARCIA DEL MURO, J. & VADELL, C. 1997. Anti-Hu antibodies in patients with small-cell lung cancer: association with complete response to therapy and improved survival. *Journal of Clinical Oncology,* 15**,** 2866-2872.
GRAUS, F., DELATTRE, J. Y., ANTOINE, J. C., DALMAU, J., GIOMETTO, B., GRISOLD, W., HONNORAT, J., SMITT, P. S., VEDELER, C., VERSCHUUREN, J. J., VINCENT, A. & VOLTZ, R. 2004. Recommended

diagnostic criteria for paraneoplastic neurological syndromes. *J Neurol Neurosurg Psychiatry,* 75**,** 1135-40.
GRAUS, F., TITULAER, M. J., BALU, R., BENSELER, S., BIEN, C. G., CELLUCCI, T., CORTESE, I., DALE, R. C., GELFAND, J. M., GESCHWIND, M., GLASER, C. A., HONNORAT, J., HÖFTBERGER, R., IIZUKA, T., IRANI, S. R., LANCASTER, E., LEYPOLDT, F., PRÜSS, H., RAE-GRANT, A., REINDL, M., ROSENFELD, M. R., ROSTÁSY, K., SAIZ, A., VENKATESAN, A., VINCENT, A., WANDINGER, K.-P., WATERS, P. & DALMAU, J. 2016. A clinical approach to diagnosis of autoimmune encephalitis. *The Lancet Neurology,* 15**,** 391-404.
GRAUS, F., VOGRIG, A., MUNIZ-CASTRILLO, S., ANTOINE, J. G., DESESTRET, V., DUBEY, D., GIOMETTO, B., IRANI, S. R., JOUBERT, B., LEYPOLDT, F., MCKEON, A., PRUSS, H., PSIMARAS, D., THOMAS, L., TITULAER, M. J., VEDELER, C. A., VERSCHUUREN, J. J., DALMAU, J. & HONNORAT, J. 2021. Updated Diagnostic Criteria for Paraneoplastic Neurologic Syndromes. *Neurol Neuroimmunol Neuroinflamm,* 8.
GREENLEE, J. E., CLAWSON, S. A., HILL, K. E., WOOD, B., CLARDY, S. L., TSUNODA, I., JASKOWSKI, T. D. & CARLSON, N. G. 2014. Neuronal uptake of anti-Hu antibody, but not anti-Ri antibody, leads to cell death in brain slice cultures. *Journal of neuroinflammation,* 11**,** 1-15.
GROSS, J., MOLLER, R., HENKE, W. & HOESEL, W. 2006. Detection of anti-EPO antibodies in human sera by a bridging ELISA is much more sensitive when coating biotinylated rhEPO to streptavidin rather than using direct coating of rhEPO. *J Immunol Methods,* 313**,** 176-82.
HAYNES, B. F., SEMPOWSKI, G. D., WELLS, A. F. & HALE, L. P. 2000. The human thymus during aging. *Immunologic research,* 22**,** 253-261.
HEBERT, J., RICHE, B., VOGRIG, A., MUNIZ-CASTRILLO, S., JOUBERT, B., PICARD, G., ROGEMOND, V., PSIMARAS, D., ALENTORN, A., BERZERO, G., DESESTRET, V., RABILLOUD, M. & HONNORAT, J. 2020. Epidemiology of paraneoplastic neurologic syndromes and autoimmune encephalitides in France. *Neurol Neuroimmunol Neuroinflamm,* 7.
HOFFMANN, L. A., JARIUS, S., PELLKOFER, H. L., SCHUELLER, M., KRUMBHOLZ, M., KOENIG, F., JOHANNIS, W., LA FOUGERE, C., NEWMAN, T., VINCENT, A. & VOLTZ, R. 2008. Anti-Ma and anti-Ta associated paraneoplastic neurological syndromes: 22 newly diagnosed patients and review of previous cases. *J Neurol Neurosurg Psychiatry,* 79**,** 767-73.
HOFTBERGER, R., ROSENFELD, M. R. & DALMAU, J. 2015. Update on neurological paraneoplastic syndromes. *Curr Opin Oncol,* 27**,** 489-95.
HONNORAT, J. & ANTOINE, J. C. 2007. Paraneoplastic neurological syndromes. *Orphanet J Rare Dis,* 2**,** 22.
HUANG, F. & NAU, W. M. 2003. A conformational flexibility scale for amino acids in peptides. *Angewandte Chemie International Edition,* 42**,** 2269-2272.
HUANG, H., BENOIST, C. & MATHIS, D. 2010. Rituximab specifically depletes short-lived autoreactive plasma cells in a mouse model of inflammatory arthritis. *Proc Natl Acad Sci U S A,* 107**,** 4658-63.
HUGHES, E. G., PENG, X., GLEICHMAN, A. J., LAI, M., ZHOU, L., TSOU, R., PARSONS, T. D., LYNCH, D. R., DALMAU, J. & BALICE-GORDON, R. J. 2010. Cellular and synaptic mechanisms of anti-NMDA receptor encephalitis. *J Neurosci,* 30**,** 5866-75.

IORIO, R., DAMATO, V., MIRABELLA, M., EVOLI, A., MARTI, A., PLANTONE, D., FRISULLO, G. & BATOCCHI, A. P. 2013. Distinctive clinical and neuroimaging characteristics of longitudinally extensive transverse myelitis associated with aquaporin-4 autoantibodies. *J Neurol,* 260**,** 2396-402.
IRANI, S. R., ALEXANDER, S., WATERS, P., KLEOPA, K. A., PETTINGILL, P., ZULIANI, L., PELES, E., BUCKLEY, C., LANG, B. & VINCENT, A. 2010. Antibodies to Kv1 potassium channel-complex proteins leucine-rich, glioma inactivated 1 protein and contactin-associated protein-2 in limbic encephalitis, Morvan's syndrome and acquired neuromyotonia. *Brain,* 133**,** 2734-48.
JAGGA, B., EDWARDS, M., PAGIN, M., WAGSTAFF, K. M., ARAGAO, D., ROMAN, N., NANSON, J. D., RAIDAL, S. R., DOMINADO, N., STEWART, M., JANS, D. A., HIME, G. R., NICOLIS, S. K., BASLER, C. F. & FORWOOD, J. K. 2021. Structural basis for nuclear import selectivity of pioneer transcription factor SOX2. *Nat Commun,* 12**,** 28.
JALAH, R., ROSATI, M., GANNERU, B., PILKINGTON, G. R., VALENTIN, A., KULKARNI, V., BERGAMASCHI, C., CHOWDHURY, B., ZHANG, G. M., BEACH, R. K., ALICEA, C., BRODERICK, K. E., SARDESAI, N. Y., PAVLAKIS, G. N. & FELBER, B. K. 2013. The p40 subunit of interleukin (IL)-12 promotes stabilization and export of the p35 subunit: implications for improved IL-12 cytokine production. *J Biol Chem,* 288**,** 6763-76.
JARIUS, S., PAUL, F., AKTAS, O., ASGARI, N., DALE, R. C., DE SEZE, J., FRANCIOTTA, D., FUJIHARA, K., JACOB, A., KIM, H. J., KLEITER, I., KUMPFEL, T., LEVY, M., PALACE, J., RUPRECHT, K., SAIZ, A., TREBST, C., WEINSHENKER, B. G. & WILDEMANN, B. 2018. MOG encephalomyelitis: international recommendations on diagnosis and antibody testing. *J Neuroinflammation,* 15**,** 134.
KARIM, A. R. & JACOB, S. 2012. Immunological markers in neurological disorders. *Ann Clin Biochem,* 49**,** 29-43.
KARNER, J., PIHLAP, M., RANKI, A., KROHN, K., TREBUSAK PODKRAJSEK, K., BRATANIC, N., BATTELINO, T., WILLCOX, N., PETERSON, P. & KISAND, K. 2016. IL-6-specific autoantibodies among APECED and thymoma patients. *Immun Inflamm Dis,* 4**,** 235-243.
KISAND, K., LILIC, D., CASANOVA, J. L., PETERSON, P., MEAGER, A. & WILLCOX, N. 2011. Mucocutaneous candidiasis and autoimmunity against cytokines in APECED and thymoma patients: clinical and pathogenetic implications. *Eur J Immunol,* 41**,** 1517-27.
KITLEY, J., WATERS, P., WOODHALL, M., LEITE, M. I., MURCHISON, A., GEORGE, J., KUKER, W., CHANDRATRE, S., VINCENT, A. & PALACE, J. 2014. Neuromyelitis optica spectrum disorders with aquaporin-4 and myelin-oligodendrocyte glycoprotein antibodies: a comparative study. *JAMA Neurol,* 71**,** 276-83.
KLEIN, L., KYEWSKI, B., ALLEN, P. M. & HOGQUIST, K. A. 2014. Positive and negative selection of the T cell repertoire: what thymocytes see (and don't see). *Nat Rev Immunol,* 14**,** 377-91.
KRAKENES, T., HERDLEVAER, I., RASPOTNIG, M., HAUGEN, M., SCHUBERT, M. & VEDELER, C. A. 2019. CDR2L Is the Major Yo Antibody Target in Paraneoplastic Cerebellar Degeneration. *Ann Neurol,* 86**,** 316-321.
KROGER, C. J., SPIDALE, N. A., WANG, B. & TISCH, R. 2017. Thymic Dendritic Cell Subsets Display Distinct Efficiencies and Mechanisms of Intercellular MHC Transfer. *J Immunol,* 198**,** 249-256.

KRUTZIK, P. O., CLUTTER, M. R., TREJO, A. & NOLAN, G. P. 2011. Fluorescent cell barcoding for multiplex flow cytometry. *Curr Protoc Cytom,* Chapter 6**,** Unit 6 31.

KRUTZIK, P. O. & NOLAN, G. P. 2006. Fluorescent cell barcoding in flow cytometry allows high-throughput drug screening and signaling profiling. *Nat Methods,* 3**,** 361-8.

LEE, W. J., LEE, S. T., MOON, J., SUNWOO, J. S., BYUN, J. I., LIM, J. A., KIM, T. J., SHIN, Y. W., LEE, K. J., JUN, J. S., LEE, H. S., KIM, S., PARK, K. I., JUNG, K. H., JUNG, K. Y., KIM, M., LEE, S. K. & CHU, K. 2016a. Tocilizumab in Autoimmune Encephalitis Refractory to Rituximab: An Institutional Cohort Study. *Neurotherapeutics,* 13**,** 824-832.

LEE, Y. H., PANG, S. W. & TAN, K. O. 2016b. PNMA2 mediates heterodimeric interactions and antagonizes chemo-sensitizing activities mediated by members of PNMA family. *Biochem Biophys Res Commun,* 473**,** 224-229.

LEITE, M. I., JACOB, S., VIEGAS, S., COSSINS, J., CLOVER, L., MORGAN, B. P., BEESON, D., WILLCOX, N. & VINCENT, A. 2008. IgG1 antibodies to acetylcholine receptors in 'seronegative' myasthenia gravis. *Brain,* 131**,** 1940-52.

LEYPOLDT, F. & WANDINGER, K. P. 2014. Paraneoplastic neurological syndromes. *Clin Exp Immunol,* 175**,** 336-48.

LIESCHKE, E., WANG, Z., CHANG, C., WEEDEN, C. E., KELLY, G. L. & STRASSER, A. 2022. Flow cytometric single cell-based assay to simultaneously detect cell death, cell cycling, DNA content and cell senescence. *Cell Death Differ,* 29**,** 1004-1012.

LIPKA, A. F., BOLDINGH, M. I., VAN ZWET, E. W., SCHREURS, M. W. J., KUKS, J. B. M., TALLAKSEN, C. M., TITULAER, M. J. & VERSCHUUREN, J. 2020. Long-term follow-up, quality of life, and survival of patients with Lambert-Eaton myasthenic syndrome. *Neurology,* 94**,** e511-e520.

LIU, J., TAN, G., LI, B., ZHANG, J., GAO, Y., CAO, Y., JIA, Z. & SUGIMOTO, K. 2021. Serum Aquaporin 4-Immunoglobulin G Titer and Neuromyelitis Optica Spectrum Disorder Activity and Severity: A Systematic Review and Meta-Analysis. *Front Neurol,* 12**,** 746959.

LOPEZ, J. A., HOUSTON, S. D., TEA, F., MERHEB, V., LEE, F. X. Z., SMITH, S., MCDONALD, D., ZOU, A., LIYANAGE, G., PILLI, D., DENKOVA, M., LECHNER-SCOTT, J., VAN DER WALT, A., BARNETT, M. H., REDDEL, S. W., BROADLEY, S., RAMANATHAN, S., DALE, R. C., BROWN, D. A. & BRILOT, F. 2022. Validation of a Flow Cytometry Live Cell-Based Assay to Detect Myelin Oligodendrocyte Glycoprotein Antibodies for Clinical Diagnostics. *J Appl Lab Med,* 7**,** 12-25.

LUCCHINETTI, C. F., GUO, Y., POPESCU, B. F., FUJIHARA, K., ITOYAMA, Y. & MISU, T. 2014. The pathology of an autoimmune astrocytopathy: lessons learned from neuromyelitis optica. *Brain Pathol,* 24**,** 83-97.

MAAT, P., BROUWER, E., HULSENBOOM, E., VANDUIJN, M., SCHREURS, M. W., HOOIJKAAS, H. & SMITT, P. A. 2013. Multiplex serology of paraneoplastic antineuronal antibodies. *J Immunol Methods,* 391**,** 125-32.

MAETZIG, T., MORGAN, M. & SCHAMBACH, A. 2018. Fluorescent genetic barcoding for cellular multiplex analyses. *Exp Hematol,* 67**,** 10-17.

MARX, A., HOHENBERGER, P., HOFFMANN, H., PFANNSCHMIDT, J., SCHNABEL, P., HOFMANN, H.-S., WIEBE, K., SCHALKE, B., NIX, W. &

GOLD, R. 2010a. The autoimmune regulator AIRE in thymoma biology: autoimmunity and beyond. *Journal of Thoracic Oncology,* 5**,** S266-S272.
MARX, A., WILLCOX, N., LEITE, M. I., CHUANG, W. Y., SCHALKE, B., NIX, W. & STROBEL, P. 2010b. Thymoma and paraneoplastic myasthenia gravis. *Autoimmunity,* 43**,** 413-27.
MARX, A., YAMADA, Y., SIMON-KELLER, K., SCHALKE, B., WILLCOX, N., STROBEL, P. & WEIS, C. A. 2021. Thymus and autoimmunity. *Semin Immunopathol,* 43**,** 45-64.
MEAGER, A. 2000. RIA, IRMA, and ELISA for cytokines and their soluble receptors. *Cytokine cell biology: a practical approach.* Oxford University Press Oxford, UK.
MEAGER, A., VINCENT, A., NEWSOM-DAVIS, J. & WILLCOX, N. 1997. Spontaneous neutralising antibodies to interferon-a and interleukin-12 in thymoma-associated autoimmune disease. *The Lancet,* 350**,** 1596-1597.
MEAGER, A. & WADHWA, M. 2014. Detection of anti-cytokine antibodies and their clinical relevance. *Expert Rev Clin Immunol,* 10**,** 1029-47.
MEAGER, A., WADHWA, M., DILGER, P., BIRD, C., THORPE, R., NEWSOM-DAVIS, J. & WILLCOX, N. 2003. Anti-cytokine autoantibodies in autoimmunity: preponderance of neutralizing autoantibodies against interferon-alpha, interferon-omega and interleukin-12 in patients with thymoma and/or myasthenia gravis. *Clinical & Experimental Immunology,* 132**,** 128-136.
MERKEL, P. A., LEBO, T. & KNIGHT, V. 2019. Functional Analysis of Anti-cytokine Autoantibodies Using Flow Cytometry. *Front Immunol,* 10**,** 1517.
MIRE-SLUIS, A. R., BARRETT, Y. C., DEVANARAYAN, V., KOREN, E., LIU, H., MAIA, M., PARISH, T., SCOTT, G., SHANKAR, G., SHORES, E., SWANSON, S. J., TANIGUCHI, G., WIERDA, D. & ZUCKERMAN, L. A. 2004. Recommendations for the design and optimization of immunoassays used in the detection of host antibodies against biotechnology products. *J Immunol Methods,* 289**,** 1-16.
MIZUGUCHI, H., XU, Z., ISHII-WATABE, A., UCHIDA, E. & HAYAKAWA, T. 2000. IRES-dependent second gene expression is significantly lower than cap-dependent first gene expression in a bicistronic vector. *Mol Ther,* 1**,** 376-82.
MONSTAD, S. E., KNUDSEN, A., SALVESEN, H. B., AARSETH, J. H. & VEDELER, C. A. 2009. Onconeural antibodies in sera from patients with various types of tumours. *Cancer Immunol Immunother,* 58**,** 1795-800.
O'DONOVAN, B., MANDEL-BREHM, C., VAZQUEZ, S. E., LIU, J., PARENT, A. V., ANDERSON, M. S., KASSIMATIS, T., ZEKERIDOU, A., HAUSER, S. L., PITTOCK, S. J., CHOW, E., WILSON, M. R. & DERISI, J. L. 2020. High-resolution epitope mapping of anti-Hu and anti-Yo autoimmunity by programmable phage display. *Brain Commun,* 2**,** fcaa059.
OFTEDAL, B. E., WOLFF, A. S., BRATLAND, E., KAMPE, O., PERHEENTUPA, J., MYHRE, A. G., MEAGER, A., PURUSHOTHAMAN, R., TEN, S. & HUSEBYE, E. S. 2008. Radioimmunoassay for autoantibodies against interferon omega; its use in the diagnosis of autoimmune polyendocrine syndrome type I. *Clin Immunol,* 129**,** 163-9.
OKANO, H. J., PARK, W.-Y., CORRADI, J. P. & DARNELL, R. B. 1999. The cytoplasmic Purkinje onconeural antigen cdr2 down-regulates c-Myc function: implications for neuronal and tumor cell survival. *Genes & development,* 13**,** 2087-2097.

PANG, S. W., LAHIRI, C., POH, C. L. & TAN, K. O. 2018. PNMA family: Protein interaction network and cell signalling pathways implicated in cancer and apoptosis. *Cellular signalling,* 45**,** 54-62.
PERFETTO, S. P., CHATTOPADHYAY, P. K., LAMOREAUX, L., NGUYEN, R., AMBROZAK, D., KOUP, R. A. & ROEDERER, M. 2006. Amine reactive dyes: an effective tool to discriminate live and dead cells in polychromatic flow cytometry. *J Immunol Methods,* 313**,** 199-208.
PERNIOLA, R. 2018. Twenty Years of AIRE. *Front Immunol,* 9**,** 98.
PESCHL, P., SCHANDA, K., ZEKA, B., GIVEN, K., BOHM, D., RUPRECHT, K., SAIZ, A., LUTTEROTTI, A., ROSTASY, K., HOFTBERGER, R., BERGER, T., MACKLIN, W., LASSMANN, H., BRADL, M., BENNETT, J. L. & REINDL, M. 2017. Human antibodies against the myelin oligodendrocyte glycoprotein can cause complement-dependent demyelination. *J Neuroinflammation,* 14**,** 208.
PIGNOLET, B. S., GEBAUER, C. M. & LIBLAU, R. S. 2013. Immunopathogenesis of paraneoplastic neurological syndromes associated with anti-Hu antibodies: A beneficial antitumor immune response going awry. *Oncoimmunology,* 2**,** e27384.
PLANAGUMA, J., LEYPOLDT, F., MANNARA, F., GUTIERREZ-CUESTA, J., MARTIN-GARCIA, E., AGUILAR, E., TITULAER, M. J., PETIT-PEDROL, M., JAIN, A., BALICE-GORDON, R., LAKADAMYALI, M., GRAUS, F., MALDONADO, R. & DALMAU, J. 2015. Human N-methyl D-aspartate receptor antibodies alter memory and behaviour in mice. *Brain,* 138**,** 94-109.
PONNUSAMY, R. & LOHKAMP, B. 2013. Insights into the oligomerization of CRMP s: crystal structure of human collapsin response mediator protein 5. *Journal of neurochemistry,* 125**,** 855-868.
POSNER, J. B. 1995. *Neurologic complications of cancer*, FA Davis Company.
PRAIN, K., WOODHALL, M., VINCENT, A., RAMANATHAN, S., BARNETT, M. H., BUNDELL, C. S., PARRATT, J. D. E., SILVESTRINI, R. A., BUKHARI, W., AUSTRALIAN, NEW ZEALAND, N. M. O. C., BRILOT, F., WATERS, P. & BROADLEY, S. A. 2019. AQP4 Antibody Assay Sensitivity Comparison in the Era of the 2015 Diagnostic Criteria for NMOSD. *Front Neurol,* 10**,** 1028.
PRASAD, S. & CHEN, J. 2019. What You Need to Know About AQP4, MOG, and NMOSD. *Semin Neurol,* 39**,** 718-731.
REINDL, M., SCHANDA, K., WOODHALL, M., TEA, F., RAMANATHAN, S., SAGEN, J., FRYER, J. P., MILLS, J., TEEGEN, B., MINDORF, S., RITTER, N., KRUMMREI, U., STOCKER, W., EGGERT, J., FLANAGAN, E. P., RAMBERGER, M., HEGEN, H., ROSTASY, K., BERGER, T., LEITE, M. I., PALACE, J., IRANI, S. R., DALE, R. C., PROBST, C., PROBST, M., BRILOT, F., PITTOCK, S. J. & WATERS, P. 2020. International multicenter examination of MOG antibody assays. *Neurol Neuroimmunol Neuroinflamm,* 7.
REINDL, M. & WATERS, P. 2019. Myelin oligodendrocyte glycoprotein antibodies in neurological disease. *Nat Rev Neurol,* 15**,** 89-102.
RICKEN, G., SCHWAIGER, C., DE SIMONI, D., PICHLER, V., LANG, J., GLATTER, S., MACHER, S., ROMMER, P. S., SCHOLZE, P., KUBISTA, H., KONECZNY, I. & HOFTBERGER, R. 2018. Detection Methods for Autoantibodies in Suspected Autoimmune Encephalitis. *Front Neurol,* 9**,** 841.
ROBERTS, W. K., DELUCA, I. J., THOMAS, A., FAK, J., WILLIAMS, T., BUCKLEY, N., DOUSMANIS, A. G., POSNER, J. B. & DARNELL, R. B. 2009. Patients with lung cancer and paraneoplastic Hu syndrome harbor HuD-specific type 2 CD8+ T cells. *J Clin Invest,* 119**,** 2042-51.

ROSE, N. R. & BONA, C. 1993. Defining criteria for autoimmune diseases (Witebsky's postulates revisited). *Immunology today,* 14**,** 426-430.
ROSENFELD, M. R., EICHEN, J. G., WADE, D. F., POSNER, J. B. & DALMAU, J. 2001. Molecular and clinical diversity in paraneoplastic immunity to Ma proteins. *Annals of Neurology: Official Journal of the American Neurological Association and the Child Neurology Society,* 50**,** 339-348.
ROUSSEAU, A., BENYAHIA, B., DALMAU, J., CONNAN, F., GUILLET, J.-G., DELATTRE, J.-Y. & CHOPPIN, J. 2005. T cell response to Hu-D peptides in patients with anti-Hu syndrome. *Journal of neuro-oncology,* 71**,** 231-236.
RUIZ-GARCIA, R., MARTINEZ-HERNANDEZ, E., GARCIA-ORMAECHEA, M., ESPANOL-REGO, M., SABATER, L., QUEROL, L., ILLA, I., DALMAU, J. & GRAUS, F. 2019. Caveats and Pitfalls of SOX1 Autoantibody Testing With a Commercial Line Blot Assay in Paraneoplastic Neurological Investigations. *Front Immunol,* 10**,** 769.
RUIZ-GARCIA, R., MARTINEZ-HERNANDEZ, E., SAIZ, A., DALMAU, J. & GRAUS, F. 2020. The diagnostic value of onconeural antibodies depends on how they are tested. *Front Immunol,* 11**,** 1482.
SABATER, L., SAIZ, A., DALMAU, J. & GRAUS, F. 2016. Pitfalls in the detection of CV2 (CRMP5) antibodies. *J Neuroimmunol,* 290**,** 80-3.
SAGGAU, C., SCHEFFOLD, A. & BACHER, P. 2021. Flow Cytometric Characterization of Human Antigen-Reactive T-Helper Cells. *Methods Mol Biol,* 2285**,** 141-152.
SATO, D. K., CALLEGARO, D., LANA-PEIXOTO, M. A., WATERS, P. J., DE HAIDAR JORGE, F. M., TAKAHASHI, T., NAKASHIMA, I., APOSTOLOS-PEREIRA, S. L., TALIM, N. & SIMM, R. F. 2014. Distinction between MOG antibody-positive and AQP4 antibody-positive NMO spectrum disorders. *Neurology,* 82**,** 474-481.
SCHAFER, K. H., KLOTZ, M., MERGNER, D., MESTRES, P., SCHIMRIGK, K. & BLAES, F. 2000. IgG-mediated cytotoxicity to myenteric plexus cultures in patients with paraneoplastic neurological syndromes. *J Autoimmun,* 15**,** 479-84.
SCHMID, I., UITTENBOGAART, C. & JAMIESON, B. D. 2007. Live-cell assay for detection of apoptosis by dual-laser flow cytometry using Hoechst 33342 and 7-amino-actinomycin D. *Nat Protoc,* 2**,** 187-90.
SECHI, E., BUCIUC, M., PITTOCK, S. J., CHEN, J. J., FRYER, J. P., JENKINS, S. M., BUDHRAM, A., WEINSHENKER, B. G., LOPEZ-CHIRIBOGA, A. S., TILLEMA, J. M., MCKEON, A., MILLS, J. R., TOBIN, W. O. & FLANAGAN, E. P. 2021. Positive Predictive Value of Myelin Oligodendrocyte Glycoprotein Autoantibody Testing. *JAMA Neurol,* 78**,** 741-746.
SHAH, S., FLANAGAN, E. P., PAUL, P., SMITH, C. Y., BRYANT, S. C., DEVINE, M. F., LENNON, V. A., MCKEON, A., PITTOCK, S. J. & DUBEY, D. 2022. Population-Based Epidemiology Study of Paraneoplastic Neurologic Syndromes. *Neurol Neuroimmunol Neuroinflamm,* 9.
SHIONO, H., WONG, Y. L., MATTHEWS, I., LIU, J. L., ZHANG, W., SIMS, G., MEAGER, A., BEESON, D., VINCENT, A. & WILLCOX, N. 2003. Spontaneous production of anti-IFN-alpha and anti-IL-12 autoantibodies by thymoma cells from myasthenia gravis patients suggests autoimmunization in the tumor. *Int Immunol,* 15**,** 903-13.
SKEIE, G., AARLI, J. & GILHUS, N. 2006. Titin and ryanodine receptor antibodies in myasthenia gravis. *Acta Neurologica Scandinavica,* 113**,** 19-23.

SMALL, M., TREILLEUX, I., COUILLAULT, C., PISSALOUX, D., PICARD, G., PAINDAVOINE, S., ATTIGNON, V., WANG, Q., ROGEMOND, V., LAY, S., RAY-COQUARD, I., PFISTERER, J., JOLY, F., DU BOIS, A., PSIMARAS, D., BENDRISS-VERMARE, N., CAUX, C., DUBOIS, B., HONNORAT, J. & DESESTRET, V. 2018. Genetic alterations and tumor immune attack in Yo paraneoplastic cerebellar degeneration. *Acta Neuropathol,* 135**,** 569-579.

SMITT, P. S., MANLEY, G. & POSNER, J. 1995. Immunization with the paraneoplastic encephalomyelitis antigen HuD does not cause neurologic disease in mice. *Neurology,* 45**,** 1873-1878.

SONG, S., MANOOK, M., KWUN, J., JACKSON, A. M., KNECHTLE, S. J. & KELSOE, G. 2021. A cell-based multiplex immunoassay platform using fluorescent protein-barcoded reporter cell lines. *Commun Biol,* 4**,** 1338.

SPADARO, M., WINKLMEIER, S., BELTRÁN, E., MACRINI, C., HÖFTBERGER, R., SCHUH, E., THALER, F. S., GERDES, L. A., LAURENT, S. & GERHARDS, R. 2018. Pathogenicity of human antibodies against myelin oligodendrocyte glycoprotein. *Annals of neurology,* 84**,** 315-328.

SUGIMOTO, K., MORI, M., LIU, J., TANAKA, S., KANEKO, K., OJI, S., TAKAHASHI, T., UZAWA, A., UCHIDA, T., MASUDA, H., OHTANI, R., NOMURA, K., HIWASA, T. & KUWABARA, S. 2019. The accuracy of flow cytometric cell-based assay to detect anti-myelin oligodendrocyte glycoprotein (MOG) antibodies determining the optimal method for positivity judgement. *J Neuroimmunol,* 336**,** 577021.

SUN, X., TAN, J., SUN, H., LIU, Y., GUAN, W., JIA, J. & WANG, Z. 2020. Anti-SOX1 Antibodies in Paraneoplastic Neurological Syndrome. *J Clin Neurol,* 16**,** 530-546.

SWANSON, S., JACOBS, S., MYTYCH, D., SHAH, C., INDELICATO, S. & BORDENS, R. 1999. Applications for the new electrochemiluminescent (ECL) and biosensor technologies. *Developments in biological standardization,* 97**,** 135-147.

SZABO, A., DALMAU, J., MANLEY, G., ROSENFELD, M., WONG, E., HENSON, J., POSNER, J. B. & FURNEAUX, H. M. 1991. HuD, a paraneoplastic encephalomyelitis antigen, contains RNA-binding domains and is homologous to Elav and Sex-lethal. *Cell,* 67**,** 325-333.

TANAKA, K., TANAKA, M., ONODERA, O., IGARASHI, S., MIYATAKE, T. & TSUJI, S. 1994. Passive transfer and active immunization with the recombinant leucine-zipper (Yo) protein as an attempt to establish an animal model of paraneoplastic cerebellar degeneration. *Journal of the neurological sciences,* 127**,** 153-158.

TAVERNA, J. A., BABIKER, H. M., YUN, S., BISHOP, M. C., LAU-BRAUNHUT, S., MEYER, P. N. & ENZLER, T. 2014. The great masquerader of malignancy: chronic intestinal pseudo-obstruction. *Biomark Res,* 2**,** 23.

TAYRI-WILK, T., SLAVIN, M., ZAMEL, J., BLASS, A., COHEN, S., MOTZIK, A., SUN, X., SHALEV, D. E., RAM, O. & KALISMAN, N. 2020. Mass spectrometry reveals the chemistry of formaldehyde cross-linking in structured proteins. *Nat Commun,* 11**,** 3128.

TOTLAND, C., HAUGEN, M. & VEDELER, C. 2021. CRMP5 Antibodies-Diagnostic Challenges. *Front Neurol,* 12**,** 729075.

TOZZOLI, R. 2020. Receptor autoimmunity: diagnostic and therapeutic implications. *Auto Immun Highlights,* 11**,** 1.

TSAO, C. M., YAN, M. D., SHIH, Y. L., YU, P. N., KUO, C. C., LIN, W. C., LI, H. J. & LIN, Y. W. 2012. SOX1 functions as a tumor suppressor by antagonizing the WNT/beta-catenin signaling pathway in hepatocellular carcinoma. *Hepatology,* 56**,** 2277-87.

VOGRIG, A., GIGLI, G. L., SEGATTI, S., CORAZZA, E., MARINI, A., BERNARDINI, A., VALENT, F., FABRIS, M., CURCIO, F., BRIGO, F., IACONO, D., PASSADORE, P., RANA, M., HONNORAT, J. & VALENTE, M. 2020. Epidemiology of paraneoplastic neurological syndromes: a population-based study. *J Neurol,* 267**,** 26-35.

VON STEMANN, J. H., RIGAS, A. S., THORNER, L. W., RASMUSSEN, D. G. K., PEDERSEN, O. B., ROSTGAARD, K., ERIKSTRUP, C., ULLUM, H. & HANSEN, M. B. 2017. Prevalence and correlation of cytokine-specific autoantibodies with epidemiological factors and C-reactive protein in 8,972 healthy individuals: Results from the Danish Blood Donor Study. *PLoS One,* 12**,** e0179981.

WADHWA, M., BIRD, C., DILGER, P., GAINES-DAS, R. & THORPE, R. 2003. Strategies for detection, measurement and characterization of unwanted antibodies induced by therapeutic biologicals. *Journal of Immunological Methods,* 278**,** 1-17.

WADHWA, M. & THORPE, R. 2010. Unwanted immunogenicity: lessons learned and future challenges. *Bioanalysis,* 2**,** 1073-1084.

WANG, C., TAI, Y., LISANTI, M. P. & LIAO, D. J. 2011. c-Myc induction of programmed cell death may contribute to carcinogenesis: a perspective inspired by several concepts of chemical carcinogenesis. *Cancer Biol Ther,* 11**,** 615-26.

WATERS, P., MCKEON, A., LEITE, M., RAJASEKHARAN, S., LENNON, V., VILLALOBOS, A., PALACE, J., MANDREKAR, J., VINCENT, A. & BAR-OR, A. 2012. Serologic diagnosis of NMO: a multicenter comparison of aquaporin-4-IgG assays. *Neurology,* 78**,** 665-671.

WATERS, P., REINDL, M., SAIZ, A., SCHANDA, K., TULLER, F., KRAL, V., NYTROVA, P., SOBEK, O., NIELSEN, H. H., BARINGTON, T., LILLEVANG, S. T., ILLES, Z., RENTZSCH, K., BERTHELE, A., BERKI, T., GRANIERI, L., BERTOLOTTO, A., GIOMETTO, B., ZULIANI, L., HAMANN, D., VAN PELT, E. D., HINTZEN, R., HOFTBERGER, R., COSTA, C., COMABELLA, M., MONTALBAN, X., TINTORE, M., SIVA, A., ALTINTAS, A., DENIZ, G., WOODHALL, M., PALACE, J., PAUL, F., HARTUNG, H. P., AKTAS, O., JARIUS, S., WILDEMANN, B., VEDELER, C., RUIZ, A., LEITE, M. I., TRILLENBERG, P., PROBST, M., SASCHENBRECKER, S., VINCENT, A. & MARIGNIER, R. 2016. Multicentre comparison of a diagnostic assay: aquaporin-4 antibodies in neuromyelitis optica. *J Neurol Neurosurg Psychiatry,* 87**,** 1005-15.

WATERS, P., WOODHALL, M., O'CONNOR, K. C., REINDL, M., LANG, B., SATO, D. K., JURYNCZYK, M., TACKLEY, G., ROCHA, J., TAKAHASHI, T., MISU, T., NAKASHIMA, I., PALACE, J., FUJIHARA, K., LEITE, M. I. & VINCENT, A. 2015. MOG cell-based assay detects non-MS patients with inflammatory neurologic disease. *Neurol Neuroimmunol Neuroinflamm,* 2**,** e89.

WINGERCHUK, D. M., BANWELL, B., BENNETT, J. L., CABRE, P., CARROLL, W., CHITNIS, T., DE SEZE, J., FUJIHARA, K., GREENBERG, B. & JACOB, A. 2015. International consensus diagnostic criteria for neuromyelitis optica spectrum disorders. *Neurology,* 85**,** 177-189.

WITEBSKY, E., ROSE, N. R., TERPLAN, K., PAINE, J. R. & EGAN, R. W. 1957. CHRONIC THYROIDITIS AND AUTOIMMUNIZATION. *Journal of the American Medical Association,* 164**,** 1439-1447.

YSHII, L., BOST, C. & LIBLAU, R. 2020. Immunological Bases of Paraneoplastic Cerebellar Degeneration and Therapeutic Implications. *Front Immunol,* 11**,** 991.

ZHANG, L., QIAN, W., CHEN, Q., YIN, L., LI, B. & WANG, H. 2014. Imbalance in circulating T lymphocyte subsets contributes to Hu antibody-associated paraneoplastic neurological syndromes. *Cell Immunol,* 290**,** 245-50.